

Stabilization and Imaging of Cohesionless Soil Specimens

by

Zbigniew David Czupak

A Thesis Presented in Partial Fulfillment
of the Requirements for the Degree
Master of Science

Approved July 2011 by the
Graduate Supervisory Committee:

Edward Kavazanjian, Chair
Claudia Zapata
Sandra Houston

ARIZONA STATE UNIVERSITY

August 2011

ABSTRACT

This dissertation describes development of a procedure for obtaining high quality, optical grade sand coupons from frozen sand specimens of Ottawa 20/30 sand for image processing and analysis to quantify soil structure along with a methodology for quantifying the microstructure from the images. A technique for thawing and stabilizing frozen core samples was developed using optical grade Buehler[®] Epo-Tek[®] epoxy resin, a modified triaxial cell, a vacuum/reservoir chamber, a desiccator, and a moisture gauge. The uniform epoxy resin impregnation required proper drying of the soil specimen, application of appropriate confining pressure and vacuum levels, and epoxy mixing, de-airing and curing. The resulting stabilized sand specimen was sectioned into 10 mm thick coupons that were planed, ground, and polished with progressively finer diamond abrasive grit levels using the modified Allied HTP Inc. polishing method so that the soil structure could be accurately quantified using images obtained with the use of an optical microscopy technique. Illumination via Bright Field Microscopy was used to capture the images for subsequent image processing and sand microstructure analysis. The quality of resulting images and the validity of the subsequent image morphology analysis hinged largely on employment of a polishing and grinding technique that resulted in a flat, scratch free, reflective coupon surface characterized by minimal microstructure relief and good contrast between the sand particles and the surrounding epoxy resin. Subsequent image processing involved conversion of the color images first to gray scale images and then to binary images with the use of contrast and image adjustments, removal of

noise and image artifacts, image filtering, and image segmentation. Mathematical morphology algorithms were used on the resulting binary images to further enhance image quality. The binary images were then used to calculate soil structure parameters that included particle roundness and sphericity, particle orientation variability represented by rose diagrams, statistics on the local void ratio variability as a function of the sample size, and the local void ratio distribution histograms using Oda's method and Voronoi tessellation method, including the skewness, kurtosis, and entropy of a gamma cumulative probability distribution fit to the local void ratio distribution.

DEDICATION

This work is dedicated to my wonderful parents, Jan and Olga Czupak, who have provided both emotional and financial support in my academic career throughout the years. This educational journey could not have happened without them.

I also want to extend very special thanks to my sister, Heather Dye, for believing in me and my ability to achieve this goal. Her guidance and patience were invaluable.

ACKNOWLEDGEMENT

It would have been impossible to complete this research work without the help of my advisor, Dr. Edward Kavazanjian. He has provided me with endless guidance, support and encouragement during my years of working as a graduate student.

Dr. Kavazanjian was instrumental in guiding me to make my decision to pursue a career in geotechnical engineering when I was an undergraduate student.

Special thanks to the Arizona State University's Geotechnical Lab Director, Peter Goguen, for the technical support and help in conducting my experiments.

I would also like to thank David Wright, the LeRoy Eyring Center for Solid State Science Senior Research Professional, for access to and training on the optical microscopy and the grinding/polishing equipment.

Many thanks go to Dr. Matt Evans, the North Carolina State University assistant professor, for providing Matlab code used in quantification of local void ratio variability.

This research is only part of a much larger project involved in characterization of post-liquefaction properties of cohesionless soils that included participation of several universities. Sincere thanks to the National Science Foundation which provided the funding for this project.

TABLE OF CONTENTS

	Page
LIST OF TABLES.....	xii
LIST OF FIGURES.....	xiv
CHAPTER	
1. INTRODUCTION	1
1.1. Objective	1
1.2. Background.....	1
1.3. Scope of Work	4
1.4. Organization of Thesis Work.....	5
2. LITERATURE REVIEW	7
2.1. Introduction.....	7
2.2. Microstructure Parameters for Cohesionless Soils	7
2.2.1. Particle Roundness and Sphericity	7
2.2.2. Particle Orientation.....	9
2.2.3. Relative Anisotropy Analysis.....	14
2.2.4. Global and Local Void Ratio.....	16
2.2.5. Frequency Distribution of Void Ratio.....	20
2.2.6. Entropy of Local Void Ratio Distribution Histogram..	25
2.2.7. Coordination Number.....	26
2.3. Stabilization Methods for Cohesionless Specimens	28
2.3.1. Freezing	31
2.3.2. Chemical Impregnation with Agar	35

CHAPTER	Page
2.3.3. Elmer’s Carpenter Glue	38
2.3.4. Epoxy Impregnation	39
2.4. Imaging of Epoxy-Stabilized Soil Samples	44
2.4.1. Bright Field Microscopy (BFM)	45
2.4.1.1. Nature of Light	47
2.4.1.4. Past Research.....	53
2.4.2. Electron Backscattered Diffraction (EBSD)	54
2.4.3. X-ray Computed Tomography (CT) Imagining	57
2.4.3.1. Tomography	59
2.4.3.2. X-ray Computed Tomography Process	60
2.4.3.3. Image Artifacts	62
2.5. Surface Preparation Techniques	63
2.5.1. Introduction	63
2.5.2. Cutting and Mounting	63
2.5.3. Planing and Manual Grinding	66
2.5.3.1. Planing.....	66
2.5.3.2. Manual Grinding	69
2.5.4. Lapping.....	71
2.5.4.1. Lap Plate.....	72
2.5.4.2. Abrasive Slurry.....	74
2.5.4.3. Truing Rings and Press Plate.....	76
2.5.4.4. Advantages of Lapping Process	76

CHAPTER	Page
2.5.5. Polishing.....	76
2.5.6. Specimen Cleaning and Preparation.....	78
2.5.7. Common Errors	79
2.6. Digital Image Processing and Analysis	82
3. TESTING PROCEDURE	86
3.1. Rationale for Selected Approach	86
3.2. Specimen Reconstitution and Sampling	88
3.2.1. Sand Properties.....	88
3.2.2. Dry Sand Specimens	90
3.2.2.1. Sand Preparation.....	91
3.2.2.2. Air Pluviation Technique for Dry Samples ...	91
3.2.3. Saturated Sand.....	96
3.2.3.1. Air Pluviation Technique for Frozen Samples	96
3.2.3.2. Freezing.....	97
3.2.3.3. Coring and Storage.....	99
3.3. Epoxy Impregnation Using Triaxial Cell Setup.....	100
3.3.1. Triaxial Test Device Setup and Modifications.....	100
3.3.2. Dry Chamber and Moisture Monitoring.....	101
3.3.3. Epoxy Impregnation Technique	103
3.3.4. Encountered Difficulties.....	105
3.4. Coupon Preparation	108

CHAPTER	Page
3.4.1. Cutting, Trimming and Planing.....	108
3.4.2. Manual Grinding	111
3.4.3. Manual Polishing.....	114
3.5. Image Capture.....	122
3.5.1. Bright Field Microscopy	122
3.5.1.1. Procedure.....	125
3.5.1.2. Image Acquisition	126
3.5.1.3. Image Resolution.....	129
3.5.1.4. Image Histogram	131
3.5.1.5. Image Distortions	133
4. RESULTS	135
4.1. Image Processing Procedure	135
4.2. Image Processing and Analysis with ImageJ Software	137
4.2.1. Grayscale Images	137
4.2.2. Procedure to Calibrate the Thresholding Value	139
4.2.3. Binary Images.....	142
4.3. Local Void Ratio.....	145
4.3.1. Representative Coupon Size.....	145
4.3.2. Oda's Method	147
4.3.3. Voronoi Tessellation	154
4.3.4. Gamma Probability Distribution	160
4.4. Particle Descriptors.....	162

CHAPTER	Page
4.4.1. Particle Roundness and Sphericity	162
4.4.2. Relative Anisotropy.....	167
4.4.3. Particle Orientation and Rose Diagrams	168
5. CONCLUSIONS AND RECOMMENDATIONS	173
5.1. Summary	173
5.2. Conclusions.....	175
5.3. Recommendations for Future Study	178
REFERENCES	180
APPENDIX	
A. EUROPEAN AND USA EQUIVALENCY GRIT GUIDE.....	190
B. SAND COUPON SURFACE PREPARATION METHOD, MODIFIED FROM BUEHLER DIALOG® METHOD	192
C. POLISHING CLOTH SELECTION GUIDE FROM BUEHLER® AND ALLIED HIGH TECH PRODUCTS INC.....	194
D. METPRET3™ SYSTEM POLISHING PROCEDURE FOR GEOLOGICAL SAMPLES FROM ALLIED HIGH TECH INC ..	197
E. GUIDE FOR SELECTING PRECISION SAW WAFERING BLADES	199
F. BOX DESIGN DRAWINGS FOR THE BOX USED IN LIQUEFACTION, FREEZING AND AND SPECIMEN ECTRACTION EXPERIMENTS	201

APPENDIX	Page
G. HAND GRINDING/POLISHING JIG DESIGN SPECIFICATIONS	205
H. CONSUMABLES USED IN MANUAL POLISHING OF EPOXY- IMPREGNATED SAND COUPONS.....	207
I. LUMINERA'S INFINITY 2-1 CCD DIGITAL CAMERA PERFORMANCE SPECIFICATIONS.....	209
J. IMAGE STICING WITH PANAVUE SOFTWARE IMAGE ASSEMBLER	211
K. IMAGE PROCESSING ALGORITHM FOR BINARY IMAGE CONVERSION USING IMAGEJ	214
L. SEGMENTATION CALIBRATION RESULTS FOR VARIOUS THRESHOLDING METHODS.....	217
M. IMAGEJ SCREEN CAPTURES AND PROGRAM SETTINGS USED IN PROCESSING OF BINARY IMAGES USING MANUAL AND MATHEMATICAL MORPHOLOGY TECHNIQUES.....	222
N. POLYGON NETWORK GENERATION AND LOCAL VOID RATIO CALCULATIONS USING VORONOI TESSELLATION METHOD	225

LIST OF TABLES

Table	Page
2.1. Properties of Epo-Tek [®] 301 Two-part Resin.	42
2.2. General Classification of Computed Tomography. (Ketcham and Carlson, 2001)	61
2.3. Specimen Surface Damage from Cutting. (www.buehler.com)	64
2.4. Parameters Used for Polishing and Grinding. (Evans, 2005)	73
2.5. List of Most Commonly Used Abrasives and Their Hardness. (www.reade.com)	75
3.1. Physical Characteristics of Ottawa 20/30 Sand.	90
3.2. Grinding Procedure.	113
3.3. Polishing Procedure for Buehler [®] Epo-Tek [®] 301 Optical Grade Epoxy- Impregnated Ottawa 20/30 Sand Coupons. (www.alliedtech.com)	117
3.4. InfiniVar GS Characteristics Based on 160 mm Tube Lens and 35mm Format. Not Adjusted for 2.2x Zoom Module. (www.infinity-usa.com)	123
4.1 Calculated Error Associated with Different Thresholding Methods	141
4.2. Standard Deviation of Global Void Ratio as a Function of Representative Image Size, Control Coupon.	146
4.3. Variability in Mean Void Ratio of Control and Frozen Coupon Based on Representative Image Size	153
4.4. Method Specific Error in Voronoi Tessellation Resulting from Polygon Network Generation.	159

Table	Page
4.5 Shape Descriptors for the Gamma Distribution Function.....	162
4.6 Particle Shape Descriptors for the Control and the Frozen Coupons. ...	164
4.7. Relative Anisotropy of Grains from the Control and the Frozen Specimens.....	168
4.8. Particle Orientation Rose Diagrams at Different Bin Sizes.....	171

LIST OF FIGURES

Figure	Page
2.1. Powers Particle Classification Based on Sphericity and Roundness. (Powers, 1982).....	8
2.2. Particle Orientation. (a) Three-dimensional. (b) Two-dimensional. (Parks, 1999)	10
2.3. Frequency Distribution of Contact Plane Angles For Specimens with 50% Relative Density. (Ibrahim and Kagawa, 1991).....	13
2.4. Frequency Distribution of Contact Plane Angles for Specimens with 50% Relative Density after Liquefaction. (Ibrahim and Kagawa, 1991)	14
2.5. Definition and Concept of Anisotropy Measurements.(Yang, 2002)	15
2.6. Local Void Ratio Measurement (Oda, 1976).....	16
2.7. Different Ways Create a Polygon using Oda's Method	18
2.8. Comparison between Oda's Method and Voronoi Tessellation: (a) Polygon Network Using Oda's Method. (b) Voronoi Tessellation Method. (Alshibli and El-Saidany, 2001)	19
2.9. Theoretical Frequency Distribution of Void Ratios for Different Density Values. (Shahinpoor and Shahrpass, 1982).....	21
2.10. Effect of Particle Shape on Frequency Distribution Function of Void Ratio. (Bhatia and Soliman, 1990)	22
2.11. Evaluation of Local Void Ratio Distribution Models Using Space of Pearson's Probability Distribution. (Pearson and Hartley, 1972).....	25

Figure	Page
2.12. Relationship between Mean Coordination Number and Void Ratio. (Oda, 1982).....	27
2.13. Relation between Co-ordination Number and Standard Deviation in Homogeneous, Two-mixed and Multi-mixed assemblies. (Oda, 1977)	28
2.14. (a) Method of Sampling by Radial Freezing. (b) One-Dimensional Freezing Test. (Yoshimi et al., 1978).....	32
2.15. (a) Effect of Surcharge on Expansive Strains Due to Freezing. (b) Expansive Strain Due to Freezing and Surcharge for Tonegawa Sand. (Yoshimi et al., 1978).....	34
2.16. Effect of All-Around Freezing in Triaxial Cell with No Drainage. (Singh, 1982).....	35
2.17. (a) Agar Solution Viscosity vs. Temperature Based on Agar Concentration. (b) Volume Change Based on Agar Concentration and Temperature.....	37
2.18. Strain Due to Curing of Epoxy-Impregnated Sand Sample in Triaxial Cell at $\sigma_3 = 50$ kPa. (Jung, 1997)	43
2.19. Episcopic Illumination System. (Davidson, 2010)	47
2.20. The Spectrum of Electromagnetic Waves, Including Visible Light Spectrum. (BIOSYNTRX, 2005)	48
2.21. Diagram of Reflections from Smooth and Rough Surfaces.....	49
2.22. Refraction of Light Passing from One Medium to Another.	50

Figure	Page
2.23. Finite-Tube and Infinity-Corrected Microscope Systems. (Davidson and Abramowitz, 2003).....	53
2.24. (a) EBSD Measurement Process (IFW-Dresden). (b) Image Capture with ESEM and Resulting Image.	56
2.25. Beam Configurations in X-ray CT Systems.	61
2.26. Rubbing, Ploughing, and Cutting Regimes of Deformation in Abrasive Machining. (Marinescu, 2004)	67
2.27. Effect of Grinding Forces on Wheel Deflection and Real Depth of Cut. (Rowe, 2009).....	67
2.28. Manual Grinding and Polishing Procedure. (Chinn, 2002)	71
2.29. Single-side Lapping Process. (www.azom.com, 2011)	72
2.30. Epoxy-Stabilized Ottawa 20/30 Sand Grains with Visible Edge Rounding and Surface Plucking.....	80
2.31. Image Processing and Analysis Philosophy According to Kuo (1994).	84
3.1. Grain Size Distribution for Ottawa Sand 20/30.....	89
3.2. Microscopic Image of Ottawa 20/30 Sand.....	89
3.3. Effect of Drop Height on Void Ratio and Density From Air Pluviation.	92
3.4. Void Ratio Reduction of Sand From e_i to e_f after Dying and Impregnation with Buehler [®] Epo-Tek [®] 301 at $\sigma_3=50$ kPa.(Jang, 1997)	93
3.5. (a) Manual Air Pluviator. (b) Dispersing Screen.	94

Figure	Page
3.6. (b) Split Mold before Air Pluviation. (b) After Air Pluviation with Sand.	95
3.7. Density Variation Due to Height Drop Change For Air-Pluviated Ottawa 20/30 Sand. (Kanyembo, 2011).....	96
3.8. The Box Used for Wet Sample Preparation during Saturation Process.	97
3.9. (a) Freezing of Fully Saturated Ottawa 20/30 Sand. (b) Resulting Semi- circular Mass of Stabilized, Frozen Soil.	98
3.10. (a) Drilling of Frozen Sand Core Samples with a Hand Drill and Guide Fig. (b) Top View of the Frozen Soil Mass after Specimen Extraction.	99
3.11. Epoxy Impregnation Setup.	101
3.12. Specimen Drying Setup.	102
3.13. (a) Sand Coupon Flooded with Epo-Tek [®] 301. (b) Overnight Curing in Vacuum Chamber (right) and Pressure Chamber (left).....	107
3.14. Dyna-Cut 18-inch Diamond Slab Saw.....	109
3.15. Haring Surface Planer.	110
3.16. (a). Buehler [®] Ecomet III Manual Grinder and Grinding/Polishing Jig. (b). Grinding/Polishing Jig Loaded with Weights During Manual Grinding Process.	112
3.17. (a) Coupon Surface After Sectioning with Diamond Chap Saw. (a) Coupon Surface After Final Grinding Step with 600 Grit SiC Abrasive.	114

Figure	Page
3.18. Effect of Sand Particle’s Relief and Edge Rounding on Quantitative Measurements. (Jang, 1999).....	115
3.19. (a) Gold Label Polishing Cloth Moistened with Lubricant and Sand Coupon Inside Polishing Jig, left. (b) Manual Polishing Setup (right).	119
3.20. Images of Ottawa 20/30 Epoxy-Impregnated Sand Coupons at Various Stages of Polishing.	121
3.21. Experimental Setup Used for Image Capture with Bright Field Microscopy.	125
3.22. Image Preview of Coupon Surface with Image Histogram and Image Capture Control Software.....	128
3.23. Scanning Order of the Coupon Surface for Subsequent Reassembly with PanaVue Image Assembler.	128
3.24. The Airy Disks of Two Points. (a) Single Airy Disk Pattern. (b) Two Airy Disks at Limit of Resolution. (c) Two Airy Disks Overlapping. (www.micro.magnet.fsu.edu).....	130
3.25. Histogram Response of 8-bit, Gray-scale Image to Different Illumination Levels and Polishing Errors.....	133
4.1. Work Flow Diagram for Image Processing.	136
4.2. Image Processing Algorithm for 8-bit Gray Scale to Binary Image Conversion.....	138

Figure	Page
4.3. Results of the Huang, Intermodes and IsoData Segmentation Methods on the Gray Scale Image.	142
4.4. Image Processing Algorithm of a Binary Image Using Manual Techniques and Mathematical Morphology.	145
4.5. Standard Deviation from Global Mean vs. Image Area.	147
4.6. Standard Deviation from Global Mean vs. Average Particle Count....	147
4.7. Polygon Network Generation for Local Void Ratio Calculations using Oda's (1976) Method. (a) Binary Image. (b) Polygon Network of Image Using Oda's Method.	148
4.8. Comparison of Local Void Ratio Distribution for a Control and Frozen Sample Using Oda's Method. (a) 16,000 μm by 16,000 μm . (b) 16,000 μm by 8,000 μm . (c) 8,000 μm by 8,000 μm . (d) 4,000 μm by 4,000 μm	152
4.9. Procedure to Generate Voronoi Polygon Network in <i>ImageJ</i>	154
4.10. Voronoi Tessellation. (a) Voronoi Polygon Network with Black Grains and Surrounding Voids in Gray. (b) Grain Areas Subtracted for A_v Calculation.	155
4.11. General Forms of Kurtosis. (www.mvpprograms.com)	156
4.12. Local Void Ratio Frequency Distribution Histograms Calculated Using Voronoi Tessellation Method.	158
4.13. Error in Voronoi Tessellation Resulting from Polygon Network Generation Based on Coupon Size.	160

Figure	Page
4.14. Gamma Probability Distribution Fitted to Local Void Ratio Frequency Histogram Using Oda's Method. (a) Control Sample. (b) Frozen Sample.....	161
4.15. Particle Circularity Histogram, Control Sample.....	165
4.16. Particle Roundness Histogram, Control Sample.....	166
4.17. Particle Aspect Ratio Histogram, Control Sample.	166
4.18. Particle Solidity Histogram, Control Sample.....	167
4.19. Feret Diameter. (a) Maximum Feret. (b) Minimum Feret. (c) Angle between Maximum Feret Diameter and the Horizontal Axis.....	169

1. INTRODUCTION

1.1. Objective

The purpose of this study was to develop techniques for stabilization and imaging of cohesionless soil specimens recovered by freezing. Funded by the National Science Foundation, this research was part of a larger study with the goal of characterizing the post-liquefaction properties of cohesionless soils. As part of the project, techniques for undisturbed sample extraction and stabilization were developed to obtain samples that could be used with Bright Field Microscopy (BFM) and X-ray Computer Tomography (CT) imaging methods for microstructure evaluation.

1.2. Background

Specimen stabilization and image analysis techniques have been widely used in study of soil fabric properties. Since cohesionless soils rely upon friction forces to maintain their structure, obtaining intact sand specimens for image analysis is very difficult due to sampling disturbance associated with inserting sampling devices into the ground, reduction of effective stress during sampling, and vibrations during transport. Therefore, stabilization of cohesionless soil is generally required prior to image analysis as well as during handling and processing for image analysis.

Since the late 1930s, several stabilization techniques for field sampling and for specimen preparation in a laboratory setting have been developed. Freezing has been used in the past to obtain frozen core samples for both triaxial testing and microstructure analysis (Langer, 1939; Hvorslev, 1949; Yoshimi and

Hatanaka, 1973; Ishihara and Silver, 1977; Yoshimi et al., 1978; Singh et al., 1982; Gilbert et al., 1988). Other reversible stabilization techniques used include the biopolymer Agar (Schneider et al., 1989; Frost, 1989; Sutterer et al., 1996), Elmer's carpenter glue (Yang, 2002; Evans, 2005) and gelatin grouting (Dickinson, 1975), have been used to stabilize sand specimens for study of stress-strain behavior and soil fabric changes. Non-reversible stabilization techniques used to study soil structure have included the use of sodium silicate grouting (Hendricksen, 1941) and impregnation with optical grade epoxy (Oda et al., 1978; Ibrahim and Kagawa, 1991; Kuo and Frost, 1996; Jang et al. 1999; Masad and Muhunthan, 2000; Evans, 2005). Freezing has been the most widely used reversible technique for in-situ stabilization and sampling of cohesionless soil specimens. Once trimmed to proper dimensions and thawed out under vacuum, samples can then be subjected to standard geotechnical testing procedures. The thawed specimen can also be stabilized for microstructure analysis. Imaging techniques used for microstructure analysis of stabilized granular soil specimens include non-destructive techniques such as X-ray Computed Tomography (CT). Specimens can also be subjected to the destructive thin sectioning techniques to capture soil fabric images with optical microscope illumination and Electron Backscattered Diffraction (EBSD) methods.

Color or gray scale thin section images captured by optical methods have to be processed and analyzed to extract information about soil fabric characteristics such as void ratio distribution, co-ordination value, entropy, anisotropy, fabric tensor, tortuosity, and mean free path. This information is usually obtained from

the images with a computerized analysis. Computerized image processing of thin sections was pioneered by Jongerius et al. (1972), who developed a classification system for void patterns. Subsequently, geotechnical researches have used this technique to study the distribution of voids in porous media (Al-Raoush and Alshibli, 2005), shear band characterization in triaxial tests (Desruses et al., 1996; Oda and Kazama, 1998; Batiste et al., 2004; Evans, 2005; Yang, 2005), sand grain characteristics (Whalley, 1980; Alshibli and Alsaleh, 2004), shear strength of granular materials (Oda, 1977), fabric anisotropy (Oda et al., 1985; Yang, 2002), and fluid permeability of porous materials (Berryman and Blair, 1986; Wildenschild et al., 2002).

Image processing was described by Frost and Kuo (1996) as a process consisting of five distinct steps;

- Image generation and capture
- Image coding
- Image reconstruction
- Image enhancement
- Image analysis

Image coding and reconstruction includes storing and opening of images in a particular type of lossless image compression format (TIFF, BMP, PNG, GIF).

Image enhancement refers to “high-level” image processing techniques, including mathematical morphology (Sierra, 1982). Mathematical morphology enhances binary images through processes of erosion, dilation, segmentation, mask copy

and outline to enhance features of interest and to remove any artifacts. Finally, image analysis is used to calculate preselected soil fabric parameters from entire area of an enhanced image or some part thereof.

1.3. Scope of Work

This study was limited to development of stabilization and imaging techniques for frozen core samples. Additional work to develop the sample extraction methodology is only briefly described in this dissertation. The research work addressed herein included storage, trimming and epoxy impregnation of the frozen soil samples. Epoxy impregnation required thawing and then thoroughly drying the frozen specimens. To facilitate thawing, drying and the impregnation procedure, a specially modified triaxial test chamber was fitted with sacrificial, disposable valve and tubing components wherever direct contact with the optical grade epoxy occurred. The work also included the design of base and cap for the modified triaxial test chamber, construction of the vacuum/pressure chamber, and proper desiccant selection in order to properly dry the specimens.

In addition to stabilization and imaging of frozen samples, dry air-pluviated Ottawa 20/30 sand samples were stabilized with optical grade epoxy for use as a control set. Once imaged, the fabric structure of the control specimens was compared to the microstructure of the frozen samples to investigate the level of disturbance associated with freezing, sampling, storage, and stabilization.

Following stabilization with the epoxy, impregnated cores were cut to 1.0 cm thick coupons, wet polished with several grades of grit paper and diamond suspension, and the particle structure was captured and saved with a microscope

connected to a computer work station, a technique known as Bright Field Microscopy (BFM). In addition, some uncut cores were sent out to an X-ray Computer Tomography facility for non-destructive three-dimensional imaging of the specimen's soil fabric.

The resulting BFM images were analyzed with open source image processing and analysis software *ImageJ*. Appropriate contrast manipulation, image filtering, mathematical morphology and measurement techniques were applied to obtain microstructure properties. Structure parameters, such as global void ratio, variation in local void ratio, fabric entropy, and particle orientation rose diagrams, were then quantified.

1.4. Organization of Thesis Work

This dissertation is divided into five chapters, including this introductory chapter. Chapter 2 examines several published works relating to the structure parameters of cohesionless soils, stabilization methods for cohesionless soils such as epoxy, paper glue, and Agar impregnation, imaging capture techniques using Bright Field Microscopy and Computer Tomography, and a variety of image processing techniques used for soil property quantification. Chapter 3 outlines the rationale for the selected stabilization procedure, dry and frozen sample preparation methods, modification of the triaxial device for stabilization purposes, the experimental setup and the epoxy impregnation technique. In addition, Chapter 3 describes stabilized sample processing for subsequent imaging including cutting, trimming, polishing and imaging. Chapter 4 presents image processing and analysis results. Chapter 4 describes image manipulation methods

used with open-source software, *ImageJ* that yielded structural properties of the soil samples. Additionally, Chapter 4 compares those results to published soil characteristics of the material used and discusses problems encountered during the experiment. Finally, Chapter 5 presents conclusions and suggests topics for future research.

2. LITERATURE REVIEW

2.1. Introduction

The purpose of this study was to develop reliable methodology to quantify microstructure properties of saturated cohesionless soils. It has long been recognized that particle gradation, particle shape, particle orientation, the number of interparticle contacts, the void ratio and its variation, typically referred to as the soil fabric, has a significant influence on the soil's engineering properties.

Difficulty arises when attempting to obtain disturbance-free samples of cohesionless soil not only for standard geotechnical testing of stress/ strain relationships but also for soil fabric quantification. The following sections review past research on soil specimen sampling, preservation and processing, imaging techniques and quantification of soil fabric properties for cohesionless soils. The discussion of imaging techniques includes an overview of past work in the field of digital image acquisition, storage, and analysis with the use of mathematical morphology.

2.2. Microstructure Parameters for Cohesionless Soils

2.2.1. Particle Roundness and Sphericity

There are several different terms used to describe particle roundness and sphericity. These terms are widely accepted but not well standardized. Wadell (1932) defined roundness as the ratio of the average of radii of corners of the grain image to the maximum radius of the inscribed circle. Powers (1953) created a new roundness/sphericity index for sedimentary particles that depended

on the sharpness of the edges and not on the particle's shape. Powers' (1953) particle classification system for the roundness/sphericity index is shown in FIG.

2.1.

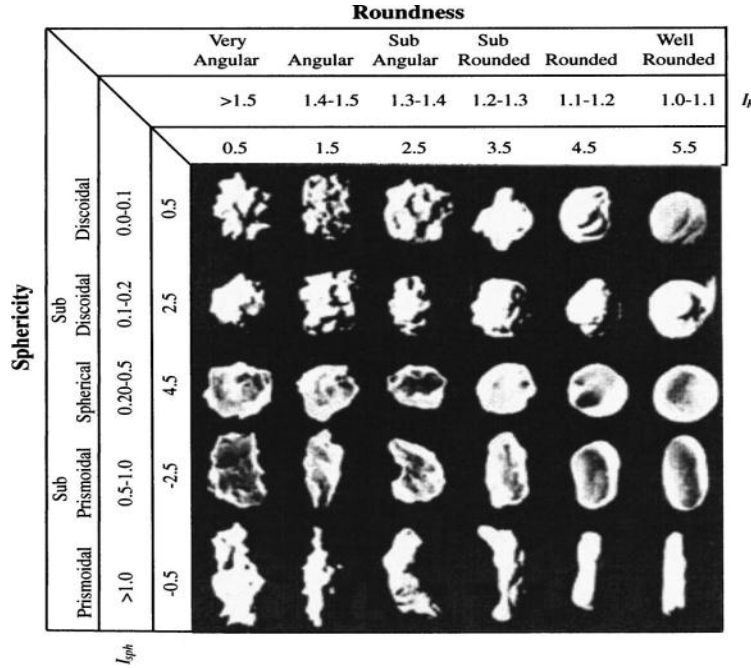


FIG. 2.1. Powers Particle Classification Based on Sphericity and Roundness. (Powers, 1982)

Masad et al, (2001) devised a sphericity parameter (SP) that they used to describe angularity of particles and a shape factor (SF) denoting the ratio of the particle's major dimension to its minor dimension as follows:

$$SP = \sqrt[3]{\frac{d_s d_l}{d_l^2}} \quad (2.1)$$

$$SF = \frac{d_s}{\sqrt{d_l d_l}} \quad (2.2)$$

where d_s , d_l , and d_L are the particle's shortest-, intermediate and longest-dimension, respectively. Another very common shape factor is the form factor (FF), sometimes referred to as circularity. Form factor is defined in Equation 2.3:

$$FF = \frac{4\pi A}{P^2} \quad (2.3)$$

where A and P are the projected area of the particle and perimeter of that area, respectively. The form factor can range from 0.0 to 1.0, with value of 1.0 being a perfect circle.

Alshibli and Mustafa (2004) developed a roundness index (I_R) and sphericity index (I_{sph}) to classify the different types of silica sand they studied with the use of an optical interferometer and image analysis software. I_R and I_{sph} were defined as follows:

$$I_R = \frac{1}{N} \sum_{i=1}^N \frac{P_{act(i)}}{\pi[(d_{s(i)} + d_{L(i)})/2]} \quad (2.4)$$

$$I_{sph} = \frac{1}{N} \sum_{i=1}^N \left[\frac{D_{equ(i)}}{d_{s(i)}} - \frac{D_{equ(i)}}{d_{L(i)}} \right] \quad (2.5)$$

$$D_{equ} = \frac{P_{act}}{\pi} \quad (2.6)$$

where $P_{act(i)}$ is the actual perimeter of the particle and D_{equ} is the equivalent particle diameter. Roundness index, I_r can range from 1.0 for well-rounded particles to greater than 1.5 for very angular particles. Sphericity index, I_{sph} can range from 0.0 for diskoidal particles to greater than 1.0 for prismoidal particles.

2.2.2. Particle Orientation

Particle orientation can be described either by the orientation of the normal of a tangential plane that passes through the interparticle contact point or by the inclination of the particle's long axes (Park, 1999). The inclination of the normal to a contact plane can be described with two angles, α and β , in three dimensional

space, as illustrated in FIG. 2.2(a). Since it is difficult to find the true orientation of the grain particle, a more simplified approach uses the orientation of the long axis of the particle described by the angle θ , in relation to a specified reference axis in two-dimensional space, as illustrated in FIG. 2.2(b).

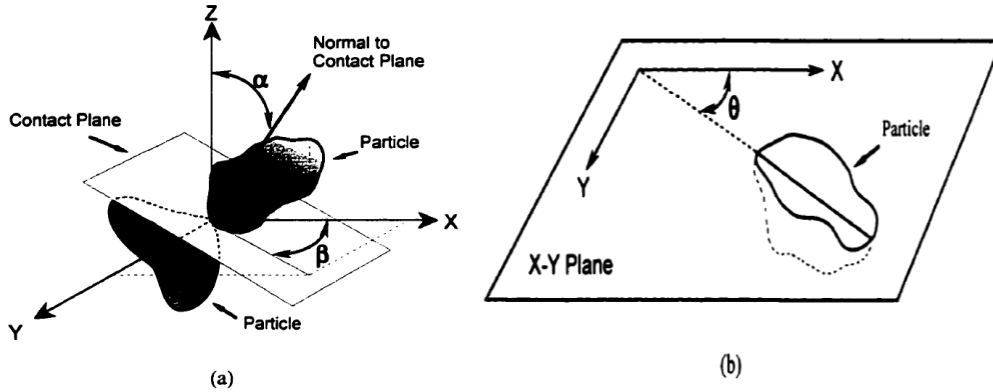


FIG. 2.2. Particle Orientation. (a) Three-dimensional. (b) Two-dimensional. (Parks, 1999)

Particle orientation distribution can be represented by a rose diagram that displays the resultant length of vector summations (orientations) and mean direction of the observed angles (Krumbein, 1939; Davis 1986; Fisher 1993). The resultant length of vector orientations (r) ranges from zero to one, with value of one indicating all particles arranged in one direction. It is defined as:

$$r = \frac{1}{\sum_{i=1}^n l_i} \sqrt{\left\{ \sum_{i=1}^n [l_i \cos(2\theta_i)] \right\}^2 + \left\{ \sum_{i=1}^n [l_i \sin(2\theta_i)] \right\}^2} \quad (2.7)$$

where θ_i is the orientation of the i^{th} particle and l_i is the length of the major axis of the best-fit ellipse for the i^{th} particle. The mean direction of observed particle angles (θ_i) represents the vector summation of the directions of all the resultant vectors for the range from 0° to 360° and can be calculated as follows:

$$\theta_r = \frac{1}{2} \tan^{-1} \left(\frac{\left\{ \sum_{i=1}^n [l_i \sin(2\theta_i)] \right\}}{\left\{ \sum_{i=1}^n [l_i \cos(2\theta_i)] \right\}} \right) \quad (2.8)$$

Equation 2.7 and Equation 2.8 need to be adjusted with a weighted value for the orientation of each particle to prevent bias that an abundant number of small particles could cause in calculations. Giving equal weight to all particles could introduce error in the rose diagram distribution by skewing the results toward the most abundant particle size class. Yang (2002) solved this problem by summing vectors so the weighted value was selected as the length of the calculated orientation in each particle divided by the summation of the lengths in the calculation orientation for all the particles.

Fisher (1993) recommended using a Rayleigh test to determine whether the calculated orientation was caused due to randomness, as in case of isotropic distributions where the resultant length is zero and all orientations are equally possible, or due to a true preferred orientation of the data. A Rayleigh test is used to check data uniformity against a unimodal distribution, with the null hypothesis that the data is uniformly distributed. The test values can be calculated according to Fisher (1993) as:

$$P(nr^2 \geq Z) = e^{-Z} \left(1 + \frac{2Z - Z^2}{4n} - \frac{24Z - 132Z^2 + 76Z^3 - 9Z^4}{288n^2} \right) \quad (2.9)$$

where n is the number of samples and Z is a critical value of nr^2 for a probability of occurrence (P) at some confidence interval (typically 95%).

Oda (1972a) studied particle orientation of four different sand types reconstituted using placement with a spoon from minimum drop height, prepared with sand plunging by air, and additional densification with tapping. Particle rose diagrams for the orientation of the long axis, θ , were generated from epoxy-impregnated thin section photographic images. Particle orientation was grouped into bins at 10° intervals in the horizontal plane. In addition, the study also applied dynamic compaction that resulted in a fairly random particle distribution. The pouring method caused particle orientation to be biased toward the horizontal direction.

Jang (1997) studied the structure of air-pluviated and moist tamped ASTM graded sand specimens. Jang (1997) studied spatial void ratio variability of specimens prepared by moist tamping and air pluviation and subjected to undrained triaxial testing. Jang (1997) quantified the particle orientation using concept of anisotropy which is a ratio of horizontal to vertical intercepts of particles in an image. The specimens were impregnated with epoxy resin to preserve their microstructure. Jang (1997) concluded that the anisotropy of sand particles is affected by the preparation method. The sand particles in moist tamped specimens were found to be more randomly oriented. Air-pluviated sand samples had particles that were more horizontally oriented. These results corroborated Oda's (1972a) findings.

Ibrahim and Kagawa (1991) studied particle anisotropy of sand specimens prepared with air pluviation, vibration and moist tamping techniques. These investigators looked at the effect of sample preparation and subsequent

liquefaction on the distribution of the orientation of the contact plane angles.

FIG. 2.3 shows the particle orientation after sample preparation and FIG. 2.4 illustrates particle orientation after liquefaction. The study demonstrated that the post-liquefaction particle arrangement in horizontal sections prepared with air pluviation and vibration becomes more random. Post liquefaction particle arrangement in the vertical direction showed preferential orientation in a discrete number of random directions. Air-pluviated samples had the smallest post liquefaction standard deviation of local void ratio but the moist tamped specimens showed no significant void ratio change after liquefaction.

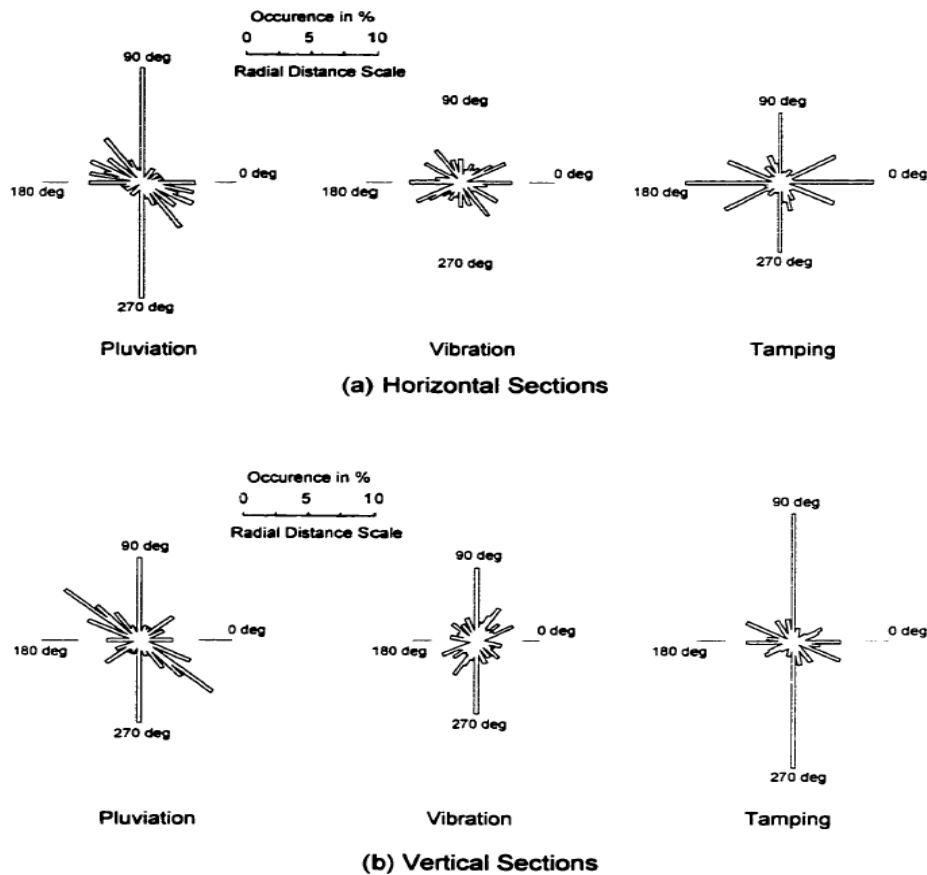


FIG. 2.3. Frequency Distribution of Contact Plane Angles For Specimens with 50% Relative Density. (Ibrahim and Kagawa, 1991)

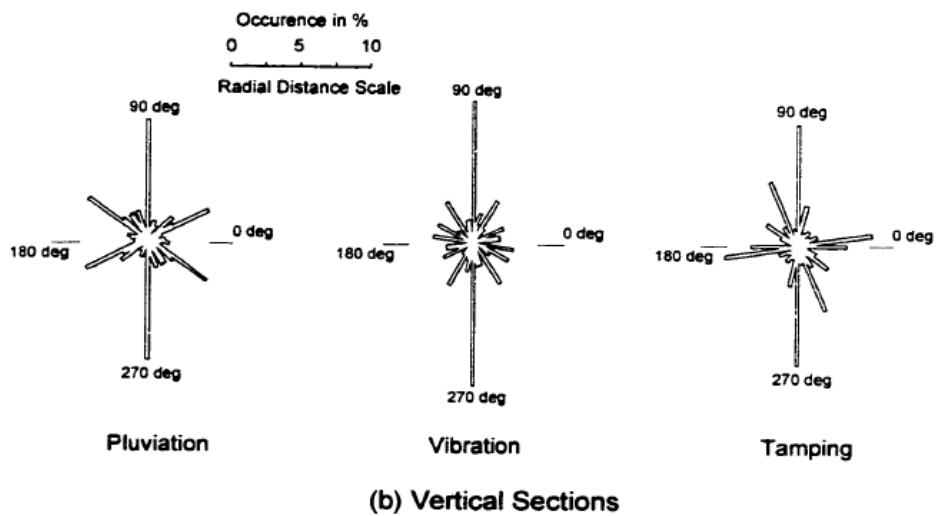
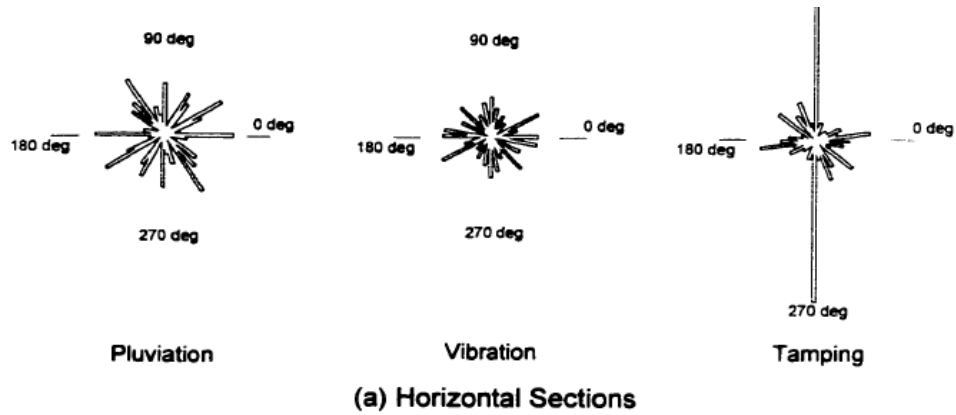


FIG. 2.4. Frequency Distribution of Contact Plane Angles for Specimens with 50% Relative Density after Liquefaction. (Ibrahim and Kagawa, 1991)

2.2.3. Relative Anisotropy Analysis

Yang (2002) developed the concept of an anisotropy measure in the image analysis of granular soils. Yang (2002) defined anisotropy as the ratio of unbroken horizontal lines to the unbroken vertical lines in the binary digital image where values greater than one indicated vertically oriented particles and values less than one indicated particles that were horizontally oriented. The process is illustrated in FIG. 2.5. The binary image is divided into horizontal and vertical

lines, one pixel in thickness. Number of uninterrupted horizontal and vertical intercepts is then summed. Ratio of total horizontal intercepts to the total of vertical intercepts represents particle anisotropy. In the Yang (2002) study the moist tamped specimens had average anisotropy of 0.96 and air-pluviated samples had average anisotropy of 0.89.

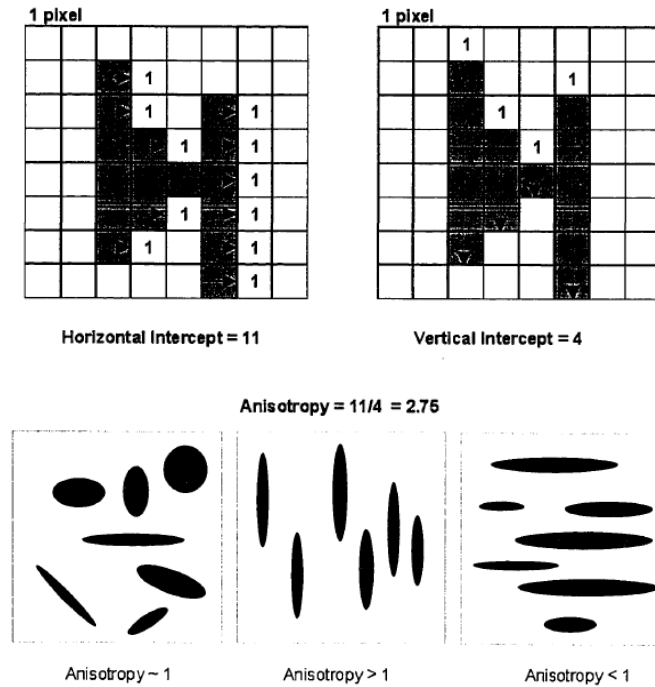


FIG. 2.5. Definition and Concept of Anisotropy Measurements.(Yang, 2002)

Yang (2002) found that his anisotropy measurement would give erroneous results for some rotated images. He found that normalized elongation index was a better representation of anisotropy, as it did not vary by sand type or by image selection and could be calculated with the “relative anisotropy” parameter, R.A. defined as:

$$R.A. = \frac{(a/b)_{int} - 1}{\max(a/b)_{int} - 1} \quad (2.10)$$

$$\max(a/b)_{\text{int}} = \frac{\sum_j a_j}{\sum_j b_j} \approx \frac{\sum_j \sqrt{A_j} \cdot (a/b)_j}{\sum_j \sqrt{A_j}} \quad (2.11)$$

where a_j is the length of the major axis of particle j , b_j is the length of the minor axis of particle j , (a/b) is defined as a ratio of the length of the major axis to the length of the minor axis in the fitted ellipse, j , $(a/b)_{\text{int}}$ is the calculated elongation index from the summation of the diameter lengths for each angle for all the particles of interest and A_j is the area for particle j . $\text{Max}(a/b)_{\text{int}}$ represents the maximum elongation value when all particles are oriented in just one direction.

2.2.4. Global and Local Void Ratio

The global void ratio and its local distribution is another widely used structure parameter. Oda (1976) was the first one to define a method to calculate local void ratio distribution of granular materials from images. Magnified images of the grains were used to create the network of polygon elements by connecting particles' centers of gravity with straight lines, as illustrated in FIG. 2.6.

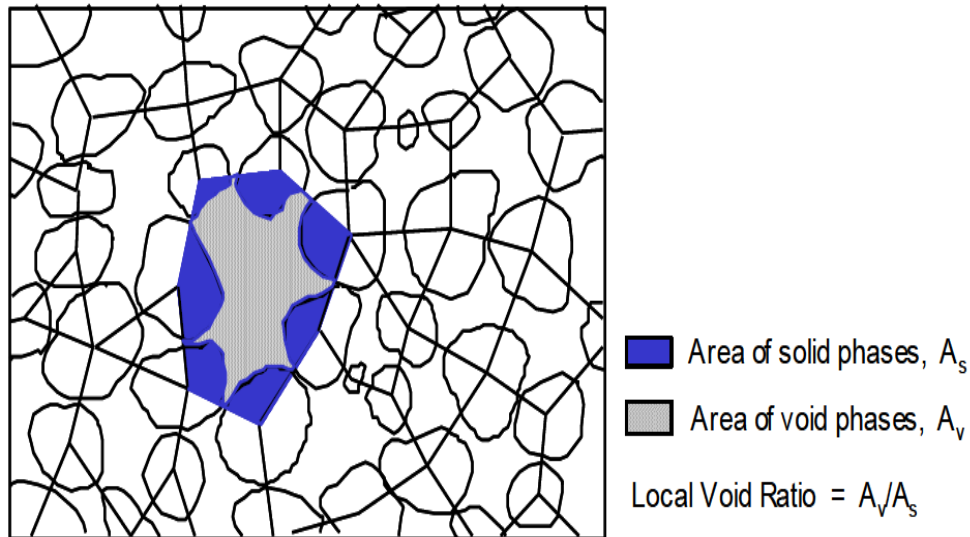


FIG. 2.6. Local Void Ratio Measurement. (Oda, 1976)

The areas occupied by the voids (A_{vi}) and solid particles (A_{si}) within each polygon were measured by hand to calculate the void ratio (e_i) of each polygon using following equation:

$$e_i = \frac{A_{vi}}{A_{si}} \quad (2.12)$$

Bhatia and Soliman (1990) used Oda's method to calculate local void ratio distributions of epoxy-stabilized thin section images of sand captured with a video monitor and a computer. They found that the mean value (\bar{e}) of the distribution given by Equation 2.13, is not equal to the global void ratio of the entire thin section (e_s) as given by Equation 2.14, unless the areas of solids (A_{si}) for all polygons were equal:

$$\bar{e} = \frac{1}{n}(e_1 + e_2 + \dots + e_n) = \frac{1}{n} \left(\frac{A_{v1}}{A_{s1}} + \frac{A_{v2}}{A_{s2}} + \dots + \frac{A_{vn}}{A_{sn}} \right) \quad (2.13)$$

$$e_s = \frac{\text{Total area of voids in an image}}{\text{Total area of solids in an image}} = \frac{A_{v1} + A_{v2} + \dots + A_{vn}}{A_{s1} + A_{s2} + \dots + A_{sn}} = \frac{A_v}{A_s} \quad (2.14)$$

where n is the number of polygons.

More problematic with Oda's method for quantifying the local void ratio distribution is the fact that the Oda's method depends on operator judgment when connecting centers of gravity of the particles, as illustrated in FIG. 2.7. No unique solution for those polygons exists because different ways of creating the polygon networks create variability in the standard deviation and mean void ratio. Bhatia and Soliman (1990) concluded that the Oda's method could not be fully automated since the method does not require the centers of gravity of particles located at the image periphery to be connected.

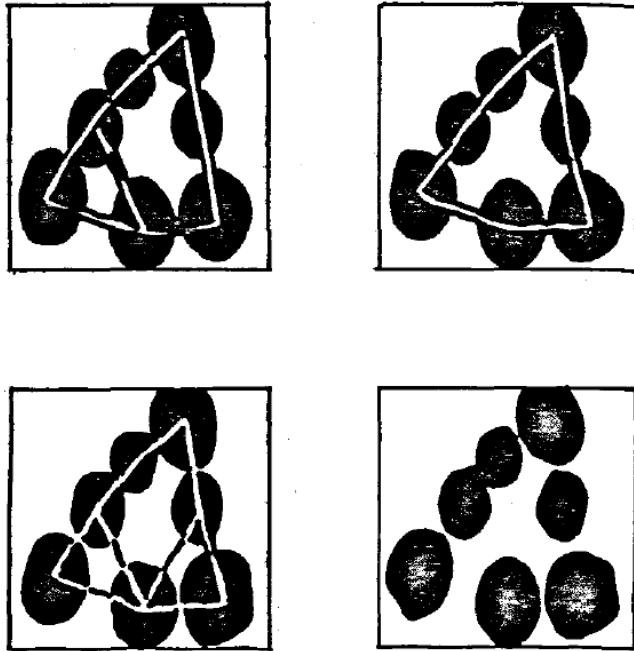


FIG. 2.7. Different Ways Create a Polygon using Oda's Method

Frost and Kuo (1996) were able to remove variability in local void ratio calculations caused by operator judgment in polygon creation by fully automating Oda's method with use of digital processing and analysis. An algorithm for Automated Determination of Local Void Ratio Distribution (AADLVRD) was developed to create a polygon network connecting centers of mass of sand grain particles within a binary image without any operator judgment or manual effort. A correction applied by Frost and Kuo (1996) to account for the thickness of the segmentation lines in the digital image resulted in a more accurate average global void ratio than reported by Bhatia and Soliman (1990). Frost and Kuo (1996) also resolved the problem of inequality between Equations 2.13 and Equation 2.14 by adjusting the mean value \bar{e} of the frequency distribution of local void ratio by the weighted solid area (A_{s_i}) in each polygon, as defined by Equation 2.15:

$$\bar{e}' = \frac{1}{\sum_{i=1}^n A_{si}} \left(\sum_{i=1}^n A_{si} \times e_i \right) \quad (2.15)$$

where \bar{e} is an adjusted mean void ratio. Substituting $e_i = \frac{A_{vi}}{A_{si}}$ into Equation 2.15

results in:

$$\bar{e}' = \frac{A_v}{A_s} = e_s \quad (2.16)$$

More recently, Alshibli and El-Saidany (2001) developed a fully automated voronoi tessellation method to quantify void ratio called an Algorithm for Automatic Determination of Local Void Ratio (AADLVR). Image processing and mathematical morphology were used on binary images to generate a proper, consistent polygon network for local void ratio calculations. Voronoi polygons illustrated in FIG. 2.8, were created from a circular growth process originated from a single particle centroid along a circular frontier. In this process, the circles are continually expanded using a watershed algorithm, resulting in contact points that created lines of a polygon network.

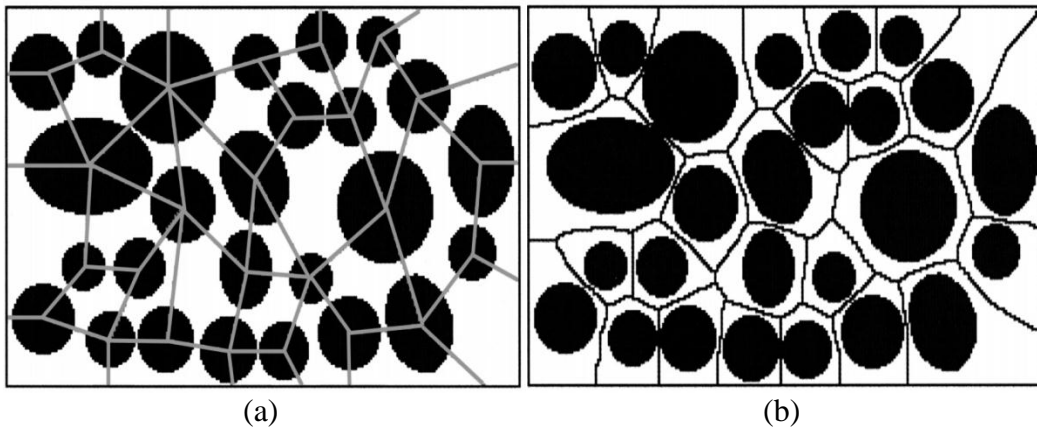


FIG. 2.8. Comparison between Oda's Method and Voronoi Tessellation: (a) Polygon Network Using Oda's Method. (b) Voronoi Tessellation Method. (Alshibli and El-Saidany, 2001)

This automated method developed by Alshibli and El-Saidany (2001) was shown to result in only a 0.4 percent local void ratio error when compared to manual calculation of voronoi polygons. Stated average void ratio (\bar{e}) from the automated method was much closer to the void ratio of the thin section (e_s), with much smaller standard deviation and smaller skewness of the void ratio distribution compared to Oda's method.

2.2.5. Frequency Distribution of Void Ratio

Shahinpoor (1981) studied local void ratio distribution in granular materials using statistical mechanics theory. He proposed that the probability distribution is a negative exponential function, skewed toward the heavier voids that can be represented by following equation:

$$f(e) = \frac{\lambda \exp(\lambda \times e)}{\exp(-\lambda e_m) - \exp(-\lambda e_M)} \text{ for } e_m \leq e \leq e_M \quad (2.17)$$

where e_m and e_M are the minimum and maximum void ratios in the packing order respectively and λ is a constant which can be determined from Equation 2.18:

$$\bar{e} = \frac{1}{\lambda} + \frac{e_m \exp(-\lambda e_m) - e_M \exp(-\lambda e_M)}{\exp(-\lambda e_m) - \exp(-\lambda e_M)} \quad (2.18)$$

where \bar{e} is the global void ratio of the packing. FIG. 2.9 illustrates the theoretical frequency distribution of void ratios for different soil densities as a function of the constant λ that can be used with both two- and three-dimensional packing orders of granular materials.

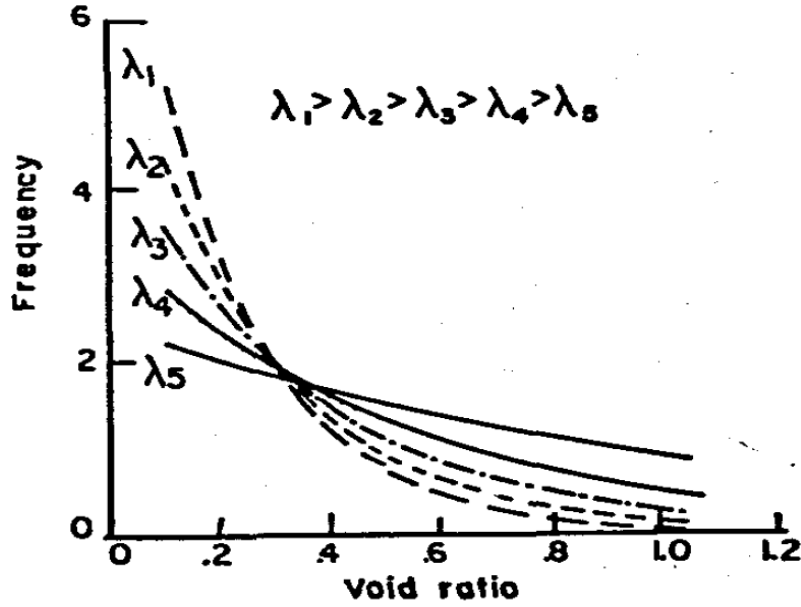


FIG. 2.9. Theoretical Frequency Distribution of Void Ratios for Different Density Values. (Shahinpoor and Shahrpass, 1982)

Bhatia and Soliman (1990) studied the frequency distribution of void ratio of glass beads, Ottawa sand and crystal silica. They found that Equation 2.17 and Equation 2.18 have a 1.0 percent Chi-square goodness-of-fit when describing the frequency distribution of glass beads previously described by Shahinpoor (1981). They found that the frequency distribution of Ottawa sand and crystal silica can be better approximated by a beta distribution as follows:

$$f(e) = \frac{\Gamma(\alpha + \beta)}{\Gamma(\alpha)\Gamma(\beta)(e_M - e_m)^{\beta-1}} \times (e - e_m)^{\alpha-1} (e_M - e)^{\beta-1} \quad (2.19)$$

where the beta distribution was fitted to the experimental distribution to find the α and β parameters. The resulting frequency distribution for the three materials they investigated is shown in FIG. 2.10.

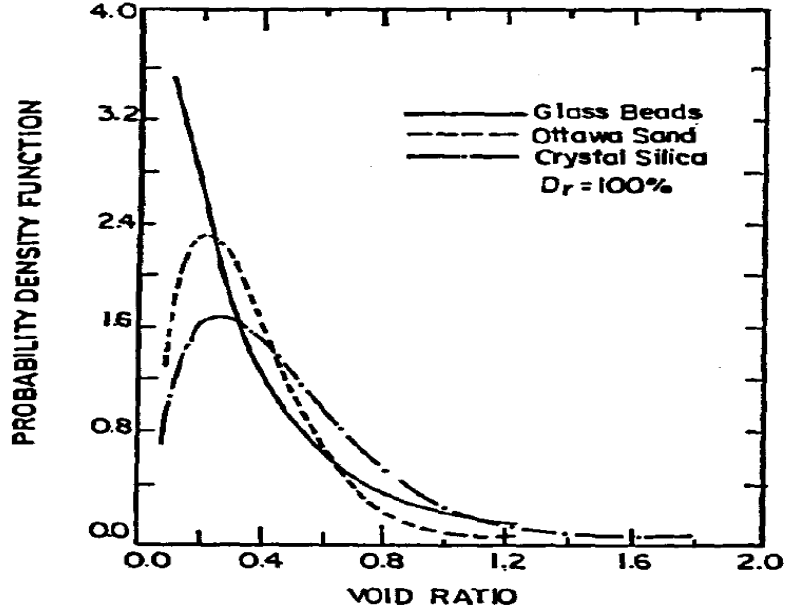


FIG. 2.10. Effect of Particle Shape on Frequency Distribution Function of Void Ratio. (Bhatia and Soliman, 1990)

Yang (2005) described use of the gamma probability distribution to describe the shape of the frequency distribution of local voids in a sample. The gamma distribution can be calculated as follows:

$$f(x) = \frac{\lambda}{\Gamma(k)} \times (\lambda x)^{k-1} \times \exp(-\lambda x) \quad \text{for } x > 0 \quad (2.20)$$

$$f(x) = 0 \quad \text{for } x \leq 0 \quad (2.21)$$

$$\Gamma(k) = \int_0^{\infty} x^{k-1} \times \exp(-x) dx \quad \text{for } n > 0 \quad (2.22)$$

where λ , k , and x are scale parameter, shape parameter and the pore size, respectively. The mean estimate (μ) and estimate of the variance (σ^2) for the gamma probability distribution of void ratios can be calculated using following equations:

$$\mu = E(x) = \frac{k}{\lambda} \quad (2.23)$$

$$\sigma^2 = V(x) = \frac{k}{\lambda^2} \quad (2.24)$$

Some investigators have suggested that the particle shape frequency distribution follows a lognormal distribution. A lognormal distribution can describe a random variable x if $y=\ln(x)$ is normally distributed with mean μ_y and variance σ_y^2 . The lognormal distribution is described by following equation:

$$f(x) = \frac{1}{\sigma_y x \sqrt{2\pi}} e^{\left[-\frac{1}{2\sigma_y^2} (\ln x - \mu_y)^2 \right]} \quad (2.25)$$

where x is the local void ratio. The mean value (μ) and variance of the lognormal distribution can be calculated as follows:

$$\mu = E(x) = \exp\left(\mu_y + \frac{1}{2} \sigma_y^2 \right) \quad (2.26)$$

$$\sigma^2 = V(x) = \left(e^{\sigma_y^2} - 1 \right) \exp\left[2\mu_y + \sigma_y^2 \right] \quad (2.27)$$

Pearson and Hartley (1972) introduced skewness and kurtosis to describe shape of the frequency distribution function. Skewness (β_1) measures asymmetry of the probability distribution and can be calculated with Equation 2.28:

$$\beta_1 = \frac{\sum_{i=1}^N (X - \mu)^3}{(N - 1)\sigma^3} \quad (2.28)$$

where N is the number of void areas, X is the variable of the distribution, μ is the mean and σ is the standard deviation of the distribution (Yang, 2005). A negative value indicates a left skew and a positive value indicates a right skew from the mean. Kurtosis (β_2) measures “peakedness” of the local voids ratio distribution and can be calculated with Equation 2.29:

$$\beta_2 = \frac{\sum_{i=1}^N (X_i - \mu)^4}{(N-1)\sigma^4} \quad (2.29)$$

The kurtosis for a standard normal distribution has a value of three. A high kurtosis value (above three) indicates a sharper peak and a longer, thicker tail and a low kurtosis value (below three) indicate a rounded peak and a shorter, thinner tail.

Once the parameters β_1 and β_2 are calculated for a random variable, the local void ratio distribution can be located in Pearson's space to determine best fitting model, as illustrated in FIG. 2.11. To determine the preferred model, the Kolmogorff-Smirnoff test is performed on each distribution function based on absolute difference (M) between the sample cumulative distribution function $F_A(x)$ and the cumulative distribution function $F_B(x)$ from the selected models (Yang,2002);

$$M = \max(F_A(x) - F_B(x)) \quad (2.30)$$

The best model is the one with the minimum M value from among all the different distributions.

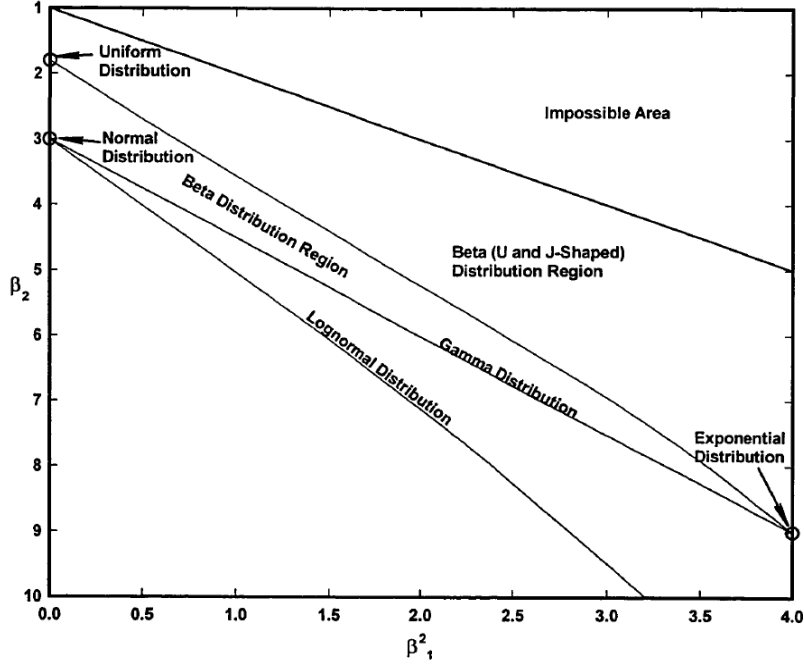


FIG. 2.11. Evaluation of Local Void Ratio Distribution Models Using Space of Pearson's Probability Distribution. (Pearson and Hartley, 1972)

2.2.6. Entropy of Local Void Ratio Distribution Histogram

Entropy describes uncertainty about the flatness of the local void ratio distribution function. Entropy evaluates the variation of the distribution of data in the histogram and was described by Shannon (1948) as an uncertainty function of discrete probabilities:

$$H = -\sum_{i=1}^N p_i \ln p_i \tag{2.31}$$

where p_i is the probability of the i^{th} bin and N is the number of void ratio intervals (bins). Yang (2005) found that local void ratio entropy of a sheared specimen is higher than those that were only isotropically consolidated. The entropy value is one for distributions having the same probability for each bin and zero if all data are in a single bin (Park, 1999).

2.2.7. Coordination Number

The coordination number (N) is the average number of contacts per particle in a three-dimensional assembly. Oda (1972) identified fabric orientation and packing as two fabric characteristics that define the spatial arrangement of solid particles and associated voids of granular materials. The following soil fabric elements can be determined by thin sections and microscope:

- Preferred orientation of long axes of particles
- Intensity of preferred dimensional orientation
- Three dimensional distribution of normal directions perpendicular to tangential planes at contacts
- Co-ordination number (or void ratio)

Oda (1977) determined experimentally that the co-ordination number value has a clear correlation to the void ratio of an assembly of particles and is independent of the characteristic of the grain-size distribution, as illustrated in FIG. 2.12. The coordination number value can be represented by a Gaussian distribution for a random assembly of homogeneous glass balls, but it becomes a polymodal distribution for multi-mixed particle assemblies.

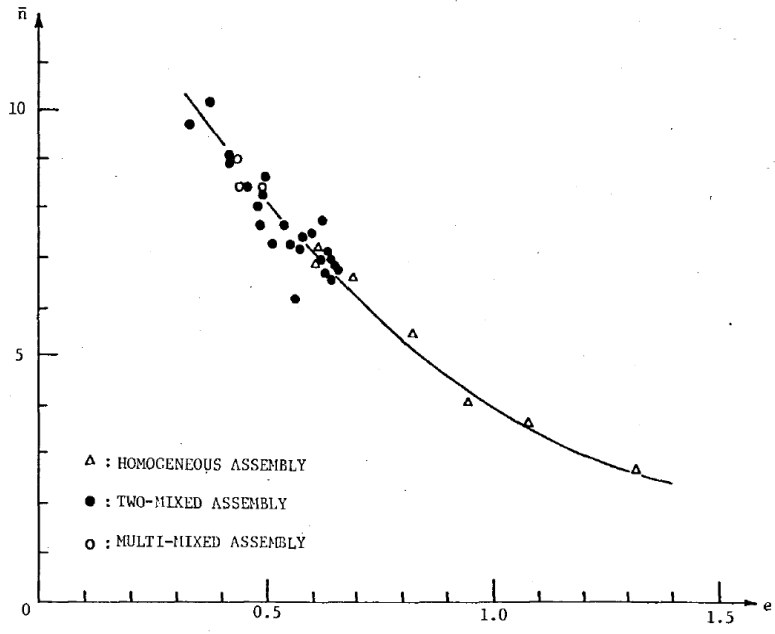


FIG. 2.12. Relationship between Mean Coordination Number and Void Ratio. (Oda, 1982)

The standard deviation of the co-ordination number describes the heterogeneity of the soil fabric throughout the assembly and is correlated to the void ratio of the assembly as illustrated in FIG. 2.13. According to Oda (1977), the forming of a denser sample by changing the characteristics of the grain-size distribution causes an increase in sample heterogeneity and an increase in the number of particle contacts, N .

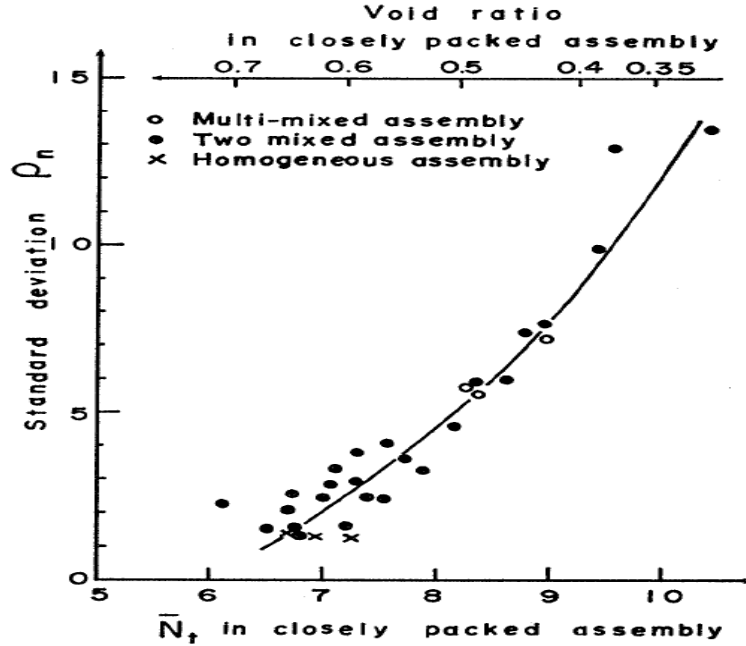


FIG. 2.13. Relation between Co-ordination Number and Standard Deviation in Homogeneous, Two-mixed and Multi-mixed assemblies. (Oda, 1977)

Oda et al. (1982) developed the following equation to quantify the density of contacts (N) within a granular soil fabric:

$$N = \frac{N^V}{V} = \frac{\bar{n}m^V}{2V} = \frac{3G(e)}{8\pi(1+e)r^3} \quad (2.32)$$

$$m^V = V\delta \quad (2.33)$$

$$\bar{n} = G(e) \quad (2.34)$$

where N^V is the total number of contacts, δ is the density of the points marking the center of particles, e is the void ratio and r is the particle radius, \bar{n} is the co-ordination number and the $G(e)$ function is defined by FIG. 2.12.

2.3. Stabilization Methods for Cohesionless Specimens

Undisturbed sampling of cohesionless soils for laboratory testing is very difficult. Clean sands primarily derive their strength from friction caused by sand particle interlocking. Disturbance caused by the sampling process, reduction of

effective stress to near zero during sampling, and vibration during transport all may result in breakdown of the soil structure (e.g. rearrangement of soil particles). According to Hvorslev (1977), the following requirements need to be satisfied during soil sampling for the soil to be considered undisturbed for laboratory testing:

- No disturbance of soil structure
- No change in water content or void ratio
- No change in constituents or chemical composition

Mitchell (2008) has shown that the shear strength of freshly deposited sand increases with time without any apparent change in void ratio, structure, or composition, thereby adding another dimension to the problem. Several methods have been devised to minimize soil structure disturbance in sampling of cohesionless soils. Shelby tubes fitted with mechanical core retainers, e.g. Denison and Mohr sampler have been used to prevent soil loss from extracted sand samples. These types of samplers may work well in cohesive soils but are not very reliable in clean sands because of excessive sample disturbance. Bishop (1948) used an auxiliary barrel to partially dewater cohesionless soil with compressed air before extracting the sample. The dewatered sample would hopefully have enough apparent cohesion from capillary forces to minimize disturbance to the soil matrix.

Various in-situ stabilization methods prior to sampling have been employed to minimize disturbance to the soil matrix of cohesionless soils during sample extraction and transport to laboratory for testing. These methods generally

require injection of some stabilizing substance into the soil voids that, once solidified, imparts cohesion to the soil and minimizes disturbance during sampling process. A reversible injection method, using a dilute emulsion of asphaltic bitumen to study the variation of density within large specimens of poorly graded, uniform sand, was described by Van Bruggen (1936). This labor intensive and difficult process required the bitumen emulsion to cure for 10 days after injection. The flushing process of the asphalt emulsion after sample extraction and drying had to be repeated several times. Flushing required repeatedly passing an evaporating fluid through the sample and recovering the fluid via a distillation process until it was free of asphalt emulsion.

Hendricksen (1941) used low viscosity sodium silicate grouting gel to stabilize sand prior to sampling. According to Hendricksen (1941) the sand properties were not affected once the gel was dissolved with sodium hydroxide or strong saline solution. Karol and Mark (1962) described a non-reversible grouting processing using water soluble AM-9 chemical grout powder prior to sampling with a split spoon. Since the grout cannot be removed from the soil matrix, this method was only used to observe small stratigraphic differences in the soil mass and direct measurements of shear strength but relative density could not be obtained. To address this shortcoming, Dickinson (1975) used a 3 % gelatin grouting solution to stabilize loose sand in-situ, prior to sampling. The gelatin grouting process could be reversed by heating the tested sand specimen to 40 ° C

in a specially modified triaxial cell to allow flushing of the gelatin from the soil matrix. Subsequent measurements of relative density and shear strength could then be performed accurately.

More recently, the reversible processes of freezing (Yoshimi et al., 1978; Singh et al., 1982; Gilbert et al., 1988), and impregnation with Agar (Arnott et al., 1974; Sutterer, 1993; Schneider et al., 1989), or Elmer's carpenter glue (Yang, 202; Evans, 2005) have been used to stabilize cohesionless soils for sampling and testing. The following sections describe the use of freezing, impregnation with Agar and impregnation with Elmer's carpenter glue for stabilization of loose soil specimens for laboratory testing. Non-reversible impregnation with optical grade epoxy for microstructure characterization with bright field microscopy and X-ray computer tomography is also discussed herein.

2.3.1. Freezing

Ground freezing has been used as a soil stabilization method for over a century, starting in England in 1862 where it was used to stabilize soil for off-shore shafts (Jones and Brown, 1994) and again in Wales in 1862 for wall stabilization of mining shafts in loose, water-logged soils (Lightfoot, 1886). Langer (1939), in France, used the freezing method to stabilize loose and very uniform sand deposits for sample extraction by pumping a mixture of dry ice and alcohol through a series of pipes driven into the ground prior to sample extraction. The first reported attempt to obtain in-situ undisturbed soil samples by freezing ground in the United States was done by the U.S. Army Corps of Engineers during construction of Fort Peck Dam (Hvorslev, 1949). The ground was frozen

by circulating a freezing coolant through seven pipes placed in circle around the soil mass to obtain frozen core samples 91.44 cm (36 inches) in diameter. The procedure resulted in formation of ice lenses in clayey soils but not in gravel and sand. A similar technique was employed by Yoshimi and Hatanaka (1973), using nitrogen circulated through three pipes. Ishihara and Silver (1977) used liquid nitrogen to stabilize sand samples extracted using a thin-walled tube for transport from field to the lab. Once extracted, the samples were allowed to drain for up to 24 hours, depending on the fines content prior to freezing. Negligible volume change was observed during freezing, indicating negligible disturbance to the soil fabric. Yoshimi et al. (1978) studied the effects of radial and one-dimensional freezing of saturated soil on sample disturbance due to volume change of the pore phase. The Yoshimi et al. (1978) experimental setups are illustrated in FIG. 2.14.

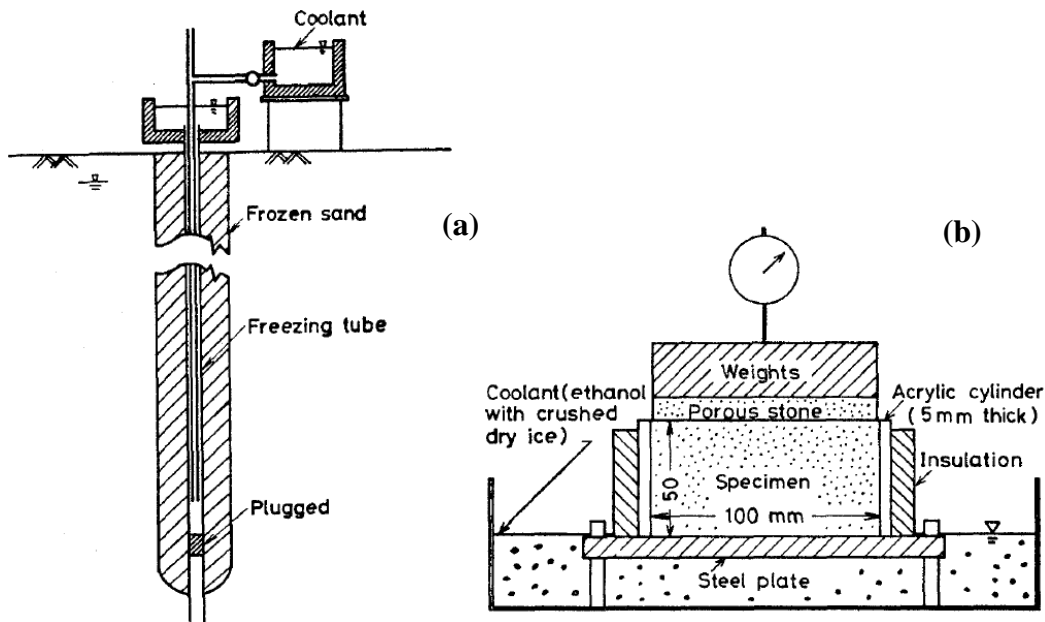


FIG. 2.14. (a) Method of Sampling by Radial Freezing. (b) One-Dimensional Freezing Test. (Yoshimi et al., 1978)

In the radial freezing test, illustrated in FIG. 2.14(a), a thin-walled steel tube was inserted into the ground, soil was removed from the tube and the bottom end of the tube was capped. A circulating mixture of ethanol and crushed dry ice was pumped through a vinyl pipe inserted into the steel tube to freeze the soil column radially. It was discovered that this process allowed excess pore water to escape outwards in fully saturated sand under moderate confining stresses. These investigations inferred that changes in shear stress due to radial freezing were relatively small if the initial mean principal stress exceeded 14.7 kPa (2.1 psi), which corresponds to 2.0 m of overburden cover for fully saturated soils.

The one-dimensional test, illustrated in FIG. 2.14(b), showed that the most important variables that influence the amount of sample disturbance due to freezing are the progress of the freezing front, the drainage conditions, confining stress, and the soil's fines content, as illustrated in FIG. 2.15. Lower permeability soils (Tonegawa sand) exhibited larger volume change when compared to soils containing fewer fines, given same surcharge load. Unidirectional freezing with unimpeded drainage and sufficient confining pressure was the best way to freeze sands in order to maintain their structure upon freezing.

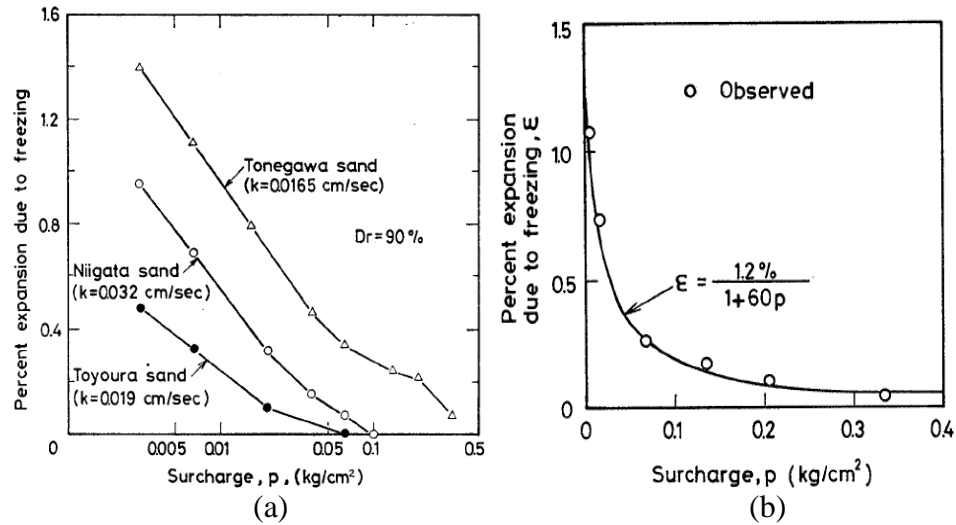


FIG. 2.15. (a) Effect of Surcharge on Expansive Strains Due to Freezing. (b) Expansive Strain Due to Freezing and Surcharge for Tonegawa Sand. (Yoshimi et al., 1978)

Singh et al. (1982) used a specially retrofitted triaxial cell to unidirectionally freeze saturated, free-draining Monterey No. 0 sand at 300 kPa (21.1 psi) and 245 kPa (35.6 psi) confining and back pressures, respectively. It was observed that the volume change and the cyclic strength characteristics of the frozen specimens remained the same after coring and thawing, and coring did not affect the sample's prior strain history characteristics.

Singh et al. (1982) and Walberg (1978) studied the effect of preparing drained frozen samples for shipment or handling. Both studies found no effects of freezing and then thawing drained samples on the dynamic strength characteristics of sand. Singh et al. (1982) demonstrated significant volume change and seismic history loss to samples with an impeded drainage path during freezing process, as illustrated in FIG. 2.16.

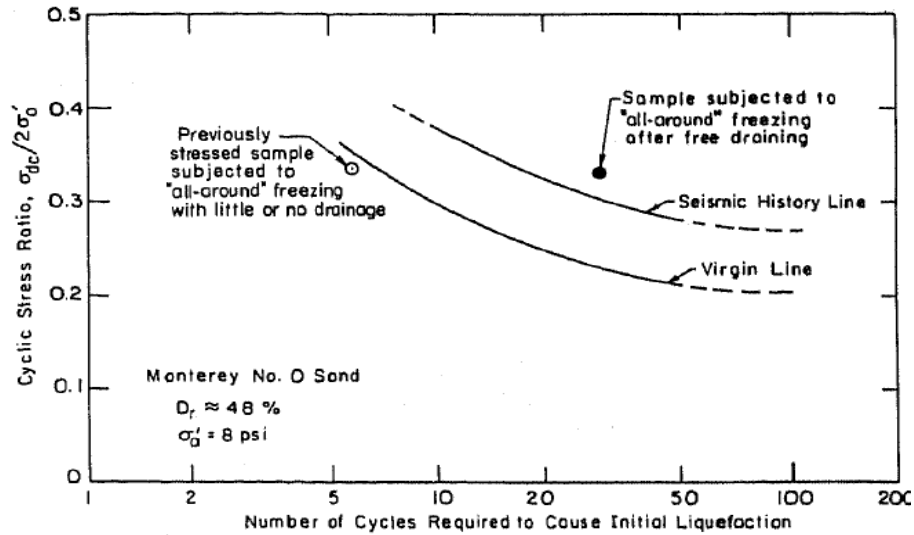


FIG. 2.16. Effect of All-Around Freezing in Triaxial Cell with No Drainage. (Singh, 1982)

Gilbert et al. (1988) used undrained cyclic triaxial tests to study density variation in cohesionless soil samples subjected to cyclic and monotonic loads. Banding sand, a clean, fine, uniform white quartz sand classified SP in the Unified Soil Classification System, was reconstituted using a wet pluviation technique, frozen, and trimmed using a lathe for placement in a triaxial cell for testing. Changes to local density caused by cyclic and monotonic loading were preserved by refreezing the samples and sectioning them into ninety six 2.54 cm (1 inch) cubes inside a dedicated cold room. The density variations within the sample could then be accurately quantified by measurement on the individual cubes.

2.3.2. Chemical Impregnation with Agar

Agar is a naturally occurring, water soluble bio polymer derived from a polysaccharide that accumulates in the cell walls of agarophyte red algae. It is non-toxic, yellow in color and odorless. Agarose and agarpectin are the two

main ingredients of agar. Agarose is a linear bio polymer composed of repeating monomeric units of agarobiose (disaccharide). It has the lowest degree of substitution and highest gelling potential of the two compounds. According to Arnott et al. (1974) the agarose gel makes a three dimensional network of interconnected strands that can provide soil structure with artificial cohesion and aid in undisturbed soil sampling. Agaropectin is composed of various similar polymers that gel poorly and are usually removed to improve gelling performance. According to Sutterer (1993), agar experiences gelling hysteresis, melting at temperatures from 50°C to 90°C and solidifying at temperatures from 8°C to 42°C, with gel strength from 1.0 to 28.5 kPa (0.145 to 4.14 psi). This polymer is widely used in microbiology in PCR DNA extraction and in the food industry as a stabilizing agent. Its thermal and mechanical properties can be varied depending on mixing, amount of impurities, and source.

Schneider et al. (1989) studied the feasibility of using agar as an impregnation material in undisturbed sampling of cohesionless soils. Sand samples were successfully recovered from below and above the water table by injecting a solution with a 0.8% concentration of agar into the soil mass and then coring. Cored out samples remained inside the sampling tubes for transport to the laboratory. Schneider et al. (1989) found that an agar solution of 0.5% by volume was sufficient to effectively stabilize sand specimens. FIG. 2.17(a) shows that at the melting point of 90° C the agar's viscosity varies from 2.0 to 4.0 cPs. FIG. 2.17(b) shows that the volume change of agar when transformed from solute to solid is less than 2.0 % for agar concentrations as high as 2.0 % by volume.

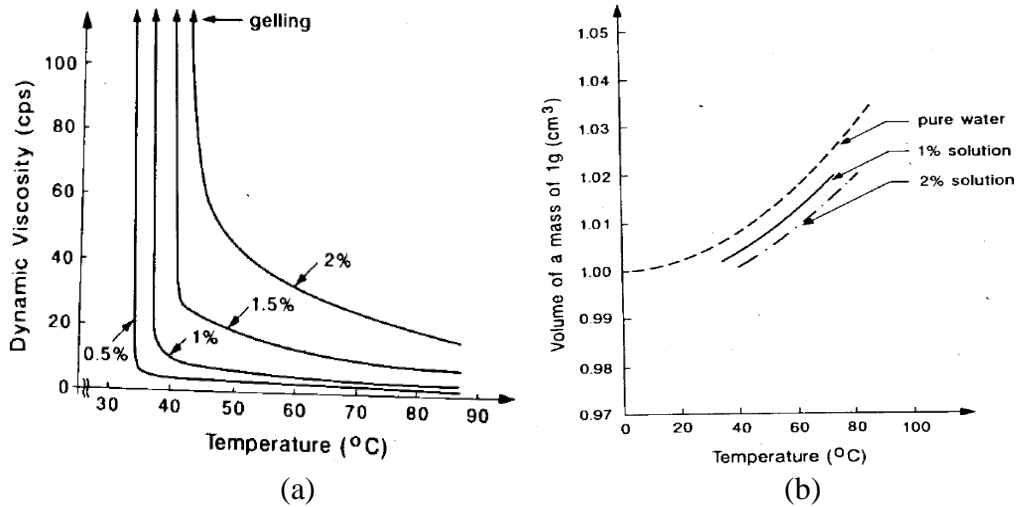


FIG. 2.17. (a) Agar Solution Viscosity vs. Temperature Based on Agar Concentration. (b) Volume Change Based on Agar Concentration and Temperature.

Frost (1989) used red dye and image capture with a Scanning Electron Microscope (SEM) to demonstrate the removal effectiveness of one directional flushing on Ottawa 20/30 sand specimens stabilized with a 1% agar solution. It was observed that the dye was initially entrapped between sand particles but was completely removed with two-directional flushing. This study showed that agar gel removal is possible and should not significantly affect the properties of clean sands.

Sutterer et al. (1996) studied the effect of agar impregnation of air-pluviated Ottawa 20/30 sand samples on contractive volume strain and cyclic shear stress. Contractive saturated specimens that were prepared in a modified triaxial cell and subjected to drained heating from 27 $^{\circ}\text{C}$ to 67 $^{\circ}\text{C}$ showed negligible structural volume changes. An agar polymer and water mixture (1.5% concentration) with 60 $^{\circ}\text{C}$ gel-melting temperature and 30 $^{\circ}\text{C}$ gelling temperature was used to assess

the effects of gel impregnation and repeated flushing on soil fabric. Undrained cyclic mobility was used as an indicator of changes in soil fabric. No significant variation in the cyclic shear stress ratio that induced liquefaction was found between samples impregnated with agar bio polymer and then flushed and the control samples. Sutterer et al. (1996) concluded that some fabric modification might have occurred within the soil fabric from leftover agar residue but not enough to affect cyclic mobility response of the sand tested.

2.3.3. Elmer's Carpenter Glue

Elmer's carpenter glue was used by several researchers (Yang, 2002; Evans, 2005) in a two stage specimen impregnation process for very loose sand samples. Initially, the soil fabric was flushed with a weak solution of Elmer's carpenter glue (5% to 7%) and water to lock the soil particles in place and to preserve the soil fabric properties prior to stabilization with epoxy. The specimen was then stabilized with optical grade epoxy for subsequent sectioning and image analysis. The initial weak bonding with Elmer's glue was deemed necessary to reduce shrinkage during the epoxy impregnation of very loose sand specimens. Yang (2002) found that when applying this two-stage process the axial strain shrinkage was reduced from 2.0% to 1.1% for liquefied sand samples in 2-D model tank test. Evans (2005) used the same two-stage procedure to stabilize triaxial sand specimens loaded to failure to study shear bands using bright field microscopy. In the Evans (2005) study, the samples were initially flushed with 7% Elmer's Glue and water solution within the triaxial cell, allowed to drain, dried for several days under low vacuum and then removed from the triaxial cell to be stabilized with

Epo-Tek[®] 301 two-part epoxy resin. This two-stage process eliminated concerns about epoxy fouling of the triaxial cell. Elmer's carpenter glue stabilized samples can be sectioned prior to impregnation with epoxy so specific areas can be preserved for further study, thus making the process less time consuming and less expensive than complete epoxy impregnation.

The two-stage system suffers from several shortcomings. Due to a high void ratio, lightly cemented loose sand specimens (e.g. Elmer's carpenter glue stabilized specimens) are prone to fracture and collapse during handling. This is especially significant for sheared samples where the reduced number grain contacts within the shear zone make it more prone to disturbance during handling than unsheared samples. Several researchers (Oda and Kazama, 1998; Stormont and Anderson, 1999; Evans, 2005) also recognized an effect of a capillary barrier formed in a sheared specimen wherein the high void ratio within the shear zone prevented adequate impregnation of the specimen above that area when using vacuum or driving pressure to advance the stabilizing medium. Increasing pressure or vacuum to compensate may result in some sample disturbance.

2.3.4. Epoxy Impregnation

Preservation of soil structure for microstructural analysis with optical grade epoxy resin is more practical than use of freezing, Elmer's carpenter glue or agar because the resulting specimens are typically harder and less susceptible to disturbance when cured. Therefore, the subsequent sectioning, grinding, and polishing procedure does not cause any loss in specimen integrity. This non-reversible process can be used in-situ or in the lab to preserve soil structure of

sand samples. Optical grade epoxy impregnation techniques to preserve the sand specimens are well documented in the literature (Oda et al., 1978; Ibrahim and Kagawa, 1991; Kuo and Frost, 1996; Jang et al. 1999; Masad and Muhunthan, 2000; Evans, 2005). Non-reversible injection methods to study the variation of density within large specimens of cohesionless soil using laminar polyester resin injection were described by Griffin (1954). However, the procedures studied by Griffin (1954) failed to produce accurate results due to high injection pressures and excessive volumetric strain during the curing process. Clayton et al. (1994) successfully used two part Stycast W19 epoxy resin and a catalyst with a reactive diluent with a low initial viscosity of 5 cPs and setting time of 6-12 hours to study density variation in reconstituted, dry sand samples.

Epoxy resins are widely used in specimen preservation because they are much harder, provide much stronger bond when cured and are more stable compared to other types of resins. The most critical consideration when selecting an appropriate epoxy for preservation of cohesionless soils is the amount of sample disturbance caused due to the impregnation and curing process. Most air-cured epoxy resins have a viscosity of 300 cPs or higher in ambient temperature when compared to the 1 cPs viscosity of water. Loose sand specimens are susceptible to disturbance during impregnation when the epoxy's viscosity is too high. Disturbance to the specimen may also result from volume change caused by differential thermal stresses. Many low viscosity resins produce significant exothermic reactions during the curing process or require elevated temperature, as high as 60-70°C, for curing to occur. Some epoxy resins may contain higher

amounts of solvent to increase viscosity that is lost during vacuum impregnation and subsequent curing, resulting in a larger amount of shrinkage than typical epoxy resins. Finally, the epoxy resin used for soil stabilization should have good resilience to cutting, sectioning and polishing, as well as good optical refractive properties for use in microscope imaging. Jang et al. (1999) recommend the following epoxy resin properties for sand specimen impregnation:

- Low viscosity
- Room temperature curing
- Low shrinkage during curing
- High hardness value and high bonding strength on curing
- Short curing time
- Nonreactive with soil and test equipment

Some of the few optical grade resins that meet above requirements include Hxtal NYL-1, Epo-Tek[®] 301 and currently discontinued Abelbond resin.

Buehler[®]'s Epo-Tek[®] 301 two-part, low viscosity epoxy meets all of the above requirements and is therefore very well suited for geotechnical applications.

Table 2.1 lists some of the physical and chemical properties of Epo-Tek[®] 301 epoxy.

Table 2.1. Properties of Epo-Tek[®] 301 Two-part Resin.

PROPERTY	VALUE
Mixing Ratio	4:1 base to hardener
Pot Life	1-2 hrs.
Minimum Bond Line Cure	24 hrs. at 23°C
Specific Gravity	1.15 (base), 0.87 (hardener)
Color	clear
Viscosity	100-200 cPs
Shore D Hardness	85
Index of Refraction @23 °C	1.51@589 nm.

Epo-Tek[®] 301 is widely used and its properties well understood in the fields of biological tissue preservation and impregnation of core specimens for geology. According to Jang et al. (1999), thanks to 100% solid formulation that contains no solvent, the linear shrinkage during curing of Epo-Tek[®] 301 is a relatively low 1.5% when compared to the more typical value of 5% for other epoxies. Yamamuro (2008) found very small axial deformation in specimens before and after the epoxy impregnation. Average, maximum, and minimum values of volumetric strain measured by Yamamuro (2008) following impregnation with Epo-Tek[®] 301 epoxy amounted to 0.15%, 0.33%, and 0.00% respectively, indicating very low disturbance to the soil fabric. Looser specimens of sand are more susceptible to larger axial strains than dense sands during the epoxy curing process. Jang (1997) demonstrated that an air-pluviated sand specimen with

initial density of 23 percent would strain 1.4 percent during impregnation, but a denser specimen with an initial relative density of 79 percent would only strain 0.16 percent at a confining pressure of 50 kPa. Below a void ratio of 0.66 ($D_r > 50\%$) axial strains due to impregnation are minimal for both air-pluviated and moist tamped sand specimens but increase linearly as density decreases, as illustrated by the initial void ratio versus total axial strain graph in FIG. 2.18.

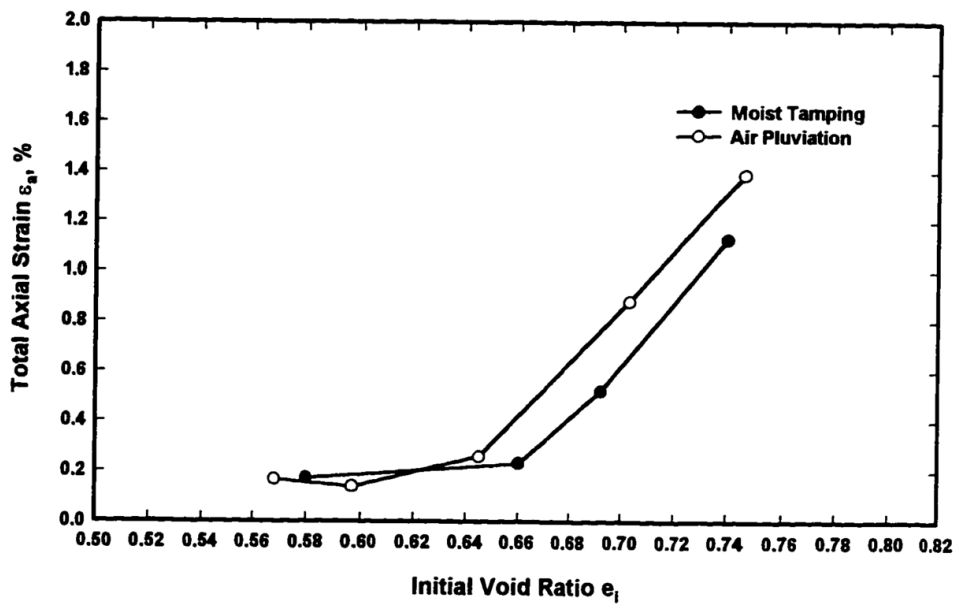


FIG. 2.18. Strain Due to Curing of Epoxy-Impregnated Sand Sample in Triaxial Cell at $\sigma_3 = 50$ kPa. (Jung, 1997)

The typical working time of 1-2 hours after mixing for Epo-Tek[®] 301, during which the epoxy's viscosity doubles, can be extended by keeping the epoxy cooled in the refrigerator prior to usage and chilled during mixing, de-airing and impregnation. Furthermore, the manufacturer recommends not to mix more than 25 ml of material at a time to reduce negative effects of heat release due to exothermic reaction that could cause volume change during the curing process and reduce working time after mixing, also known as the pot life. When cured,

the Epo-Tek[®] 301 epoxy has a very good bonding strength, a medium hardness of D =85 on the Shore scale and a lap shear strength of over 13,790 kPa (2,000 psi) that holds up very well to cutting, grinding and polishing procedures. However use of Epo-Tek[®] 301 for stabilization requires specialized impregnation equipment with sacrificial, disposable parts whenever they come in contact with the epoxy.

2.4. Imaging of Epoxy-Stabilized Soil Samples

Several destructive and non-destructive imaging methods have been used in soil mechanics to study microstructure of cohesionless soil samples. Bright field microscopy (BFM) and electron backscattered diffraction (EBSD) require extensive sample preparation e.g. epoxy impregnation, cutting, grinding and polishing, to obtain optical grade, perfectly flat coupon surfaces. Both procedures provide good quality, relatively inexpensive, high contrast images. X-ray computed tomography is a non-destructive process capable of scanning an entire specimen to acquire three-dimensional images of grain structure in real time. It is an expensive, time consuming image acquisition method that may result in relatively low image resolution and image artifacts. Selection of an appropriate imaging procedure is a compromise of price, equipment availability and limitations, sample preparation, and image processing requirements to obtain acceptable results.

2.4.1. *Bright Field Microscopy (BFM)*

Several types of optical illumination techniques are widely used in fields of biology, petrology, metallography, petrography and chemistry. According to Bradbury and Bracegirdle (1998), their purpose is to:

- Provide a magnified image of the specimen
- Help to visualize fine details in the structure of the specimen
- Measure an object's structure
- Measure optical properties of reflectance, refractive index, and phase changes

The four most common types of illumination microscopy are incident light, transmitted light, dark field, and bright field illumination methods. In incident light microscopy, the specimen is illuminated directly by one or more light sources that are set arbitrarily by the user. This method is very rarely used because it is hard to reproduce. If the illumination of the field of view is not controlled by a lens and aperture, the light bulb filament will cause disturbance in the image due to spatial variation in light intensity, surface glare, and bleaching out of fluorescent particles (Baldock and Graham, 2000). Transmitted light illumination is used in thin section imaging of high contrast biological and petrographic specimens where the transmitted light is able to pass through the specimen without too much absorption. Dark field illumination is similar to transmitted light illumination except the central light rays are blocked, allowing only oblique rays to illuminate the specimen. This is a very simple and popular method for increasing the contrast of unstained, low contrast specimens. Oblique

light rays emanating from a darkfield condenser strike the specimen from every azimuth and are diffracted, reflected, and refracted into the microscope objective, making the specimen appear bright on a black background (Davidson and Abramowitz, 2003).

Bright field microscopy, also known as reflected light or episcopic illumination, is used with thick specimens where light cannot pass through them. Instead, the light is directed onto the surface of the specimen along the microscope optic by either specular or diffused reflection. Episcopic illumination system used with optical microscopy is illustrated in FIG. 2.19. Typically, Kohler illumination is used to provide optimum specimen illumination, where the glare-free, grain-less light source does not suffer deterioration from dust or imperfections in the glass surfaces (Davidson, 2010). The light travels from the light source through collector lenses, the variable aperture iris diaphragm opening, and the opening of a variable pre-focused field iris diaphragm, strikes a partially silvered plane glass reflector, and is reflected onto the specimen's surface. Once the light reaches the specimen, it is partially absorbed and partially reflected back to the microscope as specular and scattered /diffused light. Sample microstructure that contains different types of materials will reflect or scatter the light back to the microscope lens based on surface roughness and material hardness, resulting in good contrast and definition. According to Jang (1999), flat surfaces reflect light back to the microscope and appear to be bright. The light that strikes rough surfaces is diffused and scattered, resulting in dark features. The quality of the images can be adjusted based on the degree to which the diamond abrasive used

in the final polishing stage, removes artifacts from hard surfaces while scratching soft surfaces at the same time. Bright field illumination has been proven to reveal desired surface features of metallographic, petrographic and epoxy-impregnated sand specimens.

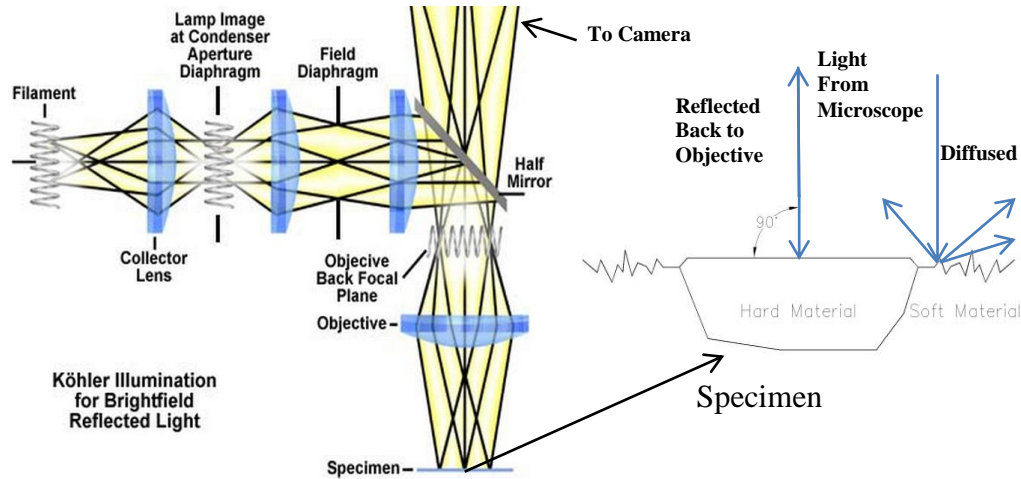


FIG. 2.19. Episcopic Illumination System. (Davidson, 2010)

Additional application specific optical microscope methods such as Rheinberg illumination, phase contrast microscopy, polarized light, Hoffman modulation contrast or Florence microscopy use optical staining, diffraction, refraction, optical gradients or radiation respectively to enhance image contrast but were not considered for this research.

2.4.1.1. Nature of Light

Since an epi-illumination (bright field) microscope takes advantage of light interaction with the specimen surface to capture high quality images, it is important to understand the physical properties of a light wave. Visible light is part of the electromagnetic radiation spectrum that is in wavelength from 400 nm to 700 nm. FIG. 2.20 shows the spectrum of electromagnetic waves including the

visible light spectrum. Visible light contains violet, blue, green, yellow, and red colors visible to human eye. A beam of light may be expressed as a two-dimensional sinusoidal curve, where wavelength represents the color of light and the amplitude of the wave gives the information about its intensity, or “brightness”.

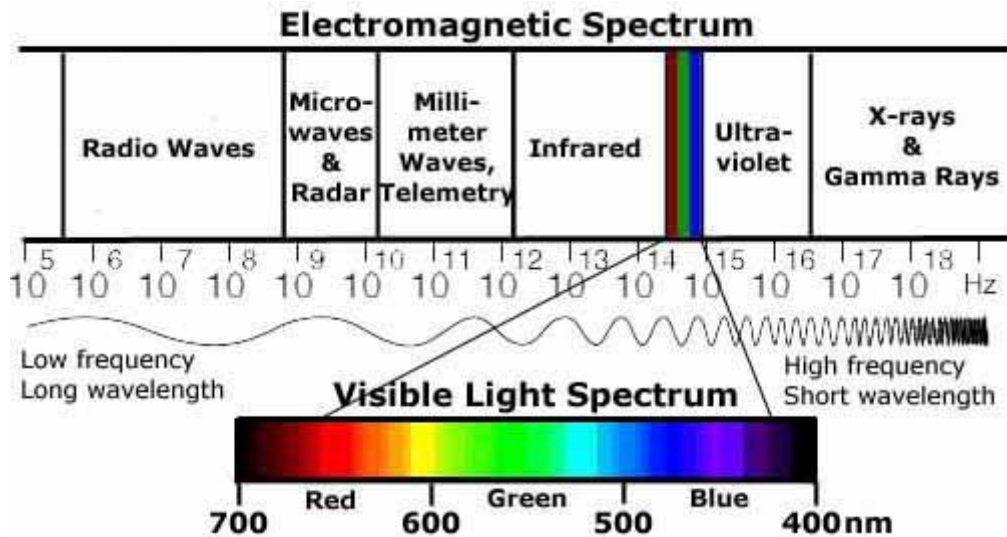


FIG. 2.20. The Spectrum of Electromagnetic Waves, Including Visible Light Spectrum. (BIOSYNTRX, 2005)

Depending on the refractive properties of the microscopic specimen and the nature of light source, the principal interaction between light and a specimen may result not only in reflection and absorption but also in refraction, diffraction or fluorescence. Each type of interaction may affect the image quality of objects viewed under the microscope. FIG. 2.21(a) and FIG. 2.21(b) show specular reflection that occurs when the light beam is reflected by a smooth surface, where the angle of incidence is equal to the angle of reflection. If the surface is rough, diffused reflection returns light in all possible directions.

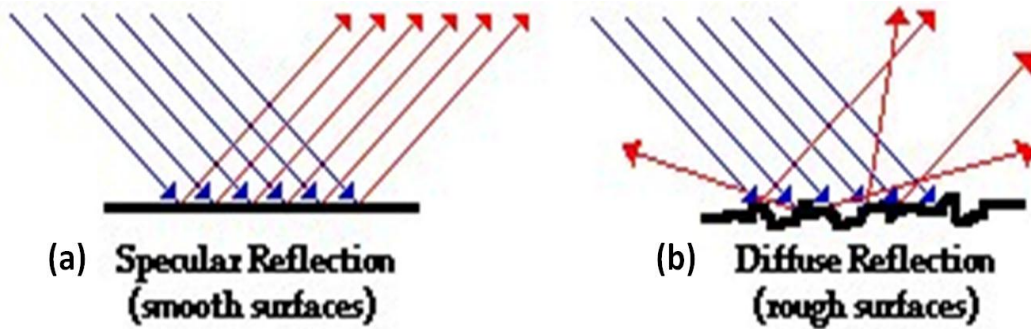


FIG. 2.21. Diagram of Reflections from Smooth and Rough Surfaces.

When the transmitted light is absorbed by the specimen, it is reduced in amplitude or intensity when compared to light that passes around it, causing a phase change or optical path difference. Absorption of some wavelengths may affect the color of the reflected light and thereby make parts of the specimen change color or appear dark, resulting in increased contrast for biological and petrographic thin sections.

Refraction occurs when light passes from one material into another of different refractive index, e.g. from air into glass. Bradbury and Bracegirdle (1998) state that the refractive index of any medium is the ratio of the phase velocity of the electromagnetic waves of light in a vacuum to their phase velocity in the medium itself. The relationship between angles of incidence and refraction in materials with different refractive indices is governed by the Snell's Law. Since the phase of the wave needs to be constant on any given plane, it follows that:

$$n_1 \sin \theta_1 = n_2 \sin \theta_2 \quad (2.35)$$

where n_1 and n_2 are the refractive indices of the incident and refracted medium, one and two respectively, θ_1 and θ_2 are the incident and refractive angles of the normal to the surface respectively, as illustrated in FIG. 2.22.

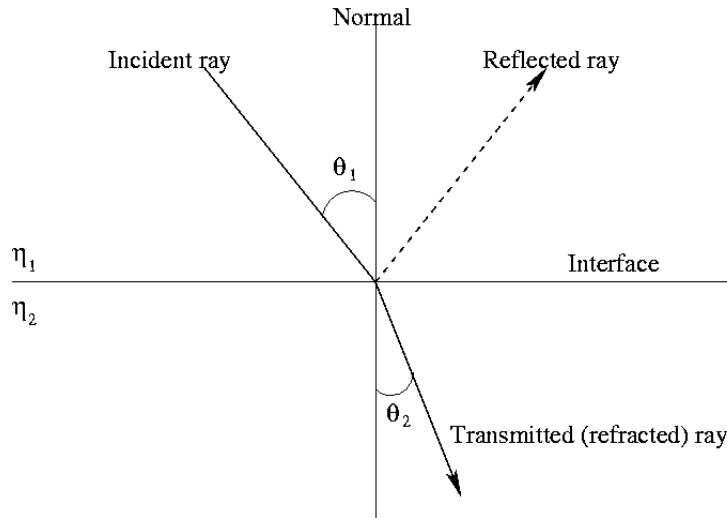


FIG. 2.22. Refraction of Light Passing from One Medium to Another.

Refraction is an important factor in the performance of optical microscopes, as it affects resolution and Numerical Aperture (N.A.), which is a measure of the light-collecting power of a lens. N.A. is quantified as:

$$N.A. = n \sin \alpha \quad (2.36)$$

where α is the half angle of acceptance of incident light rays striking an optical lens and n is the refractive index of the lens that can range from 1.0 for air to 1.52 for oil. In microscope design, an oil immersed optic provides for the highest resolution and N.A. values.

Diffraction is the scattering of light caused by the beam that passes an edge of the object. Diffraction appears as bending of the light beam that extends into the shadow areas of the image. This bending effect is most pronounced for longer wave lengths limiting image sharpness and resolution.

Fluorescence is a process where energy from light in the shorter wavelength regions is absorbed by an object and then almost immediately re-emitted as light of longer wavelengths (Bradbury and Bracegirdle, 1998). It is used in fluorescence microscopy to enhance contrast of biological specimens with use of staining techniques.

2.4.1.2. Coherent and Incoherent Illumination

A specimen viewed under an optical microscope can be illuminated by light sources that vary in wavelength composition and the phase relationship. These variations will have different effects on image quality. According to Baldock and Graham (2000), light sources that emit single wavelengths are called coherent or monochromatic. A coherent light source is used in confocal brightfield microscopy with a point detector. This type of illumination suffers from a ringing effect and shifting of sharp edges into a bright area that needs to be accounted in calculations. In addition, even small dust particles can degrade the image, requiring aberration-free optics to obtain high quality images.

Incoherent illumination is characterized by a random phase relationship. Incoherent light can be emitted directly from a source such as a halogen lamp and is used in epi-illumination microscopes and in this research. Incoherent illumination may be changed to quasi-coherent illumination by closing the aperture of the microscope into a pinhole. A method to control illumination of the pupils in the optical path of a microscope and to ensure high resolution,

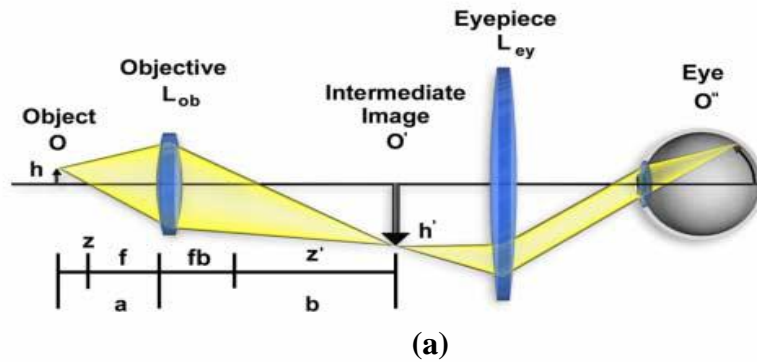
homogenous illumination was first described by Kohler in 1893, and is presented in FIG. 2.19. The advantage of this method is that the image intensity does not change with a change of the focal position.

2.4.1.3. Image Formation and Types of Microscope Systems

The two most common types of optical microscopes used in illuminated microscopy are compound microscopes and infinity corrected microscopes. In the majority of microscopes manufactured before 1980s, a magnified and real but inverted intermediate image (O') would be formed with an objective composed of several lenses inside a fixed optical tube, as illustrated in FIG. 2.23(a). The image would further pass through the eyepiece objective to form the final virtual image O'' , located at infinity. This system provides good quality, high resolution images that could be affected by optical aberrations caused by quality of the optics and an illumination method. The eyepiece has to compensate for considerable residual errors and lateral chromatic aberrations, as discussed further in section 3.5.1.5.

FIG. 2.23(b) shows an infinity-corrected microscope where the object (O) is placed in the front focal plane of the objective that forms a parallel light beam in infinity space. The intermediate, inverted image O' is created by the reference focal length tube lens and it is subsequently converted to a final, infinity focused, virtual image O'' that is free of residual aberrations.

Finite-Tube Length Microscope Ray Paths



Infinity-Corrected Microscope Ray Paths

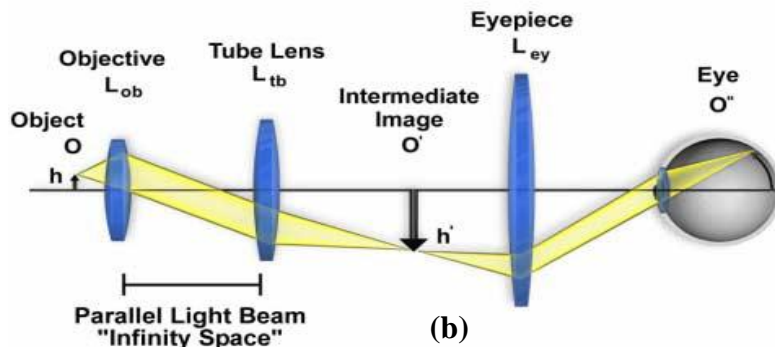


FIG. 2.23. Finite-Tube and Infinity-Corrected Microscope Systems. (Davidson and Abramowitz, 2003)

2.4.1.4. Past Research

Image capture of light illuminated sand coupon surfaces with an optical microscope has been widely used to study microstructure properties of epoxy stabilized, cohesionless sand specimens. This inexpensive method has been used in the past two decades by several researchers (Kuo, 1994; Frost and Kuo, 1996; Jang, 2000; Yang, 2002; Evans, 2005) to study changes in soil properties when subjected to triaxial testing. The sand specimen would be stabilized with optical grade epoxy, sectioned and subjected to manual grinding and polishing to obtain artifact-free, perfectly flat coupon surfaces. Captured images would be stitched and processed to calculate the two-dimensional variation in spatial and local void

ratios distribution inside and outside a shear band within the specimen, quantify particle orientation distribution, size and shape characteristics, and number of interparticle contacts.

Yang (2005) studied the three-dimensional microstructure of triaxial test specimens from reconstructed two-dimensional sections. A hand polishing technique was used to remove 5-10 μm of surface thickness at one time. Up to sixty images were captured per individual layer using BFM and then stitched together to create a two-dimensional slice. Up to 20 slices were then aligned to create a three-dimensional image used to characterize parameters such as tortuosity, throat size, global and local void ratio, and pore size.

Martys et al. (2000) used BFM to capture the grain structure of reconstituted Ottawa 30/40 sand specimens that were impregnated with Epo-Thin[®] two-part epoxy. The resulting binary images were used to obtain the statistics of the pore structure distribution to calculate permeability and permeability anisotropy. The permeability and permeability anisotropy were used to calibrate three-dimensional numerical model.

2.4.2. Electron Backscattered Diffraction (EBSD)

Electron backscattered diffraction is performed with the scanning electron microscope (SEM). The specimen is placed in a vacuum chamber on a surface that is tilted at 70° to the incoming high-energy electron beam in a raster scan pattern that is then reflected onto a phosphor screen for detection. The electrons interact with the sample's surface atoms providing information about composition, surface topography, and electrical conductivity. The information is

converted from analog to digital with a Charge Coupled Device (CCD) that functions as an image sensor inside the digital camera. The CCD data is then processed and displayed on a monitor, as illustrated in EBSD process diagram presented in FIG. 2.24(a).

Image quality and the type of information obtained using EBSD is dependent on type of electron beam used. A secondary electron beam can produce very high resolution (up to 1 nm) and large depth of field resulting in a three-dimensional image useful in the study of surface texture. The magnification can vary from 10 to 250 times. A back-scattered electron (BSE) beam emits a high energy beam that is reflected from the specimen by elastic scattering. Since the signal strength is strongly related to the atomic number (Z), heavy elements within the specimen reflect electrons more strongly than light atoms and appear brighter. The BSE beam can be used to detect contrast between areas of different chemical composition. FIG. 2.24(b) shows the SEM setup and a resulting image captured from one of the epoxy-stabilized specimens used in this research at minimum magnification. Less work is required to prepare the specimen surface for microstructure analysis using BSE compared to BFM because the BSE beam can excite subsurface atoms by adjusting the power from 5kV to 40kV to obtain information at depth between 50 and 100 nm below the surface. The specimen's surface needs to be electrically conductive and grounded to prevent accumulation of electrostatic charge. As a result, the surface of an electrically non-conductive object needs to be coated with electrically conductive material such as gold,

platinum or graphite. Environmental SEM has been used to prevent electric charge buildup on non-metallic specimens by replacing the vacuum chamber with a high pressure chamber filled with positively charged ions.

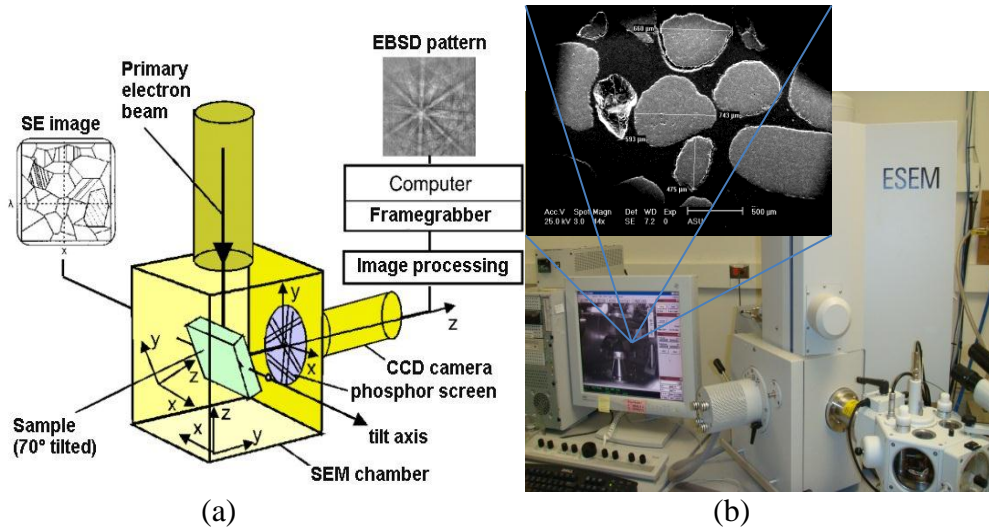


FIG. 2.24. (a) EBSD Measurement Process (IFW-Dresden). (b) Image Capture with ESEM and Resulting Image.

Yamamuro (2008) used a scanning electron microscope (SEM) in backscatter mode to study thin sections of epoxy-stabilized silty sand specimens from undrained triaxial compression tests. He found that this technique produced high quality, binary micrographs that clearly differentiate between the sand grains and the surrounding void spaces, while remaining less sensitive to sample preparation methods when compared to image capture with BFM technique. Grain contact analysis required 3-D reconstruction to verify the size of the particles. To enable 3-D reconstruction, the coupon surface was removed with a polishing process at 20 micron intervals. The surface images were then used to visually reveal gradual morphology of the sand grains in reconstructed 3-D images.

Alshibli and Sture (1999) used the same method as Yamamuro (2008) to capture binary images to study the level of homogeneity inside and outside the shear failure plane of Ottawa F-75 white silica sand specimens tested under plane strain conditions. Back-scatter electron microscope was used to collect images from thin sections. Resulting 2,000 μm by 2,000 μm images were converted to a binary form and the variation in global void ratio was calculated within and outside the shear plane.

Several petrography studies (Slatt, 1973; Whalley, 1980; Thanachit al et., 2009; Prakonghep, et al., 2010) also used SEM to analyze the microstructure of individual sand grain particles. Visual observation of images and computer assisted image analysis yielded angularity and roundness parameters, feret size (the longest distance across a grain section), surface texture, crystal growth, pitting, and mineral composition.

2.4.3. X-ray Computed Tomography (CT) Imaging

X-ray Computed Tomography is a non-destructive, reliable imagining method to obtain the three dimensional microstructure of a material through use of tomography. Its use began in radio astronomy (Bracewell, 1956) and later in 1970s as a diagnostic tool in the medical industry. Its use has since been extended to study soil properties (Al-Raoush and Alshibli, 2006; Desruses, el at. 1996; Wang, 2007), cement concrete (Landis and Keane 1999; Hall el at., 2000), asphalt concrete (Braz et al., 1999; Wang, 2004) and rock (Radaelli el at. 1998). Medical scanners for examining of human tissue are widely available but limited in power. Industrial CT scanners provide higher energy levels, higher intensities and lower

exposure times to deliver higher image resolution. Scanned slices can be reconstructed in three dimensions to perform image processing and analysis to obtain material property characteristics such as grain size, grain distribution, global and local void ratios, particle arrangement, number of contacts and permeability estimates.

Batiste et al. (2004) used X-ray CT to study the spatial density variations within Ottawa F-75 sand specimens subjected to axial compression unloading and reloading cycles in a triaxial cell under different strain regimes. The results included information on local void ratio distribution within specimens, thickness and orientation of shear bands, and volume change distribution. These investigators characterized shear bands into axial conical and radial-planar types and correlated them with nominal axial strain increases.

Al-Raoush and Alshibli (2006) used CT generated three dimensional images of porous media to develop a methodology to accurately calculate the distribution of local void ratio regardless of irregularity in shapes, sizes, or arrangements of particles. The developed algorithm used a smoothing median filter to suppress high-frequency data values while preserving the detail of the image, a watershed transform to segment touched or overlapped particles, and the distance transform to calculate the boundaries of local void regions. They discovered that porosity values are sensitive to image quality, so image filtering should be performed prior to mathematical morphology to obtain accurate results.

2.4.3.1. Tomography

Tomography is a process that takes transmitted radiation that is collected by the detector and analyzed by a computer to create a two-dimensional reconstruction of image slices with the use of complex reconstruction algorithms. The mathematical principles of CT are covered in detail by Panton (1981) and Kak and Stanley (1988). The X-ray signal is attenuated by the sample through Compton scattering and photoelectric absorption and pair production. According to Ketcham and Carlson (2001), photoelectric absorption occurs when the total energy of an incoming X-ray photon is absorbed by an inner electron, causing the electron to be ejected. In Compton scattering the incoming photon interacts with an outer electron, causing it to scatter while it is deflected in a different direction. In pair production, the photon interacts with the nucleus and is transformed into a positron-electron pair. This process of beam attenuation through homogenous material can be described by the Beer's Law:

$$I = I_0[-\mu x] \quad (2.37)$$

where I_0 is the initial X-ray intensity, μ is the linear attenuation coefficient of the specimen and x is the X-ray path through the material. Attenuation varies with Z^3 (the atomic number cubed) and emitted energy. Photoelectric absorption is dominant at low beam energy and high atomic number, Compton scattering is dominant at higher beam energy.

Image reconstruction algorithms use the Fourier slice theorem to reconstruct one-dimensional Fourier transforms of the parallel projections by assuming that it must be equal to a slice of the two-dimensional Fourier transform of the original

specimen. Detailed description of the theory behind system calibration, image collection and image reconstruction procedure are well beyond scope of this dissertation.

2.4.3.2. X-ray Computed Tomography Process

X-ray CT involves creation of incident electromagnetic radiation (x-rays or gamma rays) that is directed at the sample being studied. Some radiation enters the sample and is absorbed, but the majority of the radiation passes through the specimen and is detected on the back plate. The collected data is used to reconstruct two-dimensional slices of the specimen. CT systems can be classified based on the scanning configuration, type of energy source used or resolution.

First generation CT is done by directing an X-ray beam through an object to a single detector while changing the angular orientation of the specimen. Second generation CT scans replaced the single beam with a fan beam and the single detector by a series of detectors, as shown in FIG. 2.25(a). In third generation CT illustrated in FIG. 2.25(b), a cone beam configuration can capture an entire object so only one rotation of either the specimen or the beam is required (Ketcham and Carlson, 2001). FIG. 2.25(c) presents a parallel beam configuration used by the latest generation of third generation synchrotron CT machines, where a continuum of electromagnetic radiation produced by electrons traveling at a speed close to the speed of light are used to generate the x-ray source used in imaging.

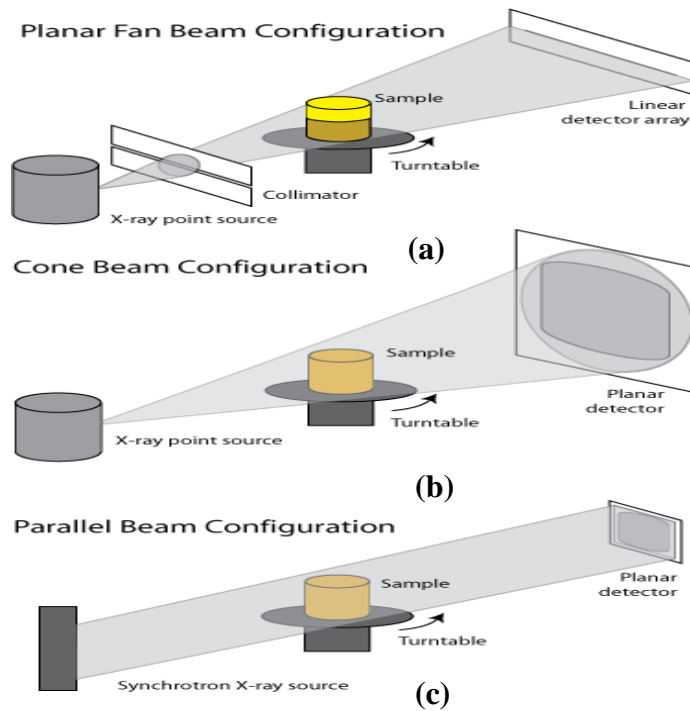


FIG. 2.25. Beam Configurations in X-ray CT Systems.

Non-destructive imaging of very dense materials is done with neutron tomography where the spallation of protons into highly excited neutrons is used to generate gamma rays. CT systems can be classified based on resulting scale of image resolution. Table 2.2 presents a CT classification system based upon image resolution.

Table 2.2. General Classification of Computed Tomography. (Ketcham and Carlson, 2001)

TYPE	SCALE OF OBSERVATION	SCALE OF RESOLUTION
Conventional	m	mm
High-resolution	dm	100 μm
Ultra-high-resolution	cm	10 μm
Microtomography	mm	μm

2.4.3.3. Image Artifacts

Scanning artifacts can affect quality of the reconstructed images by obscuring image details, changing material properties, and affecting dimensional calculations. The most common types of image artifacts are the beam hardening, ring artifacts, and partial-volume effects.

Beam hardening causes variation in brightness, where the center of the object appears darker than the edges. This problem is caused because of the increased energy of the x-ray as it passes through the specimen. Since lower energy x-rays are more attenuated by higher energy beams, the beam loses energy from the lower part of its spectrum. The incident beam would have lower energy than a direct beam, resulting in brightness variability within a specimen. In circular specimens, the middle would be darker than the periphery, but in irregular objects, there is difficulty in differentiating between beam hardening and actual material variations. This problem can be remedied with a higher energy beam and by using only the middle part of the image for analysis.

Ring artifacts occur in third-generation CT and appear as full or partial circles located around the rotational axis. They result from variation in output from individual detectors. A partial-volume effect (partial circle) is caused by material variability within a specimen, resulting in different attenuation levels. It can cause blurring of material boundaries, where the material value of a voxel can affect the value of surrounding voxels, (Ketcham and Carlson, 2001). Some

blurring can also be caused when the specimen is not centered on the rotating table along its axis, causing shifting and overlapping of images within the specimen

2.5. Surface Preparation Techniques

2.5.1. Introduction

Epoxy-stabilized sand specimens need to be subjected to several preparation steps before imaging of the surface microstructure with optical microscopy can be performed. Initially the large specimens are sectioned, planed and mounted into a mold for manual or automated grinding. Grinding is fairly standardized for most types of materials and it is performed with Silicone Carbide abrasives to obtain initial flat surface. It is followed by several polishing steps with diamond abrasive pastes or slurries to remove damage caused by previous steps and to provide perfectly flat, artifact free surface for image capture. Sample preparation techniques used in geology and metallurgy were adopted by several researchers in the past to obtain good results with specimens composed of silica grains. Those techniques were unique to the materials and equipment used. Final fine tuning through trial and error is required to obtain good imaging results.

2.5.2. Cutting and Mounting

Sectioning is the first preparation step in many metallographic, geologic and epoxy-stabilized geotechnical soil samples studied with an optical microscope. This process inevitably produces surface damage, e.g. grain pullout, beveling of the surface, surface stress fractures. Two types of laboratory cutting devices are available. The first is the abrasive cutter, a 229 to 356 mm (9 to 14 inch), water

cooled “chop saw” that can use a consumable wheel with silicon carbide (SiC), aluminum oxide (Al₂O₃), diamond, or cubic boron nitride (CBN) abrasive bonded to resin, rubber or metal disks. The second device is the low speed 76 to 203 mm (3 to 8 inch) wafering, metal-bonded diamond or cubic boron nitride saw that is used when the specimen is fragile or friable. Thinner wheel thickness offers minimal kerf loss and a cooler cut than that produced by other cutting methods, resulting in minimal surface damage and thereby a reduction in the number of subsequent grinding steps (Johnson, 2003). Diamond coated blades are a good choice for general sectioning and for polymers. CBN abrasive coated blades are best suited for cutting hard metals, particularly iron and steel. Appendix E lists a guide to selecting precision saw wafering blades. Table 2.3 lists the different cutting methods for sectioning and the associated surface damage caused by the various cutting techniques.

Table 2.3. Specimen Surface Damage from Cutting. (www.buehler.com)

METHOD	DAMAGE TYPE	POSSIBLE DEPTH
Shearing	Deep mechanical damage	5 mm
Flame/plasma cutting	Deep thermal damage	13 mm
Band/hack saw lubricated not cooled	Moderate thermal and mechanical damage	2.5 mm
Dry abrasive cutting	Moderate to severe thermal damage	1.5 mm
Wet Abrasive cut-off saw	Minimal thermal and mechanical damage	250 µm
Diamond/precision saw	Minimal thermal and mechanical damage	50 µm

Mounting involves encapsulating small samples within larger media so they're easier to handle during the grinding and polishing process. Hot compression mounting uses phenolic, phthalate, thermoplastic and epoxy powders to encapsulate samples that can withstand the heat and pressure of the mounting process. Cold mounting is used to encapsulate heat and pressure sensitive materials with acrylics and epoxies when better flow and penetration of the mounting material is needed or when a large quantity of samples must be produced at once. Simply mounting the specimen in a polymer is a good first step but, according to Voort (2000), usually not adequate for mounting metallurgical samples. Most polymeric mounting resins whether used hot under pressure or "cold" as a castable resin, do not provide a proper degree of edge flatness. The best mounting resins are the thermosetting epoxy resins that contain filler material, such as Epomet[®] resin. When the thermosetting resins are used, the embedded sample can cool at a different rate, resulting in free edge formation. A free edge will be rounded by any abrasive surface causing bleeding problems during examination of structure with the microscope and a residue solvent bleed out that can obscure edge detail. Ideally, the specimen should be mounted in material of matching thermal coefficient of expansion and of similar hardness. This problem is not as acute with epoxy mounted, epoxy-stabilized sand specimens because the epoxy matches the mounting resin in hardness and thermal expansion coefficient.

2.5.3. *Planing and Manual Grinding*

Planing and grinding processes remove saw marks from cutting of the specimen, clean, and level the surface prior to polishing. Typically, trimming of the specimen with a diamond slab saw or precision section saw will result in grain pullout, beveling of the surface and surface stress fractures that need to be removed with a surface planer prior to the grinding process. Grinding uses fixed abrasives where particles are formed into a grinding wheel, bonded to a strip or disk of paper. Only manual grinding with fixed abrasives is considered in this research.

2.5.3.1. Planing

Initial planing of the workpiece can be accomplished with a grinding wheel that cuts as the specimen passes underneath. Normal and tangential forces that are generated between the workpiece and the grinding wheel cause the abrasive to penetrate. Hahn, (1966) describes rubbing, cutting and ploughing as three stages of metal removal during surface grinding, as illustrated in FIG. 2.26. Grains that cut deep into the surface will carve out a chip, but abrasive grains that rub the surface very lightly may fail to penetrate the surface. Some grains rub without ploughing and some grains plough without cutting. Some grains experience all three stages. The transition between those three behaviors depends on increasing depth of grain penetration into the surface (Marinescu, 2004).

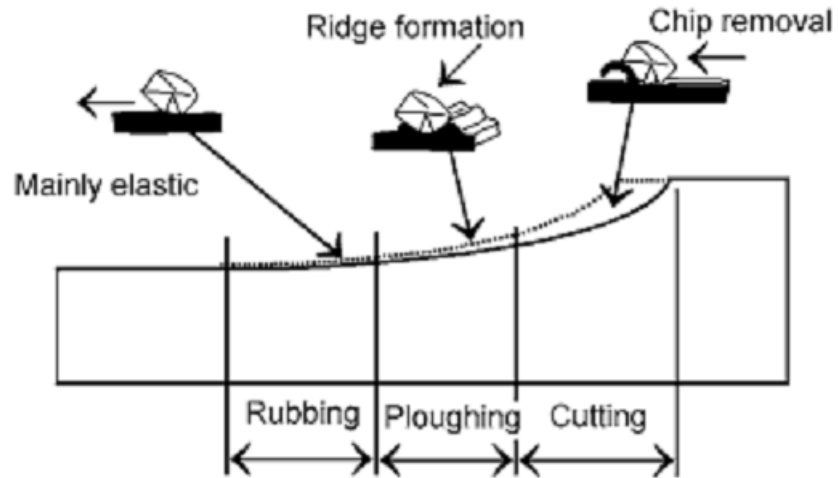


FIG. 2.26. Rubbing, Ploughing, and Cutting Regimes of Deformation in Abrasive Machining. (Marinescu, 2004)

According to Rowe (2009), the most basic grinding parameter for surface planing is the real depth of a cut, a_c . The operator sets a depth of cut, a_p , but the real depth of material removed is much less than the programmed depth of cut. Effects of grinding forces on the wheel deflection and real depth of a cut are presented in FIG. 2.27.

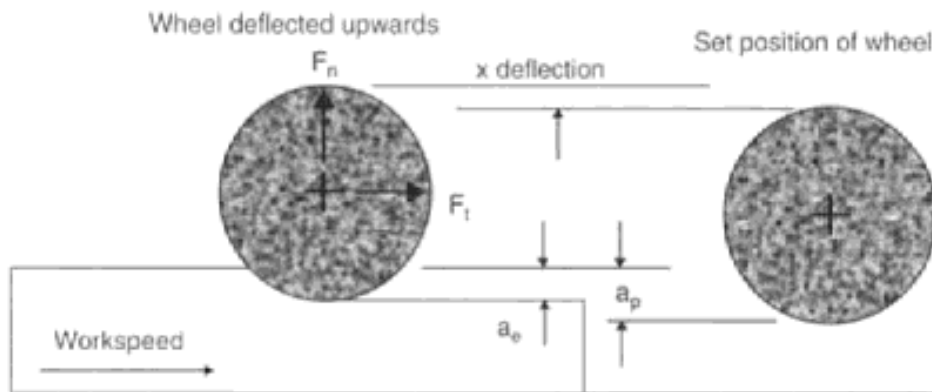


FIG. 2.27. Effect of Grinding Forces on Wheel Deflection and Real Depth of Cut. (Rowe, 2009)

Assuming horizontal surface planing with down-fed depth of cut, the set depth of cut is:

$$a_p = \frac{\pi d_w V_f}{2V_w} \quad (2.38)$$

where, d_w is workpiece diameter, V_f is the in-feed rate, and V_w is the work speed. After a number of passes, the real value approaches the set value, but typically a_e is approximately a quarter of a_p depending on workpiece hardness, wheel stiffness, contact width, work speed, and wheel speed. The actual cut depth is affected by the deflection, x of the system, wheel wear, a_s , and the thermal expansion, x_{exp} of the workpiece. The actual cut depth can be calculated using the following equation:

$$a_c = a_p - x - a_s + x_{exp} \quad (2.39)$$

Evans (2005) used surface planer for initial surface planing of epoxy-stabilized sand specimen sections mounted onto 7.11 cm (2.8 inch) diameter epoxy disks. The device consisted of a 0.64 cm (0.25 inch) wide grinding wheel that can be adjusted vertically with 2.54 μm precision and a two-degree-of-freedom hydraulically adjustable table. The table's front-to-back movement was set at 0.0254 cm per pass during coarse planing and 0.0127 cm per pass during fine planing. Initially, material was removed from the surface at the rate of 254 μm per pass and then it was reduced in stages from 127 μm to 2.54 μm to prevent grain plucking.

2.5.3.2. Manual Grinding

Manual grinding is used when depth of grinding is critical and when automatic equipment is not available. Most grinding methods use paper backed abrasive attached to a stationary belt sander or variable speed rotating disk grinders/polishers that use pressure sensitive adhesive (PSA) grinding disks. Disk sizes can vary from 10.16 to 30.48 cm (4 to 12 inches) in diameter. Silicon carbide (SiC), zirconia alumina, aluminum oxide (Al_2O_3), and diamond abrasives can either be bonded to paper, resin, and metal, or used in suspension with a specially engineered metal disk such as Buehler[®]'s Apex Hercules[®] Rigid Grinding Discs. Grit sizes for grinding range from ANSI 80 to 1500. Well-established preparation practice has been to sequentially grind specimens with a series of progressively finer water cooled silicon carbide abrasive papers in 120-, 240-, 320-, 400-, and 600-grit sizes. Typically, each abrasive disk is used for 60 to 120 seconds, after which the paper is worn out (Voort, 2000). Silicon carbide is used for coarser sizes and aluminum oxide is used more widely for sizes finer than ANSI 1000 (see Appendix A for USA and European grit equivalency guide).

According to the manufacturer's literature for Buehler[®] SUM-MET[™] (2007), grinding should commence with the finest grit size that will establish an initially flat surface and remove the effects of sectioning within a few minutes. An abrasive grit size of 180 to 240 is coarse enough to use on specimen surfaces sectioned by an abrasive cut-off wheel. Hack-sawed, band sawed, or other rough surfaces usually require abrasive grit sizes in the ranges of 120 to 180 grit. The abrasive used for each succeeding grinding operation should be one or two grit

sizes smaller than that used in the preceding step. A satisfactory fine grinding sequence might involve SiC paper with grit sizes of 220-, 320-,400-,600-grit. All grinding steps should be performed wet provided that water has no adverse effect on any constituents of the microstructure. Wet grinding minimizes specimen heating, prevents the abrasive from becoming loaded with grinding swarf and uniformly distributes the contact stresses between the platen and the specimen during grinding. Water is the most commonly used lubricant, but nonaqueous lubricants are recommended for ceramics and minerals that are easily dissolved in water.

Consecutively finer grit abrasive is used to remove damage from the previous step. To aid in this process, Chinn (2002) proposed choosing a reference point on the specimen, such as point Q in the 12 o'clock position shown in FIG. 2.28 (a). While holding the specimen surface firmly against the abrasive disc or belt such that the reference point is fixed with respect to the direction of abrasive motion, grinding continues until the saw marks are replaced by the parallel scratches of the first abrasive, as illustrated in FIG. 2.28(b). The specimen surface is cleaned with mineral soap and compressed air in between different grit sizes. Next, point Q on the specimen is rotated to the 3 o'clock position, as illustrated in FIG. 2.28(c), and the specimen is grinded with the next finer abrasive until the previous artifacts are removed. The new parallel scratches lie at a 90° angle to the previous ones, as illustrated in FIG. 2.28(d). Rotation of the mount by 90° after each abrasive step shown in FIG. 2.28(e) allows one to easily see when the artifacts of the previous preparation step have been removed.

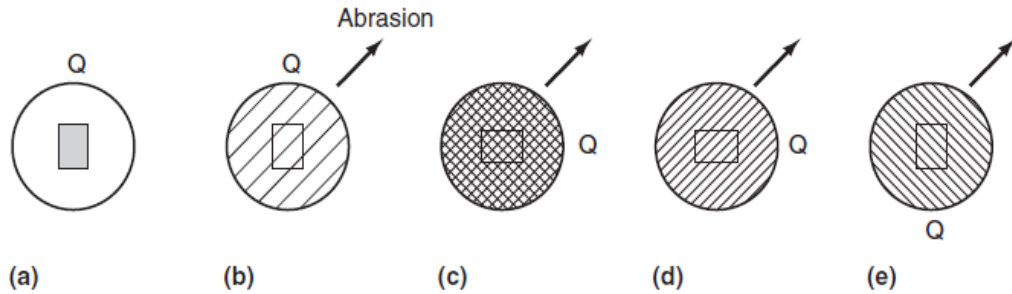


FIG. 2.28. Manual Grinding and Polishing Procedure. (Chinn, 2002)

2.5.4. Lapping

Lapping is an intermediate step between the grinding and polishing processes designed for material removal and reduction of the specimen dimensions, while decreasing the surface roughness. According to Marinescu et al. (2007), lapping is a fine finishing abrasive process aimed at imparting specific characteristics to the work piece with respect to form, size, and surface conditions. Unlike polishing, the goal of lapping is to impart dimensional tolerances and an accurate shape by concentrating more on stock removal than on surface finish. It incorporates three abrasive mechanisms: rolling, sliding, and microcutting. In the lapping process the rotation lap is charged with loose abrasive slurry that removes material from the metallic or non-metallic specimen at low speed and low pressure, resulting in fine finished surface of extreme flatness. The system is composed of four parts; lap plate, abrasive slurry, truing rings and press plate, as illustrated in FIG. 2.29.

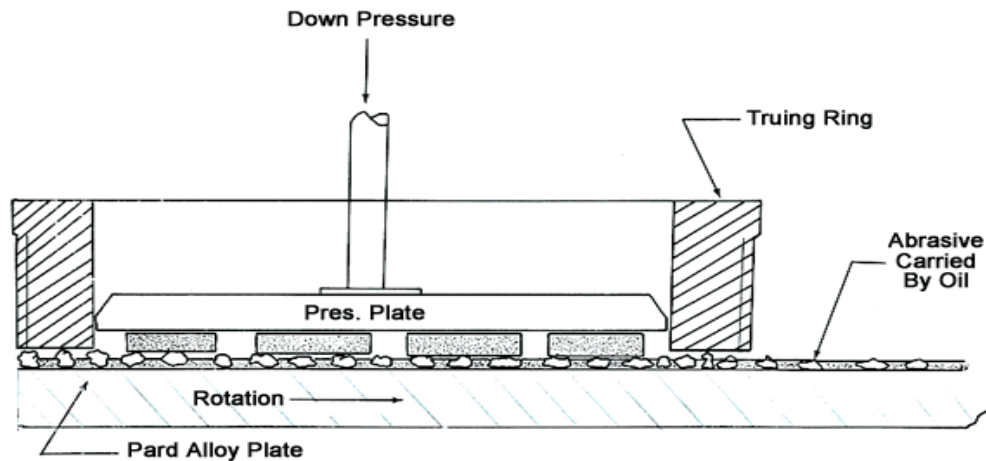


FIG. 2.29. Single-side Lapping Process. (www.azom.com, 2011)

2.5.4.1. Lap Plate

Improper selection of a lapping plate can result in a badly scratched and abrasive contaminated workpiece. When the lapping surface is too hard, it will prevent embedment of the particles within the lapping plate, resulting in rolling of abrasive on the surface and material removal via stress induced micro fractures. A softer lapping surface will enable the abrasive to partially embed within the lapping plate, resulting in more sliding motion and material removal by ploughing. The resulting surface has a finer finish but less planarity. A hard lapping surface used in combination with a very fine abrasive can create better coupon surface with respect to planarity. Best results are obtained when the lap plate surface is charged with abrasive slurry until gray in appearance.

Overcharging the lap plate surface will result in inaccuracy due to excessive rolling of the abrasive. The most common lapping plate materials are iron, copper, ceramic, and tin. An iron lap plate has an aggressive stock removal rate and it is an excellent primary or roughing lap plate, with long service life. An iron lap

plate produces a good surface finish on most materials and is typically used with an abrasive composed of coarse to medium diamond sizes. Jang, et al. (1999) used lapping with a cast iron platen and 600 grit silicon carbide and anti-freeze suspension at 13.79 kPa (2 psi) for 10 minutes as part of the initial sand coupon surface preparation method. The Jang, et al. (1999) method was modified from Buehler Dialog[®] Method (see Appendix B for details of the Buehler Dialog[®] Method). Evans (2005) successfully used a cast iron lapping plate with 600 grit silicon carbide/ Metadi Fluid slurry on a Buehler[®] MetaServ[®] polishing table with an Autopol II attachment for the initial grinding phase of epoxy-impregnated sand specimens prior to polishing. Table 2.4 lists the parameters of the grinding and polishing procedure used by Evans (2005).

Table 2.4. Parameters Used for Polishing and Grinding. (Evans, 2005)

PARAMETER	GRINDING PHASE	POLISHING PHASE
Wheel surface	Cast iron	Texmet 1000 cloth on aluminum
Abrasive	600-grit Sic powder	1000-drit Sic powder
Mixing	50 g/250 ml Metadi fluid	50 g/250 ml water
Wheel speed	120 rpm	120 rpm
Overburden stress	29 kPa	23 kPa
Duration	Until flat, 30-60 min	10-13 min

2.5.4.2. Abrasive Slurry

Abrasive slurry used in lapping has two components: the lapping abrasive and the lapping medium. The volumetric mixing ratio of the abrasive to the medium is 1:2 to 1:6, but the optimal ratio needs to be established experimentally for each application (Marinescu et al. 2007). The abrasive used in grinding, lapping, or polishing suspensions has to be harder than the material that is being machined. The material removal rates and surface roughness are directly proportional to the size and size distribution of the abrasive medium. The most common abrasive used for almost all applications is silicon carbide (SiC), a fused, hard crystalline abrasive of Mohs 9.5 hardness that is capable of fast cutting with a good crystal breakdown. Just below SiC in hardness, aluminum oxide (Al_2O_3) is a fused crystalline abrasive that has a very hard crystal structure that is slowly dulled but hard to fracture. Aluminum oxide is not well suited for fine finishes or precision lapping. Finally, a diamond suspension abrasive with Mohs 10 hardness is best suited for hard metals, where embedding may not be a factor. A diamond suspension abrasive cuts faster and produces fine finishes. Table 2.5 lists some commonly used abrasives. Abrasives with the same or similar hardness on Mohs scale may not have the same abrading power or produce a similar lapped finish due to variability in crystalline shapes, lines of cleavage, friableness, or chemical composition.

Table 2.5. List of Most Commonly Used Abrasives and Their Hardness.
(www.reade.com)

MATERIAL	MOHS HARDNESS NUMBER
Diamond	10.0
Cubic Boron Nitride	9.9
Norbide abrasive	9.7
Silicon Carbide	9.5
Aluminum Oxide	9.0
Fused Alumina	9.0
Corundum	9.0
Chromium Oxide	8.5
Quartz	7.0
Silica	6-7

The lapping fluid is used to deliver the abrasive grains to the lapping surface. The lubricant facilitates the interaction between the abrasive and the specimen whether the abrasive is fixed or free. Its function is to act as a coolant that prevents heat buildup from friction, transports the swarf away from the platen and specimen, and uniformly distributes contact stresses between the platen and the specimen during grinding (Marinescu et al., 2007). Lapping fluid is typically water based with added corrosion inhibitors and agents for increased viscosity and lubrication. Mixtures of oil, petroleum paraffin, Vaseline, and other additives are commonly used as the lapping fluid.

2.5.4.3. Truing Rings and Press Plate

Truing rings illustrated in FIG. 2.29 are used for regeneration of the surface texture and flatness of lap plates. They are used for retaining parts during processing and to maintain lap plate flatness. Cast iron rings are used for general engineering. Ceramic, Micarta and Polycarbonate rings are used for polishing applications. The press plate, on the other hand, is used to deliver the abrasive grains mixed with a lubricant and corrosion inhibitors to the plate surface. Its purpose is to lubricate the lapping surface and to apply contact pressure to the specimens.

2.5.4.4. Advantages of Lapping Process

The lapping process provides very good quality and repeatability of surface finish on all types of materials. It is well suited for polishing of brittle materials because a relatively uniform pressure is exerted on the workpiece, minimizing the potential for thermal damage or distortion. According to Marinescu et al. (2007), for flat surfaces, lapping can achieve:

- Flatness to less than one light band (He) $0.0000116''/0.3 \mu\text{m}$
- Roughness of less than $1 \mu\text{in. } R_a/0.025 \mu\text{m } R_a$
- Size control to less than $0.0001''/2.5 \mu\text{m}$

2.5.5. *Polishing*

Polishing is a final surface finishing process designed to remove any remaining artifacts leftover from grinding and/or lapping while maintaining good edge retention among various grain sizes and material types on the surface of the specimen. It is carried out without letting fine abrasive particles generate brittle

fractures on the work surface while removing material by means of plastic deformation (Marinescu, 2007). Polishing should produce a deformation free surface that is flat, scratch free, and mirror-like in appearance so true grain microstructure can be observed with various imaging techniques. The process progresses from coarse polishing and fine relief polishing, to vibratory polishing with progressively smaller abrasive sizes ranging from 30 μm and 15 μm diamond suspensions, to 0.05 μm aluminum oxide and colloidal silica slurries with optional chemical etching used as a final step. The transition from grinding to polishing may require additional time on the coarse polishing step to remove the artifacts of grinding. Cloth is used as a delivery medium for the abrasive. Napless cloth is used primarily with diamond pastes and suspensions and napped cloth used with colloidal silica and alumina slurries. Appendix C lists various types of napped and napless cloths from Buehler[®] and Allied High Tech Inc. Napless cloth is a stiff, nonwoven polyvinyl chloride (PVC) chemotextile sold under such trade names as UltraPad[®], VerduTex[®], Pellon[®], PLAN-B, Plan-Cloth, and Gold Label. Napless cloth is designed for high removal rates and good edge retention. Nonwoven, fiber-reinforced-resin perforated pads and woven silks work well for polishing ceramics with diamond pastes and suspensions. Napped cloth that is sold under such names as TexMet[®], VelTex[®], MicroFloc[®], DiaMat, and Pan-B has a fuzzy texture that conforms to the surface being polished. Napped cloth is not well suited for use with materials containing particles of different texture or hardness. Application of excessive force or duration during polishing may lead to an unevenly polished surface, creating various artifacts such

as grain rounding, grain pullout, grain surface plucking and surface variation between different material types.

A vast number of surface preparation procedures have been developed for polishing of metals, glass, ceramics and electronic components. This research is mostly concerned with sample preparation methods compatible with epoxy embedded silica crystals. Wei (2010) developed a grinding/polishing procedure to prepare 31.75 mm (1.25 in) epoxy mounted geological samples for microscope examination. Initial grinding with 600 and 800 grit silicon carbide abrasive disks using a MetPrep 3TM power head grinder/polisher was followed by polishing with 0.3 μm and 0.05 μm alumina suspension on Allied High Tech's Spec-Cloth and Imperial Cloth, respectively. Samples were washed with micro organic soap and water, then dried with compressed air to remove swarf and abrasive in-between steps. The procedure resulted in high quality, scratch and artifact free images with good surface flatness and particle edge retention. See Appendix D for the resulting images, the system polishing procedure, and consumables used by Wei (2010).

2.5.6. Specimen Cleaning and Preparation

Improper specimen handling and cleaning between the planing, grinding and polishing steps may result in lapping and cloth surface cross contamination, leading to damage to the coupon surface in the form of scratches, grain plucking and rounding. The most common solutions used in cleaning are distilled water,

organic soap, alcohol and compressed air. The use of tap water or cotton swabs may result in removal of material or scratching on samples containing soft, water soluble minerals.

Chinn (2002) developed cleaning procedure for ceramographic mounts. After each abrasive step, the specimen is rinsed with warm distilled or deionized water and then swabbed with a cotton ball soaked with a solution of distilled water mixed with a laboratory detergent such as Micro-90 or Alconox. The specimen is then placed in ultrasonic bath for 1 to 2 minutes, rinsed with warm distilled water, sprayed with ethanol, and dried under a heat gun.

2.5.7. Common Errors

Accurate interpretation and analysis of images from a polished coupon requires a properly prepared sample that is free of any artifacts, including edge rounding, constituent pullout, particle embedding, large scratches, smearing, and relief. Even an improper sample cleaning process can result in sample preparation artifacts. If the sample is not cleaned properly between stages of preparation, any remaining coolant/abrasive will contaminate subsequent cloth resulting in large scratches. If samples are not fully dried before mounting, outgassing may occur. After the final polishing step, if the sample is not properly cleaned and dried, water and residual etchant can stain the sample. Cleaning a surface that oxidizes easily in soap and water will damage the sample surface, hiding the true microstructure. The implement used for cleaning samples such as a brush or a cotton swab can scratch the sample surface and the ultrasonic cleaner can sometimes damage samples by shaking out sample constituents.

Edge rounding between the mounting material and the specimen or between different materials within the specimen can affect measurement accuracy. The image in FIG. 2.30 shows silica grains with rounded edges that are 27 microns across as well as damage (surface roughness) due to surface plucking.

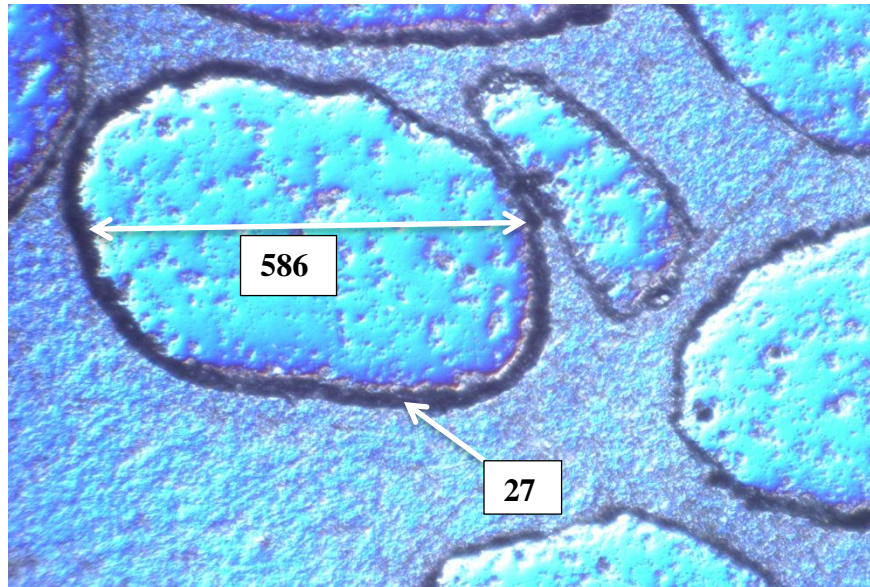


FIG. 2.30. Epoxy-Stabilized Ottawa 20/30 Sand Grains with Visible Edge Rounding and Surface Plucking.

According to Abraham (2010), edge rounding can be caused by a polishing cloth that is too soft, a polishing time that is too long, an applied force that is too high, large differences in hardness between sample and mounting material, sample edge gaps, or abrasive material that is too soft. Changing from soft, resilient cloth such as DiaMat[®] (i.e. a cloth that tries to bounce back under the load and hugs the surface features of the sample) to a more rigid, less resilient polishing cloth such as White Label (i.e. a cloth that can provide a flatter, more supportive surface for the abrasive particles) can reduce edge rounding. Since the mounting material is usually softer than the sample, it may wear away at a faster

rate. Switching to a harder mounting material such as hot mounted Black Glass-Filled Epoxy will protect sample edges more effectively. Fast curing cold mounting acrylic materials will typically shrink around the sample due to exothermic reactions and material pullback. Slower curing epoxy will set slower and harder so it will not wear away as fast or create edge gaps. Silicon carbide is effective at polishing metals and plastics but not effective at polishing ceramics, as it just rubs and chips away at the ceramic materials. A harder abrasive such as diamond may need to be used to create even surface without edge rounding.

Constituent pullout will cause any porosity measurement to become unreliable. Constituent pullout can be caused by polishing cloth fibers that are plucking out specimen constituents or insufficient lubrication. Switching from a napped cloth such as Final-P to a napless polishing cloth such as Final-A, reducing friction heat with a more viscous lubricant, and keeping the polishing cloth moist at all times should eliminate most of pullout problems. Over lubricating will cause samples to hydroplane, reducing contact between the abrasive and sample surfaces and increasing polishing time.

Particle embedding affects soft samples that contain soft metals and polymers due to frictional heat generation where the abrasive becomes embedded in the sample surface. This problem can be caused by rigid polishing cloths, insufficient lubrication, and too much force applied during the polishing process.

Large scratches can be present if they were not removed in a previous step, the polishing cloth does not support that particular abrasive size, the polishing cloth is contaminated, or the polishing cloth is worn and it is not removing the

material properly. Polishing for a longer time period to remove scratches may result in edge rounding. Abraham (2010) recommends instead of increasing polishing time to use a more rigid polishing cloth such as PLAN-B instead of Gold Label and to segregate different polishing cloths to eliminate cross-contamination (Appendix C contains a list of polishing materials). Good cleaning with micro mineral soap, rinsing with alcohol, and drying with compressed air are essential between grinding and polishing steps to get a good quality specimen.

2.6. Digital Image Processing and Analysis

Digital images captured with the previously described techniques of optical microscopy, computed tomography, or electron backscattered diffraction can be used to extract information about the soil fabric properties described in Section 2.2. As noted, image processing and analysis can be divided into five generally accepted steps: image generation and capture; image coding; reconstruction; enhancement; and analysis (Frost and Kuo,1996).

Image generation and capture involve a process of creating high quality, high resolution images that can be encoded in some digital format without losing any important data that cannot be recovered later, as discussed in Section 2.4. In the case of BFM and EBSD, image quality is highly dependent on the coupon preparation technique. In the case of X-ray CT, image quality depends on equipment calibration and equipment resolution capabilities.

Image coding is a technique of image storage (save and open) with some type of lossless image compression format (.TIFF, BMP, PNG, GIF). Typically, images are stored in 16-bit grayscale or 256-bit RGB (color) TIFF lossless compression format.

Image reconstruction is used to reconstruct image information that has been lost in the processes of image formation. Images can be degraded by optical distortions during image capture. Degradation during image capture can be avoided with proper equipment setup/calibration and good specimen preparation techniques. Degraded images can be reconstructed based on mathematical and statistical models.

Image enhancement refers to a number of methods used to improve certain image characteristics prior to image analysis. They include contrast and texture manipulation, histogram manipulation, noise deconvolution, use of masks, filters and thresholding. Separate group of image processing techniques, referred to as mathematical morphology, was developed by Serra to quantify mineral characteristics from thin sections (Serra, 1982). Mathematical morphology enhances binary images through processes of opening, closing, dilation, erosion, boundary detection, skeletonization, segmentation with a watershed algorithm and a “Hit-or-Miss” transform used for object recognition, thinning and pruning. More detailed description of these processes will be presented in Chapter 4.

Kuo (1994) recommended that the maximum effort should be expended in the preparation, illumination and capture of images to minimize the need for image processing and alteration. FIG 2.31 illustrates Kuo’s (1994) image processing

work flow diagram. Kuo (1994) recommended that any processing should be performed on the grayscale images until all the enhancement techniques have been exhausted. The image can then be converted to a binary image for processing with mathematical morphology operations and for image analysis.

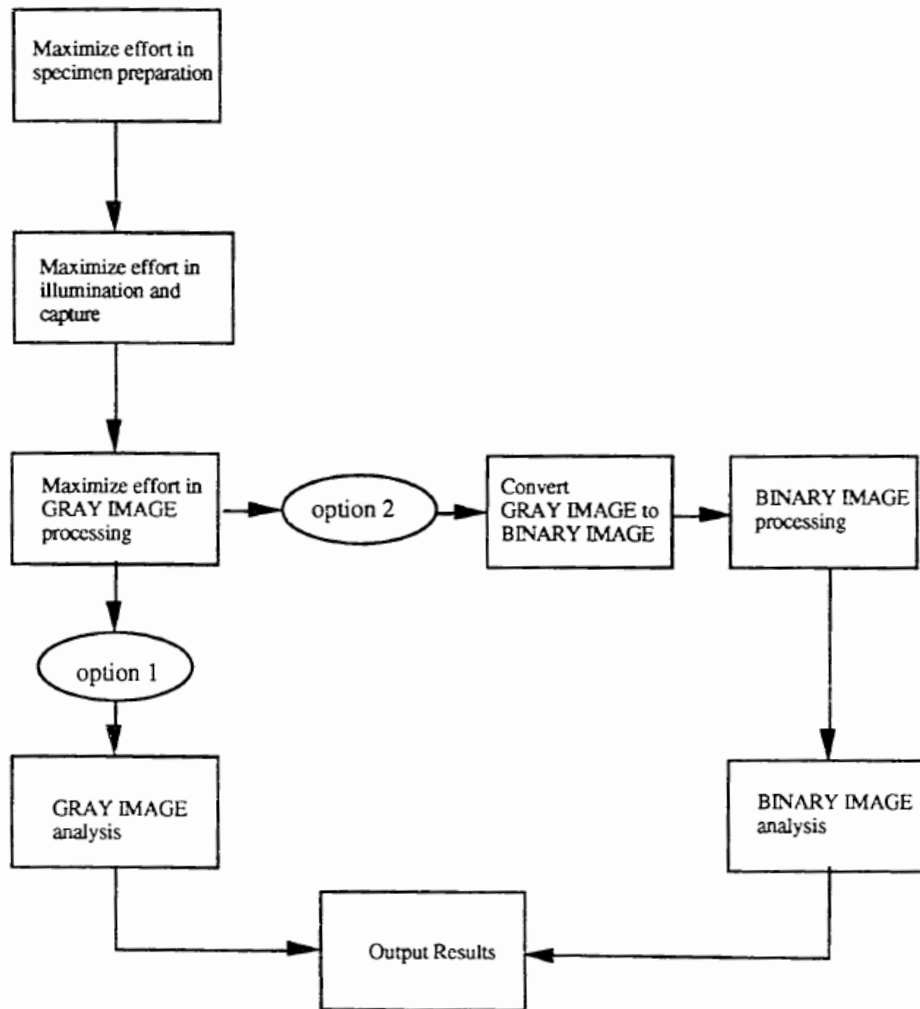


FIG 2.31. Image Processing and Analysis Philosophy According to Kuo (1994).

Image analysis uses what Frost and Kuo (1996) refer to as “low-level” image processing to extract information about soil fabric characteristics such as void ratio distribution, co-ordination value, entropy, anisotropy, fabric tensor,

tortuosity, and mean free path. This information is obtained from the images with a computerized analysis technique first pioneered by Jongerius et al. (1972), who initially developed a classification of void patterns. Subsequently, geotechnical researches have used this technique in the study of the distribution of voids in porous media (Frost and Kuo,1996; Kuo and Frost, 1996, Al-Raoush and Alshibli, 2005;Evans et al., 2009), shear band characterization in triaxial tests (Desruses et al., 1996; Oda and Kazama, 1998; Batiste et al., 2004; Evans, 2005; Yang, 2005), sand grain characteristics (Whalley, 1980; Alshibli and Alsaleh, 2004), shear strength of granular materials (Oda, 1977), fabric anisotropy (Oda et al., 1985;Yang, 2002), and the fluid permeability of porous materials (Berryman and Blair, 1986; Wildenschild et al., 2002)

3. TESTING PROCEDURE

3.1. Rationale for Selected Approach

Several methods were considered to sample and stabilize soil for laboratory testing and to quantify changes in microstructure. Critical criteria included the use of proven, well researched stabilization methods, equipment and image analysis software availability, and time and budget constraints. Uni-directional freezing, described in Section 2.3.1, was chosen for initial stabilization to enable sampling of saturated cohesionless soil. Extensive past research has shown minimum effects of this sampling method on soil structure, when used properly. Chemical impregnation with agar, Elmer's carpenter glue, or bitumen solution were eliminated due to limited background information and/or complicated, time consuming sampling procedures. Freezing was not suitable for image processing since that would require a dedicated cold room facility for sectioning, grinding, polishing and imaging. Instead, Buehler[®]'s optical grade epoxy was used to stabilize the frozen sand specimens inside a specially modified triaxial cell for subsequent imaging. As mentioned in Section 2.3.4, epoxy's performance characteristics and application are well documented. It has been widely used in a number of scientific fields, including geotechnical engineering research, for stabilization of soil specimens for imaging. More specifically the low viscosity, medium hardness, and low shrinkage/strain of Buehler[®]'s Epo-Tek[®] 301two-part optical grade epoxy when cured, are well suited for sample preparation techniques required in image capture with Bright Field Microscopy (BFM) or X-ray Computed Tomography (CT).

BFM and CT were the chosen methods for microstructure image capture. BFM required the development of a coupon preparation procedure to capture the microstructure of individual image slices (2-D) with a digital camera connected to an optical microscope. To obtain three dimensional images of the specimen, the epoxy-impregnated sand specimens were sent off-site for X-ray CT scans. 2-D image capture with electron backscattered diffraction process was considered, but rejected. Benefits of using a scanning electron microscope (SEM), instead of BFM, for image capture include a less rigorous grinding and polishing procedure to obtain quality images since SEM does not depend on the surface properties as much as on the difference in material properties when exposed to a high energy electron beam. However, at minimum magnification, a 2500 μm diameter field of view could only capture eight to ten individual grain particles. Slow image acquisition rate and excessive image stitching, required to obtain a representative image, made SEM impractical for this study.

Digital image processing was used to quantify local and global void ratios for this study. It can also be used to quantify structure anisotropy, number of particle contacts per particle (coordination number) and particle shape descriptors such as roundness and angularity. In subsequent studies, several commercial image processing programs (Avizo Fire, Materialise, Adobe Photoshop) were considered for particle analysis but the licensing fees and computer hardware requirements were prohibitive. Instead, *ImageJ* was used to perform image processing for this research. *ImageJ* is an open-source, Java-based freeware program widely used in biology, astronomy and geology to perform particle analysis. Over one hundred

downloadable macros and plug-ins can be modified to fit specific applications or can be combined with Matlab to develop new sub routines. *ImageJ* was used for image processing, mathematical morphology, and core sample microstructure analysis.

3.2. Specimen Reconstitution and Sampling

A procedure was devised to create reconstituted, air-pluviated Ottawa 20/30 dry sand samples for placement inside a triaxial cell to calibrate and test the epoxy impregnation procedure. A saturation technique and a unidirectional freezing method were devised to obtain frozen core samples from a prototype model container. Frozen samples, recovered from the model container, were stabilized with epoxy for microstructure analysis.

3.2.1. Sand Properties

The sand used in this study is Ottawa 20/30 sand from U.S. Silica Company located in Ottawa, Illinois. Ottawa 20/30 sand is a poorly graded subrounded sand composed primarily (99.8%) of silicon dioxide (quartz) with trace amounts (less than 0.02%) of iron oxide and aluminum oxide. Ninety seven percent of the material is retained on #30 sieve (0.6 mm), 1 percent is retained on # 20 sieve (0.85mm) and the rest is retained on the pan (U.S. Silica Company, 2011). This sand is widely used in geotechnical testing due to the uniform grain size and the presumed uncontaminated nature of the grains that do not show any visible signs of clay, silt or iron particles. The grain size distribution curve for Ottawa 20/30 sand is presented in FIG. 3.1.

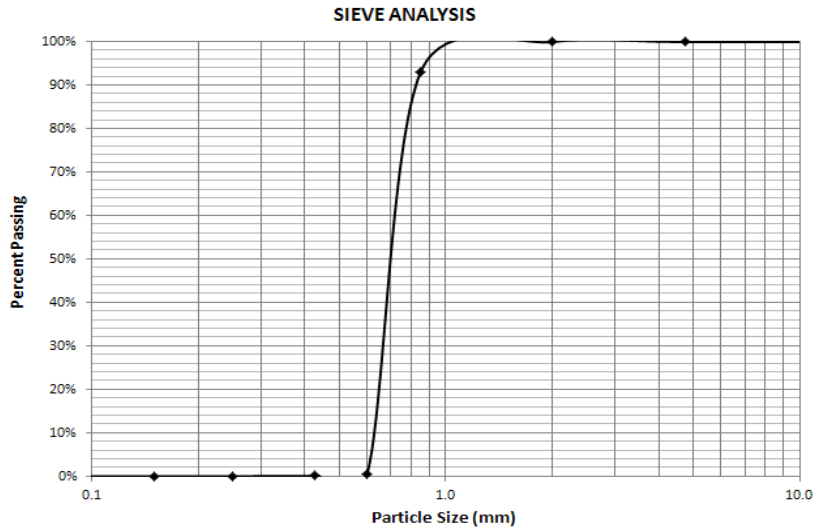


FIG. 3.1. Grain Size Distribution for Ottawa Sand 20/30.

FIG. 3.2 shows an image of Ottawa 20/30 sand. Raveia et al. (2008) discovered that besides quartz, 1-2 percent of the grains are chert fragments. Scanning electron microscopy (SEM) performed by Raveia et al. (2008) indicate a variety of trace impurities including carbon, iron, manganese, chromium, chlorine, and potassium. Significant soil properties of Ottawa 20/30 sand are presented in Table 3.1 (Santamarina and Cho, 2001).

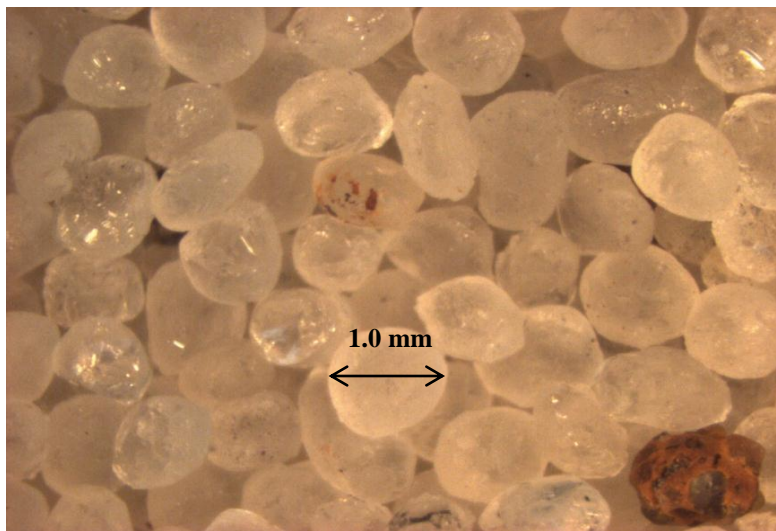


FIG. 3.2. Microscopic Image of Ottawa 20/30 Sand.

Table 3.1. Physical Characteristics of Ottawa 20/30 Sand.

PARAMETER	VALUE	REFERENCE
D ₁₀	0.65 mm	Santamarina and Cho (2001)
D ₅₀	0.72 mm	Santamarina and Cho (2001)
e _{max}	0.742	Santamarina and Cho (2001)
e _{min}	0.502	Santamarina and Cho (2001)
C _u	1.15	Santamarina and Cho (2001)
C _c	1.02	Santamarina and Cho (2001)
G _s	2.65	Santamarina and Cho (2001)
φ _{cr}	28° (undrained)	Santamarina and Cho (2001)
Slope of CSL in e log p'	0.053 (undrained)	Santamarina and Cho (2001)
D ₁₀	0.64 mm	ASTM D422
D ₃₀	0.66 mm	ASTM D422
D ₅₀	0.70 mm	ASTM D422
D ₆₀	0.72 mm	ASTM D422

3.2.2. Dry Sand Specimens

Two types of sand specimens were prepared for epoxy stabilization and digital image processing; air-pluviated dry control samples formed inside a vacuum split mold and air-pluviated, saturated, and then frozen cored sand samples formed inside an aluminum model container. The specimens formed in the split mold were used as a control to gauge the effect of freezing on soil microstructure.

3.2.2.1. Sand Preparation

Initially some of the Ottawa 20/30 sand used for frozen specimens was re-used for dry sample preparation. However repeated coring with a 35.56 mm (1.4 inch) diameter hollow diamond core barrel, handling, and drying, resulted in an increased amount of fines, crushed particles, and an overall change in the gradation curve for the reused soil. Furthermore, foreign matter such as lint and high density polyethylene particles dislodged from the geosynthetic drainage liner accumulated over time in the reused soil. An excessive amount of fines and foreign matter would make microscope imaging and image analysis more difficult due to the increased presence of visual artifacts. Therefore, prior to air pluviation, the sand was sieved to ensure proper particle gradation, repeatedly washed to remove any remaining fines and foreign matter, and then oven dried for 24 hours.

3.2.2.2. Air Pluviation Technique for Dry Samples

An air pluviation technique was used to form reconstituted sand specimens inside a split mold to obtain control samples for soil fabric analysis. The density of the sand after pluviation was controlled by regulating the flow rate and drop height of the sand (Katapa, 2011). In general, denser specimens can be obtained by reducing the flow rate to allow particle rearrangement or by increasing the drop height resulting in larger kinetic energy. Therefore, a variation in drop height can be used to create specimens of different densities (Miura and Toki (1982). Kolbuszewski (1948) studied the effect of drop height on the void ratio of air-pluviated Ottawa C-109 and Leighton Buzzard sands. As illustrated in FIG.

3.3(a) the higher kinetic energies were associated with higher densities as the height of drop increased, until the particle's terminal velocity was reached. Increasing drop height beyond this point did little to increase sand compaction. According to the UC Berkeley (2004) study, to achieve maximum density of Ottawa 20/30 sand with the air pluviation technique, a minimum drop height of 66 cm (25.98 inches) from top of the specimen needs to be maintained during the air pluviation process utilizing three sieves (No. 8, No. 4, No.8, in that order) stacked in such a way that the sand particles cannot fall freely through the opening of the sieves. Density data on air-pluviated Ottawa 20/30 sand specimens generated from UC Berkeley (2004) study are presented in FIG. 3.3(b).

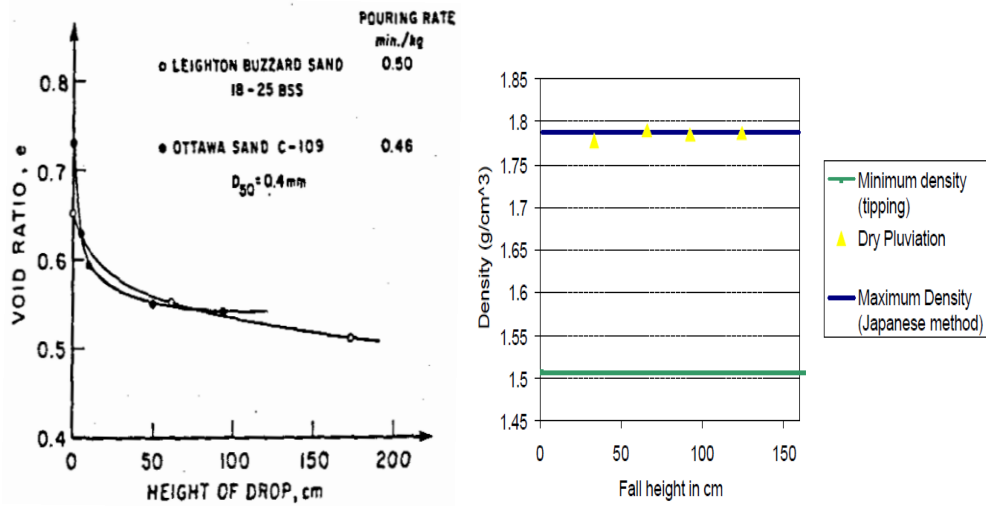


FIG. 3.3. Effect of Drop Height on Void Ratio and Density From Air Pluviation.

The air pluviation method is preferred to moist tamping for sample reconstitution because according to Frost (2003), moist tamping can result in a non-uniform, layered profile with a high standard deviation of local density. Jang (1997) studied the amount of strain within air-pluviated sand specimens caused by

curing of Epo-Tek[®] 301 as a function of initial void ratio. His research showed that a void ratio reduction of less than 1 percent could be achieved when the initial relative density of the specimen was higher than 70 percent ($e_i \leq 0.60$) for specimens confined with $\sigma_3=50$ kPa. Results from the work of Jang (1997) are presented in FIG. 3.4.

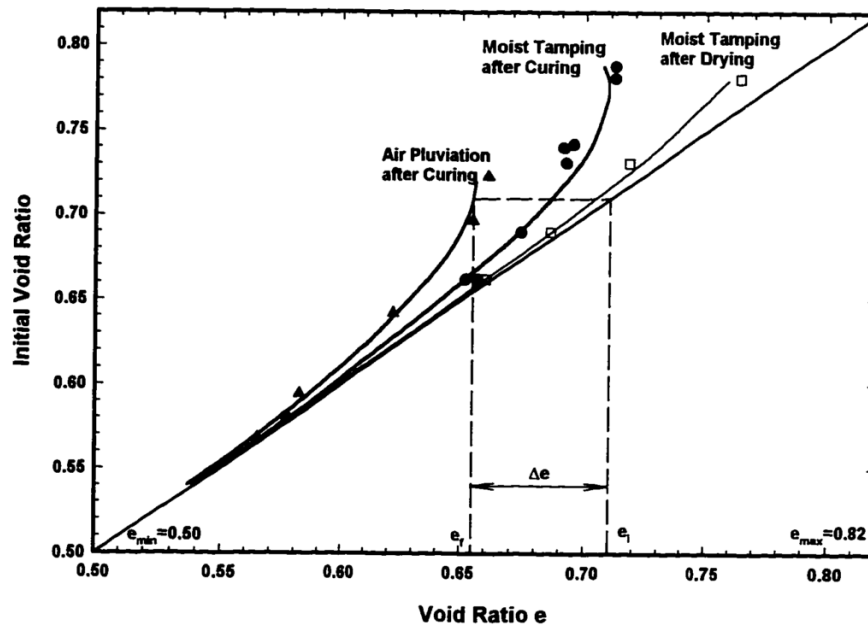


FIG. 3.4. Void Ratio Reduction of Sand From e_i to e_f after Drying and Impregnation with Buehler[®] Epo-Tek[®] 301 at $\sigma_3=50$ kPa. (Jang, 1997)

In this study, Ottawa 20/30 sand was introduced through a funnel with a 1.0 cm (0.4 inch) opening connected to the top of a 66 cm (25.98 inch) PVC tube having the same inside diameter as the 3.8 cm (1.5 inch) split mold. Fine wire mesh was placed at the tube's center as shown in FIG. 3.5. The resulting specimens had the following properties:

- Dry Density $\rho_d = 1.71 \text{ gm/cm}^3$
- Dry Unit Weight $\gamma_d = 16.81 \text{ kN/m}^3$
- Void Ratio $e = 0.5470$
- Relative Density $D_r = 81.25 \%$

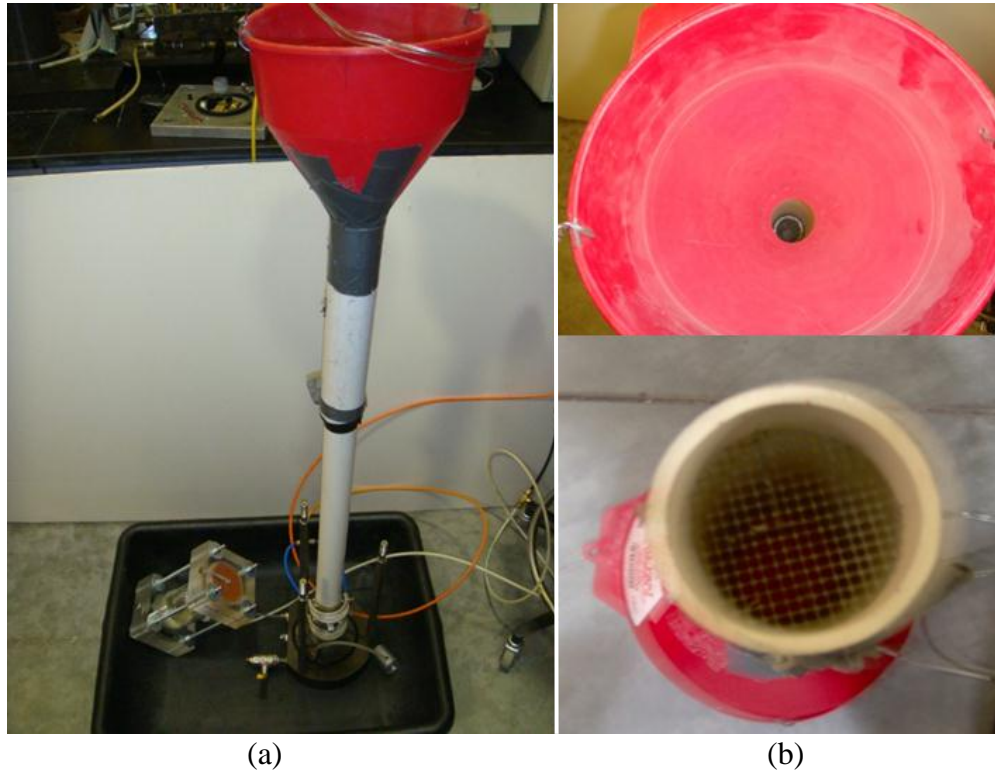


FIG. 3.5. (a) Manual Air Pluviator. (b) Dispersing Screen.

The specimen was formed in a vacuum split mold lined with a 3.56 cm (1.40 inch) diameter latex membrane sealed with rubber gaskets and attached to a triaxial cell base pedestal. Disposable, 0.032 cm thick Porex Polyethylene porous stones with an average pore size of 125 to 175 microns and 3.56 cm (1.4 in.) in diameter, were cut out from a larger sheet using a hand held punch (Porex). A Porex filter stone was placed on the base prior to pluviation and on top of the specimen after pluviation. After the filter stone was placed on the bottom of the

mold, a vacuum of 25 kPa was applied to pull the membrane tight against the split mold, and the pluviator extension was placed over the top of the split mold to prevent overflow. The sample was then filled to within 0.5 cm of the top with Ottawa 20/30 sand using the pluviator. The split mold before and after pluviation is shown in FIG. 3.6.

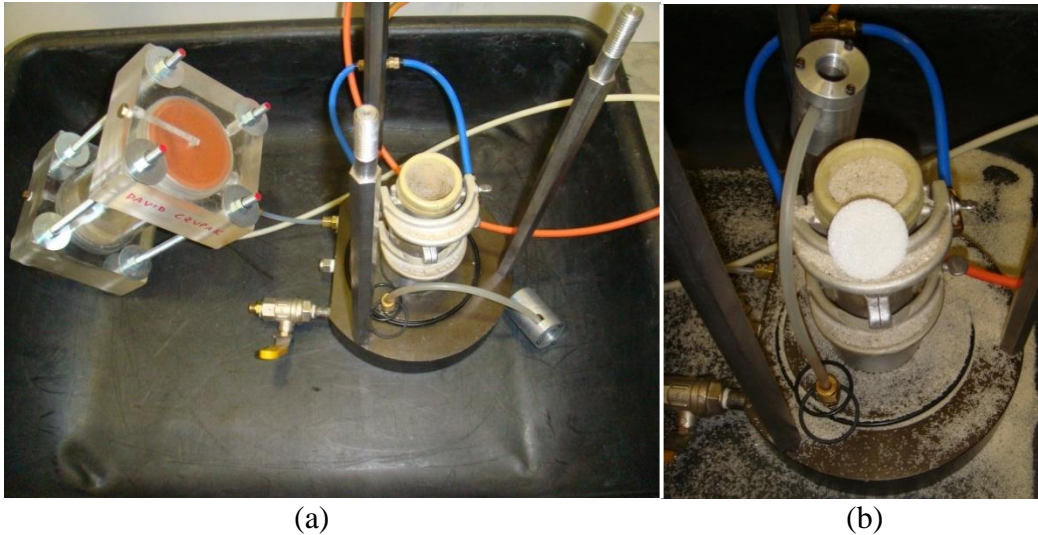


FIG. 3.6. (a) Split Mold before Air Pluviation. (b) After Air Pluviation with Sand.

After pluviation was complete, another Polyethylene porous stone was placed on top of the sand specimen, and then covered with the triaxial top cap that was placed on top of the porous stone. Next, the rubber membrane was pulled over the top cap and sealed against the cap with two rubber gaskets. Once the membrane was secured to the top cap, the vacuum was switched from the split mold to the sand specimen to minimize the possibility of sample disturbance due to vibration. At this point, the sand specimen was ready for stabilization with optical grade epoxy.

3.2.3. Saturated Sand

3.2.3.1. Air Pluviation Technique for Frozen Samples

The air pluviation technique was also used to form samples used with a model container for sampling by freezing. The Ottawa 20/30 sand was dropped, at a steady rate from height of 66 cm through a funnel and two sieves with opening size of 0.025 cm (top) and 0.05 cm (bottom), into an aluminum box enclosed with side panels to prevent spillage (Katapa, 2011). Drop height was maintained as the box filled to assure an even density distribution. The average sample density upon falling to the container was $\rho = 1.73 \text{ gm/cm}^3$. The calibration curve shown in FIG. 3.7 was developed to establish variation in sample density for different drop heights (Katapa, 2011).

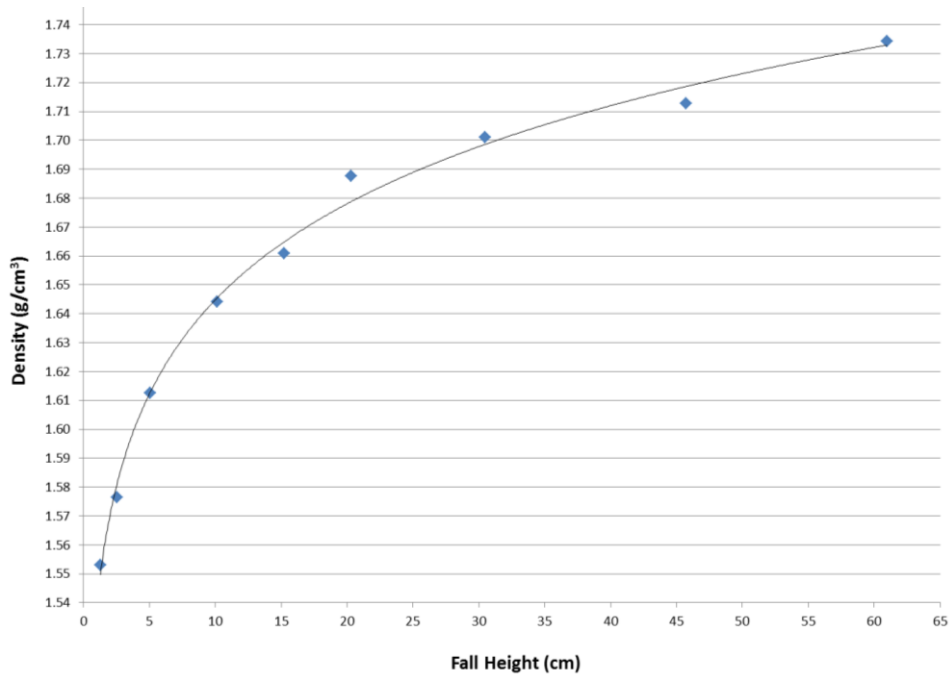


FIG. 3.7. Density Variation Due to Height Drop Change For Air-Pluviated Ottawa 20/30 Sand. (Kanyembo, 2011)

3.2.3.2. Freezing

The model container was a rectangular box with inside dimensions of 55.9 cm (L) x 27.9 cm (W) x 17.8 (H). The box, modeled after the container described by Fiegel et al. (1994) for use in geotechnical centrifuge testing is shown in FIG. 3.8. Three sides, the bottom, and the top cover of the box were constructed using 1.27 cm (0.5 inch) thick, 6061-T651 grade aluminum plates to minimize the deflection of the box during the saturation and freezing processes. To facilitate visual inspection of the freezing front, the front panel was constructed out of 1.27 cm (0.5 inch) thick, clear Lexan Polycarbonate. The top cover was fitted with pressure gauge, compression fittings, valves and six pull latches to ensure a tight fit during the saturation process (see Appendix F for the complete list of design drawings).



FIG. 3.8. The Box Used for Wet Sample Preparation during Saturation Process.

Sand was placed in the model box using an air pluviation technique described in section 3.2.3.1. The cover was then placed on top of the box and secured with the in-line clamps to make an air-tight fit. Carbon dioxide was then pumped into

the soil mass for 10 minutes to displace air from the pore space, followed by slow hydration of the sand with water introduced through inlet ports located on the bottom of the box. To prevent soil disturbance from piping, a 0.95 cm (0.38 inch) geocomposite drainage net with a non-woven geosynthetic fabric on top was placed at the bottom of the box.

Once the soil mass became fully saturated with water, metal trays filled with a mixture of 200 proof ethanol and dry ice were placed on top of the soil mass as shown in FIG. 3.9(a). The freezing front created by this approach is a hybrid between a radial and one-dimensional methods described by Yoshimi et al. (1978), result in a half-cylinder freezing front spanning between the front and back walls of the box, as illustrated in FIG. 3.9(b). In three- to four-hours this process would freeze the soil to -60°C with minimal volume change in the configuration shown in FIG. 3.9(b), reaching to within 1.5 mm of the drainage composite at the base of the box. Visual observation and numerical analysis confirmed that the freezing front created in this manner was created in a uni-directional manner.



FIG. 3.9. (a) Freezing of Fully Saturated Ottawa 20/30 Sand. (b) Resulting Semi-circular Mass of Stabilized, Frozen Soil.

3.2.3.3. Coring and Storage

The freezing procedure was terminated before the freezing front could reach the sides or bottom of the box. This produced a uni-directional freezing front with free draining conditions that minimized volume change and disturbance to the soil structure. A specially designed drilling guide jig was used with the 3.56 cm (1.4 inch) inside diameter, diamond tipped coring bit to extract frozen soil specimens. The jig, coring bit, and the frozen soil after extraction of a series of cores are shown in FIG. 3.10(a). Once extracted, the samples were trimmed, encased in latex rubber membranes, placed in cylindrical Plexiglas split molds, and placed in deep freeze storage for future testing. Up to eight frozen cores could be extracted from a single model, as illustrated in FIG. 3.10(b).

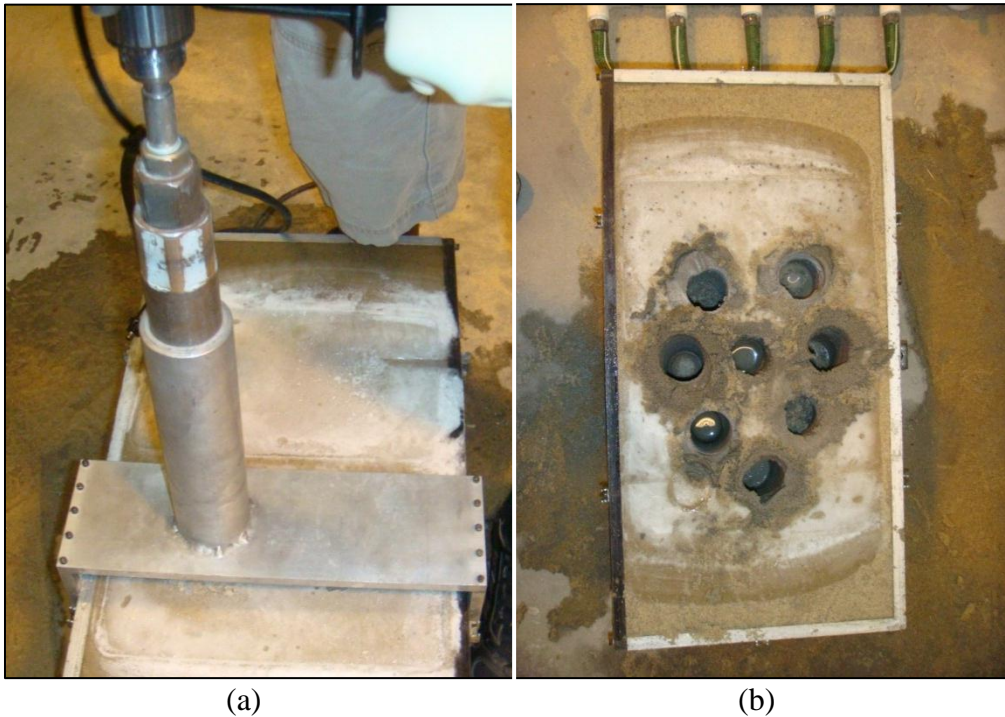


FIG. 3.10. (a) Drilling of Frozen Sand Core Samples with a Hand Drill and Guide Jig. (b) Top View of the Frozen Soil Mass after Specimen Extraction.

3.3. Epoxy Impregnation Using Triaxial Cell Setup

Impregnation with optical grade epoxy was used to stabilize the frozen cores for micro structure imaging and analysis.

3.3.1. Triaxial Test Device Setup and Modifications

A specially modified triaxial cell was used to impregnate 3.56 cm (1.4 inch) in diameter, 7.11 cm (2.8 inch) tall frozen sand cores with Buehler[®]'s Epo-Tek[®] 301 two-part optical grade epoxy. A schematic drawing of the modified triaxial cell setup is presented in FIG. 3.11. All parts of the setup in FIG. 3.11 that would come in contact with the epoxy, including 0.48 cm (0.19 inch) I.D. polyethylene tubing, Porex porous stones, and the rubber membrane, were disposed of after each impregnation procedure. The pedestal, top cap, inside of the rubber membrane and some of the tubing were coated with a thin film of vacuum release grease to facilitate easier disassembly once the epoxy has set. The cell was refitted with 0.48 cm (0.19 inch) compression type Swagelok[®] fittings to accept smaller diameter tubing so the amount of epoxy required for each procedure was reduced. All mechanical valves that could become fouled with the epoxy were replaced with hose clamps. The setup in FIG. 3.11 used air for confining pressure but water could be used as well to perform any conventional type of triaxial test prior to impregnation with the epoxy to study soil structure under applied stress or strain conditions.

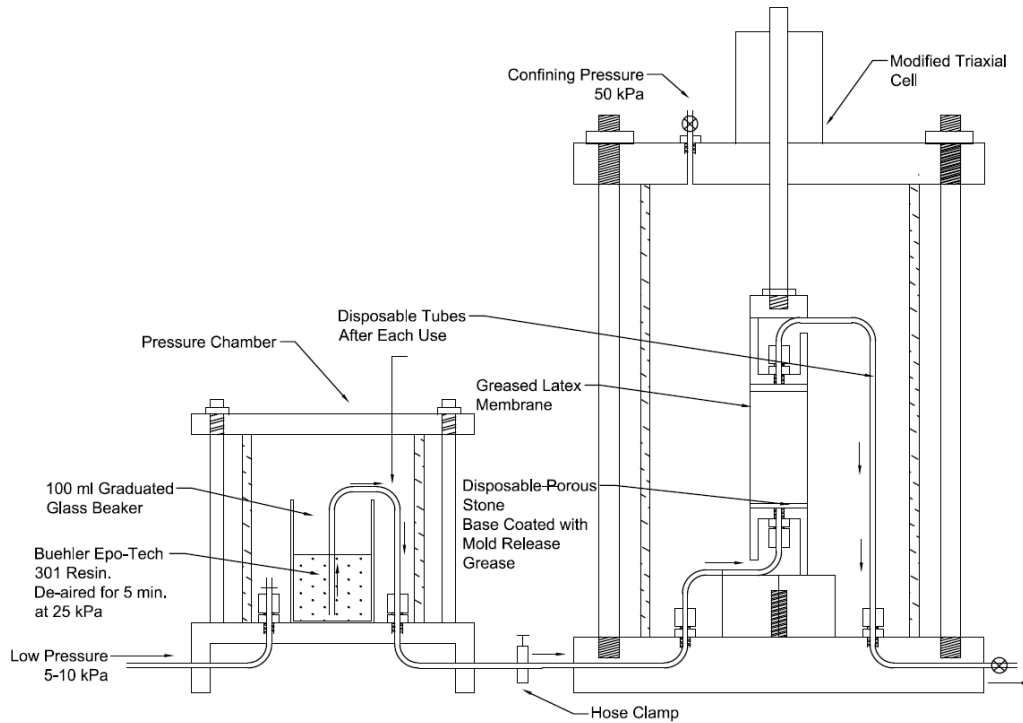


FIG. 3.11. Epoxy Impregnation Setup.

A dual purpose pressure/vacuum chamber, made out of clear Lexan plastic, was fitted with two compression type fittings and a removable top to allow for easy placement of 100 ml graduated glass beaker filled with epoxy within the chamber. A second top cover was fabricated to accept a humidity gauge to monitor moisture levels during the drying process required to properly impregnate a thawed specimen with epoxy.

3.3.2. Dry Chamber and Moisture Monitoring

Buehler[®] Epo-Tek[®] 301 epoxy cannot cure well in a moist environment. A humidity level less than 40% is required for proper curing of the epoxy.

Therefore, for the frozen core samples, it was necessary to thaw, drain, and thoroughly dry the sand prior to epoxy impregnation. The specimen drying system employed for this purpose was similar to that used by Jang et al. (1999)

and Yamamuro (2008). Yamamuro (2008) found that the average, maximum, and minimum values of specimen shrinkage in axial direction were 0.066%, 0.18%, and 0.02% respectively during the drying process.

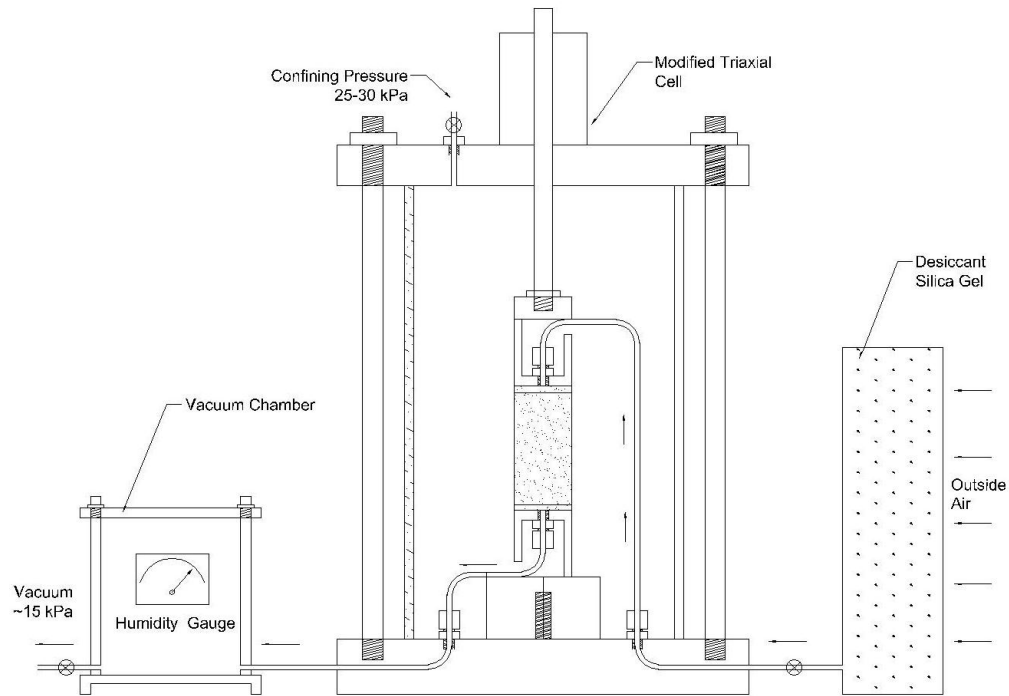


FIG. 3.12. Specimen Drying Setup.

Initially, the frozen core sample was placed in the triaxial cell shown in FIG. 3.12, confined with 50 kPa of air pressure, and allowed to thaw. Next, 15 kPa of pore air pressure would be applied through the top cap to expel free water from the soil sample. Next, the 15 kPa vacuum was drawn through silica gel (SiO_2) desiccant before being drawn through the sand specimen. A humidity gauge was monitored from three to seven days until the gauge indicated a relative humidity of no more than 20%. The duration of this drying process will vary due to environmental factors (ambient humidity level), choice of a desiccant, specimen volume, and permeability. Humid climates may require use of anhydrous calcium

sulfate (CaSO₄), Calcium Oxide (CaO), molecular sieve (porous crystalline aluminosilicates) or a dedicated desiccant dehumidifier system to achieve the desired results. Fortunately this study was conducted in central Arizona, where ambient humidity level varied from 2 to 20 percent. Therefore, a maximum of five days was required to drop humidity level inside the vacuum chamber from 100 to 13 percent resulting in moisture content, ω , equal to approximately 0.75 percent within the core.

3.3.3. Epoxy Impregnation Technique

Air-pluviated specimens and dried frozen cores were preserved using Buehler[®] Epo-Tek[®] 301 two-part optical grade epoxy resin. Based on several trials, it was established that 32 to 35 ml of epoxy was required to saturate the 3.56 cm (1.4 inch) in diameter, 7.11 cm (2.8 inch) high specimen with epoxy. A volume greater than the pore volume of approximately 25 ml was required to prevent air from getting into the system from the epoxy reservoir and to account for the volume of the tubing and the connections. The Epo-Tek[®] 301 epoxy was mixed in 25 ml batches in accordance with the manufacturer's recommendations. Mixing larger volumes is not recommended due to the exothermic reaction that occurs once the base and hardener are combined that could result in shortened pot life.

The epoxy components were combined using graduated pipets in a re-sealable 118 ml (4 ounce) jar and thoroughly mixed for 2 minutes until the solution became clear and uniform in consistency. This process introduces air into to the solution that has to be removed prior to specimen impregnation. According to the

EpoTech technical data (2009), the three most common methods to accomplish this task are vacuum degas, use of a centrifuge, and heating. Vacuum degas requires at least 98.2 kPa (14.2 psi) of vacuum to allow the air trapped inside the epoxy to easily escape. The container used for this process needs to be at least 5 times larger than volume of the epoxy to allow for volume expansion. Excessive vacuum has to be avoided to prevent a “rolling boil” that will cause additional air entrapment. A centrifuge can be used to remove air bubbles from epoxy placed in syringes by rotating them at 1000 to 3000 RPM for 3 minutes. In the centrifuge process, the air is ejected through the nozzle of the syringe. Air can also be removed from the epoxy by placing it in relatively wide pan (to increase surface area) and pre-heating it to 35°C to 40°C for 10 minutes. However, the heat might affect the pot life of the epoxy by acting as a catalyst.

Vacuum degas was used to remove air entrapped inside the epoxy. The 118 ml jar the epoxy was mixed in was sealed with a perforated screw-on top connected to 172 kPa (25 psi) of vacuum and de-aired for 5 to 8 minutes until all the air was forced out of the solution and migrated to the epoxy’s surface. The jar contents were then transferred over to the pressure chamber using a syringe.

Epoxy impregnation was performed by introducing epoxy into the specimen very slowly at a very low differential pressure (between the base and top cap) of 7 to 14 kPa (1 to 2 psi) to minimize disturbance to the soil structure and to prevent air entrapment within the soil matrix. For Ottawa 20/30 sand, impregnation time ranged from 20 to 60 minutes. However, impregnation time could vary for specimens with different hydraulic conductivity or due to changes in the applied

differential pressure or viscosity/ temperature of the epoxy. Impregnation time for the air-pluviated dry samples did not exceed 25 minutes. The thawed cores required more time to impregnate (up to 60 minutes) than the never frozen air-pluviated samples, possibly due to increased amount of fines caused by sample extractions with the hollow stem, diamond core bit. Dry-pluviated samples also required more epoxy (~35 ml) than the thawed core samples (~32 ml) to fully impregnate the sample, fill the inflow tubes, and maintain a reserve in pressure chamber.

Once the initial 25 ml volume of the epoxy was introduced to the specimen, the inflow tubing was clamped to prevent draining of the epoxy. The graduated beaker in the pressure chamber was then replenished with the remaining 7 to 10 ml of epoxy. It was critical not to allow the graduated beaker containing the epoxy to go dry during the impregnation process or air bubbles would be introduced into the specimen, impairing the procedure. Once the specimen became fully saturated with the epoxy, the inflow port was once again clamped and the sand specimen allowed to cure for 24 hours at room temperature.

3.3.4. Encountered Difficulties

Initially, components of the two-part epoxy were kept in the refrigerator to extend their shelf life. A cooled mixture could also provide the additional benefit of increasing pot life (working time) for large diameter or low permeability specimens where the impregnation process might exceed one hour. It was observed that the epoxy that was stored and then mixed at room temperature (~21°C) would become visibly more viscous and begin to skim over after one

hour inside the vacuum chamber. In practice, Epo-Tek[®] 301 was found to have only one hour of working time, at which point increased viscosity of the epoxy could affect the specimen's microstructure and promote uneven saturation of the core.

Previously cooled epoxy was used to impregnate the dry, air-pluviated samples with very good results. However, the same procedure failed to consistently saturate the thawed and dried sand cores, possibly due to the epoxy's increased viscosity. The problem was mostly overcome by allowing the epoxy components temperature to equalize with room temperature overnight.

Impregnation of specimens by vacuum was initially considered but rejected. Vacuum epoxy resin impregnation of petrographic specimens is very common in preparation of thin section for optical mineralogy. The epoxy fills voids and cracks in between rigid crystalline arrangements. However Jang (1997) failed to produce quality sand specimens using vacuum because reacting agents in the Epo-Tek[®] 301 epoxy can easily volatilize under vacuum, resulting in voids once cured. In this research work, a problem of void formation after curing was encountered when diluting the epoxy with 2 percent of 99.9 percent Isopropyl alcohol to reduce viscosity and to extend pot life.

In some instances, full saturation of the specimen could not be achieved resulting in air voids within the grain structure. To salvage those samples, several methods were tried to re-saturate voids of the coupon's surface. The goal was to improve image quality obtained later from the optical microscopy procedure. The coupons would be subjected to the planing and grinding steps described in Section

3.4, wrapped in aluminum foil and the surface flooded with small amount of epoxy resin, as illustrated in FIG. 3.13(a). Some coupons were then placed on a shake table to remove air bubbles and allowed to cure in room temperature, others were placed in a vacuum chamber (-85 kPa) or pressure chamber (150 kPa) and allowed to cure overnight, as illustrated in FIG. 3.13(b).

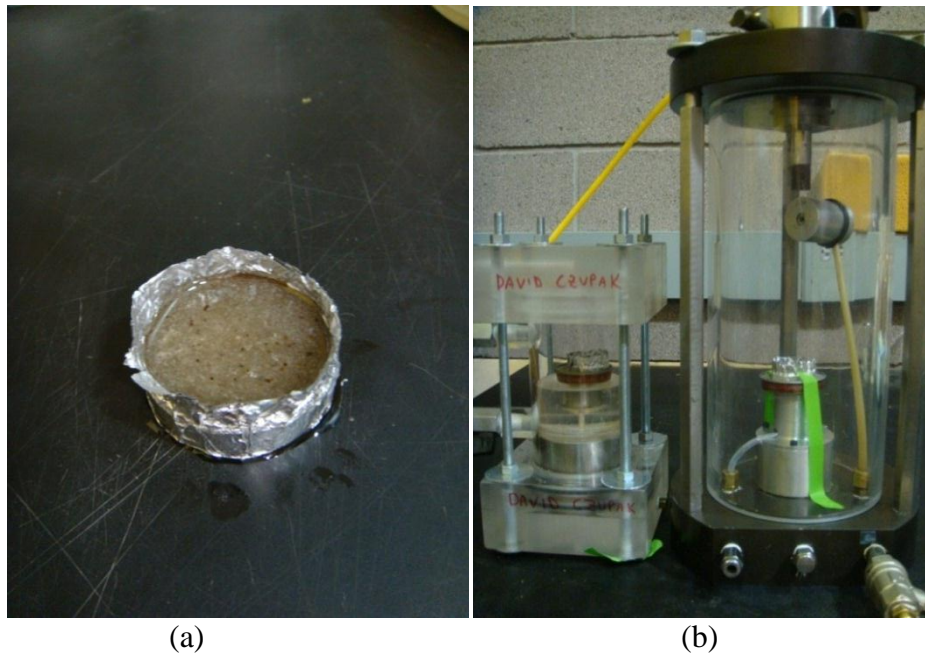


FIG. 3.13. (a) Sand Coupon Flooded with Epo-Tek[®] 301. (b) Overnight Curing in Vacuum Chamber (right) and Pressure Chamber (left).

Best results were obtained when the coupon surfaced was flooded with epoxy and then allowed to cure overnight inside the vacuum chamber at -85 kPa vacuum. Most air voids were fully filled and no air bubbles were present. The surface was then grinded down with 600 grit SiC abrasive and polished with the procedure described in section 3.4.3.

Epo-Tek[®] 301 does not set properly in a moist environment. According to Jang (1997) to prevent water used as confining pressure medium within the triaxial cell from diffusing into the specimen through the latex membrane, a thin

layer of vacuum grease needs to be applied to the outside of the membrane.

However, since the confining pressure used in this study was only ~50 kPa, air pressure was used instead of water to apply confinement to the specimen.

3.4. Coupon Preparation

Once the epoxy-impregnated sand specimen was fully cured, it was removed from the drying cell, both ends were trimmed to remove the disposable plastic porous stones, and the specimen was cut, planed, ground and polished in preparation for Bright Field Microscopy. Accurate quantification of soil fabric depends on the quality of images obtained from illumination microscopy. The quality of these images is directly related to the surface finish quality of the coupons being imaged.

3.4.1. Cutting, Trimming and Planing

Initial rough cuts of the impregnated specimens were made with the National Scientific Corporation Dyna-Cut 48.72 cm (18-inch) diamond blade, water cooled, slab saw shown in FIG. 3.14 to section the 3.56 cm diameter (1.4 inch), 7.11cm high (2.8 inch) specimen into 1.0 cm thick coupons. Coupons were taken from the bottom, middle and the top of the specimen for horizontal images.



FIG. 3.14. Dyna-Cut 18-inch Diamond Slab Saw.

Cuts with the 48.72 cm diamond slab saw caused concave, non-parallel surfaces because of blade flexure and operator error. The 100 to 150 micron deep regions of disturbance had to be removed with a combination of grinding and planing steps. Some researchers (Evans, 2005) used a metal-bonded diamond wavering saw to cut coupons from a larger specimen. Thinner wheel thickness offers minimal kerf loss and a cooler cut than that produced by other cutting methods. Specimen sectioning with a wavering saw results in minimal surface damage which reduces the number of subsequent grinding steps, as discussed in Section 2.5.2. In this research, the entire coupon surface was subjected to the planing, grinding and polishing steps. A wafering saw was not used because the cutting depth of equipment available was well below the diameter thickness of the specimen being sectioned. Fabrication of a custom jig to make rotating cuts was rejected in favor of more planing and grinding steps to remove surface imperfections.

The coupon surface was subjected to manual rough grinding with 120-, 240-, 320-grit, silicon carbide abrasive attached to 20.32 cm (8 inch), pressure sensitive adhesive (PSA) backed paper disks to establish an initial flat surface plane. The opposite side of the coupon was then planed with an OS Walker LBP's Haring 618 Automatic surface grinder, shown in FIG. 3.15, using 120-grit and 240-grit abrasive wheels to establish a parallel surface. During initial trials, both surfaces were planed using the grinding wheel, but this process was discontinued due to excessive fracturing of the silica sand grains. Subsequent hand grinding, to remove damage in excess of 800 microns (the median sand particle diameter), was deemed impractical due to the time required and the large number of samples being processed. Fractured silica grains result in image artifacts (which are caused by light scattering during illumination microscopy) that require additional back-end image processing and should be avoided if possible.



FIG. 3.15. Haring Surface Planer.

A surface planer was also used to trim the coupon diameter to fit inside the polishing/grinding jig. Refer to Appendix G for the polishing /grinding jig design specifications. The coupon diameter varied due to side disturbance from frozen core extraction. The coupon diameter was also larger than the specified 3.56 cm diameter due to the latex membrane expansion when the dry air-pluviated sand specimens were prepared inside the vacuum split mold. An edge chamfer, of 45 degrees, was formed around the coupon's edges to reduce wear on grinding disks and to extend the service life of the polishing cloths.

3.4.2. Manual Grinding

The vast majority of research literature on epoxy-stabilized sand coupon surface preparation techniques for image analysis, e.g. Jang et al. (1999) and Evans (2005), describe the use of a lapping technique during initial grinding to obtain fast removal rates and superior surface flatness, as noted in Section 2.5.4.1. This would have been a preferred method to use in this study but the necessary equipment was not available at ASU. Several alternative methods, suggested by the Buehler[®] and Allied High Tech Products Inc. technical representatives, were considered. These alternatives included silicon carbide paper disks, metal and resin bonded diamond disks, lapping Mylar film coated with resin containing diamond, aluminum oxide (Al_2O_3), silicon oxide (SiO), or silicon carbide (SiC) abrasive. Silicon carbide abrasive resin bonded to adhesive backed 8-inch paper disks, was chosen for its uniform cutting, minimum surface distortion, and deformation. Allied High Tech Product's silicon carbide abrasive disks were used with Buehler[®]'s Ecomet III 8-inch Grinder/Polisher, rotated at 150 rpm for 2 to 3

minutes per disk, for this stage of the process. The sand coupon was mounted inside the grinding/polishing jig with double-sided Scotch tape. Its depth was adjusted with the inset bolt to expose no more than 0.01 cm of edge surface to the abrasive wheel surface, as illustrated in FIG. 3.16(a).



FIG. 3.16. (a). Buehler[®] Ecomet III Manual Grinder and Grinding/Polishing Jig. (b). Grinding/Polishing Jig Loaded with Weights During Manual Grinding Process.

A contact pressure of 29 kPa was applied to the coupon with weights placed on top of the mounting jig, as illustrated in FIG. 3.16(b). The abrasive disks had to be replaced frequently because the abrasive would wear out within a few minutes. A steady stream of water was used to provide lubrication, prevent heat buildup, facilitate swarf removal, and evenly distribute the contact stresses. Coupon was rotated 90 degrees during each consecutive grinding step to help gauge removal rates of damage caused by previously used larger abrasive grit. Grinding steps employed to prepare coupons are listed below in Table 3.2.

Table 3.2. Grinding Procedure.

	STEP	1	2	3	4
Consumables	Abrasive, US Industrial Grit Size	120	240	320	600
	Type	SiC	SiC	SiC	SiC
	Carrier	Adhesive Paper	Adhesive Paper	Adhesive Paper	Adhesive Paper
	Coolant	Water	Water	Water	Water
Settings	Platen Speed (RPM)	150	150	150	150
	Pressure (kPa)	29	29	29	29
	Number of Disks	5	5	5	5
	Time/Disk (min)	2-3	2-3	2-3	2-3

The sand/epoxy coupon and the polishing jig were thoroughly cleaned before switching to a finer size abrasive. The coupon was removed from the jig, washed with mineral soap, rinsed with tap water, placed in an ultrasonic bath, rinsed again with distilled water, and then dried with compressed air. The polishing jig was scrubbed with a brush and mineral soap and then dried with compressed air. In addition, the polishing wheel surface and the grinder/polisher housing were rinsed with soapy water and then clean water to remove scarf and prevent cross contamination with larger size abrasive. This cleaning step was critical in obtaining a good quality surface finish. The raw surface of the coupon, after it was sectioned with a diamond chap saw, is presented in FIG. 3.17(a). The coupon surface shows grain fractures, grain plucking and large surface grooves prior to grinding. At the completion of last grinding step, most of the deep scratches and

fractured grain particles had been removed, but distinguishing between silica grains and the background is still difficult, as illustrated by the image in FIG.

3.17(b).

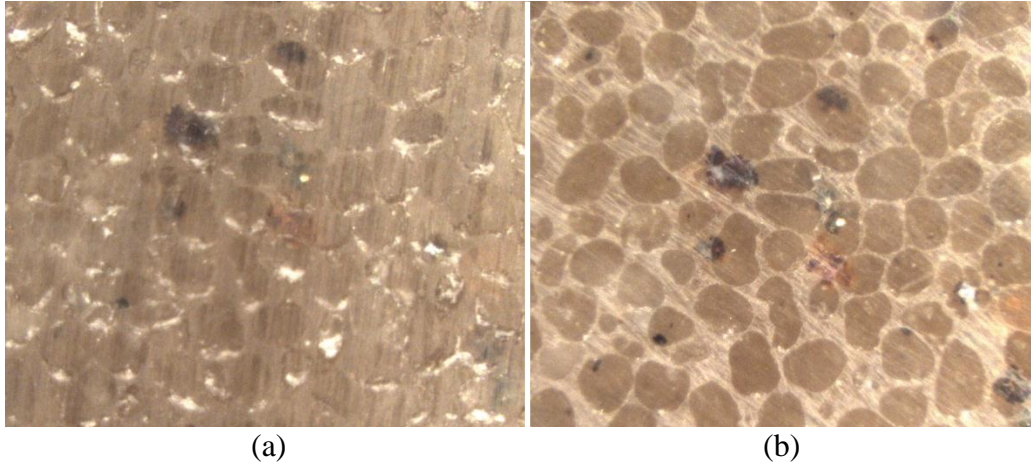


FIG. 3.17. (a) Coupon Surface After Sectioning with Diamond Chap Saw. (a) Coupon Surface After Final Grinding Step with 600 Grit SiC Abrasive.

3.4.3. *Manual Polishing*

Manual polishing was used to remove any damage caused by the grinding process and to obtain an almost perfectly flat, scratch and artifact free surface that can be used for image capture with an optical microscope. This step is critical in obtaining accurate quantitative measurements of the soil structure. However the hardness difference between silica sand grains and the epoxy can result in uneven cutting of those materials during the polishing stage. According to Jang (1999), uneven cutting can result in microstructure relief of grains in relation to the epoxy and edge rounding, where the grain's flat, sharp edge becomes a radius, as

illustrated in FIG. 3.18. This blurring will affect accuracy in calculating the microstructure properties of the specimen by underestimating the grain areas and overestimating the void ratio.

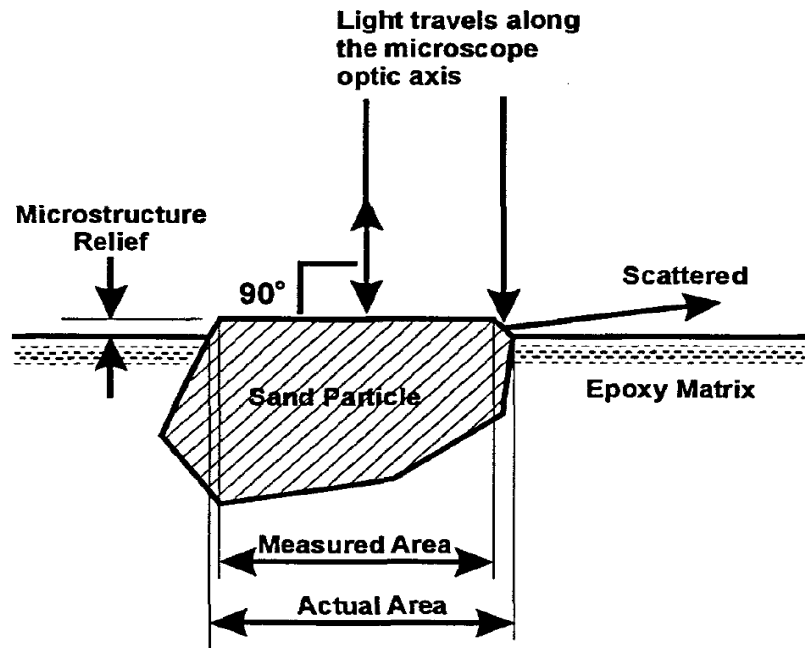


FIG. 3.18. Effect of Sand Particle's Relief and Edge Rounding on Quantitative Measurements. (Jang, 1999)

Structure relief and grain rounding are caused by over polishing, excessive pressure on the coupon surface, excessive platen speed, and under lubrication of the abrasive carrying media. Not enough pressure on the coupon surface, short polishing time, and over lubrication with polishing extenders, alternatively, can result in insufficient removal rates and surface artifacts. Accordingly, the polishing procedure used in this study needs to be monitored with settings adjusted properly to obtain good results.

Initially, the grinding and polishing procedure used by Yang (2002) and Evans (2005), and described in section 2.5.4.1, was used but failed to produce good results. A possible cause for this failure may have been caused by the substitution of the lapping process with silicon carbide paper disks for the initial grinding process. The modified Buehler Dialog[®] Method, used by Jang (1999) and included in Appendix B, was also considered for polishing but rejected due to the lack of lapping equipment. Instead, the modified Allied HTP Inc.'s multi-step polishing procedure was tried. This procedure employs several nappless and napped cloth abrasive-carrying mediums, diamond colloidal suspensions and paste abrasives, and polishing extender fluid. The method calls for six polishing steps, with the smallest abrasive size of 0.3 μm grit alumina in colloidal suspension. This approach, however, resulted in over polishing and reduced the contrast between the sand particles and the epoxy. After several trials, the steps in this process were reduced to three steps which are described in Table 3.3. Appendix C lists the material properties and design specification for the polishing cloths. Appendix H lists the material descriptions of all other consumables obtained from Allied HTP Inc. and listed in Table 3.3.

Table 3.3. Polishing Procedure for Buehler® Epo-Tek® 301 Optical Grade Epoxy-Impregnated Ottawa 20/30 Sand Coupons. (www.alliedtech.com)

	STEP	1	2	3
Consumables	Abrasive (µm)	15	9	6
	Type	Diamond	Diamond	Diamond
	Carrier	Paste	Suspension	Suspension
	Polishing Cloth	PLAN-Cloth	Gold Label	Gold Label
	Coolant	GreenLube	GreenLube	GreenLube
Settings	Coolant Application Rate	Moisten cloth initially, 5-8 drops/15 sec afterwards. Keep on wet side	Moisten cloth initially, 5-8 drops/15 sec afterwards. Keep on dry side	Moisten cloth initially, 5-8 drops/15 sec afterwards. Keep on dry side
	Abrasive Application	10 cm bead initially then 2 cm/2 min afterwards	12 drops initially, 4-5 drops/15 sec afterwards	12 drops initially, 4-5 drops/15 sec afterwards
	Platen Speed (RPM)	120	120	120
	Pressure (kPa)	19	14	14
	Time(min)	5	5	8 or more

The Allied polishing method uses several types of polishing cloths mounted on 0.03175 cm (0.125 inch) thick sheets of glass and attached to the polishing wheel surface with double sided Scotch tape. Each polishing cloth was washed with tap water and stored in a separate Ziploc bag after every use to prevent cross-contamination. The cloth would be saturated with GreenLube™ antifreeze and then loaded with either a 10 cm long bead of diamond compound or 12 drops of diamond suspension. Diamond paste and diamond suspension were substituted

several times with no adverse effect on final results. The sand coupon was mounted inside the polishing jig with double sided tape and its seating depth adjusted so only a small edge of no more than 0.01 cm was exposed. The coupon was marked with reference points to aid in proper positioning, as shown in FIG. 3.19(a). The coupon was rotated 90 degrees for each polishing step to aid in the assessment of material removal rates. Each step had to continue until perpendicular scratch marks made by preceding abrasive were removed.

The polishing jig was positioned on the outer portion of the polishing cloth and weights were stacked on top of the jig to obtain the required contact pressure, as illustrated in FIG. 3.19(b). Lubricant and abrasive suspension were administered in front of the coupon every 15 seconds continuously. For the first polishing step, with 15 μ m diamond paste, the wheel would be stopped every two minutes and loaded with an additional 2 cm bead of diamond paste abrasive. The polishing cloth was kept on the wet side to facilitate swarf removal and to prevent surface tear outs due to relatively aggressive material removal rates at this polishing stage.

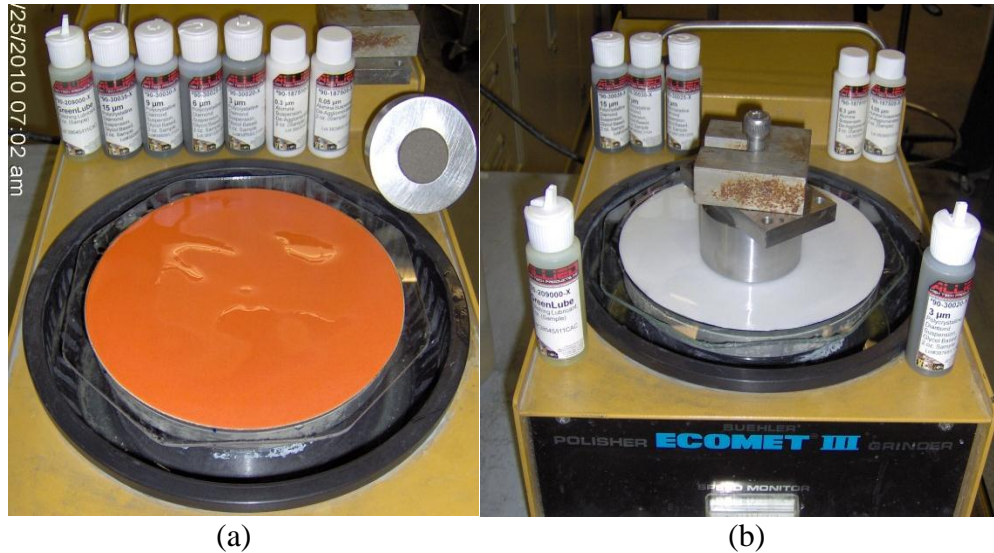


FIG. 3.19. (a) Gold Label Polishing Cloth Moistened with Lubricant and Sand Coupon Inside Polishing Jig, left. (b) Manual Polishing Setup (right).

The initial polishing step, using 15 μm diamond paste abrasive, removed major artifacts from the grinding process and made the coupon surface perfectly flat. Grinding with similar size silicon carbide abrasive, on the other hand, would cause deep gouges on top of the silicon grains. Since the epoxy is a much softer material than the sand grains, its removal rate would be much greater, causing grain relief and edge rounding. The initial polishing step removed scratches from the sand particles and then from the surrounding epoxy while maintaining very good edge retention. The resulting low contrast images made it very difficult to distinguish between sand grains and the surrounding epoxy, as illustrated by FIG. 3.20(a).

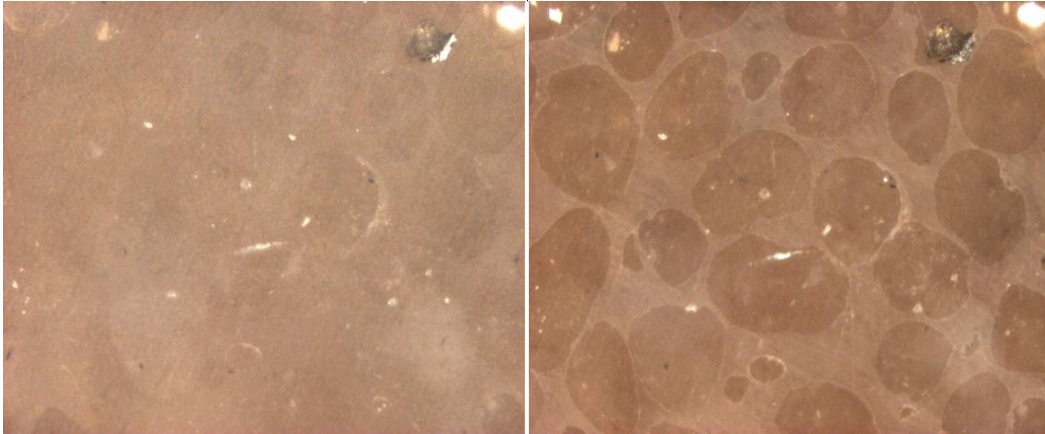
The second polishing step, with 9 μm grit diamond suspension, used lower contact pressure of 14 kPa. During this step, surface artifacts such as scratches were removed at a higher rate from the epoxy matrix than from the sand grain particles. Polishing with 9 μm grit abrasive resulted in a progressively better

image contrast, as shown in FIG. 3.20(b). The grain particles began to appear darker than the surrounding epoxy and the grain relief was no more than 2 μm above the epoxy matrix when observed under a high power microscope. Some of the surface scratches were still apparent after 5 minutes but extending this step beyond the specified 5 minutes was found to result in excessive edge rounding of the grain particles.

The final polishing step used a relatively low contact pressure, with duration in excess of eight minutes, or until the desired image quality was obtained, as illustrated in FIG. 3.20(c). The polishing cloth was loaded with a small amount of anti-freeze coolant and kept on the dry side to ensure good surface contact. Scratches on top of the sand particles were removed at a higher rate than the surrounding epoxy resulting in a high contrast image. The sand grain particles appeared darker than the epoxy with good edge retention. Grain relief was confirmed with a high power microscope not to exceed 4 μm above the epoxy surface. The time required to obtain good results may vary and needs to be monitored until satisfactory results are achieved. The process described above should provide consistent, repeatable results for epoxy-impregnated sand coupons composed of Ottawa 20/30 silica and for specimens composed of sand of similar hardness and shape. However, it may not be applicable to soil specimens with variability in particle hardness. Ultimately, the process will have to be refined by trial and error for any new material.

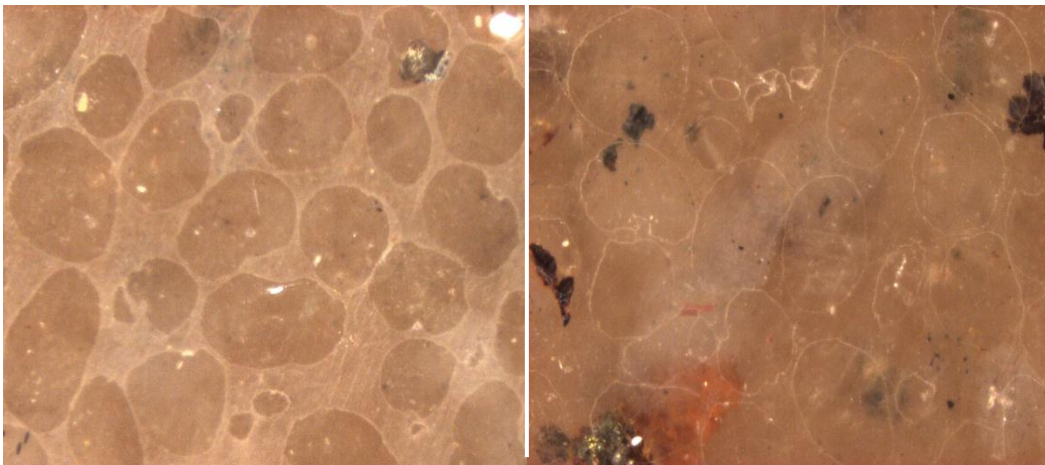
Excessive polishing with one size abrasive will lead to particle edge rounding and should be avoided. The objective in this process is not to achieve a perfectly

polished surface. Instead, the aim is to create a matrix of flat surfaces and very fine scratches produced by the hardness differences between silica and the epoxy. When viewed under a bright field microscope, this process should result in a good image contrast without introducing an excessive number of artifacts that have to be removed on the back end of the imaging process with image analysis software.



(a) Polished with 15 μm Abrasive.

(b) Polished with 9 μm Abrasive.



(c) Polished with 6 μm Abrasive.

(d) Over Polished Sample, 0.3 μm .

FIG. 3.20. Images of Ottawa 20/30 Epoxy-Impregnated Sand Coupons at Various Stages of Polishing.

FIG. 3.20(d) shows a coupon surface subjected to a manual polishing procedure using 30 μm , 15 μm , 9 μm , 6 μm , 3 μm diamond abrasive and 0.3 μm alumina suspension abrasive to obtain a mirror-like finish. Once viewed with the BFM procedure, the resulting image displayed grains with good flatness and edge retention but was deficient in high grain-to-background contrast that could be used to successfully perform image segmentation during the digital image processing procedure. Those types of mistakes can be corrected by resurfacing the coupon with larger sized abrasive and repeating several polishing steps while monitoring the progress with an optical microscope. Past experience has demonstrated that the coupon surface would have to be re-surfaced using the last step of the grinding process (600 grit SiC abrasive) and the entire polishing procedure repeated. The attempts to correct over polishing by reverting to step one, described in Table 3.3, and repeating the polishing procedure, resulted in low contrast, poor quality images similar to the one shown in FIG. 3.20(d).

3.5. Image Capture

Epi-illumination (BFM) was used to image the microstructure of the epoxy-stabilized cohesionless soil specimens. BFM was used to image specimens that were subjected to procedure outlined in Sections 3.3 and 3.4 above (epoxy impregnation and manual surface polishing).

3.5.1. Bright Field Microscopy

Image capture for this research was accomplished with an optical microscope with built-in light source connected to a digital camera and personal computer. The InfiniVar CFM-2/S manufactured by the INFINITY Photo Optical Company

(www.infinity-usa.com), with standard length tube lens, digital camera and software was used. According to the company's technical data, the InfiniVar CFM-2/S is a continuously focusable microscope with infinity-correction that requires Infinity Tube Lenses to establish final focus. In this research, a standard tube lens was used to obtain a theoretical resolution range from 23.68 μm to 1.42 μm for a corresponding magnification ranging from 0.18-times to 9-times depending on the working distance (WD) from the surface of the specimen to the lens and the field of vision (FOV). Table 3.4. describes the characteristics of the optical microscope used, including the working distance (WD), magnification, resolution, and field of vision (FOV). The field of vision describes how much of the object's depth can be held at reasonable focus for a particular working distance and magnification. Anything outside of that FOV will appear blurred. The air immersed objective used in this research has a Numerical Aperture NA=1.5. The microscope objective was also fitted with a zoom module that can vary from 1x to 2.2x magnification. In this research the zoom module was set at 2.2x magnification.

Table 3.4. InfiniVar GS Characteristics Based on 160 mm Tube Lens and 35mm Format. Not Adjusted for 2.2x Zoom Module. (www.infinity-usa.com)

N.A.	0.24	0.21	0.17	0.11	0.07	0.06	0.04	0.04	0.02	0.01
WD (mm)	18	20	25	38	58	75	95	115	220	300
Magnification	9.00	8.00	5.00	2.00	1.00	0.75	0.60	0.50	0.25	0.18
Resolution, (μm)	1.42	1.58	1.97	3.00	4.58	5.92	7.50	9.08	17.37	23.68
FOV (mm)	0.7	0.8	1.3	3.2	6.4	8.5	10.7	12.8	25.6	35.6

The optics were combined with a Lumenera[®] Corporation's Infinity 2-1, 1.4 megapixel charge-coupled device (CCD) camera capable of taking high quality RGB (Red-Green-Blue) color images over a wide range of lighting conditions with a maximum resolution of 1392 x 1040 pixels. Appendix I provides a complete list of specifications for the camera. The camera was controlled with proprietary Infinity Analyze software for advanced camera control, image processing, measuring, and annotation. The Infinity Capture user interface software was used to control the camera and to capture images (www.lumenera.com).

Sample illumination was provided with two banks of 150 watt, fiber optic EKE ring lights that supplied 380,000 foot-candles of high intensity, highly-directed, cold light, FIG. 3.21. Inner and outer light rings, attached around the microscope objective, could be adjusted separately to create appropriate lighting pattern. To ensure an even lighting pattern, free of glare and variation in surface intensity, the specimen was leveled in X and Y directions in relation to the microscope's objective using a specially constructed leveling table.

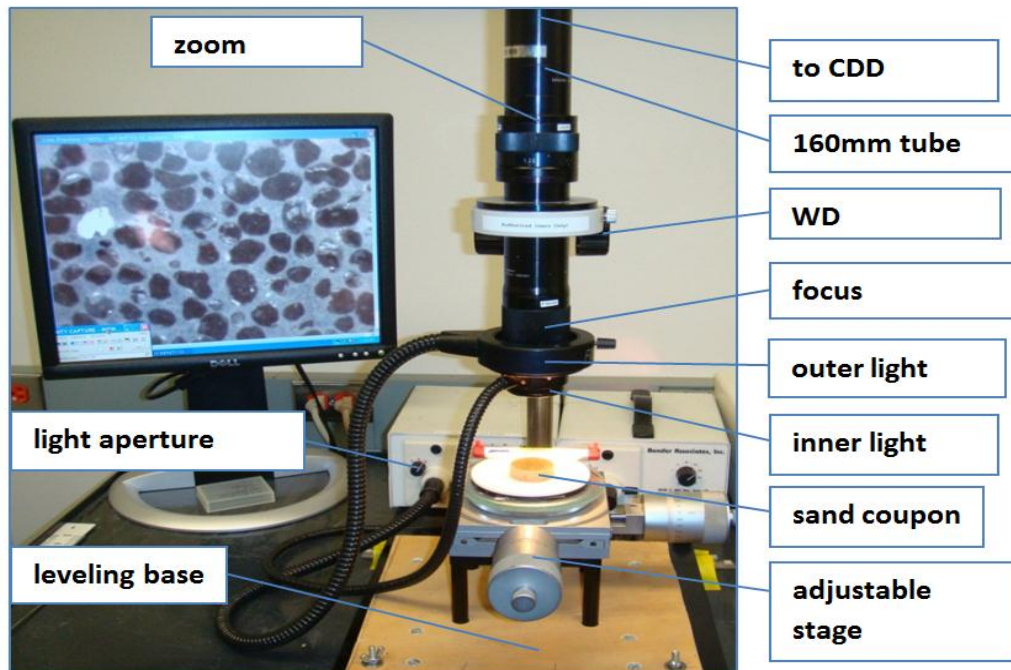


FIG. 3.21. Experimental Setup Used for Image Capture with Bright Field Microscopy.

3.5.1.1. Procedure

Individual and sets of images, used to recreate the surface of the entire coupon with a stitching technique, were obtained with the equipment setup described in the previous section. A high resolution image of the entire coupon could not be obtained with a single shot due to equipment limitations. When the distance between the coupon surface and the microscope's objective (known as the working distance, WD), is set too far, optical aberrations can prevent an entire image from coming into sharp focus. If grain particles in the center of the image are in-focus, the grain particles on the periphery will appear slightly fuzzy and blurred, and vice versa. In addition, a large WD value will result in uneven illumination of the specimen with over- and under-exposed areas. After the zoom module was set at 2.2x magnification, it was found that the optimum working

distance was 5.8 cm to 7.5 cm, corresponding to a magnification of 2.2x to 1.65x. This WD resulted in high quality, evenly illuminated, aberration-free images. Since only a small section of the coupon (7mm x 5 mm) could be imaged at a time, close to 100 individual images had to be taken to create a mosaic which could be stitched together using image processing software to recreate the coupon surface.

In the initial setup, it was essential that the surface of the sand coupon was parallel to the surface of the microscope's objective. To achieve this goal, the microscope's base was shimmed and leveled. The 3.56 cm diameter coupon was then centered and attached to the top of the specimen stage with double sided adhesive Scotch tape. The adjustable stage was placed on top of the leveling table shown in FIG. 3.21 and the coupon was checked for level in X and Y directions. Moving the InfiniVar GS unit to a working distance of 5.8 cm to 7.5 cm, the magnification and potential depth of field were adjusted to the previously discussed levels. Since the image exposure and gain can be controlled with the Infinity Capture software, the EKE fiber optic light apertures were fully open and the light intensity was set to medium level. No further adjustments to the illumination source were required from then on.

3.5.1.2. Image Acquisition

When microscopes fitted with conventional objectives are used for imaging, focusing is done either by moving the stage and the specimen relative to the objective or by moving the entire tube relative to the stage. According to Bradbury and Bracegirdle (1998), when infinity-corrected objectives are used, the

distance between the objective and the tube lens may be varied significantly without detriment to the image quality. Obtaining best quality images requires only setting the working distance to a value that corresponds to a field of vision between 0.64 cm – 0.85 cm and then adjusting the focus ring to acquire a sharp image of the coupon surface.

Infinity Capture software was used for image preview, adjustment of initial white balance, image brightness, exposure and gain, and image capture. FIG. 3.22 shows the image preview of a coupon surface with the image histogram and image capture control software settings. The maximum digital resolution used to capture color (RGB) images was 1392 x 1040 pixels, equivalent to 4.65 μm square pixels. Typically, however, lower resolutions were used for image preview to speed up the image acquisition process. The gain (used to electronically brighten the image) was permanently set at 10x and only the extended range exposure was varied for different images in order to obtain desired characteristics of the image histogram used to gauge the quality of the image. For reasons described in more detail in Section 3.5.1.4., the exposure was adjusted in each image to maintain the image histogram within the central portion of the gray scale pixel intensity range to reduce brightness and contrast variations among consecutive images. The coupon surface was scanned from right-to-left and from bottom-to-top to create a mosaic grid, as illustrated in FIG. 3.23. The scanning sequence becomes significant in the subsequent image stitching process because the *PanaVue Image Assembler*, used to create a final image, can only be used with images assembled in reverse order from the one mentioned above. Finally, the

captured color images were saved in Tagged Image File Format (TIFF), a lossless data compression storage format popular in the publishing and scientific fields.

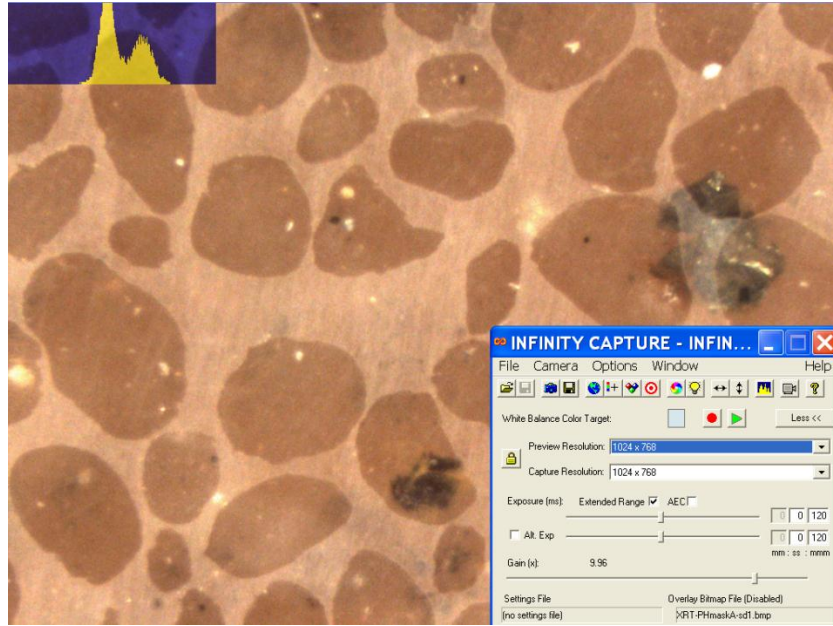


FIG. 3.22. Image Preview of Coupon Surface with Image Histogram and Image Capture Control Software.

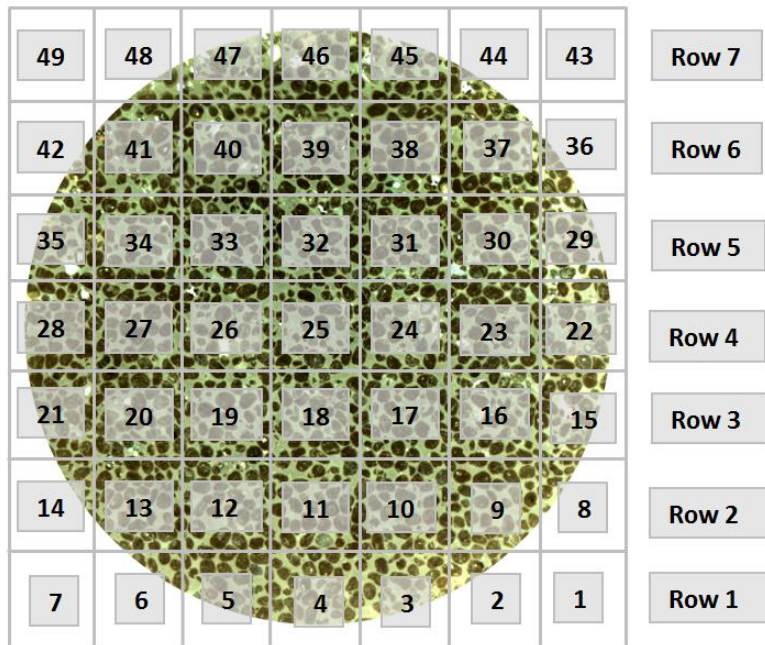


FIG. 3.23. Scanning Order of the Coupon Surface for Subsequent Reassembly with PanaVue Image Assembler.

3.5.1.3. Image Resolution

To effectively observe image details under a microscope, magnification and good resolution are required. Magnification of a poor resolution image is pointless, since it would not yield any additional information about the specimen. Resolution is a combination of the theoretical resolution of the microscope optics combined with the maximum resolution of the charge-coupled device (CCD) sensor in the digital camera. Image resolution can also be diminished by insufficient contrast caused by improper specimen illumination and the use of lower resolution images for analysis and storage.

Optical resolution (minimum resolved distance) is defined as the least separation between two points at which they may be resolved as being separate. As the light waves pass through the objective, they are diffracted on their way to the camera detector creating a diffraction pattern of light and dark bands. The center band of undisturbed, zero-order maximum light that is surrounded by rings of 1st, 2nd, and higher orders of interference is called the Airy disc. The Airy disc typically contains 84 percent of the luminous energy (the rest is lost to diffraction) and represents the smallest size that the microscope can be focused on. Fig. 3.24(a) illustrates a single Airy disk pattern. The maximum resolution is the smallest distance between two Airy disks where they are still resolvable. Fig. 3.24(b) illustrates two resolvable Airy disks. Once the separation between two disks exceeds their radii and their intensity distributions merge, the image detail is lost. Fig. 3.24(c) illustrates a case in which image detail will be lost.

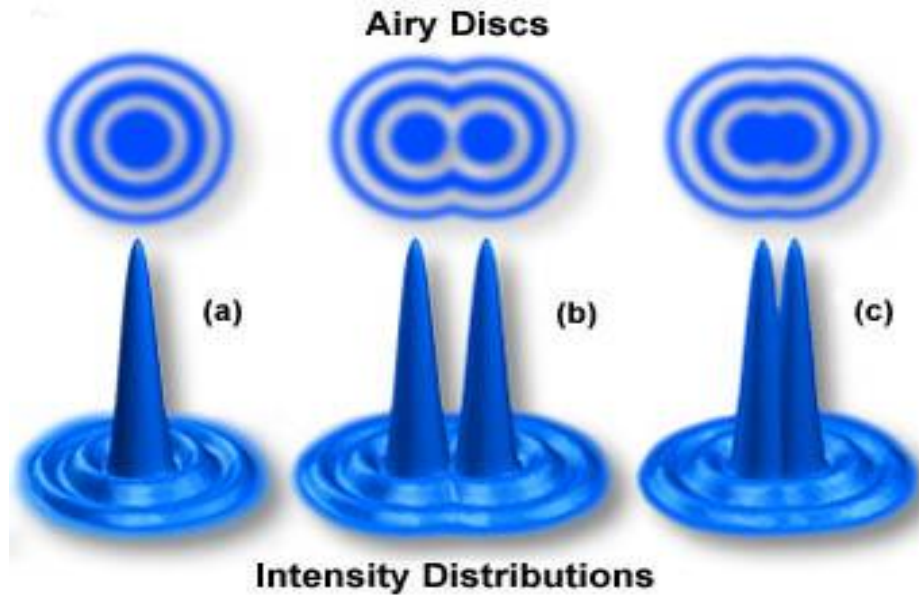


Fig. 3.24. The Airy Discs of Two Points. (a) Single Airy Disk Pattern. (b) Two Airy Disks at Limit of Resolution. (c) Two Airy Disks Overlapping. (www.micro.magnet.fsu.edu)

Larger numerical apertures increase resolution and image quality because they reduce light diffraction. The larger the aperture is, the higher (brighter) the Airy disk and the smaller its diameter. The maximum resolution, R , of an image is described by the Raleigh criterion which states that the maximum resolution is a function of the light wavelength, λ , used for specimen illumination (typically a $\lambda=550$ nm is used for white light source) and the size of the numerical aperture, N.A:

$$R = \frac{0.61\lambda}{N.A.} \quad (3.1)$$

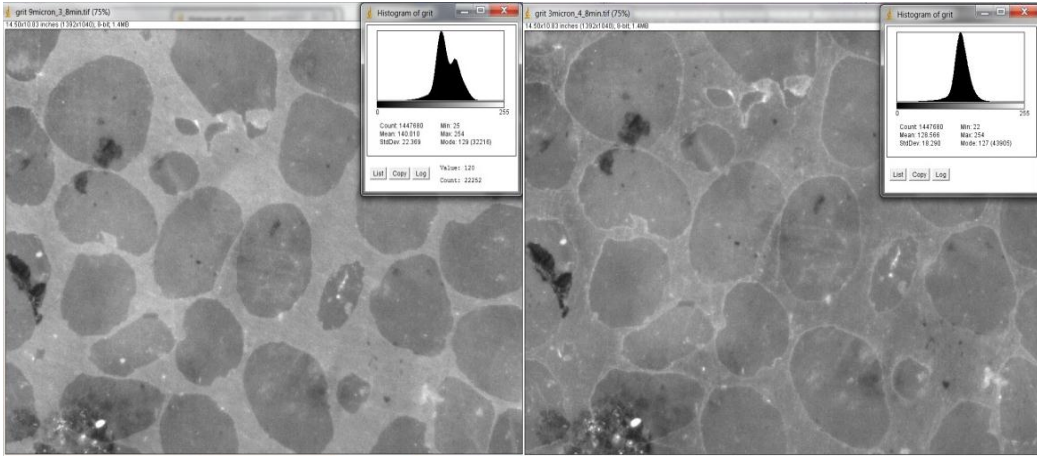
Image sharpness and resolution are also affected by the quality of the CCD sensor that is used to convert image formed by the microscope into its digital equivalent. The 1.4 megapixel CCD sensor provided a maximum pixel resolution of 1392 x 1040 in this research, which is equivalent to a maximum resolution of

4.65 $\mu\text{m}/\text{pixel}$. Depending on the level of magnification chosen, either the theoretical resolution of the optics or actual resolution of the digital camera can be a limiting factor in image quality. For example, using 2x magnification referenced from Table 3.4 will result in 3 μm theoretical resolution with 1070 lines/mm or 1 $\mu\text{m}/\text{pixel}$, but the actual resolution is limited by the CCD sensor to 4.65 $\mu\text{m}/\text{pixel}$. Assuming 0.75x magnifications with a theoretical resolution of 5.92 μm with 218 lines/mm, the image quality is limited by the optics instead. Storing images in lower resolution formats, or saving them using compression algorithms, results in data loss that cannot be recovered during subsequent image processing and analysis.

3.5.1.4. Image Histogram

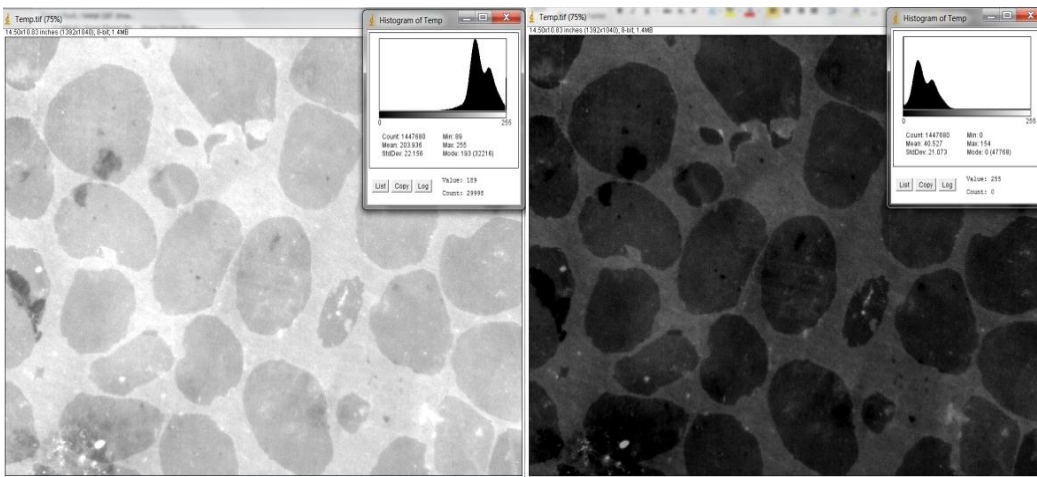
An image histogram is a valuable tool to quickly assess image quality. It is a graphical representation of the tones contained within an image. An image histogram shows the relative number of pixels at different light intensity levels, the calculated luminescence, and the individual red, green and blue intensities for color images or gray tones in black and white images. In this research, RGB images were converted to 8-bit gray scale images with a possible range of 256 tones from black (0) to white (255). For epoxy-impregnated sand coupons, the ideal histogram should have two distinct peaks; right peak that represents the lighter epoxy and left peak that represents the sand grain particles, as illustrated in FIG. 3.25(a). This characteristic is crucial later on during image processing to successfully threshold each image into a binary format. FIG. 3.25(b) shows a histogram containing only one distinct peak. This single peak indicates a very low

contrast between the background and the grain particles, where the majority of gray scale intensities are centered around one mean value. This result is indicative of a failed finishing procedure that either over- or under-polished the coupon surface. FIG. 3.25(c) and FIG. 3.25(d) display over- and under- exposed images with the histograms shifted to the extreme right or left, respectively. As mentioned in Section 3.5.1.3, over- or under-illuminated images can be corrected by adjusting the exposure level during the image acquisition process until the image histogram is in the central part of the intensity range. It should be noted that some errors during image capture can be corrected for brightness variability, sharpness, and contrast with most image analysis software, but not without some information loss that could affect the accuracy of measurements later on.



(a) Optimally Illuminated Image.

(b) Poorly Polished Coupon Surface



(c) Overexposed Image

(d) Underexposed Image

FIG. 3.25. Histogram Response of 8-bit, Gray-scale Image to Different Illumination Levels and Polishing Errors.

3.5.1.5. Image Distortions

Image distortions, also known as optical aberrations, are caused by artifacts due to the interaction of glass lenses with the light source. Just as a poor specimen preparation can create image artifacts, lens aberrations can add another layer of “noise” to the image. Davidson and Abramowitz (2003) identified two primary sources of image distortions: the geometrical aberrations caused by the spherical nature of the lens and chromatic aberrations caused by the variations in the refractive indices of the wavelengths found in visible light.

Spherical aberrations are caused by the spherical nature of the objective, where light rays passing through the periphery of the objective are refracted more than those passing through the intermediate areas and the center. The rays cannot focus on one spot, creating a zone of confusion. Chromatic aberration is caused by the variation in the refractive properties of glass for different wavelengths. It is larger for short wave lengths (blue) than for longer wave lengths (red). The point of focus varies and the image is blurred due to chromatic aberrations. Coma and astigmatism also cause blurring of non-axial points. In coma, the marginally passing rays meet at a different point than the axially passing rays. In astigmatism, geometric distortion can cause the magnification of the image to vary from the center to the periphery causing either greater magnification at the center or at the periphery. In compound microscopes, the objectives are classified by the level of optical correction and vary from the least corrected achromatic objectives and fluorite objectives to the most corrected (and expensive) apochromatic objectives.

The Infinity-corrected system that was used in this research is almost free of residual aberrations. The image formation is not fixed at finite tube length but is formed in infinity with parallel rays that eliminate the need for most image corrections. It was found that the InfiniVar microscope system still suffered from some geometric distortion where it was difficult to focus both central and peripheral sections of the image at the same time. This problem seemed to diminish with magnification levels of 0.75x and higher.

4. RESULTS

4.1. Image Processing Procedure

Images of the coupon cut and polished from the epoxy-stabilized sand specimens, and generated with the use of the BFM technique described in Section 3.5, were processed with image processing software to extract information about their microstructure properties. Following guidelines on image manipulation, presented by Frost and Kuo (1996) and discussed in Section 2.6 of this dissertation, five necessary image processing steps were identified: image generation, image coding, image assembly, image processing, and measurement.

Image generation was accomplished with the BFM optical microscopy technique. For image coding, two types of lossless compression formats were used: Tagged Image File Format (TIFF) for storage and processing of color (RGB) and grayscale images and Bitmap Image File format (BMP) for binary image processing and analysis. Individual 0.7 cm by 0.5 cm (1024 by 768 pixels) images were assembled to form a single image of the entire coupon with the use of *PanaVue Image Assembler* software. Appendix J presents a mosaic stitch procedure that combines individual red-green-blue (RGB) images to recreate a surface image of the entire coupon. Image processing involved the conversion of RGB images with *ImageJ* software, manipulation of 8-bit gray scale images to enhance image quality, and the removal of noise and image artifacts. Images were then converted to black and white binary images and subjected to mathematical morphology algorithms. The individual sand grain particles in the image were separated from each other and the boundaries of the void space

associated with the individual particles were defined with voronoi, watershed, outline, erode, and dilate algorithms. Measurements performed on the binary image generated information about particle shape parameters and local void ratio distribution. FIG. 4.1 presents the image processing work flow diagram.

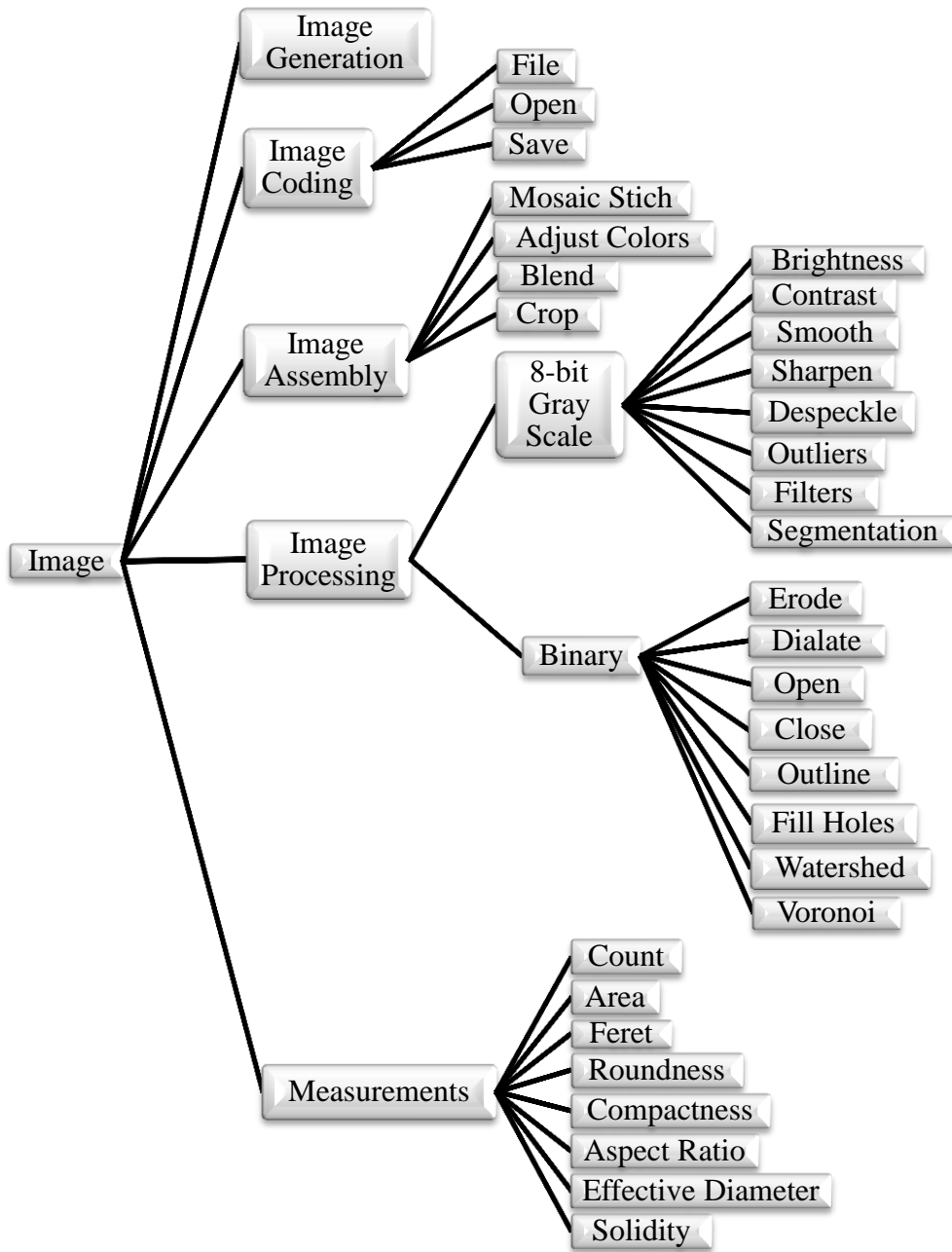


FIG. 4.1. Work Flow Diagram for Image Processing.

4.2. Image Processing and Analysis with *ImageJ* Software

Image processing and specimen microstructure analysis were performed with *ImageJ*, an open source, Java based image processing program that provides simple and usable plug-ins and macros for file manipulation, image conversion, arithmetic operations, and common image processing. *ImageJ* supports standard image processing functions such as contrast manipulation, sharpening, smoothing, edge detection and image filtering. It also supports image stacking and mathematical morphology operations on binary images. *ImageJ* does geometric transformations such as scaling, rotation and image flipping. It can generate histograms and line profile plots. There are currently over 100 free plug-ins written for image processing in multiple scientific fields, including microbiology, physics, geology, and astronomy. These are available for downloading at no cost. *ImageJ* can display, zoom, scroll, edit, analyze, process and print 8-bit to 32-bit images in TIFF, GIF, JPEG, BMP, DICOM or “raw” formats. User generated macros can be developed to perform several consecutive image processing steps more efficiently.

4.2.1. Grayscale Images

Color (RGB) images that were assembled with the *PanaVue Image Assembler* were converted to 8-bit gray scale images. Only a center area of the image, 2.54 cm (1 inch) in diameter, was kept for image processing. The image perimeter was discarded to minimize the possibility of processing sand grain particles disturbed by the extraction process. The image quality of the coupon’s edge suffered from overexposure and optical distortions. The gray scale images were processed to

correct image defects and for image enhancement. Steps involved in this stage of the process included contrast expansion, correction for noise, illumination correction, histogram manipulation, processing of the image in frequency space with image filters, and finally segmentation and thresholding. The goal of this stage was to minimize loss of data and, at the same time, enhance image quality so that consistent results could be obtained from the images after conversion to a binary format. Through trial and error, an automated procedure (with use of a macro) for achieving this goal was devised. The algorithm for the automated process is illustrated in FIG. 4.2. The coupon preparation technique and image acquisition procedure, described in the preceding chapter 3, provides consistent results between different coupons from the same specimen and among different core samples for input through this automated procedure. Appendix K shows individual settings and screen captures for each step outlined in FIG. 4.2 for automated image processing using ImageJ.

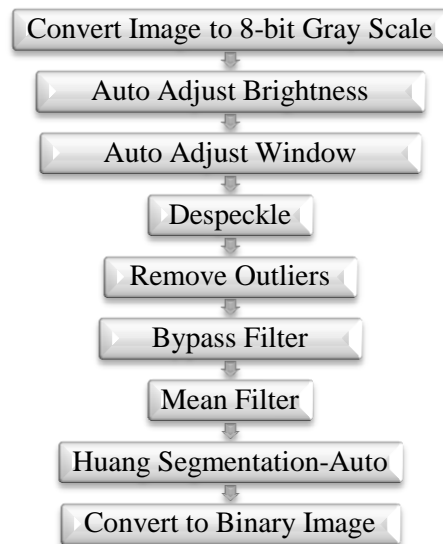


FIG. 4.2. Image Processing Algorithm for 8-bit Gray Scale to Binary Image Conversion.

Auto adjustment of image brightness and window values ensures that the pixel values and image histograms are shifted to the optimum value level and image brightness and contrast are similar among different specimens. The despeckle function removes image noise from the image. The outlier function removes white or black image artifacts of specified pixel size. Band pass and mean filters are designed to filter large and small image features to a specified pixel size, and to smooth particle perimeters, respectively.

The final step before conversion to a binary (black and white) image is called thresholding/segmentation. This process is designed to select the pixels within a range of brightness values that belong to the foreground and reject all of the other pixels in the background. The resulting image is displayed as a binary image, using black and white colors, to distinguish foreground and background regions. This process is called thresholding and must be calibrated using a control image of known properties in order to establish the correct threshold value, as illustrated in the following section. An auto adjusted Huang thresholding procedure, available in *ImageJ*, was applied to a gray scale image to create black sand grain particles (value of 0) on a white background (value of 255).

4.2.2. Procedure to Calibrate the Thresholding Value

The accuracy of parameters calculated from the binary images depend on a threshold value set during the segmentation process. This threshold value divides an image histogram, composed of a grayscale intensity frequency distribution, into two groups of values corresponding either to the background or to foreground. The optimal threshold value was established for this study by

selecting a small (2000 μm x 2000 μm) subsection of the RGB image from the control sample. The image was converted to an 8-bit gray scale image that was then adjusted for image artifacts, noise, brightness, and contrast. The grain outlines were then created manually at the maximum image magnification and filled. After the grayscale image was converted to a binary one, the true global void ratio, e , was established as 0.4894. In order to establish the automatic segmentation procedure, this true void ratio was compared to the void ratio obtained from the same 8-bit gray scale image and subjected to 15 different segmentation methods offered through the *ImageJ* software. For each segmentation method, the thresholding value was set to “Automatic”. The image was then subjected to the mathematical morphology, as operations discussed in Section 4.2.3, and the image void ratio calculated. Threshold value was progressively adjusted until the calculated error for each method could not be minimized any further. Table 4.1 lists the first five segmentation methods, and the inherent errors associated with using them, as established from the above comparison. FIG. 4.3 displays results from employing the Huang, Intermodes, and IsoData segmentation methods on the gray scale image with the resulting final binary image. Appendix L presents the segmentation calibration results, and associated images, for all fifteen thresholding methods. Huang segmentation was chosen as the preferred method because when applied in the automatic mode and then adjusted by a value of 7 toward darker intensities, it resulted in an error of only 0.1 percent when compared to the control image.

Table 4.1 Calculated Error Associated with Different Thresholding Methods

THRESH- OLDING METHOD	AREA OF SOLIDS, A_s (μm^2)	AREA OF VOIDS, A_v (μm^2)	VOID RATIO, e	Error (%)	VALUE AUTO +7
Control	2,689,477	1,316,215	0.4893	0	NA
Huang	2,690,461	1,315,231	0.4888	0.11	139
Intermodes	2,658,092	1,347,600	0.5069	3.59	138
IsoData	2,652,443	1,353,249	0.5101	4.24	132
Li	2,543,526	1,462,166	0.5748	17.46	119
MaxEntropy	2,580,488	1,425,204	0.5523	12.85	121

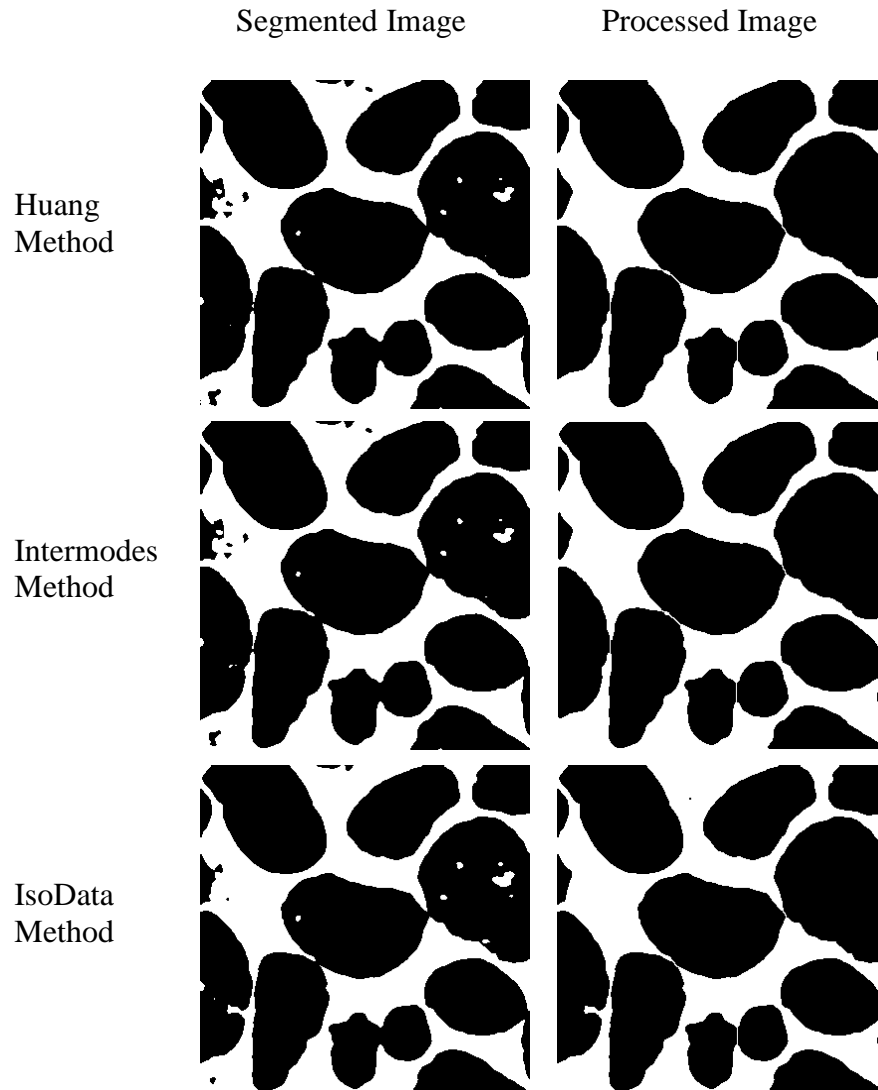


FIG. 4.3. Results of the Huang, Intermodes and IsoData Segmentation Methods on the Gray Scale Image.

4.2.3. Binary Images

Segmented 8-bit gray scale images were processed, as described in previous sections, using *ImageJ* to create binary images containing white (value of 1) particles on a black (value of 0) background. *ImageJ* requires that those values are reversed for binary image processing and analysis. Raw binary images can exhibit a substantial number of artifacts caused by fractured grains, foreign matter imbedded within the soil matrix, and the presence of trace impurities (carbon,

iron, manganese, chromium) which appear as holes or chips within the grain particles. Those artifacts can be corrected manually with a pointer and drawing tool suite available in *ImageJ* program. This correction process can be tedious, is prone to errors, and is not practical for larger images. As an alternative, another class of automated editing procedures based on neighbor relationships (Rosenfeld and Pfaltz, 1966), from a field known as mathematical morphology (Matheron, 1975; Sierra, 1982), was employed. The underlying theory is beyond the scope of this dissertation, but a brief overview of the functionality of each operator is provided herein.

In mathematical morphology, erosion and dilation functions are used to smooth out feature outlines, join discontinuous features, and separate touching features. The erosion function examines each binary pixel and changes it from ON to OFF if it has any neighbors that are OFF. This global process reduces image features all around their periphery. Dilation is the inverse of erosion (etching), wherein a pixel is switched from OFF to ON if it has at least one ON neighbor. This results in feature dilation that fills small breaks, internal voids, or small indentations.

Erosion and dilation can be used together leading to a smoothed shape that recovers most of its original size. Opening is the process of erosion, and followed by dilation, removes small features (noise) and sharp protuberances from the feature outline. The resulting features almost fully maintain their original size but may become more rounded and smooth with gaps forming between touching

grains. Closing is the process of dilation followed by erosion that results in some loss of the original area and smoothing of internal corners.

Skeletonization, also known as medial axis transform (MAT), is a specialized form of erosion that creates lines of pixels that mark the midline of the features. Skeletonization is useful for the reduction of broad features, such as grain boundaries that have been widened by dilation.

Watershed segmentation is another mathematical morphology operation. Watershed segmentation uses a distance map to separate touching features so they can be measured separately. In a gray scale image, it uses local maxima to find most of the elevated parts of the object (highest localized intensities). Starting with those points, it dilates outward either until the edge of the object is reached or the edge of the region of another maxima erosion point is reached.

The voronoi algorithm forms a polygon network through the void space and particle contacts that is a result of growth process of simultaneous circular growth outward from particle centroids. Growth stops at a point of contact but the remaining points of the circle continue to expand and the points of contact become midpoints of growing straight line segments along which growth frontiers meet and freeze (Alshibli, et al., 2001).

A combination of manual image corrections and mathematical morphology algorithms was used to prepare the binary images for microstructure analysis. The required sequence of image corrections, performed on the binary image, is presented in FIG. 4.4. See Appendix M for a complete list of *ImageJ* screen captures and software settings.

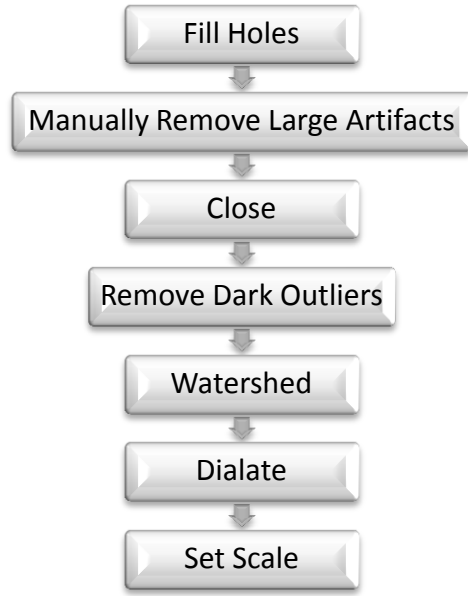


FIG. 4.4. Image Processing Algorithm of a Binary Image Using Manual Techniques and Mathematical Morphology.

4.3. Local Void Ratio

4.3.1. Representative Coupon Size

The distribution of the local void ratio in the processed images, obtained from the air-pluviated control sample, was analyzed to establish the representative area of a coupon. A binary image, with a diameter, d , equal to 23,649 microns, and a global void ratio, e , of 0.5475, was divided into progressively smaller images.

The local void ratio of each of the smaller images, and the standard deviations of each set of images with the same size, was calculated. Table 4.2 presents the resulting standard deviation versus the size of the smaller images.

Table 4.2. Standard Deviation of Global Void Ratio as a Function of Representative Image Size, Control Coupon.

SIZE (μm)	IMAGE COUNT	AREA, A_T (μm^2)	AVE. # OF GRAINS	WEIGHTED MEAN	STANDARD DEVIATION
D=23,649	1	439,243,686	927	0.5475	0.000
16000 x 16000	1	256,000,000	546	0.54091	0.000
16000 x 8000	2	128,000,000	284	0.54101	0.012
8000 x 8000	4	64,000,000	148	0.54128	0.023
4000 x 4000	16	4,000,000	43	0.54000	0.057

As the image size decreases, the standard deviation of the smaller images increases, as shown by the values in Table 4.2. The minimum representative image size can be established by observing the inflection point in the graph of the image size versus the standard deviation, as presented in FIG 4.5. FIG. 4.6 presents a graph of the average particle count in the image versus the standard deviation of the void ratio. From FIG 4.5 and FIG. 4.6 it was established that the area of a representative image should at a minimum be $100,000,000 \mu\text{m}^2$ (10 mm x 10 mm) or contain at least 200 to 250 particles.

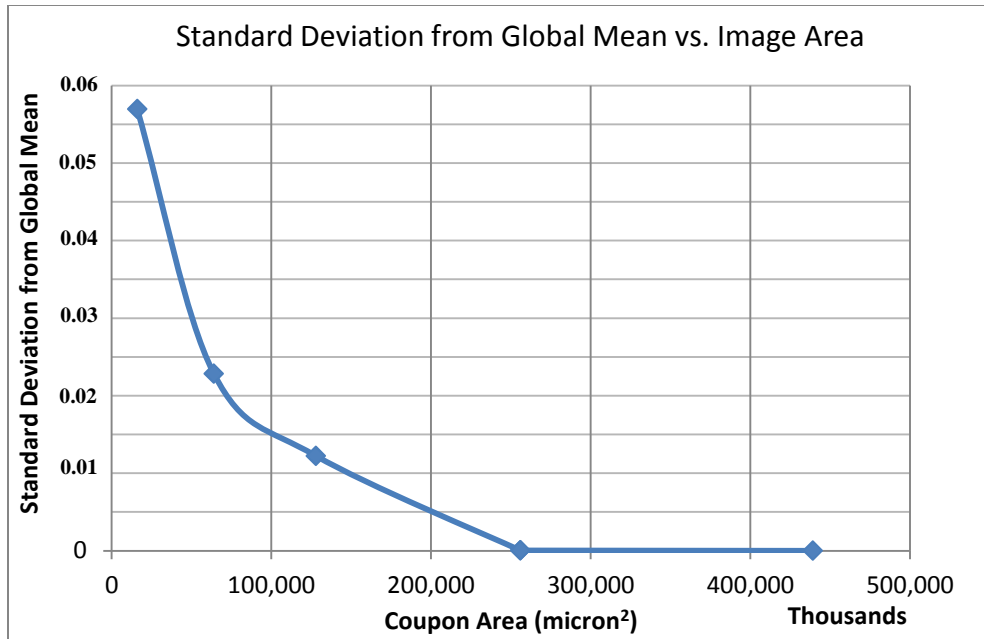


FIG 4.5. Standard Deviation from Global Mean vs. Image Area.

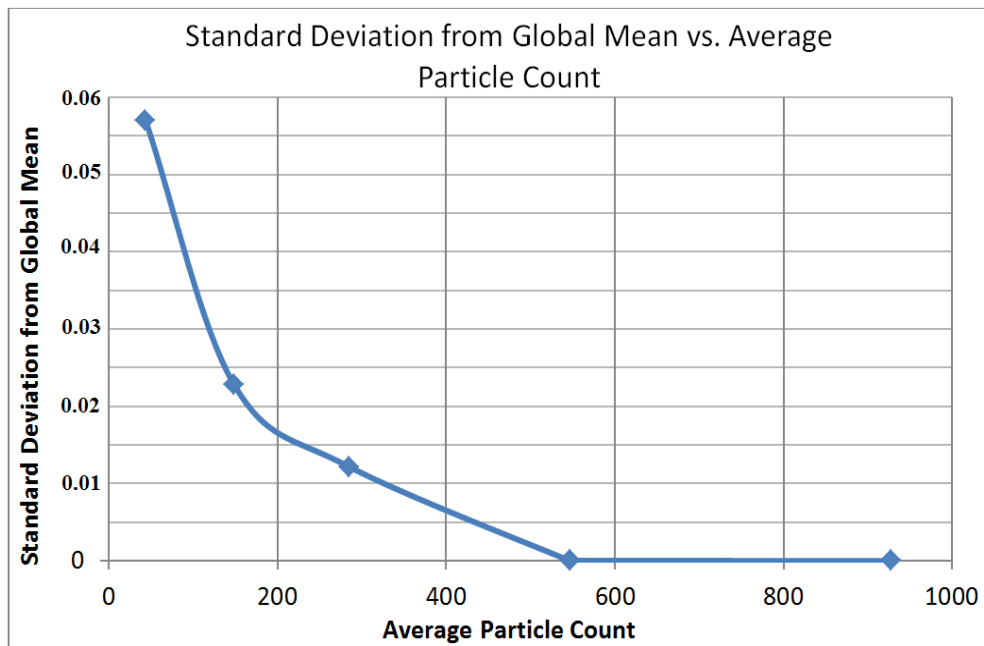


FIG. 4.6. Standard Deviation from Global Mean vs. Average Particle Count.

4.3.2. Oda's Method

The local void ratio distribution was also calculated on progressively smaller sized images, with the same dimensions as the areas in Table 4.2, using Oda's

(1976) method which is described in Section 2.2.4. The calculations were performed on images obtained from the control air-pluviated, never frozen specimen, and from the previously frozen sand specimen. The Matlab programming code, written by Matt Evans, an assistant professor from North Carolina State University and used in his doctoral dissertation (Evans, 2005), was employed to generate polygon networks for subsequent generation of local void ratio histogram frequency distributions. The polygons developed using this method are illustrated in FIG. 4.7.

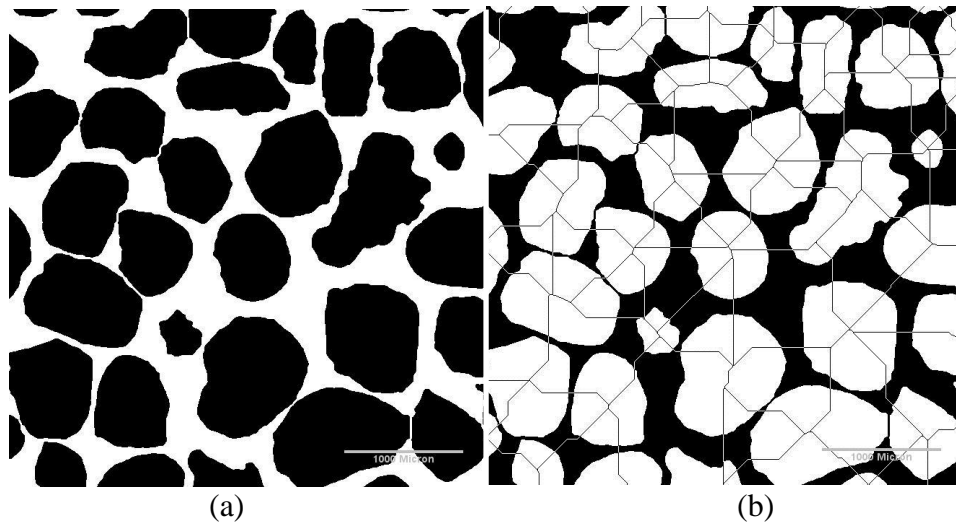
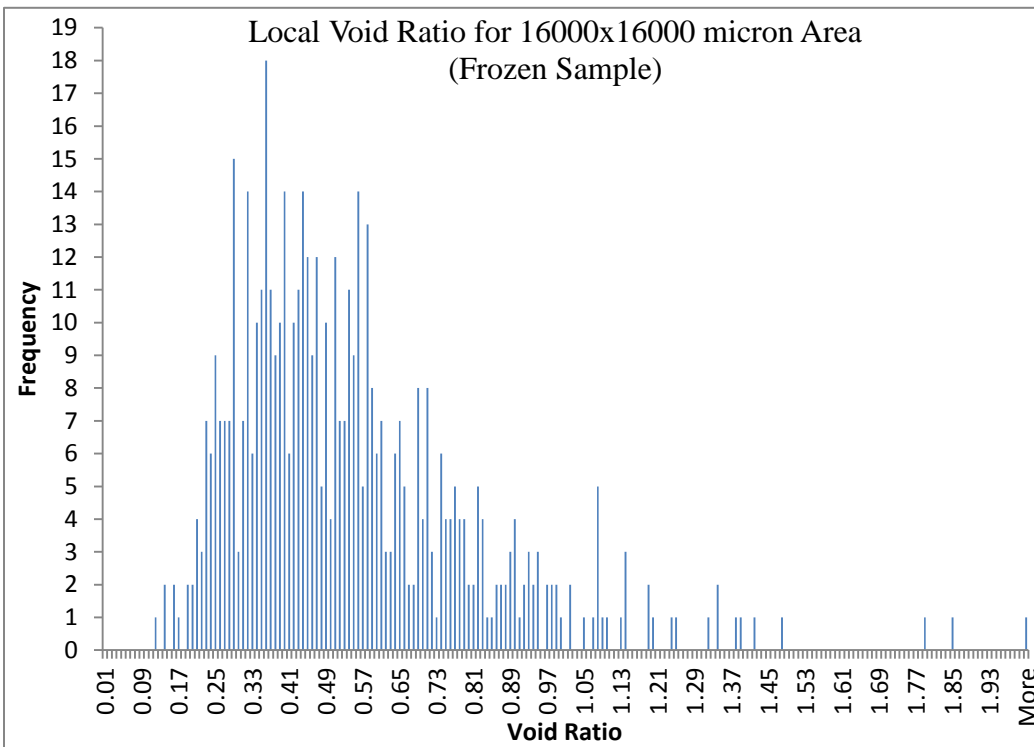
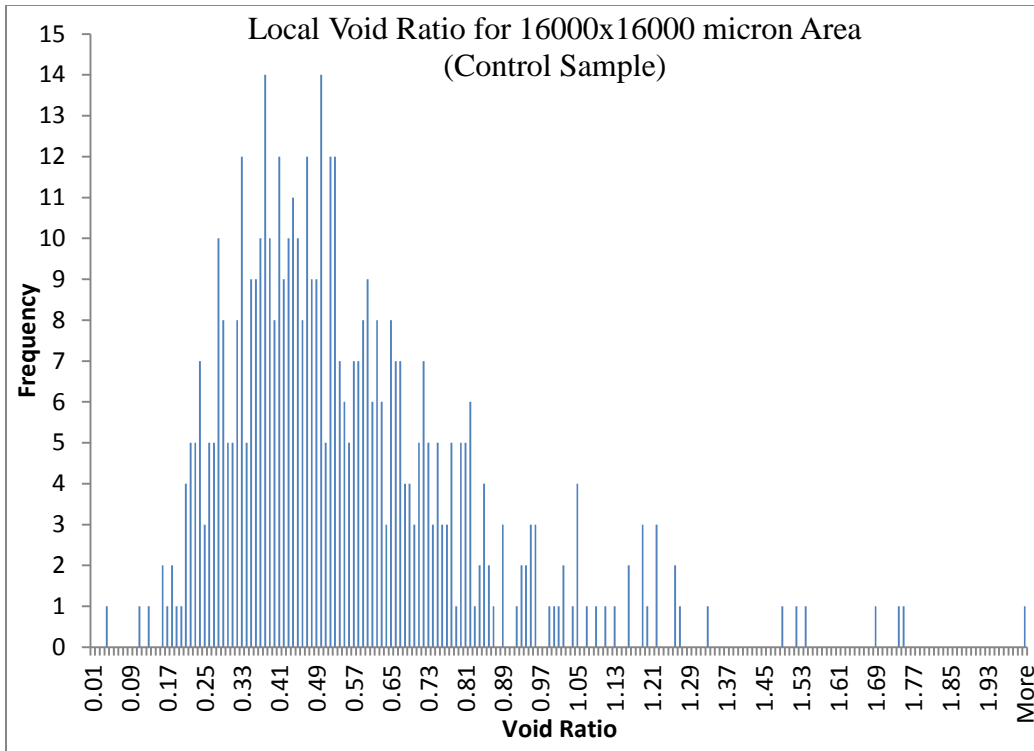
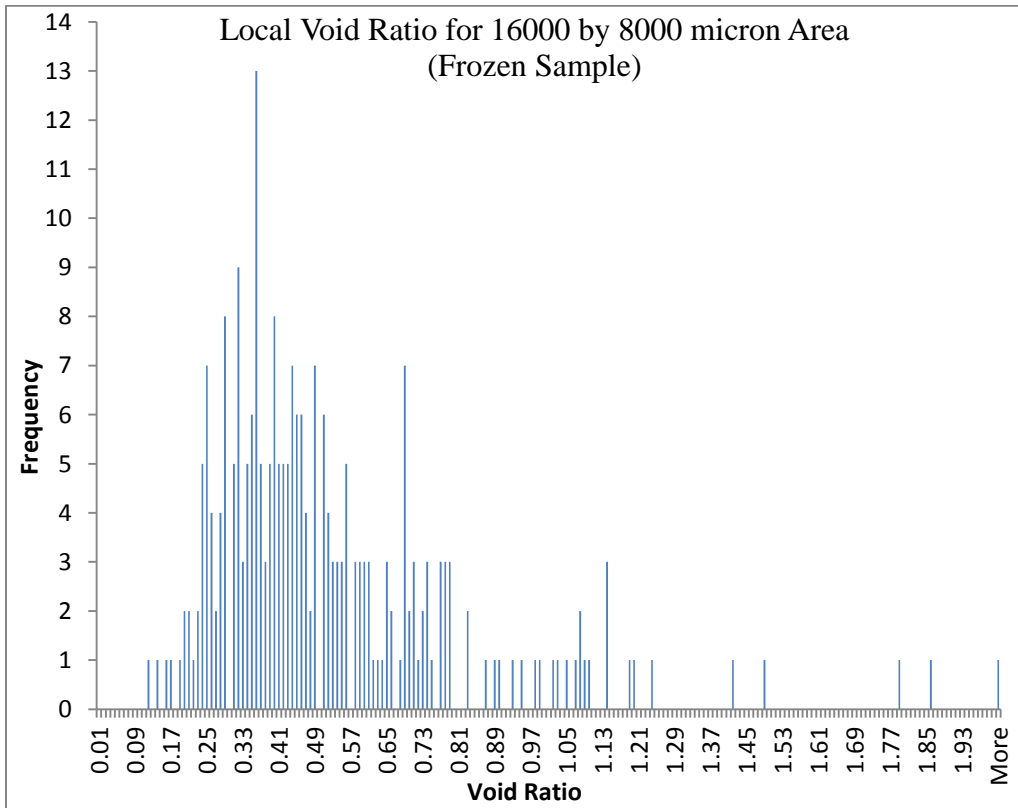
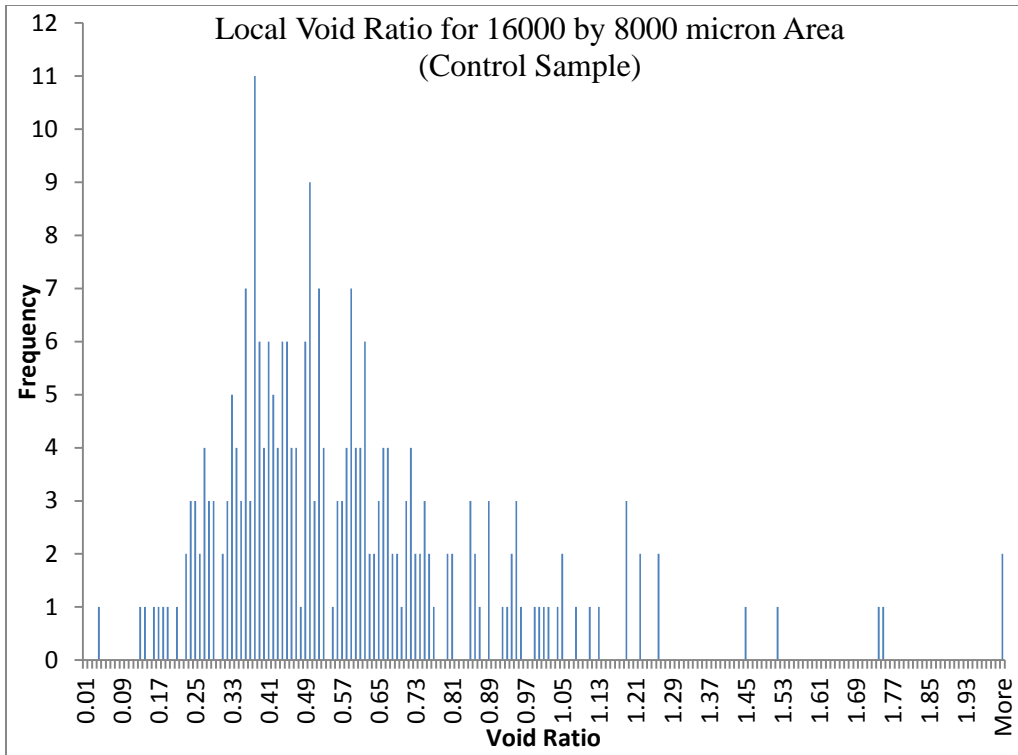


FIG. 4.7. Polygon Network Generation for Local Void Ratio Calculations using Oda's (1976) Method. (a) Binary Image. (b) Polygon Network of Image Using Oda's Method.

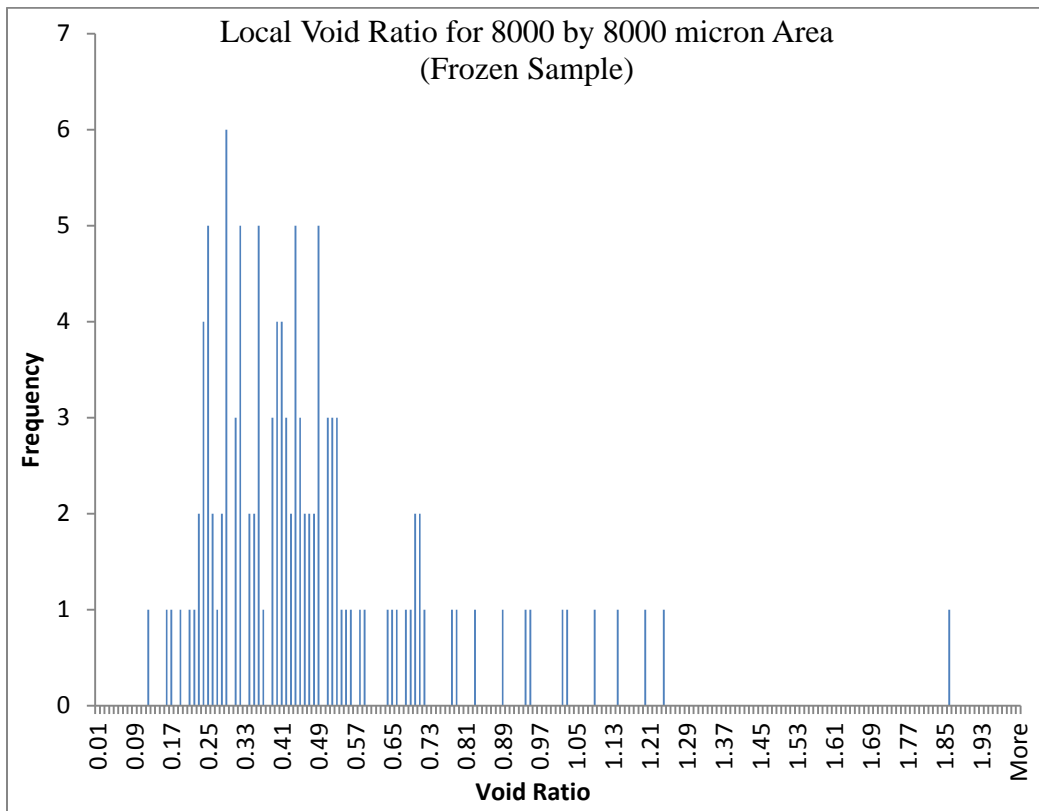
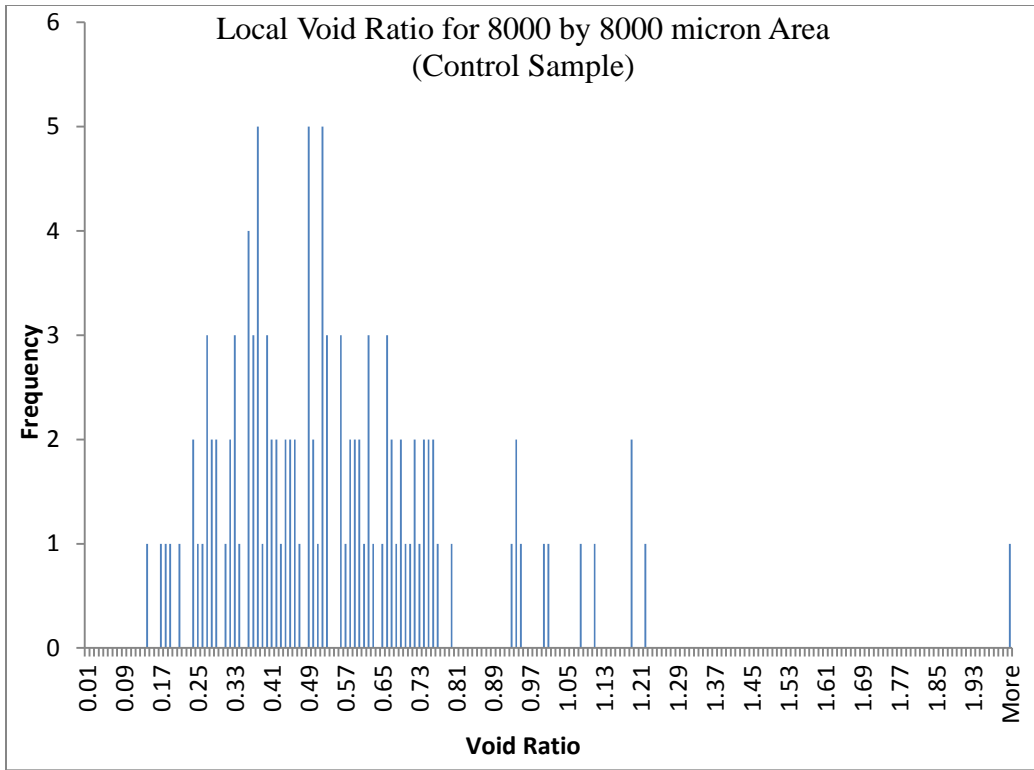
The local void ratio distribution frequency histograms, for different size images, were generated using the Evans (2005) Matlab program. Images, 16,000 μm x 16,000 μm , obtained from the air-pluviated control coupon and the frozen sample were divided into the progressively smaller sizes listed in the first column of Table 4.2. The void ratio distribution frequency histograms, for the two coupons, are presented in FIG. 4.8 for different sample sizes.



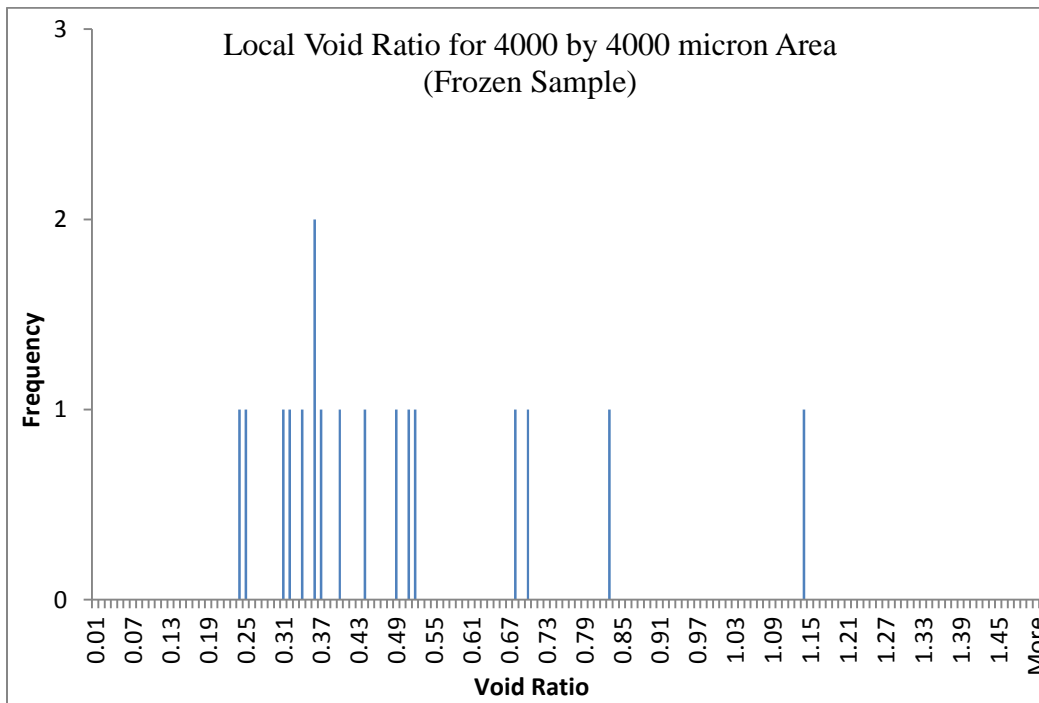
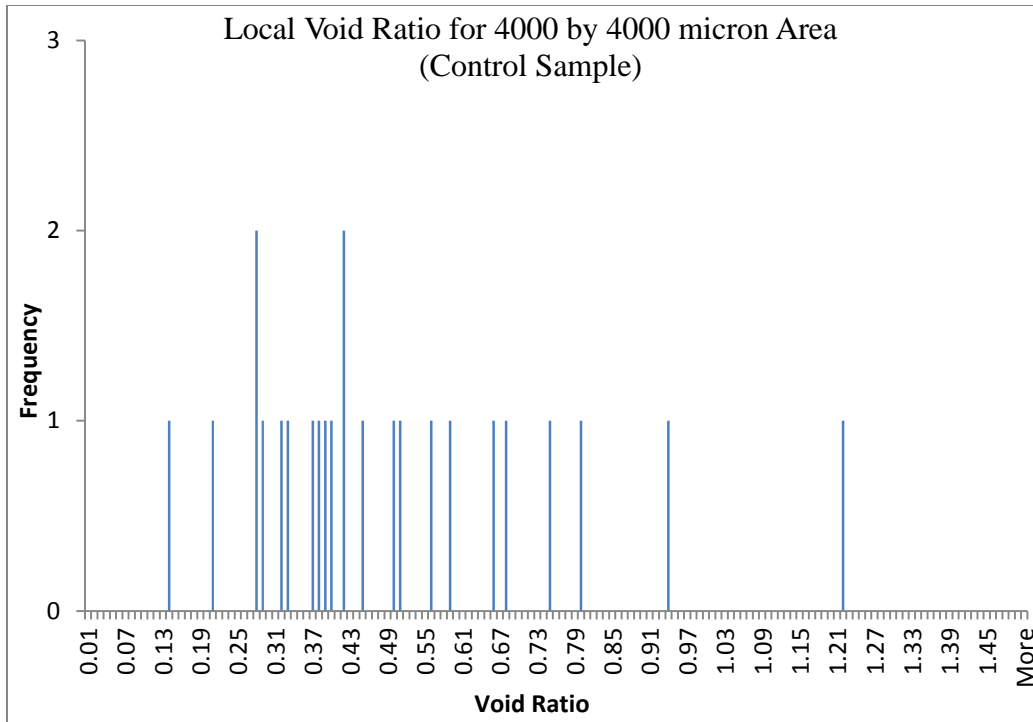
(a)



(b)



(c)



(d)

FIG. 4.8 Comparison of Local Void Ratio Distribution for a Control and Frozen Sample Using Oda's Method. (a) 16,000 μm by 16,000 μm . (b) 16,000 μm by 8,000 μm . (c) 8,000 μm by 8,000 μm . (d) 4,000 μm by 4,000 μm .

There is conformity in the shape of the frequency distribution of the local void ratio histograms of the control and the frozen coupon generated from the largest image ($16,000^2 \mu\text{m}^2$). However, the histogram in FIG. 4.8 (a) contains a larger number of outlying frequencies with higher local void ratios. This may be attributed to the frozen sample containing crushed particles caused by the reuse of the sand in the model container during the experiments. As the image size and the number of particles in the image decreases, the histogram shape and local mean void ratio of the smaller images becomes more variable, as illustrated by FIG. 4.8 (b) through FIG. 4.8 (c). Information on the local void ratio, from Oda's method for different sub-area sizes, and the local void ratio deviation, from the global void ratio calculations are presented in Table 4.3. This corresponds well with the finding in Section 4.3.1 on minimum representative sample size.

Table 4.3. Variability in Mean Void Ratio of Control and Frozen Coupon Based on Representative Image Size

		CONTROL		FROZEN	
SIZE (μm)	AREA, A_T (μm^2)	VOID RATIO, e	ERROR	VOID RATIO, e	ERROR
D=23,649	439,243,686	0.5475	-	0.5455	-
16000 x 16000	256,000,000	0.5491	0.29	0.5414	0.75
16000 x 8000	128,000,000	0.5513	0.69	0.5312	2.63
8000 x 8000	64,000,000	0.5429	0.84	0.4781	12.35
4000 x 4000	4,000,000	0.4561	16.69	0.4917	9.86

4.3.3. Voronoi Tessellation

The local void ratio distribution, calculated using the voronoi tessellation method on the control coupon, was compared to the Oda's method. Voronoi tessellation is a much more consistent and repeatable technique than Oda's method. Voronoi polygon network can be easily generated with *ImageJ* program and as described by Alshibli et al. (2001). All steps were performed manually for the work presented herein. A programming code, in Matlab or Java could be written to handle a large volume of images at one time. The voronoi command is executed in *ImageJ* on a binary image (black grains). The image is then subjected to several image processing steps aimed at enhancing definition and contrast of the polygon network, so that measurements can be performed. These steps are listed in FIG. 4.9 (see Appendix N for actual program settings and the screen captures).

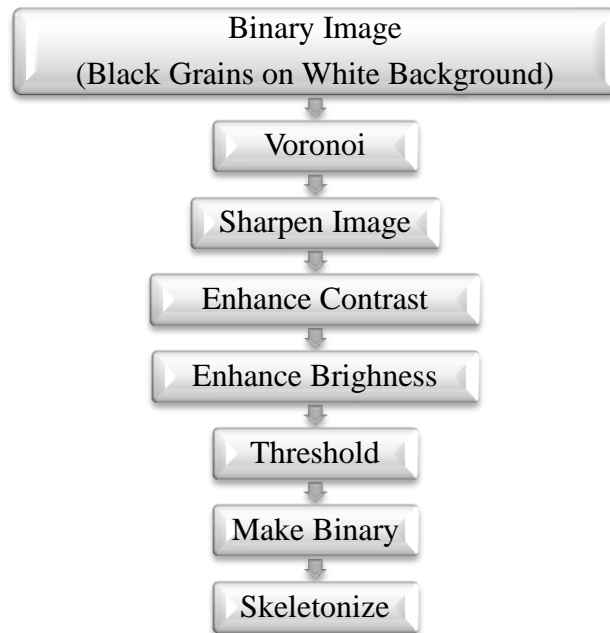


FIG. 4.9 Procedure to Generate Voronoi Polygon Network in *ImageJ*.

To calculate the local void ratio distribution, the binary image of the particles is overlain onto the image of the voronoi network, as illustrated in FIG. 4.10 (a). The areas of the particles are calculated first and then subtracted from the total areas encompassed by the polygon network, as illustrated in FIG. 4.10 (b), to obtain the areas of the individual voids, A_{vi} . *ImageJ* can generate numbered outlines that correspond to the tabulated values for the areas of each particle, and the areas enclosed by each polygon, making the local void ratio calculation straightforward.

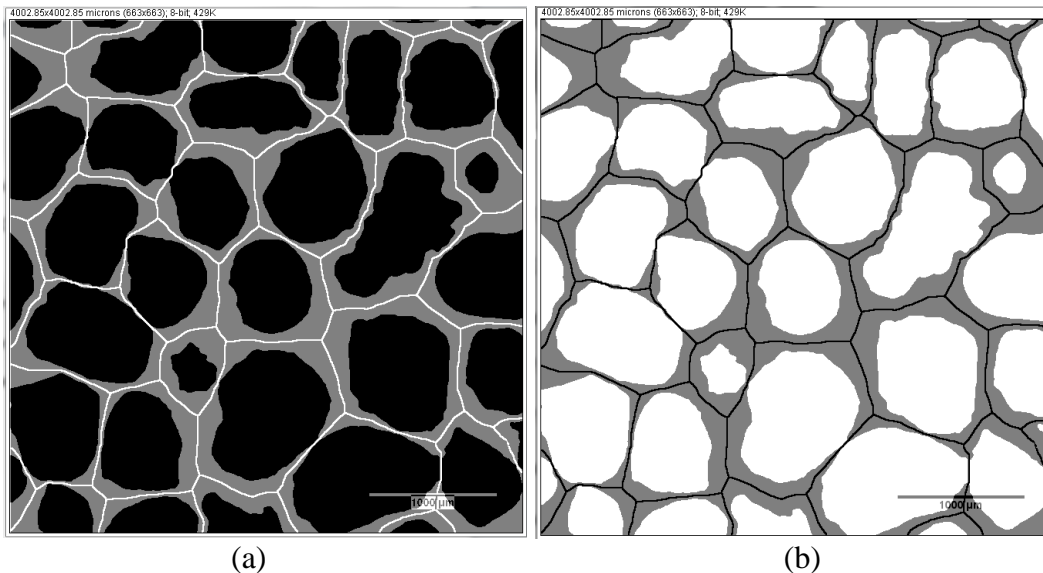


FIG. 4.10. Voronoi Tessellation. (a) Voronoi Polygon Network with Black Grains and Surrounding Voids in Gray. (b) Grain Areas Subtracted for A_v Calculation.

Local void ratio distribution frequency histograms, using the voronoi tessellation method, were generated on the image areas listed in Table 4.2 for the control coupon and are presented in FIG. 4.12. The voronoi tessellation method calculates a larger number of high local void ratios than Oda's method, resulting in increased positive skewness of the histograms. The voronoi tessellation

method also generates higher local void ratio frequencies around the image's global mean, increasing the "peakedness" or kurtosis of the distribution that can be characterized as Leptokurtic. A leptokurtic distribution has a higher peak than a normal (Mesokurtic) distribution and heavier tails. A Platykurtic distribution has a lower peak than a normal distribution and lighter tails, as illustrated in FIG 4.11 (MVP programs).

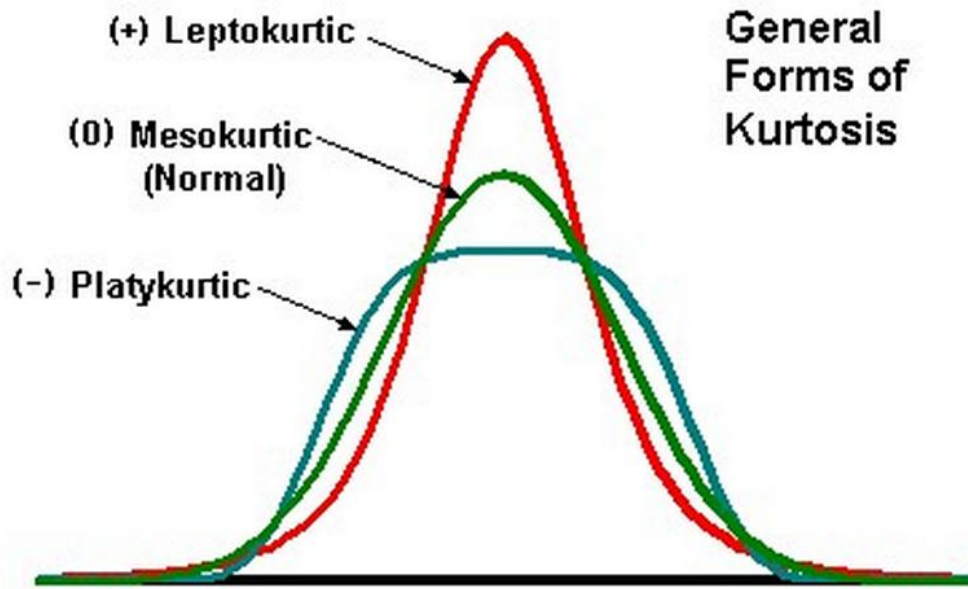
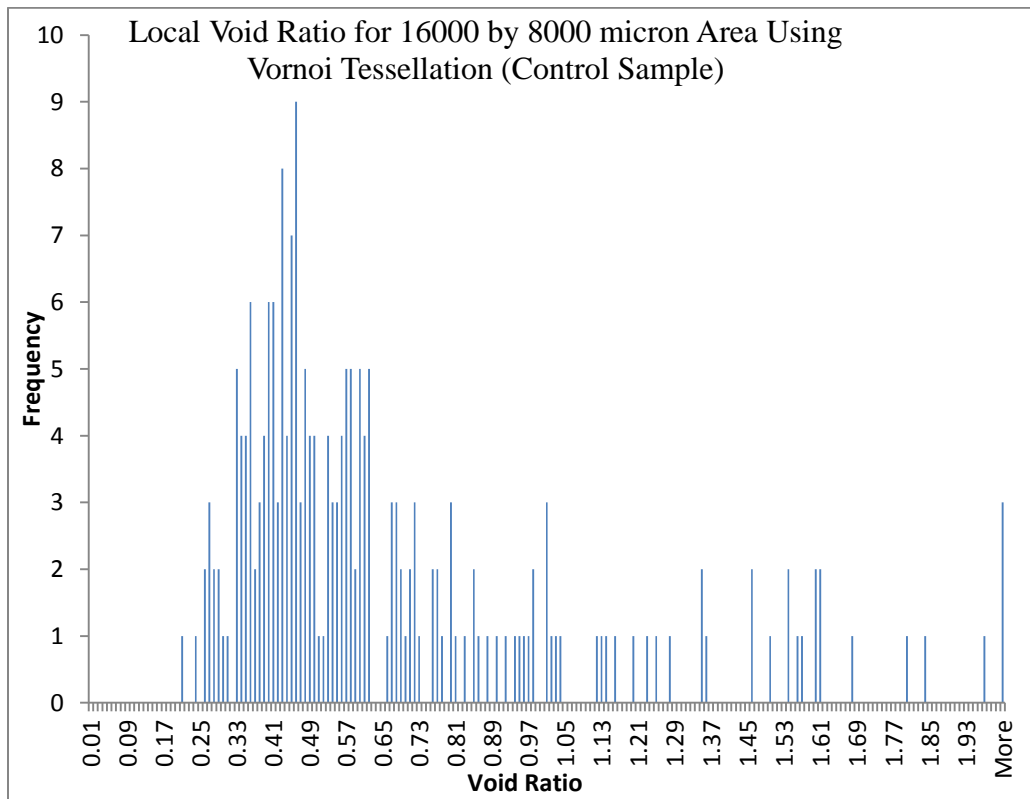
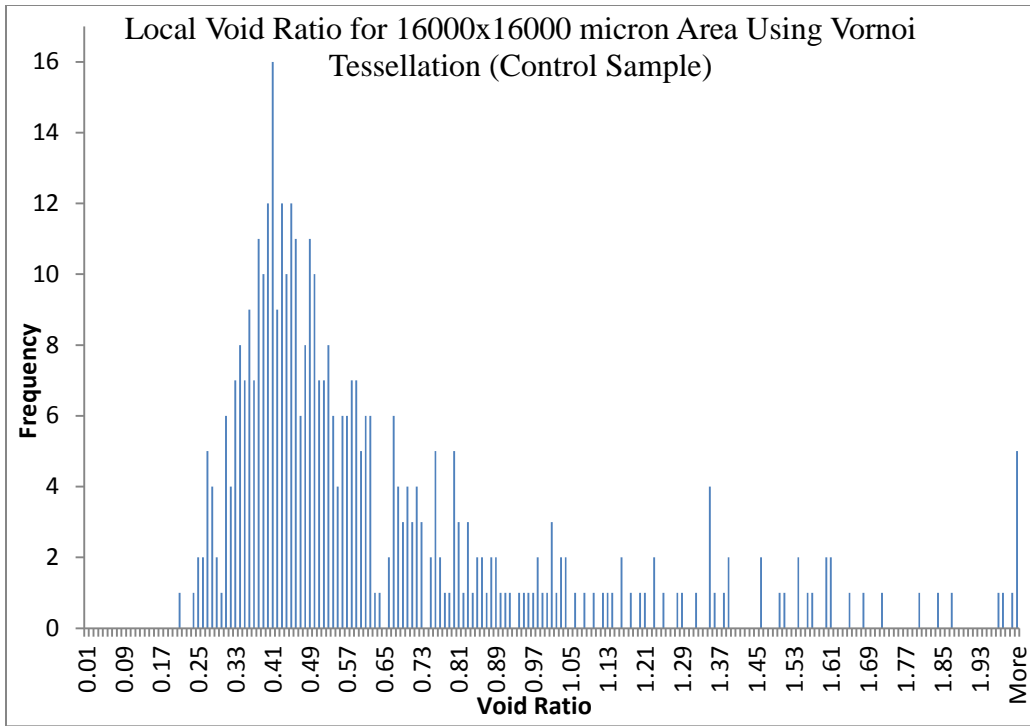


FIG 4.11. General Forms of Kurtosis. (www.mvpprograms.com)



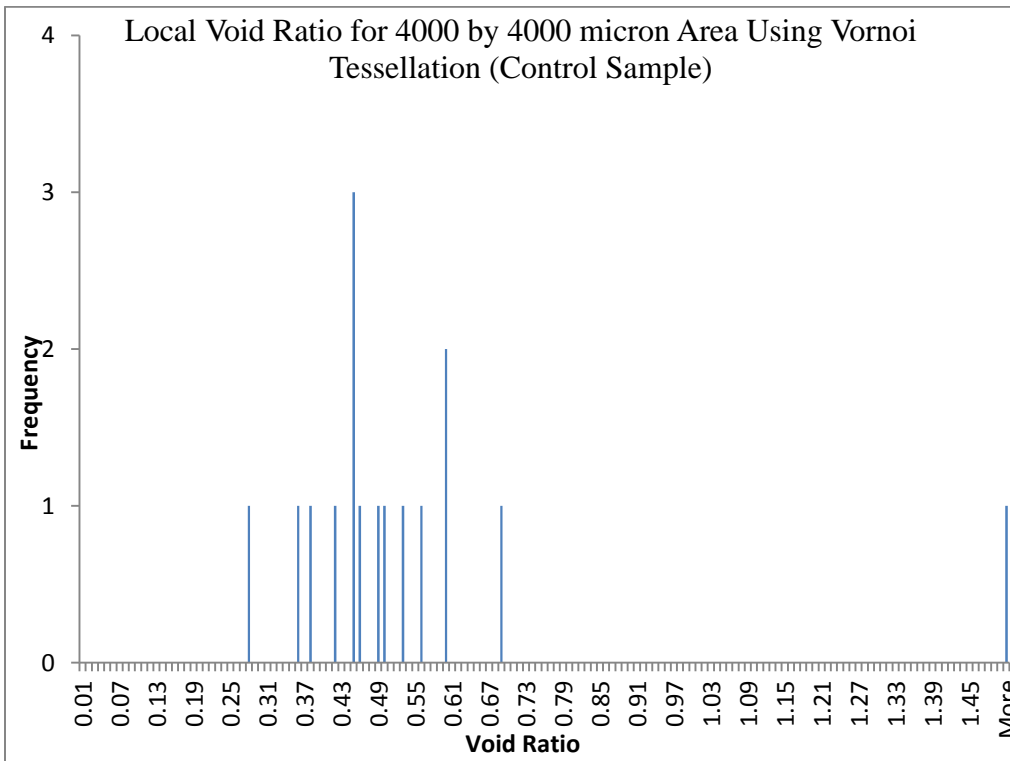
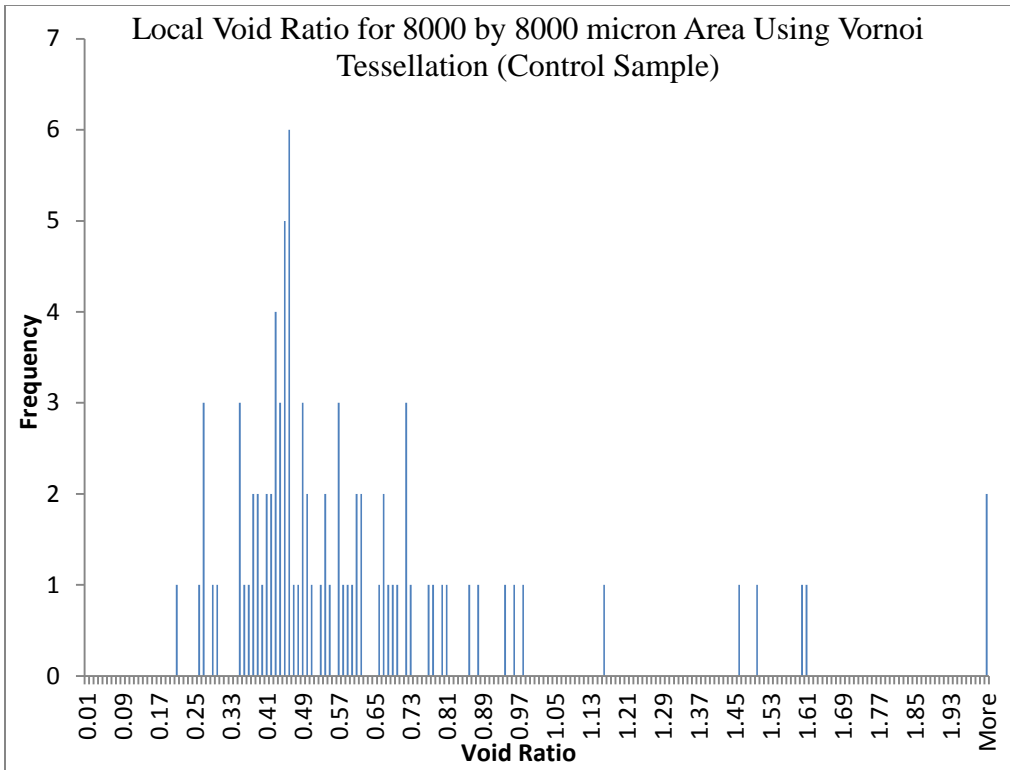


FIG. 4.12. Local Void Ratio Frequency Distribution Histograms Calculated Using Voronoi Tessellation Method.

In voronoi tessellation, the network of polygons is generated with straight lines, one pixel in widths, that are part of the total image area but are not taken into account during the local void ratio calculations. Consequently, the VT method has a built in error that varies with the image size. This error, presented in Table 4.4 and illustrated in FIG. 4.13, can approach 2 percent for the specimens evaluated herein. In this process, the total area of the voronoi polygon lines, A_{VR} , is divided by the total coupon area, A_T , to arrive at the calculated error value percentage.

Table 4.4. Method Specific Error in Voronoi Tessellation Resulting from Polygon Network Generation.

COUPON WIDTH, W (μm)	COUPON HEIGHT, H (μm)	TOTAL AREA, A_T (μm^2)	VORONOI POLYGONS, A_{VR} (μm^2)	ERROR (%)
16,000	16,000	256,000,000	5,046,724	1.97
16,000	8,000	128,000,000	2,457,331	1.92
8,000	8,000	64,000,000	1,147,581	1.79
4,000	4,000	16,000,000	274,192	1.71

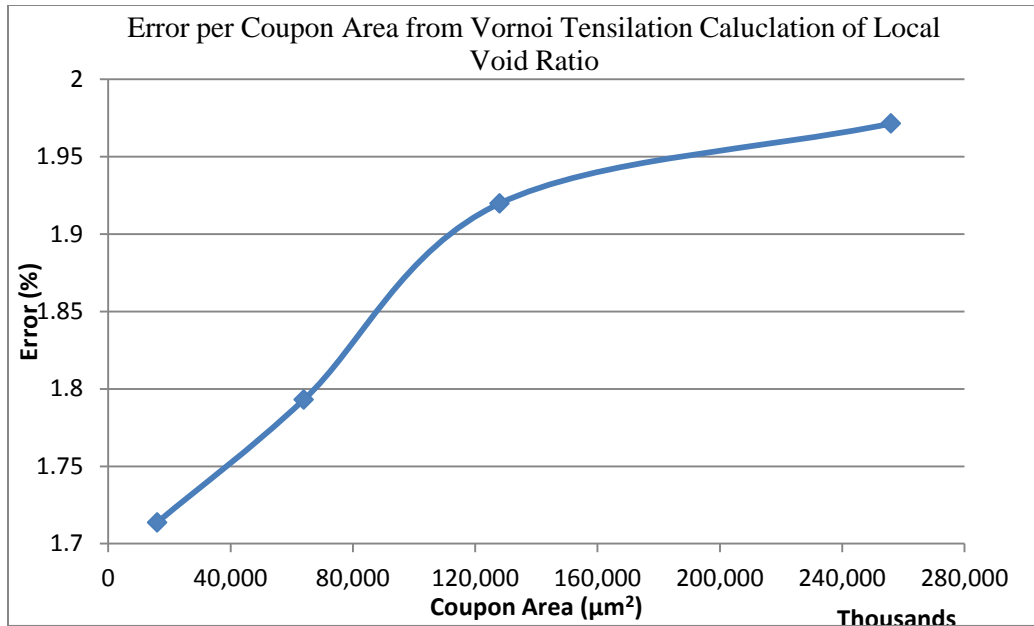
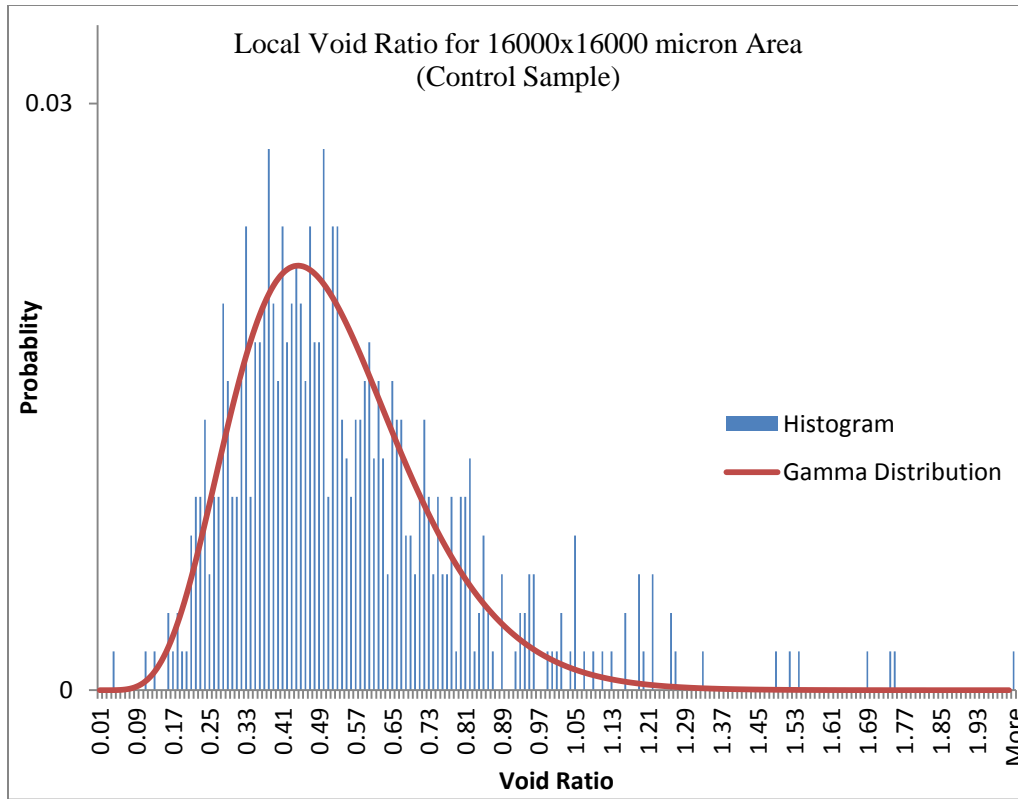


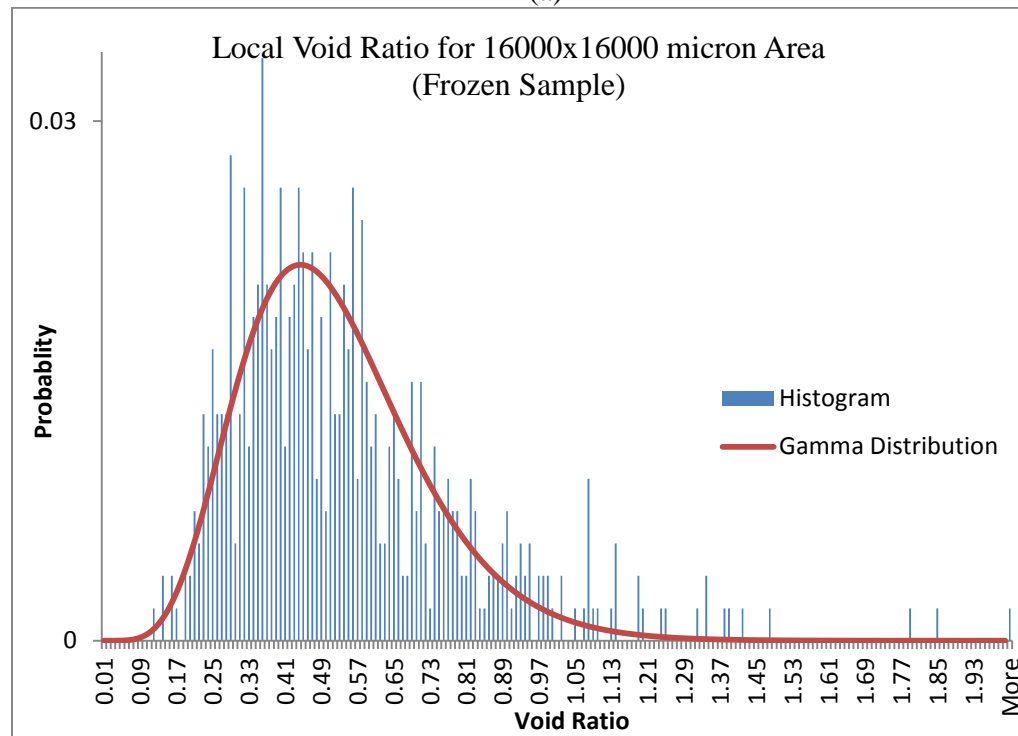
FIG. 4.13. Error in Voronoi Tessellation Resulting from Polygon Network Generation Based on Coupon Size.

4.3.4. Gamma Probability Distribution

A frequency histogram of the local void ratio can be represented by a probability distribution function, as described in Section 2.2.5. Several function types were considered to fit the histograms generated herein, including the normal, beta, gamma and lognormal distributions. The space of Pearson's probability distribution, previously presented in FIG. 2.11, was used to estimate the best type of function to fit the histograms generated herein. This analysis indicated that the gamma probability distribution was optimal. The gamma distribution was therefore fitted to the local void ratio frequency histograms, obtained from the control and frozen sand samples using Oda's method on 16,000 μm by 16,000 μm images, for comparison purposes. The fitted histograms are presented in FIG. 4.14.



(a)



(b)

FIG. 4.14. Gamma Probability Distribution Fitted to Local Void Ratio Frequency Histogram Using Oda's Method. (a) Control Sample. (b) Frozen Sample.

The calculated shape descriptors for the gamma distribution function included kurtosis (Equation 2.28), which is a degree of peakedness of the distribution, skewness (Equation 2.29), which is a measure of the asymmetry around the mean value, and the entropy of the histogram, which quantifies the uniformity of the distribution (Equation 2.31). The calculated results are presented in Table 4.5. Good agreement was observed between the calculated values for the two samples. The values of symmetry and kurtosis indicate local void ratio probability distribution functions characterized by right skewness and leptokurtic graph shapes.

Table 4.5 Shape Descriptors for the Gamma Distribution Functions

COUPON	SKEWNESS	KURTOSIS	ENTROPY
Control Sample	1.25	5.31	7.38
Frozen Sample	1.11	4.26	4.36

4.4. Particle Descriptors

4.4.1. Particle Roundness and Sphericity

ImageJ can generate several types of particle shape descriptors from binary images. The calculated data for these descriptors includes the mean and standard deviations (SD) and a tabulated list of individual particle characteristics that can be used to generate frequency distribution histograms and probability distribution curves. Table 4.6 lists the particle shape descriptor mean standard deviations calculated by *ImageJ*, for the control coupon and the frozen coupon for the four common descriptors: circularity, roundness, aspect ratio, and solidity.

Particle circularity is defined as a degree to which a particle approaches a circular (spherical) shape and can be calculated with Equation 2.3. A value of 1.0 indicates a perfect circle, whereas a value close to 0.0 indicates an elongated polygon.

Particle roundness refers to the sharpness of the corners and the edges of a particle. Roundness is defined by Wadell (1932) as the ratio of the average radius of the curvature of the corners to the radius of the largest inscribed circle. More commonly, the particle roundness is calculated using Equation 4.1:

$$Roundness = \frac{4 \cdot \pi \cdot A}{d_L^2} \quad (4.1)$$

where A is the particle area, and d_L is the particle's longest axis.

Particle aspect ratio (AR) is the ratio of the particle's long axis, d_L , to short axis, d_S . AR is used in the calculation of grain anisotropy as described later, in Section 4.4.2.

Solidity of the grain particle describes the ruggedness of the boundary profile. It is a ratio of the particle area, A_P to particle's convex area, A_{CNV} :

$$Solidity = \frac{A_P}{A_{CNV}} \quad (4.2)$$

$$A_{CNV} = \frac{TautStringPerimeter}{Perimeter} \quad (4.3)$$

The solidity is equal to 1.0 for particles that have no concave areas in its boundary and is lower for particles with perimeter indentations.

Table 4.6 Particle Shape Descriptors for the Control and the Frozen Coupons.

	CONTROL COUPON				FROZEN COUPON			
	COUPON AREA (in millions, μm^2)				COUPON AREA (in millions, μm^2)			
	256	128	64	16	256	128	64	16
VOID RATIO, e	54.09	55.14	54.29	45.61	54.14	53.12	47.81	49.17
CIRCULARITY	0.793	0.792	0.791	0.790	0.794	0.795	0.801	0.797
SD	0.073	0.062	0.066	0.080	0.082	0.078	0.074	0.076
ROUNDNESS	0.730	0.710	0.720	0.740	0.710	0.710	0.710	0.690
SD	0.120	0.120	0.130	0.140	0.140	0.130	0.130	0.140
ASPECT RATIO	1.420	1.450	1.430	1.420	1.470	1.470	1.460	1.530
SD	0.280	0.270	0.290	0.340	0.360	0.320	0.310	0.390
SOLIDITY	0.730	0.710	0.720	0.740	0.710	0.710	0.710	0.690
SD	0.120	0.120	0.130	0.140	0.140	0.130	0.130	0.140

This data was generated using the “Particle Analysis” and the “Shape Descriptor 1u” plug-ins available in *ImageJ*. The calculations did not include particles touching the perimeter of the image because that would introduce errors into the results. It appears, based on the data listed in Table 4.6, that there is very little variability in values calculated for image sizes above 16 million μm^2 . Larger image sizes are preferred for the generation of frequency distribution histograms so that all the representative particle sizes are captured.

Frequency distribution histograms were generated for circularity, roundness, aspect ratio, and solidity. FIG. 4.15 presents a circularity frequency distribution

histogram for a control coupon. Most circularity values range from 0.70 to 0.90, which is characteristic of the subrounded particle shape of Ottawa 20/30 sand.

FIG. 4.16 presents the particle roundness frequency distribution for the control sample. The majority of the circularity values for the control coupon are concentrated in the value range from 0.5 to 0.95, as would be expected for Ottawa 20/30 sand. FIG. 4.17 shows the particle aspect ratio frequency distribution for the control coupon. Most AR values are concentrated in a range from 1.0 to 1.75. The particle solidity frequency distribution histogram of the control coupon is illustrated in FIG. 4.18. The shape of the solidity frequency distribution is very similar to the particle roundness frequency distribution, with most of the particles falling within the value range from 0.5 to 0.95. This value range indicates that most of the particle perimeters are smooth and have very few jagged, chipped edges.

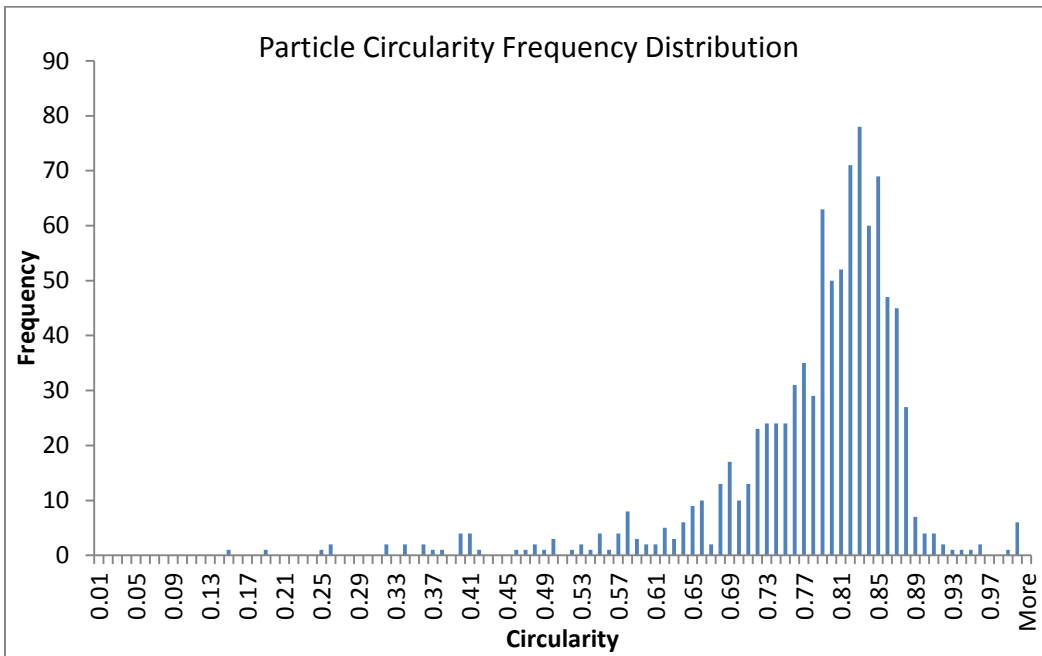


FIG. 4.15. Particle Circularity Histogram, Control Sample.

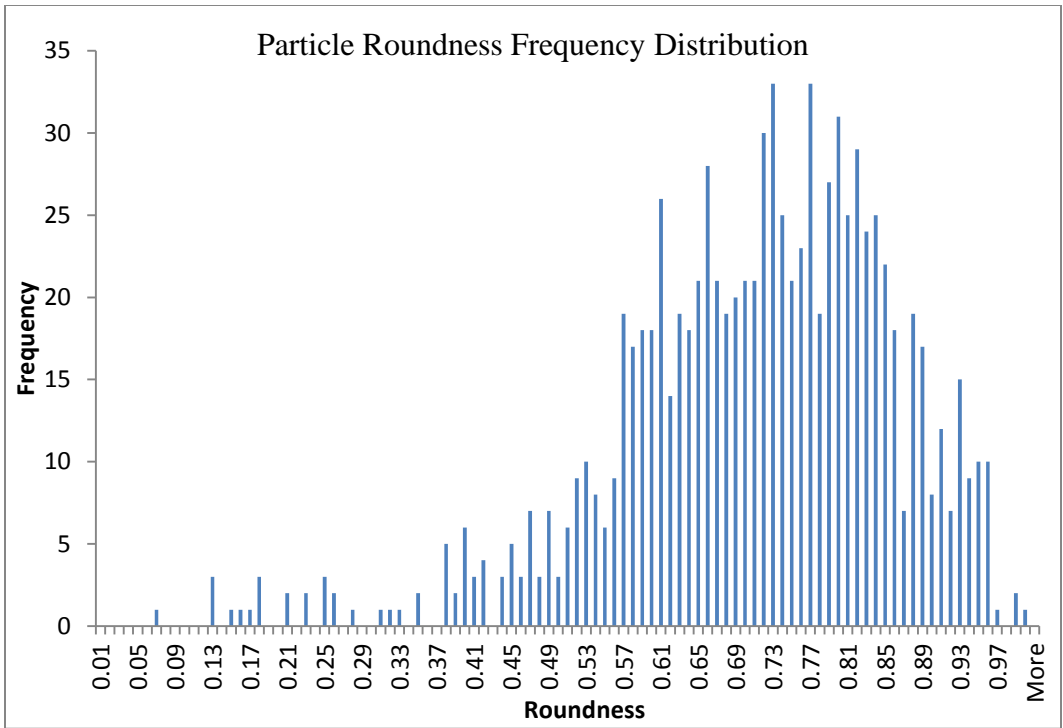


FIG. 4.16. Particle Roundness Histogram, Control Sample.

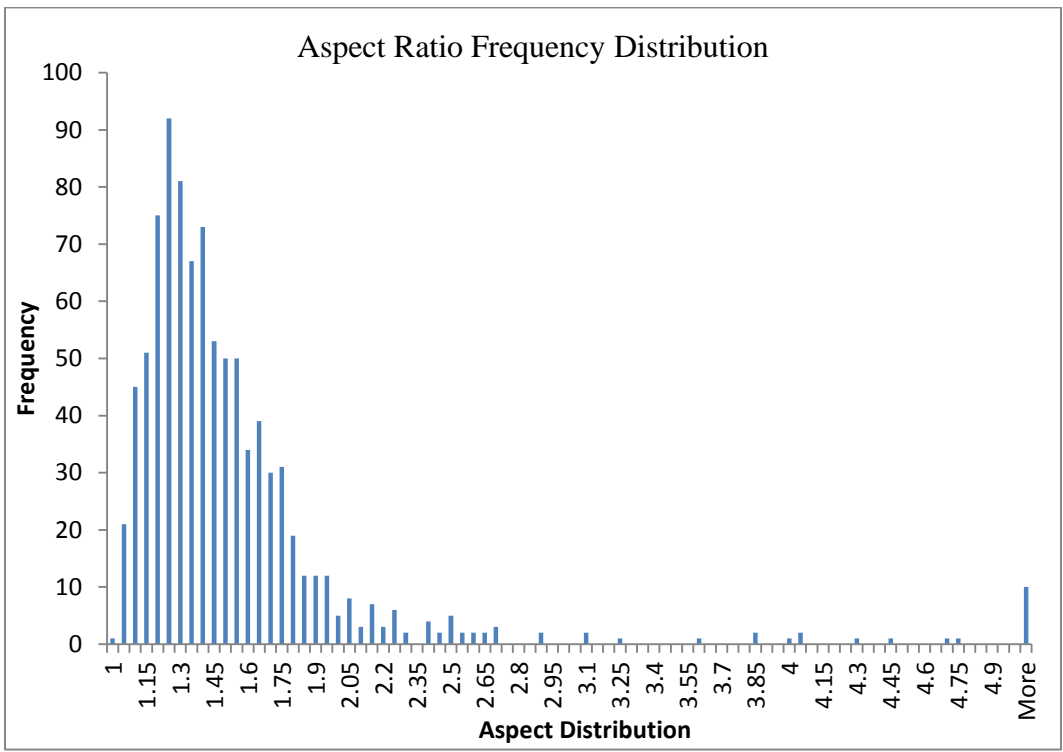


FIG. 4.17. Particle Aspect Ratio Histogram, Control Sample.

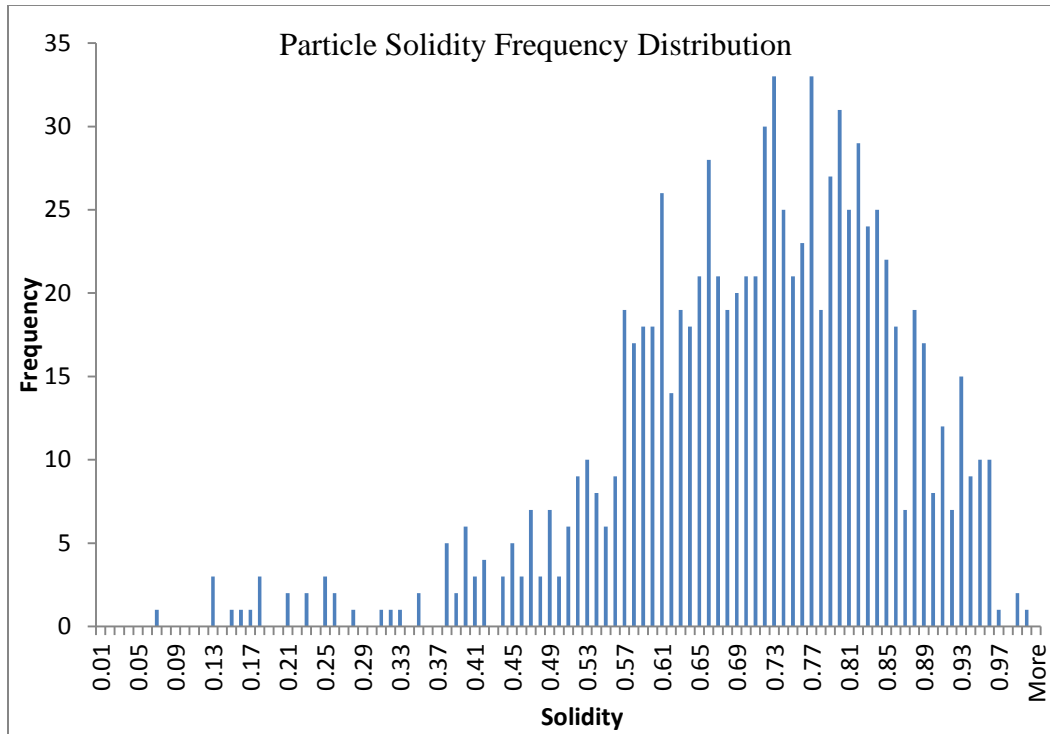


FIG. 4.18. Particle Solidity Histogram, Control Sample.

4.4.2. Relative Anisotropy

Relative anisotropy (RA) was defined by Yang (2002) as a ratio of unbroken horizontal lines to the unbroken vertical lines in the binary image and is calculated using Equation 2.10 and Equation 2.11. RA measures relative particle alignment in the image. RA values greater than one indicate vertically aligned particles and values of less than one indicate horizontally aligned particles. The relative anisotropy of the particles was calculated on two images; a coupon obtained from the control specimen and a coupon obtained from the frozen specimen. The *ImageJ* “Shape Descriptor 1u” plug-in was used to obtain information on the individual particle’s long axis (a), short axis (b) and the aspect ratio (a/b), the variables defined by Yang (2002) in Section 2.2.3. Particles in

contact with the image border were discounted from the calculations to remove unrepresentative particle shapes. Table 4.3 lists the results for both specimens.

Table 4.7. Relative Anisotropy of Grains from the Control and the Frozen Specimens.

SPECIMEN	DIAMETER, (μm)	AREA (μm) ²	VOID RATIO	RELATIVE ANISOTROPY
Control	23,660	439.24	0.5475	1.07
Frozen	23,661	439,70	05455	1.21

For the air-pluviated control specimen, the RA is very close to 1.0 thereby indicating no preferential alignment of particles in the image. The RA value calculated for the frozen sample, which was greater than one, would indicate more particles were vertically aligned in the image. Yang (2002) calculated the relative anisotropy for a rotated synthetic image and obtained RA values ranging from 0.17 to 6.48. The RA value for the frozen sample is within the range for an isotropic specimen, but the 13 % discrepancy for the control coupon could have been caused by the differences in the sample preparation technique. The RA values are only valid for the images analyzed and might not have any real significance for the specimens sampled. The imaged coupons should be referenced to the sampling location and their relative orientation preserved during the imaging process.

4.4.3. Particle Orientation and Rose Diagrams

The orientation of each sand particle was measured using the *ImageJ* function “Shape Descriptor 1u” plugin which can generate information on particle angle

and also generate particle orientation plots. The particle orientation can be defined as the angle between the feret diameter and the horizontal axis (or any other reference axis). The feret diameter is a “slide gauge” measurement of the particle, which is the distance between two tangents to the contour of the particle in a well-defined orientation, as illustrated in FIG. 4.19. Maximum and minimum feret diameters are considered by looking at all possible angles. The maximum feret is established first and then the minimum feret is calculated at a 90° angle to the maximum feret. Maximum feret and the angle it forms to the arbitrary (typically horizontal) reference axis of all the particles contained in the binary image is used to generate the particle orientation rose diagrams in *ImageJ*. The minimum feret diameter is sometimes considered to be the diameter equivalent to the particle size measurement in a sieve analysis.

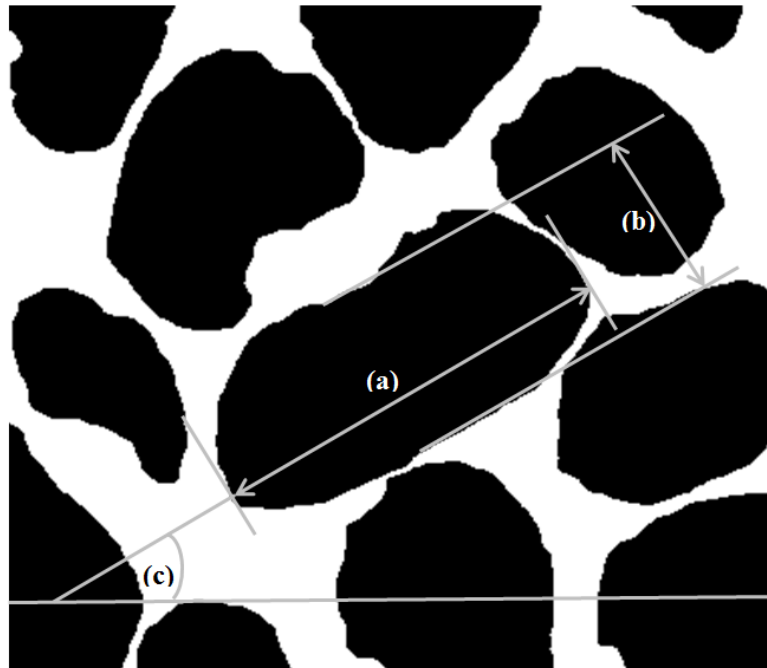
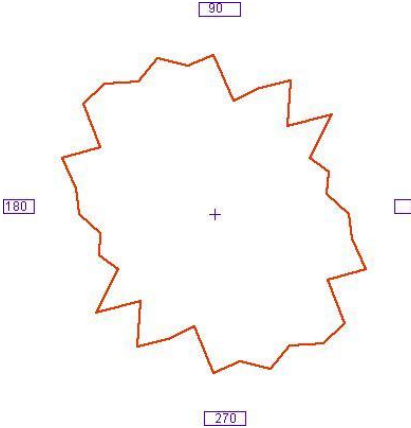
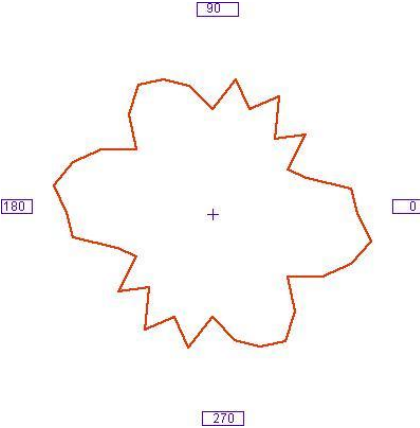
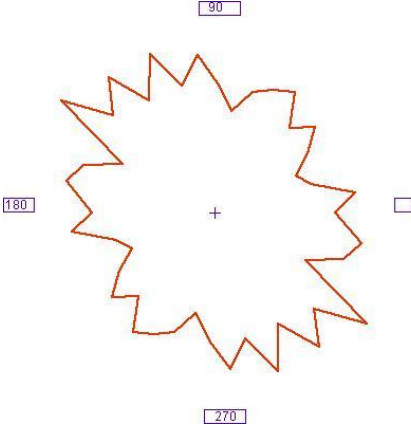
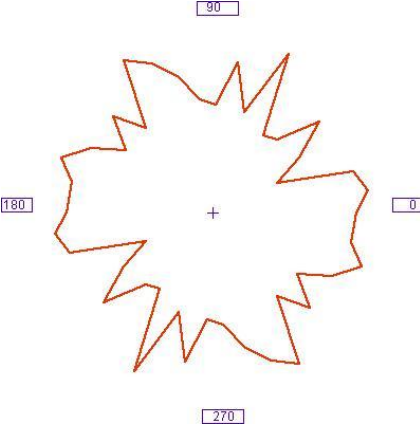
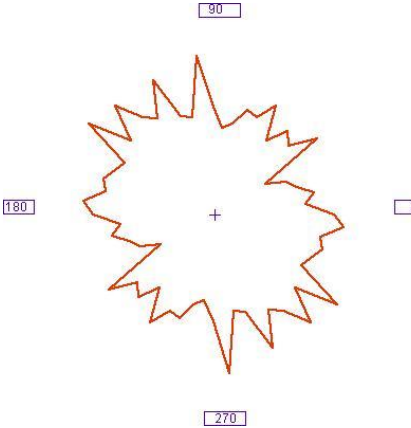
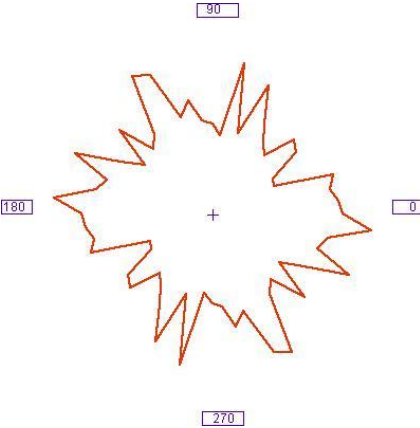


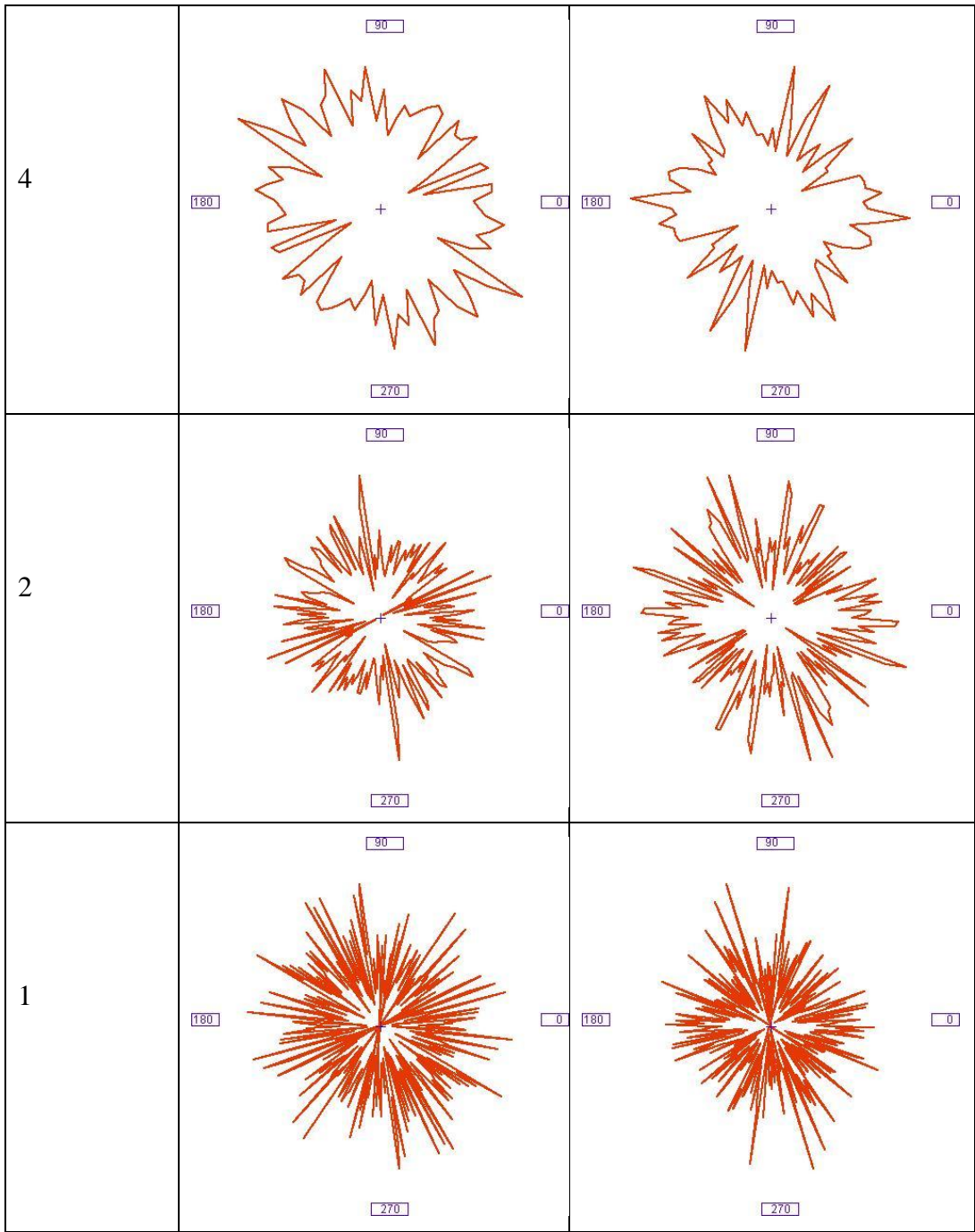
FIG. 4.19. Feret Diameter. (a) Maximum Feret. (b) Minimum Feret. (c) Angle between Maximum Feret Diameter and the Horizontal Axis.

The particle maximum feret diameter and feret angle were used to generate polar/rose diagrams based on single particle orientations. The rose diagrams are generated using the weighted value for the orientation of each particle, where the weight is based upon the area (volume) of the particle. Weighting the particle orientation in this manner prevents the rose diagram from being controlled by the presence of small particles in certain instances. The weighted particle rose diagram gives a higher significance to the orientation of larger particles, as described in Yang (2002).

In generating the rose diagram, particle orientations are grouped into bins of fixed interval width (angle range). Ibrahim and Kagawa (1991) used a ten degree bin interval in their research on particle orientation differences in cohesionless soil due to different sample preparation techniques. Reducing bin size increases the amount of detail in the plot, as demonstrated in Table 4.8, but also increases computational effort. Images obtained from the control and frozen samples were used to generate polar plots of particle orientations for bin sizes ranging from 10 degrees to 1 degree. As the bin size decreases, the level of detail for a range of possible angles increases. The average feret angle calculated for the entire image was 92.68° and 92.17° for the control sample and the frozen sample coupons, respectively. The results demonstrate that the particle orientation between both samples is similar, indicating that the effects of freezing on sample disturbance is minimal.

Table 4.8. Particle Orientation Rose Diagrams at Different Bin Sizes.

BIN SIZE (DEGREES)	CONTROL SAMPLE (Feret Angle=92.68°)	FROZEN SAMPLE (Feret Angle=92.17°)
10		
8		
6		



5. CONCLUSIONS AND RECOMMENDATIONS

5.1. Summary

The objective of this dissertation was to develop means of characterizing changes in the microstructure of cohesionless soils due to freezing and sampling (and ultimately due to liquefaction). Microstructure characterization of granular cohesionless soils is a complex, time consuming and labor intensive process. Specimen sampling may introduce microstructure disturbance due to vibration, particle displacement, and changes in the effective stress. In this dissertation, the microstructure of never-frozen samples reconstituted with the use of an air-pluviation technique and the air-pluviated specimens subjected to uni-directional freezing process were characterized using bright field microscopy imaging and image analysis. The frozen samples were extracted with a hollow stem drill bit, and then drained, dried and impregnated with optical grade epoxy in a modified triaxial cell to preserve soil structure. The air-pluviated and never frozen specimens were also stabilized by impregnation with optical grade epoxy.

A specialized equipment set-up was developed to impregnate the frozen samples with epoxy after they were thawed. Proper curing of the optical grade epoxy required that the thawed specimen be thoroughly dried such that the relative humidity in the pore space was less than 40 percent. A modified triaxial cell, as described by Jang et al. (1999), was used to draw, under low vacuum, ambient air through a desiccant, and the specimen for several days to remove moisture from the pore space. The same set-up was used to impregnate the air-pluviated samples with epoxy, however, dehumidification was not required. All

portions of the epoxy impregnation setup that came in contact with epoxy (e.g. the drainage lines leading into the cell by which the epoxy was introduced, the porous stone at the base of the cell) were disposed of and replaced after each sample was stabilized.

Through trial and error, a cutting, grinding and polishing procedure was developed to prepare individual epoxy-impregnated sand coupons for image capture with a bright field microscopy technique. Since coupon preparation can affect image quality and the accuracy of subsequent measurements, coupon preparation is the most critical step when using an optical microscope to image coupons from stabilized sand specimen.

Characterization of soil fabric was accomplished with digital image processing using *ImageJ*, an open source computer program for image analysis. Individual, high resolution color images were stitched together to form a mosaic of the entire coupon surface and then converted to an 8-bit gray scale format for processing. An algorithm for processing the gray scale images was developed using a standard set of image processing tools, including contrast and brightness adjustment, filtering, and thresholding. Segmented binary images were then subjected to a set of mathematical morphology filters to clean up any remaining image artifacts and ready the images for particle analysis. *ImageJ* generated information on particle count, area, circularity, feret, compactness, circularity, aspect ratio, and solidity. From the data, global void ratio and local void ratio variability was calculated. Local void ratio frequency histograms were fitted with gamma distribution curves that can be characterized by skewness, kurtosis and

entropy. Particle shape descriptors were used to generate frequency distribution histograms of circularity, feret, and roundness and rose diagrams for particle orientation. These operations were conducted on both control samples from the air-pluviated but never frozen samples and from the frozen samples.

5.2. Conclusions

In this study, a methodology was developed to stabilize and process cohesionless specimens for soil fabric analysis. With respect to sample stabilization and coupon preparation, conclusions arrived at in the course of this research include:

- Cold storage of Epo-Tek[®] 301 epoxy will extend its shelf and pot life but increases its viscosity. Better saturation outcomes of previously frozen core samples were achieved with the epoxy mixed at room temperature.
- Epoxy impregnation time can vary greatly based on amount of fines in the specimen, grain gradation, size of the sample, and the differential impregnation pressures used.
- The cutting, planing, grinding, and polishing procedure developed for this dissertation is only applicable to Ottawa 20/30 sand and Epo-Tek[®] 301 epoxy. Other sands with different particle hardness, shape, and amount of fines may require deviation from this procedure to achieve satisfactory image quality.
- Planing of coupon surfaces with a silicon carbide wheel fractures grain particles and should be avoided.

- Silicon Carbide abrasives are best suited for the grinding process.
Diamond abrasives loaded onto nappless polishing cloths achieve superior removal rates, flatness and minimal edge rounding during the polishing procedure.
- Errors during a polishing process can be corrected by resurfacing the coupon surface with 600 grit silicon carbide abrasive, used in last step in the grinding process.
- Maximum effort should be applied in achieving a perfectly flat, artifact free coupon surface during grinding and polishing to minimize the amount of image corrections required during image processing .

With respect to image analysis, conclusions arrived in the course of this research include:

- Most of the image processing can be automated with the use of user defined macros when a large number of images need to be processed. However, some manual work to remove artifacts from individual grains, a time consuming process for large images, may still be required.
- *ImageJ* software can generate microstructure parameters on particle area, orientation, sphericity, roundness, aspect ratio and solidity that can be used to calculate global void ratio, variation in local void ratio and particle orientation rose diagrams.
- Local void ratio calculations using the Oda's method and voronoi tessellation, yielded similar results, but voronoi tessellation is more consistent at generating polygon networks around individual particles.

- The void ratio of the air-pluviated Ottawa 20/30 sand specimens was calculated by laboratory measurements to be $e = 0.5470$. The calculated global void ratio for coupons obtained from control specimens created using an air pluviation technique resulted in $e = 0.5475$. Measurements of the void ratio on the air-pluviated and then frozen sand specimen resulted in a void ratio of $e = 0.5455$. The slightly lower void ratio of the coupon from the frozen sand samples may be due to an increased amount of fines in the specimen from reusing sand from previous model tests.
- Representative coupon size for image analysis and processing was established to be at least 10 mm by 10 mm and to contain at least between 200 and 250 grains. Local void ratios calculated from the images falling below these criteria exhibited substantially higher deviation from the global void ratio.
- Calculated microstructure parameters included circularity, roundness, aspect ratio and solidity. The obtained values matched well with the subrounded, smooth characteristics of the Ottawa 20/30 sand. The calculated values were less sensitive to the image size used, as opposed to the local void ratio calculations, exhibiting very similar values for images as small as 1.6 mm by 1.6 mm. Resizing did not affect the structure of the sample
- The shape of the rose diagrams of particle orientation obtained from both, the control and frozen coupon specimens, displayed very uniform but very

random plot in each case. It can be concluded that, based on those results, freezing has no significant effect on soil structure

- Relative anisotropy of the control sample and the frozen sample were calculated to be 1.07 and 1.21, respectively. The value of 1.0 would indicate a perfectly isotropic soil fabric structure. The 13 % percent discrepancy might be a result of the variability in the air-pluviation preparation technique between both samples, as well as, image processing/analysis error. That requires further study.

5.3. Recommendations for Future Study

This study developed a procedure to characterize the microstructure parameters of the saturated cohesionless soil specimens. The procedures described in this dissertation can be used to quantify and analyze the variability of the local void ratio in saturated cohesionless soils subjected to liquefaction. The variability of the local void ratio, and the change in fabric anisotropy, can also be quantified inside and outside of their shear failure zones. Standard statistical analysis can be performed to assess variability. However, the work was limited to two coupons extracted from the middle portion of specimen cores: one obtained from an air-pluviated dry sand sample used as a control and one obtained from an air-pluviated sand sample that was then saturated, frozen, cored, and thawed. Additional coupons from the bottom part and top of these samples should be analyzed to study the variability in specimen uniformity. More work could also be performed in the future to characterize the coordination number (number of particle contacts, or N-value) of the specimens as an additional microstructure

parameter of interest. However, this will require additional programming in Java or Matlab within or outside of the *ImageJ* environment.

More extensive analysis needs to be performed to develop an analytical model for the local void ratio frequency distribution histogram. This model can then be used with the Kolmogoroff-Smirnoff test, or some other statistical test, to compare results from different specimens and make statements regarding the confidence that that microstructure is similar or different between two samples.

Additional work needs to be done to verify the inherent built-in error resulting from the use of the Oda's method in calculating the local void ratio when the polygon network is generated. It can then be compared to the error resulting from the use of the voronoi tessellation method, calculated in the results section.

Additional samples need to be processed to study the relative anisotropy variation in frozen sand samples. In this study, a 13 percent discrepancy between the control and the frozen sand coupon was calculated, indicating less than isotropic soil fabric arrangement for the frozen sample. Additional work needs to be done to link this error to either the sample preparation technique or to the image processing and analysis procedure.

6. REFERENCES

- Abraham, IV, G.K. (2010). "How sample preparation influences Metallographic interpretation and image analysis." *Advanced Materials and Processes Webinar*. <<https://asminternational.webex.com/asminternational/ldr.php?AT=pb&SP=MC&rID=15793362&rKey=bae9ccddfe82ef7b>>
- Al-Raoush, R., and Alshibli, K.A. (2005). "Distribution of local void ratio in porous media systems from 3-D x-ray microtomography images." *Physica*, Vol. 361: 441-456.
- Alshibli, K.A., and Sture, S. (1999). "Sand shear band thickness measurements by digital imaging techniques." *J. of Computing in Civil Engrg.*, 3(2): 103-109.
- Alshibli, K. A., and Sture, S. (2000). "Shear band formation in plane strain experiments of sand." *J. of Geotechnical. and Geoenvironmental Engrg.*, 126(6): 495-503.
- Alshibli, K.A., and Alsaleh, M.I. (2004). "Characterizing surface roughness and shape of sands using digital microscopy." *J. Comp. in Civil Engrg.*, Vol.1: 36-45.
- Arnott, S. Fulmer, A., Scott, W.E., Dea, I.C.M., Moorhouse, R., and Rees, D.A. (1974). "The agarose double helix and its function in agarose gel formation." *J. of Molecular Biology*, Vol. 90: 269-284.
- ASTM. (2007). "Standard test method for particle-size analysis of soils D422." *American Society for Testing and Materials*, West Conshohoken, PA.
- Baldock, R., and Graham, J. (2000). "*Image processing and analysis: A practical approach*." New York, NY: Oxford University Press Inc.
- Barryman, J.G., and Blair, S.C. (1986). "Use of digital image analysis to estimate fluid permeability of porous material: Application of two-point correlation functions." *J. Applied Physics*, 60(6): 1930-1938.
- Batiste, S.N., Alshibli, K.A., Sture, S., and Lankton, M. (2004). "Shear band characterization of triaxial sand Specimens using Computed Tomography." *Geotech. Testing J.*, 27(6): 1-13.
- Bhatia, S.K., and Soliman, A.F. (1990). "Frequency distribution of void ratio of granular materials determined by an image analyzer." *Soils and Foundations*, 30(1): 1-17.
- BIOSYNTX, (2005). "Artificial lighting and the blue light hazard." <<http://www.biosyntrx.com/articles.php?id=955>>

- Bishop, A.W. (1948). "A new sampling tool for use in cohesionless sands below groundwater level." *Geotechnique*, 1(2): 125-131.
- Bracewell, R.N. (1956). "Strip integration in radio astronomy." *Australian J. of Physics*, Vol. 9: 198-217.
- Bradbury, S., and Bracegirdle, B. (1998). "*Introduction to light microscopy*." Oxford, UK: BIOS Scientific Publishers.
- Braz D., Da Motta L.M.G., and Lopes R.T. (1999). "Computed tomography in the fatigue test analysis of an asphaltic mixture." *Applied Radiation and Isotopes*, 50(4): 661–71.
- Buehler[®] SUM-MET[™] (2007). "The science behind material preparation: A guide to materials preparation and analysis." <www.buehler.com>
- Chinn, R.E. (2002). "Ceramography: Preparation and analysis of ceramic microstructures." *ASM International*, Materials Park, OH.
- Clayton, C.R.I., Bica, A.V.D., and Moore, S.R. (1994). "Resin impregnation technique for the determination of the density variations in completed specimens of dry cohesionless soil". *Geotechnique* 44(1): 165-173.
- Davidson, D.W. (2010). "Kohler microscope Illumination." <<http://micro.magnet.fsu.edu/primer/anatomy/reflectkohler.html>>
- Davidson, D.W., and Abramowitz, M. (2003). "Optical Microscopy." <<http://micro.magnet.fsu.edu/primer/pdfs/microscopy.pdf>>
- Davis, J.C. (1986). "*Statistics and data analysis in geology*." New York, NY: Wiley.
- Desruses, J., Chambon, R., Mokni, M., and Mazerolle, F. (1996). "Void ratio evolution inside shear bands in triaxial sand specimen studied by Computed Tomography." *Geotechnique*, 46(3): 529–46.
- Dickinson, G.R.E. (1975). "The undisturbed sampling of saturated cohesionless soil using a gelatin injection technique." *MS Thesis*, McMaster University, Hamilton, Ontario, Canada.
- Epotech (2009). "Removing bubbles from epoxy. Tech Tip 4." <<http://www.epotek.com/SSCDocs/techtips/Tech%20Tip%204%20-%20Removing%20Bubbles.pdf>>

- Evans, T.M. (2005). "Microscale physical and numerical investigations of shear banding in granular soils." *PhD Dissertation*. Georgia Institute of Technology, School of Civil and Environmental Engrg., Atlanta.
- Evans, T.M., Chall, S., and Rhyne, T.M. (2009). "Visualization and analysis of microstructure in three-dimensional discrete numerical models." *J. Computing in Civil Engrg.* Vol. 5: 277-287.
- Fiegel, G.L., Hudson, M., Idriss, I.M., and Kutter, B.L. (1994). "Effect of model containers on dynamic soil response." *Proc. International Conference, Centrifuge '94*, Singapore: 145-150.
- Finno, R. J., and Rechenmacher, A. L. (2003). "Effects of consolidation history on critical state of sand." *J. of Geotechnical. and Geoenvironmental Engrg.*, 129(4): 350-360.
- Fisher, N.I. (1993). "*Statistical analysis of circular data.*" London, UK: Cambridge University Press.
- Frost, J.D. (1989). "Studies on the monotonic and cyclic behavior of sand." *PhD Dissertation*, Purdue University, West Lafayette, Indiana.
- Frost, J.D., and Kuo, C.Y. (1996). "Automated determination of the distribution of local void ratio from digital images." *Geotech. Testing J.*, 19(2), 107-117.
- Frost, J.D., and Park, J.Y. (2003). "A critical assessment of the moist tamping technique." *Geotech. Testing J.*, 26(1): 57-70.
- Gilbert, P.A. and Marcuson III, W.F. (1988). "Density variation in specimens subjected to cyclic and monotonic loads." *J. of Geotech. Engrg.*, 114(1): 1-20.
- Griffin, D.F. (1954). "Study and development of methods for determining in-place densities of cohesionless soils." *Proc. American Society for Testing and Material*, Vol. 54: 1270-1287.
- Hahn, R.S. (1966). "On the mechanics of the grinding process under plunge cut conditions." *Trans ASME, J. of Engrg. for Industry*: 72-80.
- Hall C.C., Jupe S.L., Jacques A.C., Livingston S.D.M., Ramadan R., Made A.O.A., Barnes A., and Paul W. (2000). "Non-destructive tomographic energy dispersive diffraction imaging of the interior of bulk concrete." *Cement and Concrete Research*, 30(3): 491-5.
- Hendricksen, K.N. (1941). "Soil stabilization for undisturbed sampling by chemical grouting." *MS Thesis*, University of Maine, Orono, Maine.

- Hvorslev, M.J. (1948). "Foundation exploration: A review of methods and requirements." *Proc. 2nd International Conference on Soil Mechanics and Foundation Engrg.*, Rotterdam.
- Hvorslev, M.J. (1977). "Subsurface exploration and sampling of soils for civil engineering purposes." *Report of Committee on Sampling and Testing. Soil Mechanics and Foundations Division, ASCE*, 521.
- Ibrahim, A.A., and Kagawa. T. (1991). "Microscopic measurement of sand fabric from cyclic tests causing liquefaction." *Geotech. Testing J.*, 14(4): 371-382.
- IFW-Dresden. "Electron Backscatter diffraction."
<<http://www.ifw-dresden.de/institutes/ikm/organisation/dep-31/methods/electron-back-scatter-diffraction-ebds>>
- Insaco, (2011). "Abrasive machining of brittle materials and engineering ceramics." Insaco Technical Note.
<<http://www.azom.com/article.aspx?ArticleID=5588>>
- Ishihara, K., and Silver, M.L. (1977). "Large diameter sand sampling to provide specimens for liquefaction testing." *Proc. 9th ICSMFE Specialty Session 2*, Tokyo, Japan: 1-6.
- Jang, D.J. (1997). "Quantification of sand structure and its evolution during shearing using image analysis." *PhD Dissertation*, Georgia Institute of Technology, Georgia.
- Jang, D.J. (2000). "Use of image analysis to study the microstructure of a failed sand specimen." *Canadian Geotech. J.*, Vol. 37: 1141-1149.
- Jang, D.J., Frost, J.D., and Park, J.Y., (1999). "Preparation of epoxy-impregnated sand coupons for image analysis." *Geotech. Testing J.*, GTJODJ, 22(2), 147-158.
- Johnson, A., Fisher, D., and Voort G.V. (2003). "Precision cutting: The science of the cut." *Tech-Notes, Using Microstructural Analysis to Solve Practical Problems*, 3(6). <<http://www.buehler.com>>
- Jones, Jr., J.S., and Brown, R.E. (1994). "Artificial ground freezing for tunnel construction." *ASCE Annual Convention and Exhibition*, San Francisco, California.
- Jongerious, A., Schoonderbeek, D., and Jager, A. (1972). "The application of the Quantimet 720 in soil micromorphometry." *The Microscope*, Vol. 20: 243-254.

- Kak, A.C., and Slaney, M. (1988). "Principles of computerized tomography." IEEE Press: Piscataway, N.J.
- Karol, R.H., and Mark, L.E. (1962). "Unique use of chemical grout solution promises precise sampling of loose soil." *Engrg. and Mining J.*
- Katapa, K. (2011). "Undisturbed sampling of cohesionless soils for evaluation of mechanical properties and microstructure." *MS Thesis*, Arizona State University, Tempe, Arizona.
- Ketcham, R.A., and Carlson, W.D. (2001). "Acquisition, optimization and interpretation of X-ray computed tomographic imagery: Applications in the geosciences." *Computers and Geoscience*, Vol. 27: 381-400.
- Kolbuszewski, J.J. (1948). "An empirical study of maximum and minimum porosities of sand." *Proc. 2nd ICSMFE*. Vol. 1: 158-165.
- Kuo, C.Y. (1994). "Quantifying the fabric of granular materials: An image analysis approach." *PhD Dissertation*, Georgia Institute of Technology, Georgia.
- Kuo, C.Y., and Frost, J.D. (1996). "Uniformity evaluation of cohesionless specimens using digital image analysis." *J. of Geotech. Engrg.* 122(5): 390-396.
- Krumbein, W.C. (1939). "Preferred orientation of pebbles in sedimentary deposits." *J. Geology*, 47(7): 673-706.
- Landis, E.N., and Keane, D.T. (1999). "X-ray microtomography for fracture Studies in cement-based materials." *Proc. SPIE – The International Society for Optical Engrg.*, 3772. Bellingham, WA, USA, Society of Photo-Optical Instrumentation Engineers: 105–13.
- Lightfoot, T.B. (1886). "Institute of Mechanical Engrg." London, Vol. 5, 238.
- Marinescu, I.D., Uhlmann E., Doi, T.K., Dimitrov, B., and Inasaki, I. (2007). "*Handbook of lapping and polishing*." Boca Raton, FL: CRC Press, Taylor and Francis Group.
- Marinescu, I.D., and Rowe, B.W., (2004). "Trilogy of abrasive machining processes." Norwich, NY: Noyes Publications William Andrew Inc.
- Martys, N., Masad, E., and Muhunthan, B. (2000). "Simulation of fluid flow and permeability in cohesionless soils." *Water Resources Research*, 36(4): 851-864.

- Masad, E., and Muhunthan, B. (2000). “Three-dimensional characterization and simulation of anisotropic soil fabric.” *J. of Geotech. and Geoenvironmental Engrg.*, 126(3): 199-207.
- Masad, E., Olcott, D., White, T., and Tashman, L. (2001). “Correlation of fine aggregate imaging shape indices with asphalt mixture performance.” *Transportation Research Record 1757*, Transportation Research Board, Washington, D.C: 148–156.
- Matheron, G. (1975). “*Random sets an integral geometry.*” Wiley, NY
- Mitchell, J.K. (2008). “Aging of sand: A continuing enigma?” *Proc. 6th International conference on Case Histories in Geotech. Engrg.*, Arlington, VA: SOAP 11.
- Miura, S., and Toki, S. (1982). “A sample preparation method and its effect on static and cyclic deformation: Strength properties of sand.” *Soil and Foundations*, 22(1): 61-77.
- Mooney, M. A., Finno, R. J., and Viggiani, M. G. (1998). “Unique critical state for sand.” *J. of Geotechnical. and Geoenvironmental Engrg.*, 124(11): 1100-1108.
- Oda, M. (1972). “Initial fabric and their relations to mechanical properties of granular materials.” *Soils and Foundations*, 12(1):17-36.
- Oda, M. (1972a). “The mechanism of fabric changes during compressional deformation of sand.” *Japanese Society of Soil Mechanics and Foundation Engrg.*,12(2):1-18.
- Oda, M. (1976). “Fabric and their effects on the deformation behavior of sand.” Special Issue, Dept. of Foundation Engineering, Saitama University, Japan.
- Oda, M. (1977). “Coordination number and its relation to shear strength of granular materials.” *Soil and Foundations*, 17(2): 29-42.
- Oda, M., Koishikawa, I., and Higuchi, T. (1978). “Experimental study of anisotropic shear strength of sand by plane strain test.” *Soils and Foundations*, 18(1), 24-38.
- Oda, M., Nemat-Nasser, S., and Mehrabadi, M.M. (1982).”A statistical study of fabric in a random assembly of spherical granules.” *International J. for Numerical and Analytical Methods in Geomechanics*, Vol. 6:77-94.

- Oda, M., and Kazama, H. (1998). "Microstructure of shear bands and its relation to the mechanisms of dilatancy and failure of dense granular soils." *Geotechnique*, 48(4): 465-481.
- Panton, D.M. (1981). "Mathematical reconstruction techniques in computer axial tomography." *Math. Sci.*, Vol.6: 87-102.
- Park, J.Y. (1999). "A critical assessment of moist tamping and its effect on the initial and evolving structure of dilatant triaxial specimens." *PhD Dissertation*, Georgia Institute of Technology, Georgia.
- Pearson, E.S., and Hartley, H.O. (1972). "Biometrika tables for statistics" London, UK: Cambridge University Press, Vol. 2.
- Porex. "Sheet specs." *Interstate Specialty Products*. Sutton, MA. <<http://www.interstatesp.com/porshtsp.html>.>
- Powers, M. C. (1953). "A new roundness scale for sedimentary particles." *J. Sediment. Petrol.*, 23(2): 117-119.
- Powers, M. C. (1982). "Comparison charts for estimating roundness and sphericity." *AGI Data Sheets*, American Geological Institute, Alexandria, Va.
- Prakongkep, N., Suddhiprakarn, A., Kheoruenromne, I., and Gilkes, R. (2010). "SEM image analysis for characterization of sand grains in Thai paddy soils." *Geoderma*, Vol. 156: 20-31.
- Radaelli F., Balzarini M., Nicula S., and Ortenzi A. (1998). "Rock structure characterization through imaging techniques integration." Society of Petroleum Engineers : *Proc. European Petroleum Conference*, Vol. 1. Richardson, TX.
- Raveia, M.A., Hendrickson, S.B., Fitzgerald, J.T., Krekeler, M.P.S., and Kearns, L.E. (2008). "Investigation of impurities of the Ottawa standard sand." *Geological Society of America*, 40(6): 360.
- Rosenfeld, A. and Pfaltz, J.L. (1966). "Sequential operations in digital picture processing." *J. ACM*, Vol. 13: 471-494.
- Rowe, B.W. (2009). "Principles of modern grinding technology." Burlington, MA: William Andrew Elsevier Inc., 1st edition.
- Santamarina, J.C., and Cho, G.C. (2003). "Determination of critical state parameters in sandy soils: Simple procedure." *Geotech. Testing J.*, 24(2): 185-1923.

- Schneider, H.R., Chameau J., and Leonards G.A. (1989). "Chemical impregnation of cohesionless soils." *Geotech. Testing J.*, 12(3): 204-210.
- Sergio, R., and Otazu, D. (1992). "The Influence of fines content and specific surface area on freezing of sandy soils." *MS Thesis*, University of Alberta.
- Shahinpoor, M. (1981). "Statistical mechanical considerations on storing bulk solids." *Bulk Solids Handling*, Vol. 1: 31-36.
- Shahinpoor, M., and Shahrpass, A. (1982). "Frequency distribution of voids in monolayers of randomly packed equal spheres." *Bulk Solid Handling*, Vol. 2: 825-838.
- Shannon, C.E. (1948), "A mathematical theory of communication." *Bell Sys. Tech. J.*, Vol. 27.
- Sierra, J. (1982). "*Image analysis and mathematical morphology.*" London, UK: Academic Press. Vol. 1.
- Singh, S., Seed, B.H., and Chan, C.K. (1982). "Undisturbed sampling of saturated sands." *J. of Geotech. Engrg.*, 108(2): 247-264.
- Slatt, R.M. (1973). "Frosted beach sand grains on the Newfoundland continental shelf." *Geological Society of American Bulletin*, (84): 1807-1812.
- Stormont, J. C., and Anderson, C. E. (1999). "Capillary barrier effect from underlying coarser soil layer." *J. of Geotechnical and Geoenvironmental Engrg.*, 125(8): 641-648.
- Sutterer, K.G. (1993). "Undisturbed sampling of cohesionless soils using polymer impregnation." *PhD Dissertation*, Georgia Institute of Technology, Atlanta, GA.
- Sutterer, K.G., Frost, J.D., and Chameaou, J.A. (1996). "Polymer impregnation to assist in undisturbed sampling of cohesionless soils." *J. of Geotech. Engrg.*, 1996(3): 209-215.
- Thanachit, S., Uddhiprakaru, A., Kheoruenromne, I., and Gilkes, R.J. (2009). "Quartz sand grain size and surface morphology in some tropical soils." *Thai J. of agricultural Science*, 42(1): 41-60.
- U.C. Berkley (2004). "Relationship between height of fall and density of Ottawa 20/30 sand." Personal Content, Dr. Michael Reiner, U.C. Berkeley, CA to Prof. Edward Kavazanjian, Arizona State University, Tempe, AZ.

- U.S. Silica Company (2011). "Product Data, ASTM 20/30 Underground Silica." Berkeley Springs, WV.
<<http://www.u-s-silica.com/media/12643/ottastm2030sand2000.pdf>>
- UTCT, (2009). "High resolution x-ray CT facility: Lab capabilities and Instrumentation." <<http://www.ctlab.geo.utexas.edu/labcap/index.php>>
- Van Bruggen, J.P. (1936). "Sampling and testing undisturbed sand from boreholes." *Proc. International Conference on Soil Mechanics*, Harvard, Vol. 1: 3-6.
- Vander, G.F.V. (2000). "Trends in specimen preparation." *Advanced Materials and Processes J.* <<http://www.buehler.com>>
- Yamamuro, J.A. (2008). "Effect of depositional method on the undrained behavior and microstructure of sand with silt." *Canadian Geotech. J.*, 45(11): 1525-1537.
- Yang, C. (2002). "Boundary condition and inherent stratigraphic effects on microstructure evolution in sand specimens." *PhD Dissertation*, Georgia Institute of Technology, Georgia.
- Yang, X. (2005). "Three-dimensional characterization of inherent and induced sand microstructure" *PhD Dissertation*, Georgia Institute of Technology, School of Civil and Environmental Engineering, Atlanta.
- Yoshimi, Y., and Hatanaka, M. (1973). "In-situ density measurement of a loose saturated sand deposit" *Proc. 10th Symposium of Disaster Science*: 341-342.
- Yoshimi, Y., Hatanaka, M., and Oh-oka, H. (1978). "Undisturbed sampling of saturated sands by freezing." *Soils and Foundations*, 18(3): 59-73.
- Wadell, H. (1932). "Volume shape and roundness of rock particles." *J. Geol.*, Vol.40: 443-488.
- Wang L.B. (2004). "Characterization of asphalt concrete using X-ray tomography." *Proc. 1st International Workshop on X-ray CT for Geomaterials, Soils, Concrete and Rock*, Kumamoto, Japan.
- Wang, L., Park J.Y., and Fu, Y. (2007). "Representation of real particles for DEM simulation using X-ray Tomography." *Construction and Building Materials*, Vol. 21: 338-346.
- Whalley, W.B. (1980). "A scanning electron microscope examination of subglacial quartz grains from camp century cores, Greenland: A preliminary study." *J. of Glaciology*, 25(91): 125-132.

Wei, S.H. (2010). "Application Lab Report." <<http://www.alliedhightech.com>>

Wildenschild, D., Hopmans, J.W., Vaz, C.M.P., Rivers, M.L., Rikard, D., and Christensen, B.S.B. (2002), Using X-ray computed tomography in hydrology: Systems, resolutions, and limitations." *J. Hydrology*, Vol. 267: 285-297.

APPENDIX A
EUROPEAN AND USA EQUIVALENCY GRIT GUIDE
(WWW.BUEHLER.COM)

European/USA Equivalency Grit Guide				
FEPA (Europe)		ANSI/CAMI (USA)		
Grit Number	Size(μm)	Grit Number	Size(μm)	Emery Grit
P60	269.0	60	268.0	
P80	201.0	80	188.0	
P100	162.0	100	148.0	
P120	127.0	120	116.0	
P180	78.0	180	78.0	3
P240	58.5	220	66.0	2
P280	52.2	240	51.8	
P320	46.2			
P360	40.5	280	42.3	1
P400	35.0	320	34.3	0
P500	30.2	360	27.3	
P600	25.8	400	22.1	00
P800	21.8			
P1000	18.3	500	18.2	000
P1200	15.3	600	14.5	
P1500	12.6	800	12.2	0000
P2000	10.3	1000	9.2	
P2500	8.4	1200	6.5	
P4000*	5.0*			

The chart shows the midpoints for the size ranges for ANSI/CAMI graded paper according to ANSI standard B74.18-1996 and for FEPA graded paper according to FEPA standard 43-GB-1984 (R1993). The ANSI/CAMI standard lists SIC particles sizes ranges up to 600 grit paper. For finer grit ANSI/CAMI papers, the particles sizes come from the CAMI booklet, Coated Abrasive (1996).

*FEPA grades finer than P2500 are not standardized and are graded at the discretion of the manufacturer. In practice, the above standard values are only guidelines and individual manufactures may work to a different size range and mean value.

APPENDIX B

SAND COUPON SURFACE PREPARATION METHOD, MODIFIED FROM
BUEHLER DIALOG[®] METHOD (JANG, 1999).

A. Sectioning:

Saw: ISOMET 1000 (with rotating chuck)
Blade: 15LC watering blade
Load: 300 gram after balance
Speed: less than 350 rpm, make sure the cutting is smooth
Cutting fluid: 9 parts water : 1 part cutting fluid

B. Grinding and Polishing:

Grinder: 12" wheel grinder

Wheel Surface	Abrasive Type/Size	Mixing	Cutting Powder Quantity	Speed, rpm	Pressure	Process Time	Lubrication Extender	Maintenance
Cast Iron Platen	600 grit SIC	3 oz./quart anti-freeze	as needed	120	1.5-2 psi	Until flat, takes about 8 - 10 minutes	-	Clean with a Nylon brush, wipe the platen dry with paper or cloth, and apply oil to prevent rusting, which can happen overnight. Resurface the surface when it is not flat.
Ultra Plan	9 µm METADI II paste		4" ribbon initially and then add 1" every 3 minutes	120	1.5-2 psi	4 - 5 minutes	METADI fluid every 30 seconds, 10 drops	Occasionally wash the surface with water to clean out the powder residue. Replace the Ultra Plan only when strands start to break or it can not grind the specimen effectively.
Texmet 1000	6 µm METADI II paste		4" ribbon initially and then add 1" every 3 minutes	120	0.5-1 psi	about 10 minutes, or until getting desired features image	METADI fluid every 30 seconds, 10 drops. However, keep the polishing cloth on the dry side.	Replace after approximately 8-10 hours of use or when it starts to tear.



APPENDIX C

POLISHING CLOTH SELECTION GUIDE FROM BUEHLER® AND ALLIED

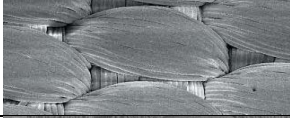
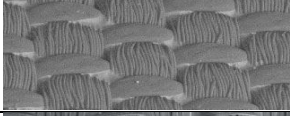
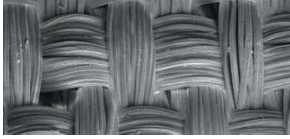
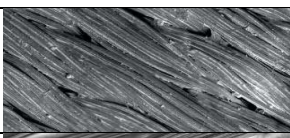
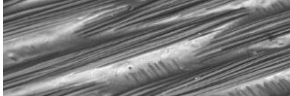


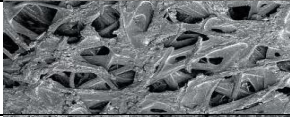
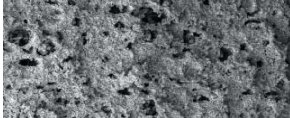
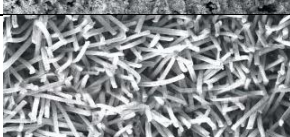
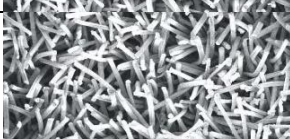
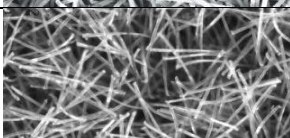
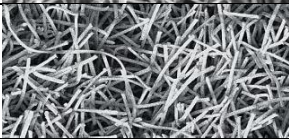
HIGH TECH PRODUCTS INC

(WWW.BUEHLER.COM AND WWW.ALLIEDHIGHTECH.COM)

BUEHLER® Polishing Cloths

Premium Cloths	Recommended Micron Size	Abrasive Type	Cloth Characteristics	Usage Guide	Applications
UltraPad™	15-3	Diamond	Hard Woven, No Nap with High Material Removal	Used to Replace Multiple SiC Grinding Steps	Ferrous Materials and Thermal Spray Coatings
UltraPol™	15-1	Diamond	Hard Woven, No Nap	Excellent Surface Finish used to retain flatness in medium to hard specimens	Minerals, Coal, and Ceramics, Inclusion Retention in Steels, and Refractory Metals
Nylon	15-1	Diamond	Medium Hard Woven, No Nap	Used to Retain Flatness and Hard Phases	Ferrous Materials, Sintered Carbides and Cast Irons
TexMet® P	15-3	Diamond	Hard Perforated Non-woven Pad for High Material Removal	Used for Material Removal and Flatness of Hard Specimens	Ceramics, Carbides, Petrographic, Hard Metals, Glass, Metal Matrix Composites
 TexMet®	15-3	Diamond, Al ₂ O ₃	Non-woven Pad for Surface Finish	Most Popular Cloth for Intermediate Steps, Good for Most Materials	Ferrous and Nonferrous Metals, Ceramics, Electronic Packages, PCB's, Thermal Spray Coatings, Cast Irons, Cermets, Minerals, Composites, Plastics
TriDent™	15-1	Diamond	Softer, Durable, Woven Synthetic, No Nap	Used to Maximize Flatness and Retain Phases while Providing Excellent Surface Finish	Ferrous and Nonferrous Metals, Microelectronics, Coatings
VerduTex	15-1	Diamond	Durable, Medium Hard Synthetic Silk	Used for rough and final polishing.	Ferrous and Nonferrous Composite Material and Plastic (CFK, GFK)
VelTex	9-1	Diamond	Short-napped Synthetic Velvet	Ideal for final polishing	Steel, Non Ferrous and Soft Materials
WhiteFelt®	6-0.02	Diamond, Al ₂ O ₃ , SiO ₂	Soft and Durable Matted Wool Cloth	General Usage for Intermediate to Fine Steps	Ferrous and Nonferrous Metals
MicroFloc	6-1	Diamond	Medium Hard, Napped Rayon Cloth	Good results when used with unmounted specimens	Ferrous and Nonferrous Materials
PolCloth	6-1	Diamond	Medium Hard, Woven Wool Cloth	General Usage	Cast iron, copper and aluminum alloys, coal and other soft materials
 MicroCloth®	5-0.02	Diamond, Al ₂ O ₃ , SiO ₂	Synthetic Cloth with Medium Nap	Most Popular General Usage Final Polishing Cloth	Ferrous and Nonferrous Metals, Ceramics, Composites, PCB's, Cast Irons, Cermets, Plastics, Electronics
MasterTex®	1-0.05	Al ₂ O ₃ , SiO ₂	Soft Synthetic Velvet with Low Nap	Softer Final Polishing Cloth	Soft Nonferrous and Microelectronic Packages
ChemoMet®	1-0.02	Al ₂ O ₃ , SiO ₂	Soft Synthetic Cloth	General Usage Cloth that Removes Smear Metal from Tough Materials during Chemomechanical Polishing	Titanium, Stainless Steels, Lead/Tin Solders, Electronic Packages, Soft Nonferrous Metals, Plastics

Allied High Tech, Inc. Polishing Cloths

Name	Image	Description
PLAN-Cloth		Durable, coarsely woven polyester with hard resin coating used with diamond (30-6 micron) and either BlueLube™ or GreenLube™ lubricant. Provides aggressive stock removal and excellent flatness on all types of materials
PLAN-B		Rigid, densely woven polyester used with diamond (15-3 micron) and any lubricant. Maintains superior edge retention and flatness, providing aggressive material removal for coarse to intermediate polishing of metals, ceramics and refractory materials
Gold Label		Specially woven, extremely durable, long-lasting napless nylon used with diamond (15-3 micron) and any lubricant*. Provides excellent flatness and material removal on a wide variety of materials, especially those with varying hardness. Exceptional for intermediate polishing of refractory metals, glass, ceramics, coatings and composites.
TECH-Cloth		Tightly woven silk used with diamond (9-1 micron) and either GreenLube™ or RedLube™ lubricant. Reduces smearing and pullout, providing excellent finish, flatness and edge retention. Especially good for coatings and samples composed of materials with varying hardness
White Label		Durable, densely woven napless silk with plastic barrier used with diamond (6-0.25 micron) and any lubricant*. Provides excellent flatness and edge retention prior to final polishing on a wide variety of materials
Nylon		Napless woven nylon used with diamond (15-3 micron) and any lubricant. Provides good flatness and edge retention for most materials
DiaMat		Medium-napped, low resilient durable woven wool used with diamond (6-0.25 micron) and any lubricant. Provides excellent edge retention and surface finish on hard materials, often good enough for a final polish using 3 or 1 micron diamond.
Pan-B		Dense, non-woven, planarized textile used with diamond (9-1 micron) and either RedLube™ or GreenLube™ lubricant. Provides superior cutting rates, edge retention and flatness on a variety of different materials
Final A		Dense, napless polyurethane used with diamond (1-0.05 micron), colloidal (0.06-0.02 micron) or alumina suspensions. Excellent for final polishing a wide variety of materials. Especially effective in eliminating smearing and pullout when preparing soft metals (e.g. copper, aluminum, etc.) and porous structures/ceramics.
Final P		Dense, rigid, low napped synthetic flock used with diamond (3-0.1 micron) and any lubricant, or with colloidal silica and/ or alumina. Ideal for final polishing soft metals such as copper and aluminum.
Imperial		Rigid, medium-low-napped, synthetic rayon flock used with diamond (9-0.25 micron), colloidal silica (0.06-0.02 micron) or alumina and either RedLube™ or GreenLube™ lubricant. Very good all-purpose final polishing cloth
Spec-Cloth		Soft, medium-napped, synthetic rayon flock used with diamond (1-0.25 micron) or alumina and either RedLube™ or GreenLube™ lubricant. For general polishing of a wide range of materials.
Red Final C		Dense, low-napped silk used with colloidal silica (0.06-0.02 micron) or alumina to provide an excellent final polish on a wide variety of materials. Especially effective when preparing materials for SEM or TEM evaluation

APPENDIX D

METPREP 3™ SYSTEM POLISHING PROCEDURE FOR GEOLOGICAL

SAMPLES FROM ALLIED HIGH TECH INC (WEI, 2010)

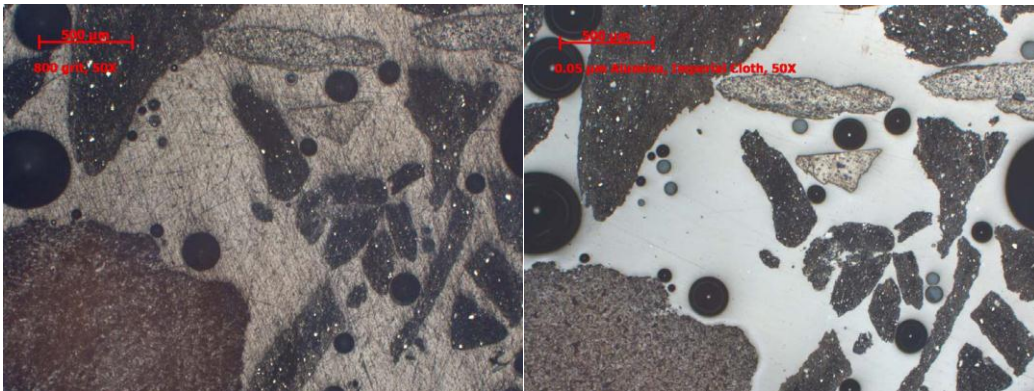
Table on a Polishing Procedure for Geological Samples.

	Step	1	2	3	4
Consumables	Abrasive	600 Grit	800 Grit	0.3 μm	0.05 μm
	Type	SiC	SiC	Alumina	Alumina
	Carrier	Abrasive Paper	Abrasive Paper	Suspension	Suspension
	Polishing Cloth	-	-	Spec-Cloth	Imperial Cloth
Settings	Coolant	Water	Water (drip)	Water*	Water*
	Platen Speed (RPM) / Direction	150 / comp	150 / comp	120 / contra	120 / contra
	Sample Speed (RPM)	60	60	60	60
	Force (lbf)/Sample	4	4	4	4
	Time (min)	Until Flat	2	2	2

Comp: platen and sample holder rotate in the same direction.

Contra: platen and power head rotate in opposite directions.

* Water is only used to pre-soak and final rinse the cloths.



Resulting Images: Surface Condition after the 800 Grit Step, 50x, Brightfield (left), Surface Condition after the 0.05 μm Step, 50x, Brightfield (right).

APPENDIX E
GUIDE FOR SELECTING PRECISION SAW WAFERING BLADES
(JOHNSON, 2003)

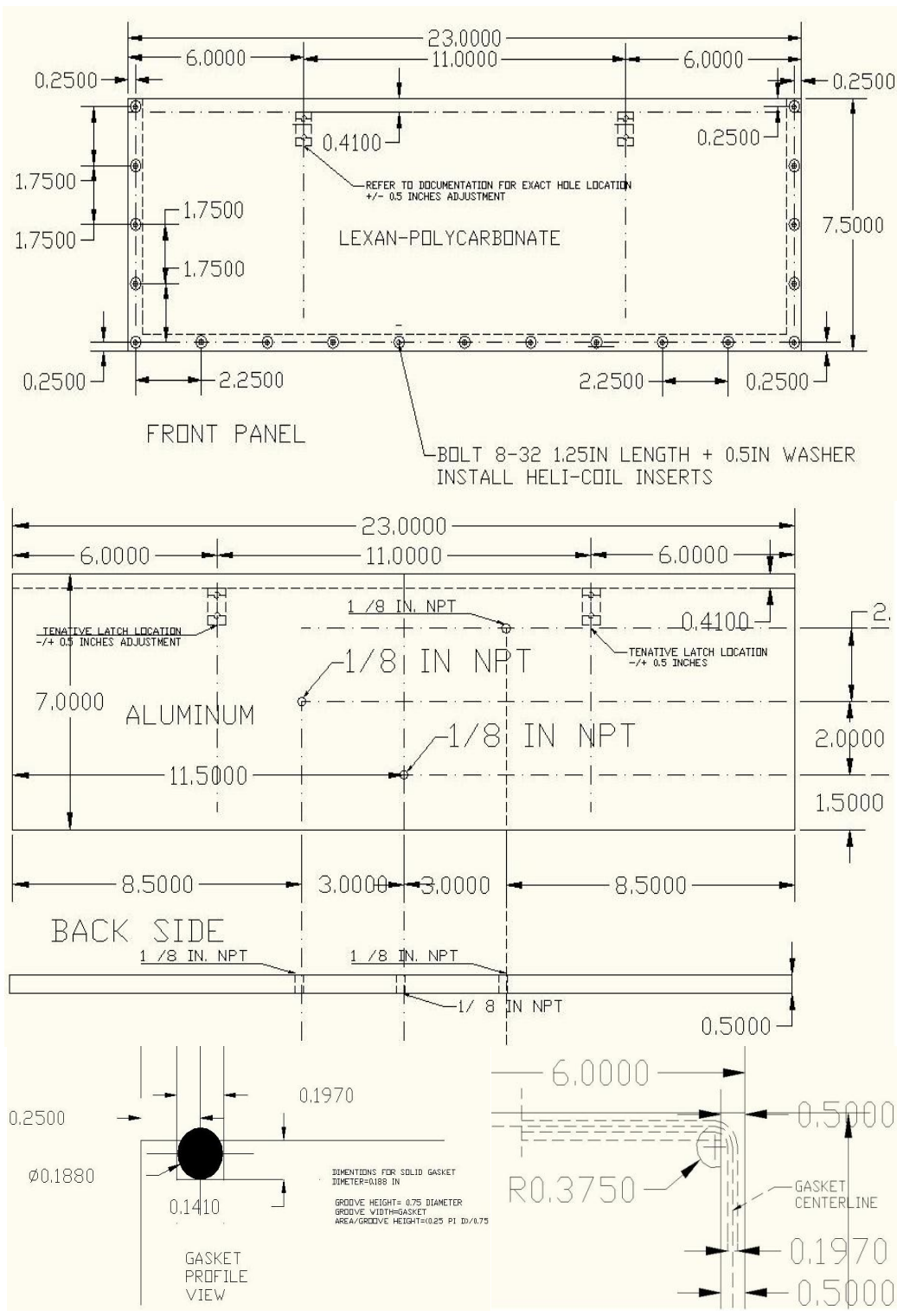
BLADE SERIES/SIZE	Abrasive	Particle Size	Applications	Diameters Available
30 High Concentration	Diamond	Very Coarse	For polymers, rubber and other soft, gummy materials	5, 7 and 8 inch (127, 178 and 203mm)
20 High Concentration	Diamond	Coarse	For aggressive cutting of ferrous and harder nonferrous metals	5, 7 and 8 inch (127, 178 and 203mm)
15 High Concentration	Diamond	Medium Coarse	For routine use, for metal-matrix composites, PC boards, bone, most nonferrous metals and refractory metals, such as titanium, and thermal spray coated specimens	3, 4, 5, 6, 7 and 8 inch (76, 102, 127, 152, 178 and 203mm)
20 Low Concentration	Diamond	Coarse	For use with very hard materials: ceramics, carbides and nitrides	5 and 8 inch (127 and 203mm)
15 Low Concentration	Diamond	Medium Coarse	For use with very hard materials (less aggressive than 20LC) plus glass, electronic devices, and concrete	3, 4, 5, 6, 7 and 8 inch (76, 102, 127, 152, 178 and 203mm)
10 Low Concentration	Diamond	Fine	For use with lower hardness ceramics, electron devices and packages, GaAs, AlN and glass-fiber reinforced composites	3, 5, 7 and 8 inch (76, 127, 178, and 203mm)
5 Low Concentration	Diamond	Very Fine	For use with softer, friable ceramics, composites with fine reinforcements, CaF ₂ , MgF ₂ and carbon composites	5 inch (127mm)
ISOCUT®	Cubic Boron Nitride	Medium Coarse	For iron and iron-based alloys, superalloys, nickel, cobalt and lead (and their alloys)	3, 4, 5, 6, 7 and 8 inch (76, 102, 127, 152, 178 and 203mm)
METABRASE™	Al ₂ O ₃	NA	For iron-based alloys	7 inch (178mm)
METABRASE™	SiC	NA	For nonferrous metals and alloys	7 inch (178mm)
ACU-THIN™	Al ₂ O ₃	NA	For hard steels, ≥45 HRC	5 inch (127mm)
ACU-THIN™	Al ₂ O ₃	NA	For soft steels, ≤45 HRC	5 inch (127mm)

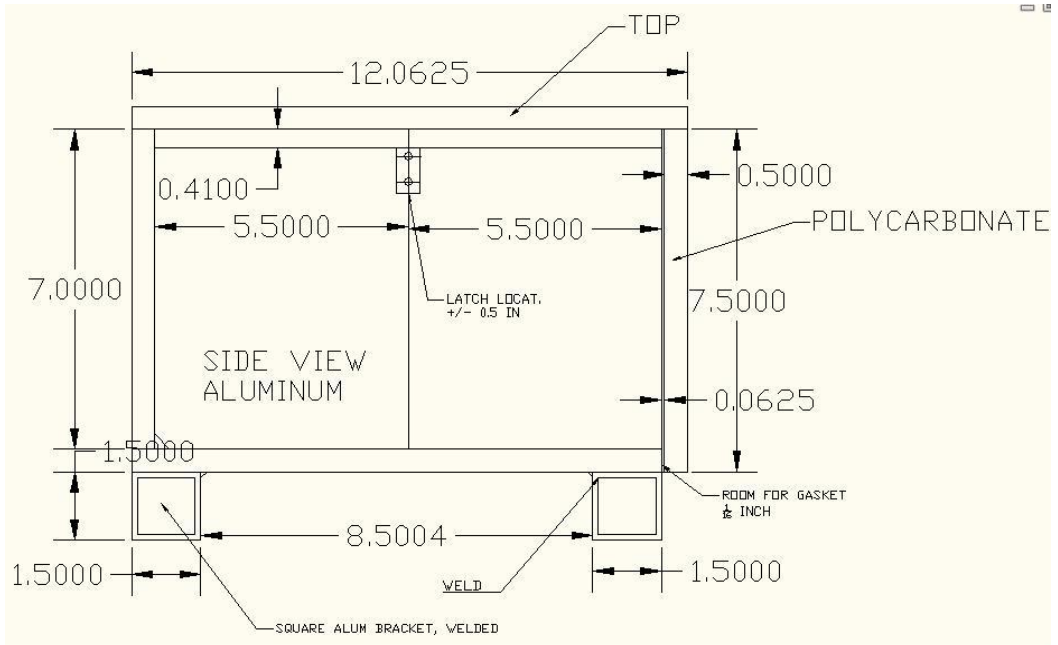
NA-not applicable

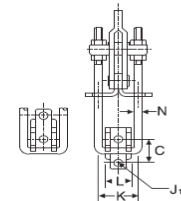
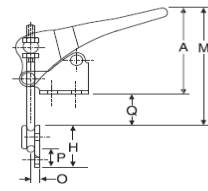
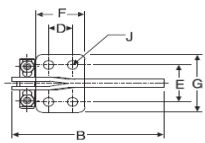
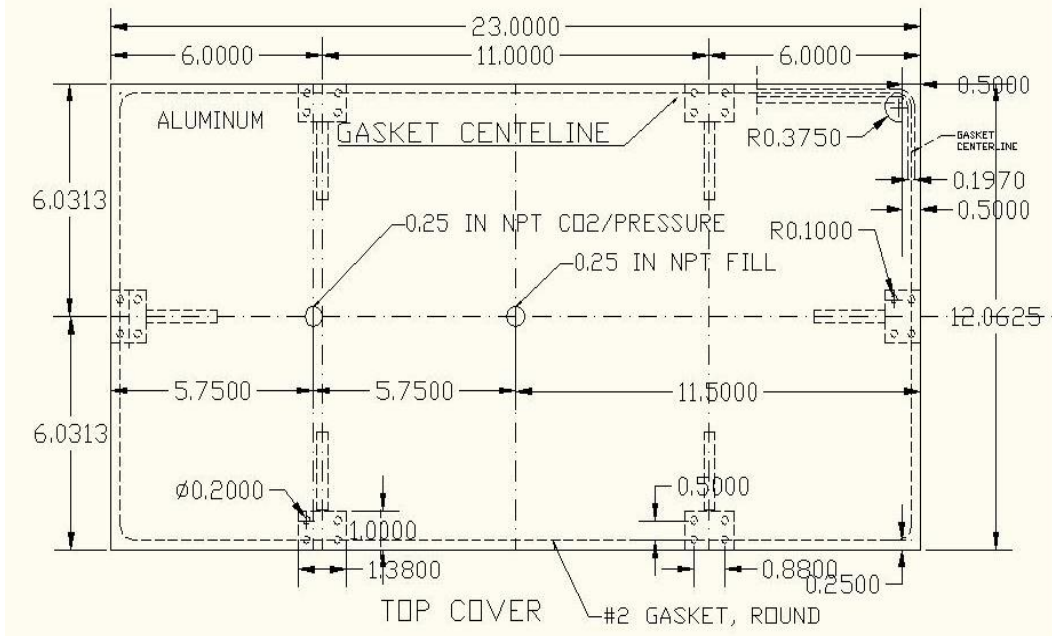
APPENDIX F

BOX DESIGN DRAWINGS FOR THE BOX USED IN LIQUEFACTION,

FREEZING AND SPECIMEN EXTRACTION EXPERIMENTS





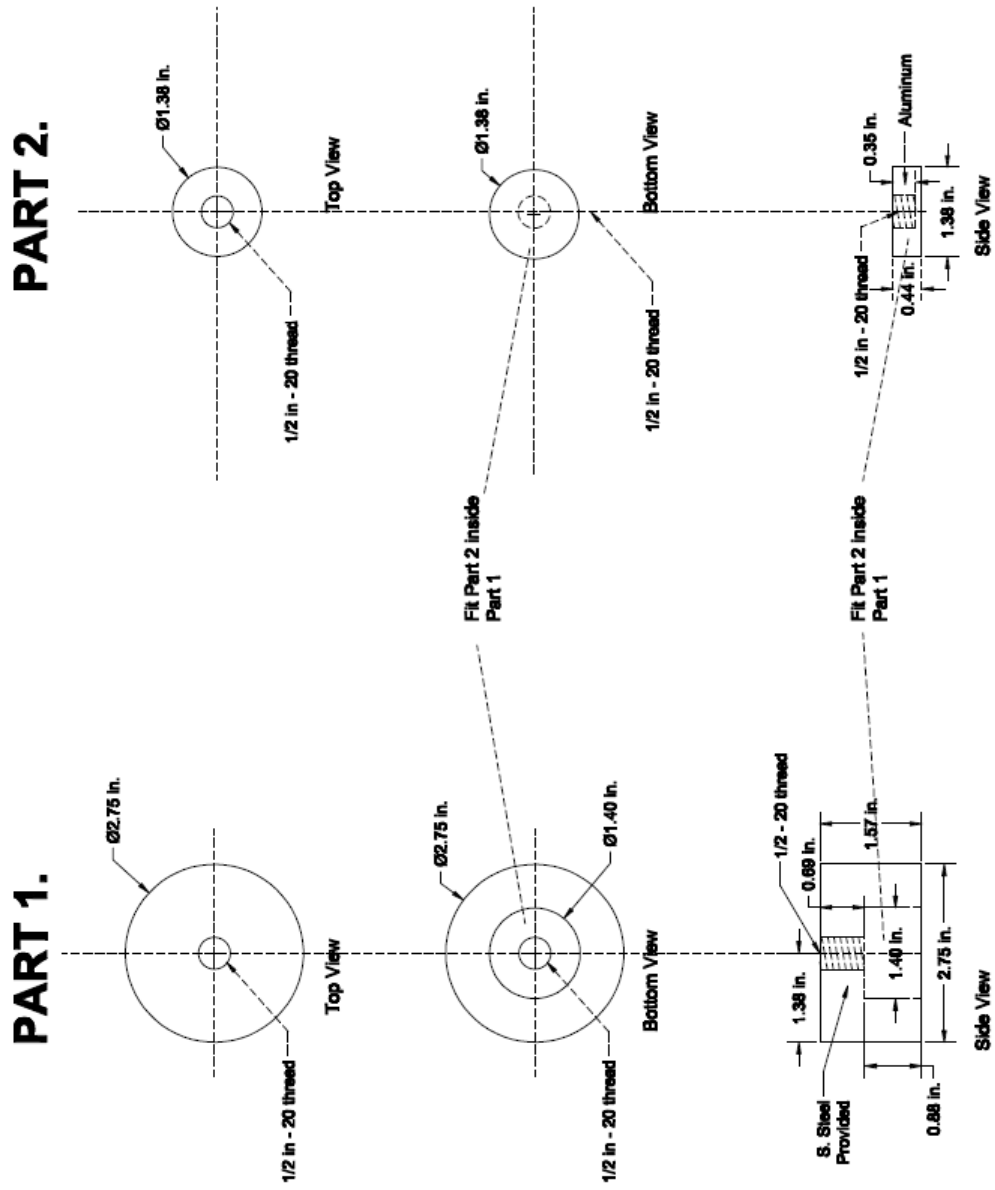


Latch plate included with all clamps listed below except TC-374. Furnished with a thumb control lever.
Discount 29 applies.

Cat. No.	A	B	C	D	E	F	G	H	Drawing Movement	J	J1	K	L	M	N	O	P	Q	Thread Size	Holding Capacity (Lbs)	Price Each 1-49	
Steel																						
TC-324	2.00	3.35	.56	.50	.88	1.00	1.38	1.00	1.53	.20	.17	.81	.53	2.69	.14	.19	.63	.91	M4	500	17.43	
TC-334	2.44	4.25	.81	.75	1.00	1.31	1.56	1.50	2.00	.28	.22	1.13	.68	3.69	.25	.35	.69	1.35	M6	1,000	21.63	

APPENDIX G

HAND GRINDING/POLISHING JIG DESIGN SPECIFICATIONS



APPENDIX H

CONSUMABLES USED IN MANUAL POLISHING OF EPOXY-
IMPREGNATED SAND COUPONS (WWW.ALLIEDTECH.COM)

1. **Diamond Abrasive Compound Paste (Monocrystalline)**
Provides good stock removal and finish. It has slightly irregular shape with multiple cutting edges and is recommended for general applications. Water soluble and compatible with glycol or alcohol based lubricants. Used alone or as a base product before applying diamond suspension to polishing cloths. Monocrystalline grit 45 μm to 0.25 μm .



2. **Diamond Suspensions (Water Based)**
The diamond particles remain suspended and separated throughout the stable liquid carrier to distribute diamond easily and uniformly over the cloth or platen surface. 99% water based formula recommended for manual application. Monocrystalline grit 45 μm to 1 μm .



3. **Alumina Suspension**
De-agglomerated and water based. Chemically stable. Clean alternative to powers. Ideal for the finest finishes. Pre-mixed. Grit sizes 1 μm to 0.05 μm .



4. **Green Lube**



Used to enhance the polishing performance of diamond suspensions, compounds and sprays. They reduce friction, increase the life of polishing cloths and are also used with lapping film for polishing hard, dense materials or soft ductile metals. This is water based lubricant used for general metallographic preparation. Recommended for bot manual and automatic applications.

APPENDIX I

LUMENERA'S INFINITY 2-1 CCD DIGITAL CAMERA PERFORMANCE

SPECIFICATIONS (WWW.LUMENERA.COM)

Camera Sensor

Image Sensor	1/2" Interline Sony ICX205 1.4 megapixel color or monochrome progressive scan CCD sensor 7.6mm x 6.2mm array
Effective Pixels	1392x1040, 4.65µm square pixels
Frame Rate	15 fps at 1392 x 1040, >200 fps with binning and ROI
Dynamic Range	>66dB
Digital Output	8 and 12-bit
Read Noise	12 e- rms
Readout Frequency	28.6 MHz
Dimensions (W x H x D)	2.25 x 3.85 x 1.56 inches (enclosed)

Camera Controls

Mass	300g
Power Requirement	USB bus power, or external 5VDC - 500mA
Power Consumption	~2.5Watts
Operating Temperature	0° C to +50° C
Operating Humidity	5%-95%, Non-condensing
Integration Time	1/1000 to 16 sec.
Shutter	Global Shutter
ROI	User Selectable
Auto Exposure	Automatic / Manual
White Balance	Automatic / Manual
Gain	Programmable / 1 to 10x optimizable
Interface Connector	Standard USB 2.0 high-speed interface
Dimensions (L x W x H)	3.85 x 2.00 x 2.75 inches
Lens Mount	C-Mount lens adapter
Binning Options	2x2, 3x3, 4x4

Recommended PC Specs:

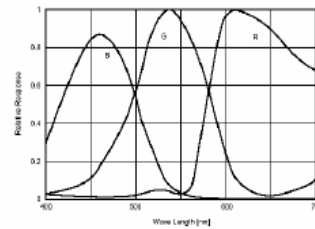
- Pentium 4, 1.3 GHz or higher
- 512MB RAM
- 60 MB hard drive free space or more
- USB 2.0 Port
- Windows 2000 or XP

Minimum PC Specs:

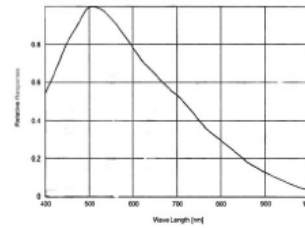
- 600 MHz Processor
- 256 MB of SDRAM
- 20 MB hard drive free space
- USB 2.0 Port
- Windows 98 or ME with a USB 2.0
- Add-in card and driver

Product Includes:

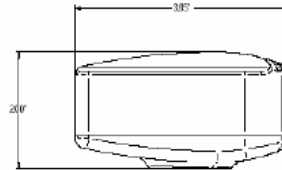
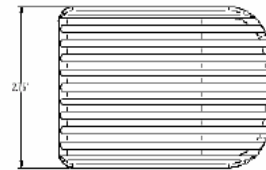
- INFINITY2-1 digital camera for USB 2.0
- CD-ROM with Infinity user application software
- TWAIN driver
- Documentation
- USB 2.0 cable



Color Response Curve



Mono Response Curve



Ordering Information

INFINITY2-1C – Color Camera

INFINITY2-1M – Monochrome Camera

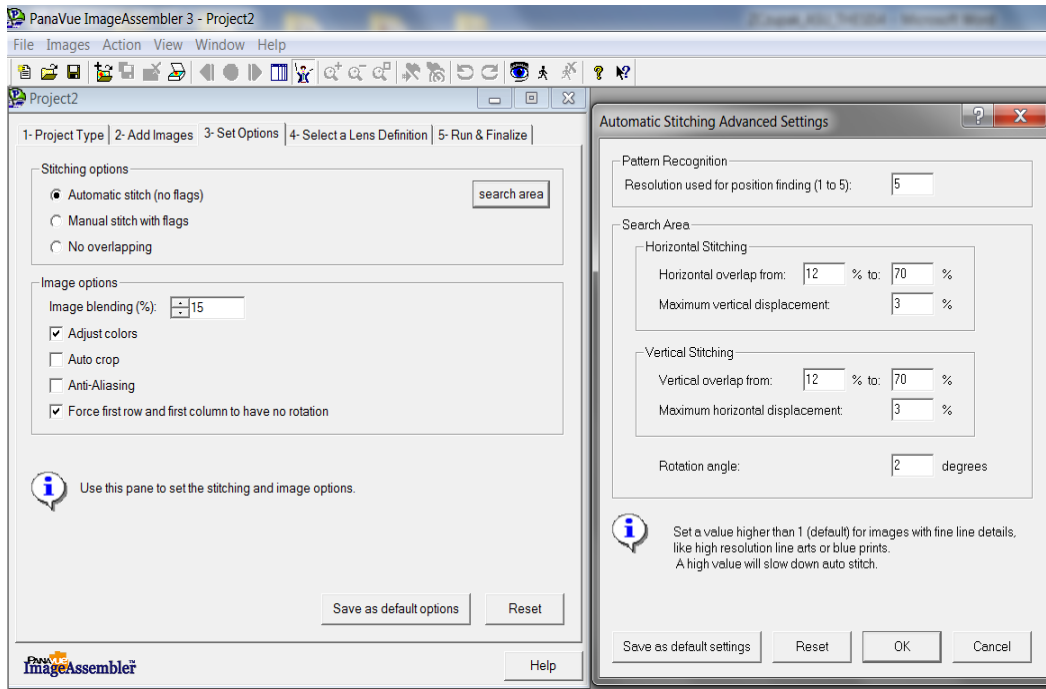
**Full customization available
to meet your exact needs!**

APPENDIX J

IMAGE STICHING WITH PANA VUE SOFTWARE IMAGE ASSEMBLER

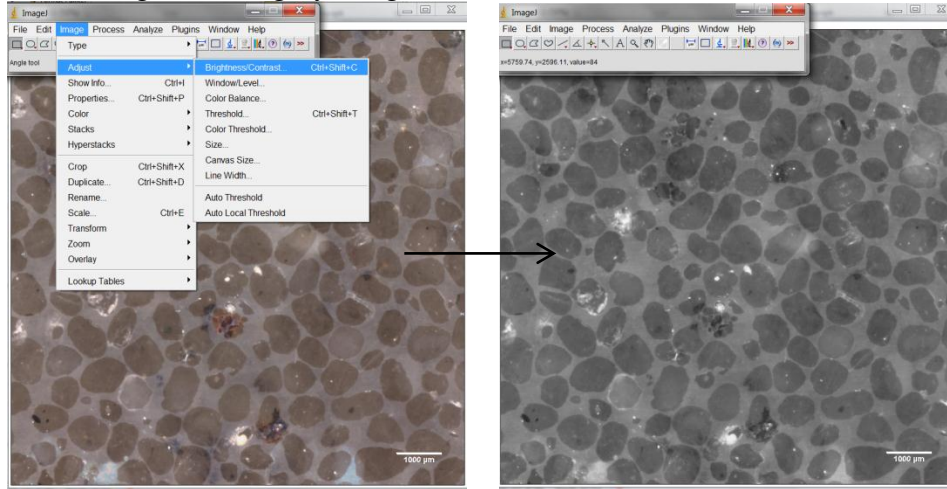
(WWW.PANAVUE.COM)

1. File → New Project → Mosaic Stitching
2. Add Images:
 - a. Stich images from top-to-bottom and left-to-right only.
 - b. Initially combine sets of images into single rows (load left-to-right).
 - c. Combine rows to form a final image (load top-to-bottom).
 - d. Stitching large subsets can result in errors; switch to manual alignment, eliminate some images to reduce overlap.
3. Automatic stitching setup.
 - a. Increase Pattern Recognition resolution to prevent loss of image quality.
 - b. Minimize rotational displacement and rotational angle (vertical and horizontal) to prevent blurring.
4. Manual stitching setup.
 - a. Used when automatic stitching fails.
 - b. Stich points are tagged manually.
 - c. Minimize image blending to prevent blurring and loos of data.
 - d. No Image Aliasing, it causes blurring.
 - e. Force first row and first column to have no rotation .

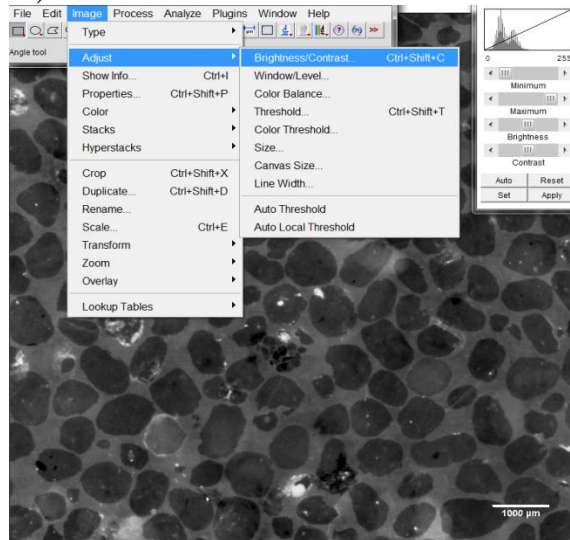


APPENDIX K
IMAGE PROCESSING ALGORITHM FOR BINARY IMAGE CONVERSION
USING IMAGEJ

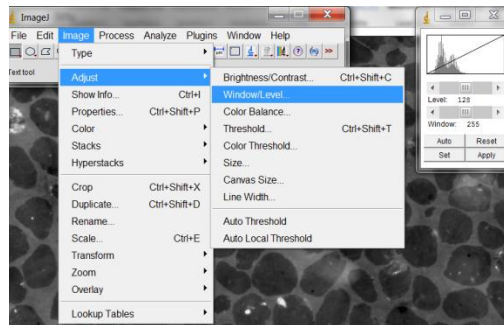
1. Color image to 8 bit gray image.



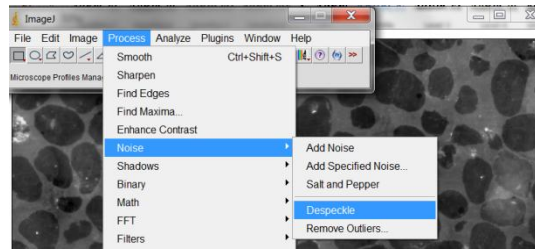
2. Brightness (Auto)



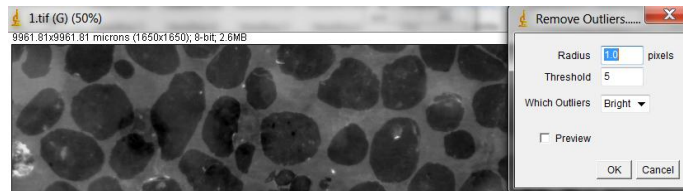
3. Window (Auto)



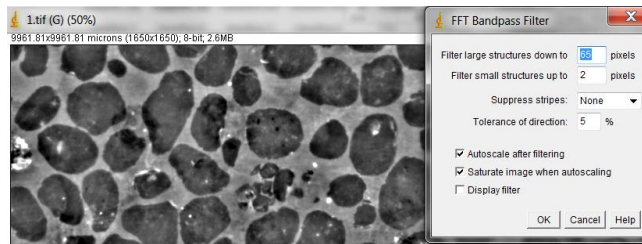
4. Despeckle



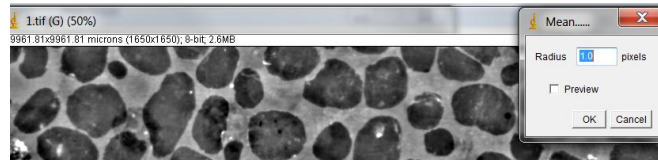
5. Outliers



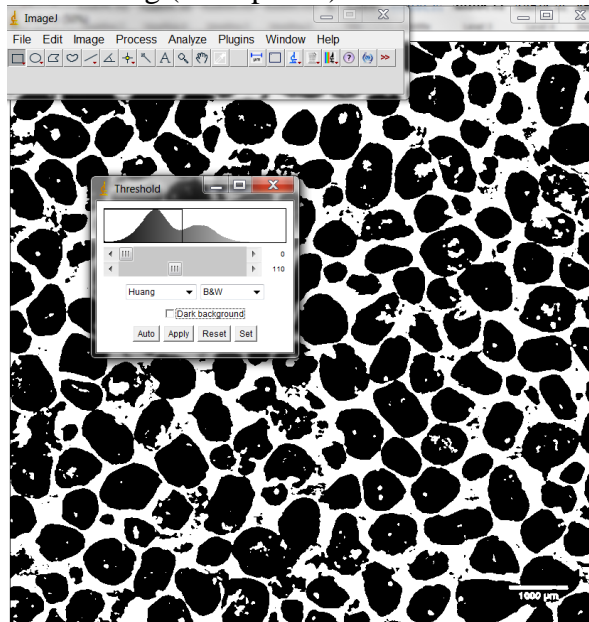
6. Bandpass Filter



7. Mean Filter

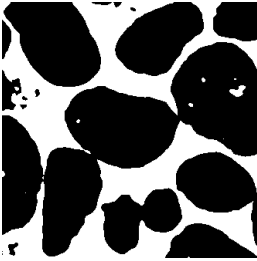
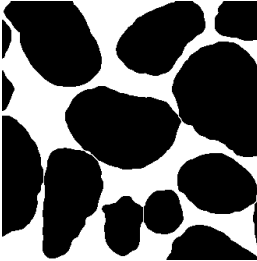
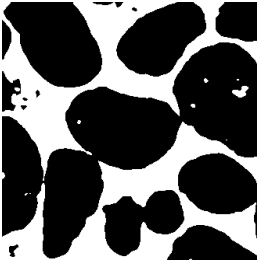
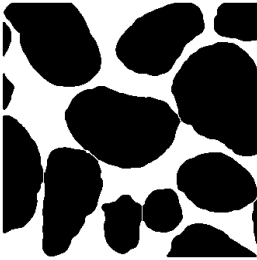
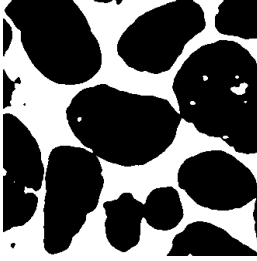
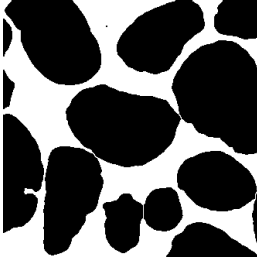
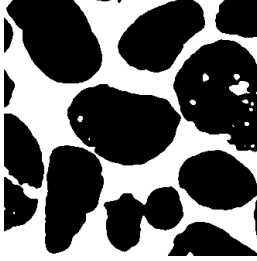
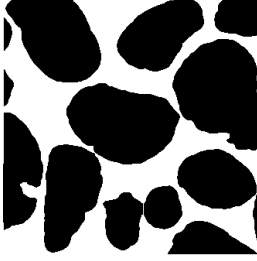
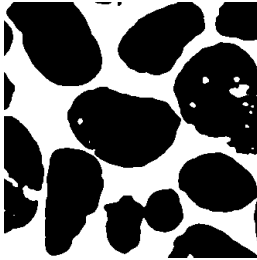
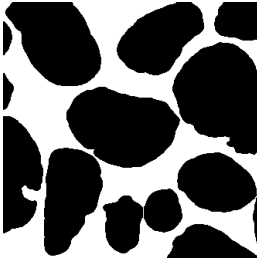


8. Threshold with Huang (Auto plus 7)

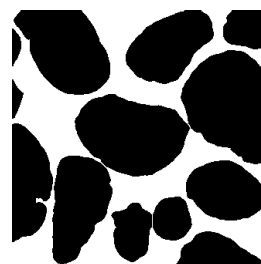
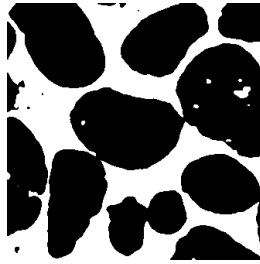


APPENDIX L
SEGMENTATION CALIBRATION RESULTS FOR VARIOUS
THRESHOLDING METHODS

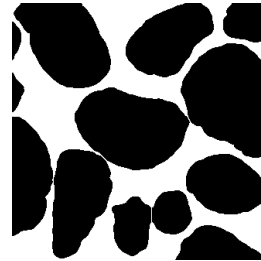
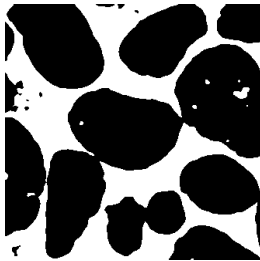
THRESH- OLDING METHOD	A_{total} (μm^2)	A_s (μm^2)	A_v (μm^2)	E (%)	Error (%)	VALUE AUTO +7
Control	4,005,692	2,689,477	1,316,215	48.934	0	NA
Huang	4,005,692	2,690,461	1,315,231	48.885	0.111	139
Intermodes	4,005,692	2,658,092	1,347,600	50.698	-3.593	138
IsoData	4,005,692	2,652,443	1,353,249	51.019	-4.249	132
Li	4,005,692	2,543,526	1,462,166	57.486	-17.463	119
MaxEntropy	4,005,692	2,580,488	1,425,204	55.230	-12.854	121
MinError	4,005,692	2,656,707	1,348,985	50.777	-3.754	133
Minimum	4,005,692	2,675,152	1,330,541	49.737	-1.630	136
Moments	4,005,692	2,542,506	1,463,186	57.549	-17.592	117
Otsu	4,005,692	2,650,912	1,354,780	51.106	-4.427	132
Percentile	4,005,692	2,203,656	1,802,036	81.775	-67.094	95
RenyiEntropy	4,005,692	2,575,676	1,430,016	55.520	-13.446	120
Shabthag	4,005,692	2,670,850	1,334,842	49.978	-2.122	135
Triangle	4,005,692	2,650,328	1,355,364	51.139	-4.495	132

METHOD	SEGMENTED IMAGE	PROCESSED IMAGE
• Huang		
• Intermodes		
• IsoData		
• Li		
• MaxEntropy		

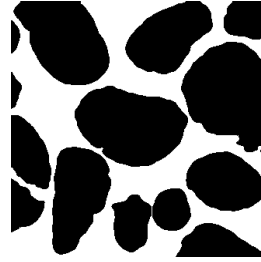
- MinError



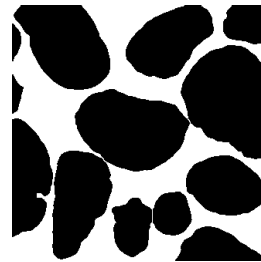
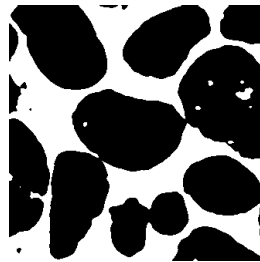
- Minimum



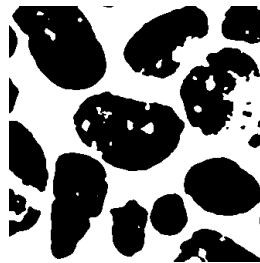
- Moments



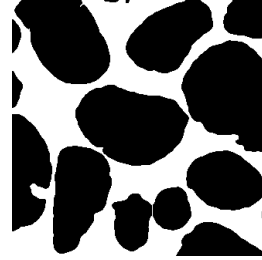
- Otsu



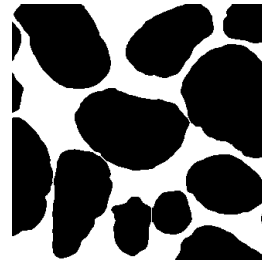
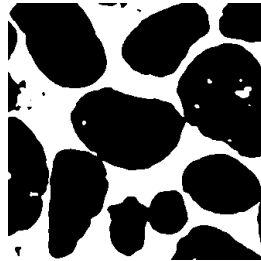
- Percentile



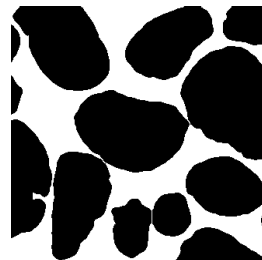
- RenyiEntropy



- Shabhag



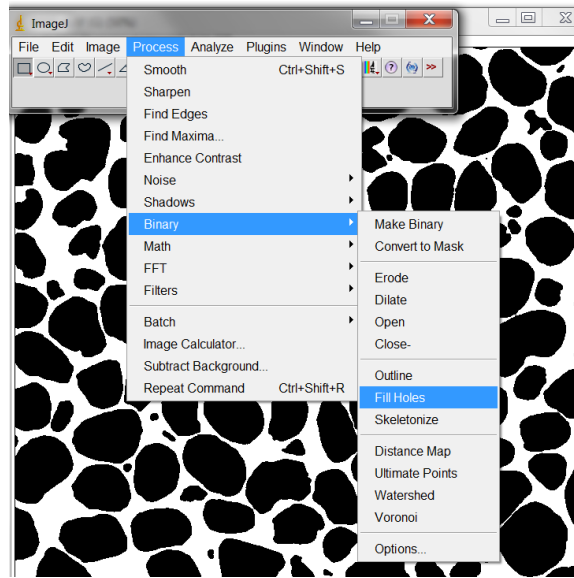
- Triangle



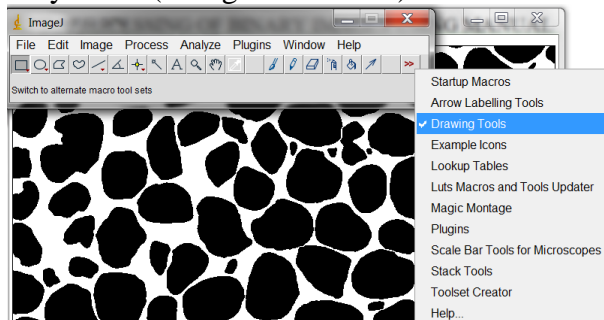
APPENDIX M

IMAGEJ IMAGE SCREEN CAPTURES AND PROGRAM SETTINGS
USED IN PROCESSING OF BINARY IMAGES USING MANUAL
AND MATHEMATICAL MORPHOLOGY TECHNIQUES

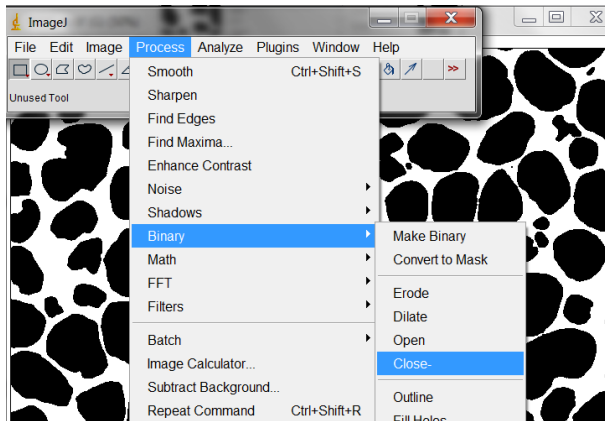
1. Fill Holes



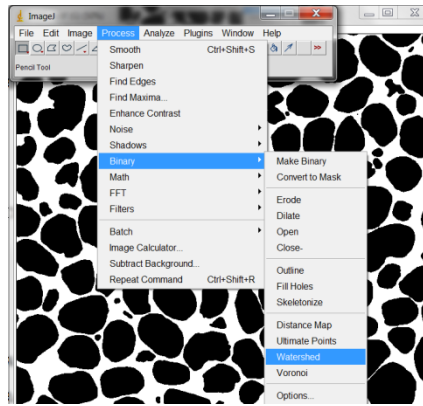
2. Remove Outliers by Hand (Using Draw Tools)



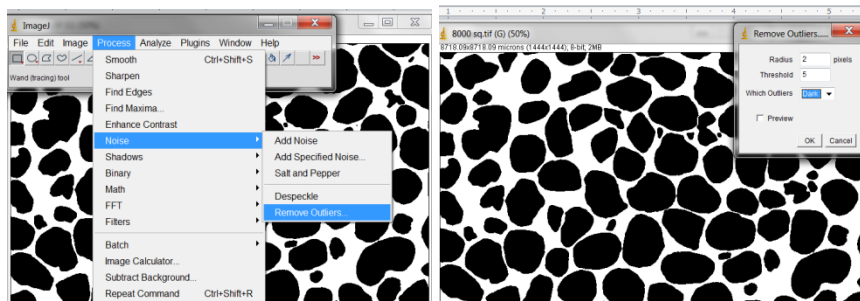
3. Close



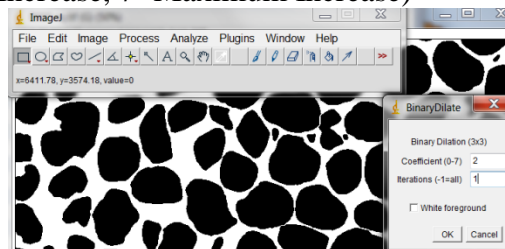
4. Watershed



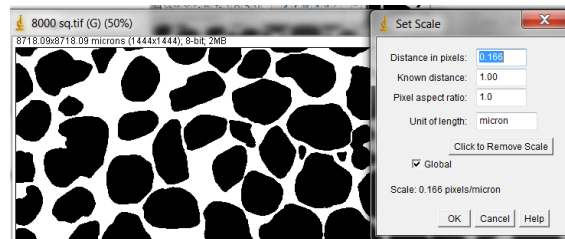
5. Remove Outliers



6. Binary Dilate (Plugin→Morphology→Binary Dilate)
Coefficient (0-No Dilation, 7- Maximum Dilation)
Iteration (1-Small Increase, 7- Maximum Increase)



7. Analyze → Set Scale



Based on Total Image Dimensions:

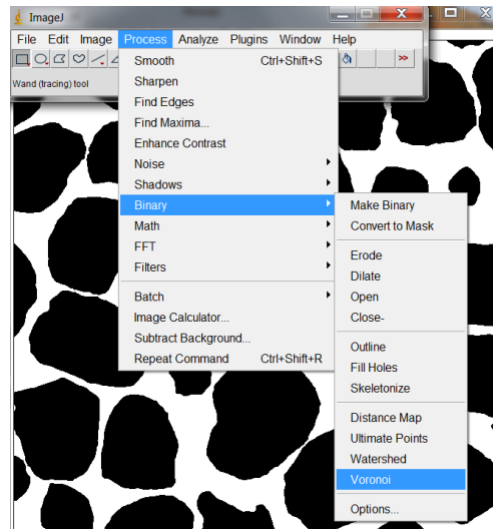
Distance in Pixels: Based on Image Resolution

Known Distance: Image Width Measured During BFM

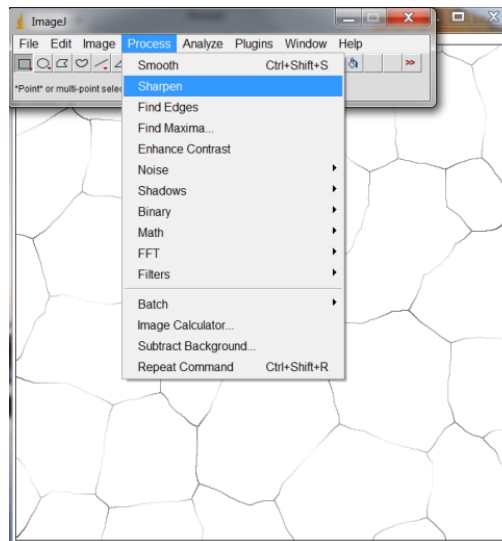
Unit Length: Use Microns for Better Accuracy where 1 mm = 1000 μ m

APPENDIX N
POLYGON NETWORK GENERATION AND LOCAL VOID
RATIO CALCULATIONS USING VORONOI TESSELLATION
METHOD

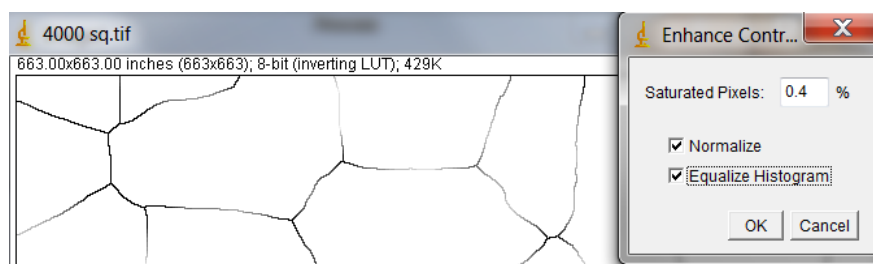
1. Voronoi (Process → Binary → Voronoi).



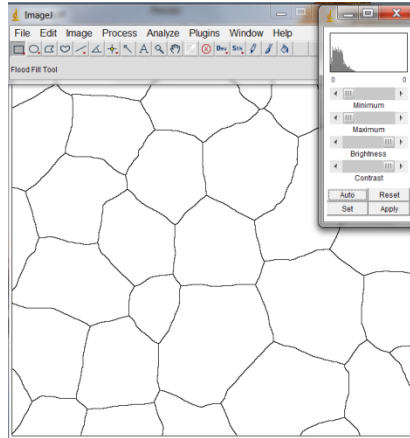
2. Sharpen.



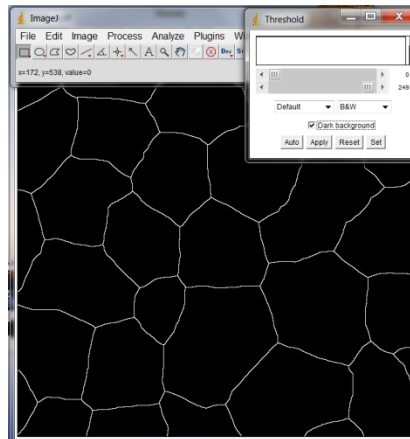
3. Enhance Contrast (Process → Enhance → Contrast).



4. Adjust Brightness/Contrast (Image → Adjust → Brightness/Contrast).



5. Threshold (Image → Adjust → Threshold)



6. Make Binary (Process → Binary → Make Binary).
7. Skeletonize (If Polygon Network Thickness > 1 pixel).
8. Calculate Areas Within Polygon Networks, $(A_T)_i$.
9. Subtract Grain Area $(A_V)_i$ to Obtain Area of Air Voids, $(A_V)_i$.
10. Calculate $e_i = (A_V)_i / (A_V)_i$